

Sheffield Hallam University

Noise and crosstalk analysis of all-optical time division demultiplexers.

CHEUNG, Chin Ying.

Available from the Sheffield Hallam University Research Archive (SHURA) at:

<http://shura.shu.ac.uk/19455/>

A Sheffield Hallam University thesis

This thesis is protected by copyright which belongs to the author.

The content must not be changed in any way or sold commercially in any format or medium without the formal permission of the author.

When referring to this work, full bibliographic details including the author, title, awarding institution and date of the thesis must be given.

Please visit <http://shura.shu.ac.uk/19455/> and <http://shura.shu.ac.uk/information.html> for further details about copyright and re-use permissions.

SHEFFIELD S1 1WB

101 624 182 8



Return to Learning Centre

Fines are charged at 50p per hour

21 AUG 2003 5 PM

29 MAY 2004

5 PM

-5 OCT 2004

REFERENCE

ProQuest Number: 10694336

All rights reserved

INFORMATION TO ALL USERS

The quality of this reproduction is dependent upon the quality of the copy submitted.

In the unlikely event that the author did not send a complete manuscript and there are missing pages, these will be noted. Also, if material had to be removed, a note will indicate the deletion.



ProQuest 10694336

Published by ProQuest LLC (2017). Copyright of the Dissertation is held by the Author.

All rights reserved.

This work is protected against unauthorized copying under Title 17, United States Code
Microform Edition © ProQuest LLC.

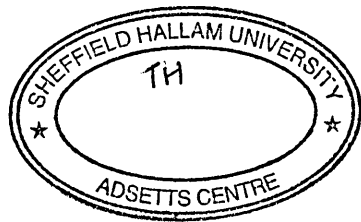
ProQuest LLC.
789 East Eisenhower Parkway
P.O. Box 1346
Ann Arbor, MI 48106 – 1346

**Noise and Crosstalk Analysis of All-optical Time
Division Demultiplexers**

Chin Ying CHEUNG

**A thesis submitted in partial fulfilment of the requirements
of Sheffield Hallam University for the degree of
Doctor of Philosophy**

December 2001



ABSTRACT

Bandwidth limitation of conventional electrical demultiplexer restricts the data capacity of long-haul optical time division multiplexing (OTDM) systems. It is desirable to demultiplex the OTDM signal in optical domain, thereby lifting the bandwidth limitation of the electrical demultiplexer. The general principle of all-optical time division demultiplexing is to effect asymmetric changes to the optical properties of the target and non-target channels. The different optical properties of the target and non-target channels facilitate the separation of the target channel(s) from the aggregate OTDM signal. The change of optical properties of the OTDM signal can be achieved by exploiting various types of nonlinear optics effects, such as cross-phase modulation and four-wave mixing. Although the technical viability of all-optical demultiplexing has been successfully demonstrated in laboratories, there is still a lack of understanding regarding the noise and crosstalk characteristics of all-optical demultiplexers. This PhD study attempts to investigate noise and crosstalk performance of two types of all-optical time division demultiplexers, namely nonlinear optical loop mirror (NOLM) and terahertz optical asymmetric demultiplexer (TOAD).

In order to evaluate the noise and crosstalk performance of NOLM and TOAD demultiplexers, mathematical models are developed to simulate the transmission window for demultiplexing the target channel. The shape of the transmission window is dependent on the device parameters of the demultiplexers. Varying input parameters of the mathematical models can simulate the effects of changing device parameters on the transmission window. Nevertheless, it is onerous to calculate transmission windows for infinite combinations of device parameters. To simplify the noise and crosstalk analysis, device parameters of NOLM and TOAD demultiplexers are optimised for maximising the peak of the transmission windows. Noise and crosstalk models are also developed for

NOLM and TOAD demultiplexers. The optimised device parameters of NOLM and TOAD demultiplexers are fed into the noise and crosstalk models for analysis. Simulation results show that a tradeoff between noise and crosstalk exists for the two types of demultiplexers. Device parameters can be optimised to minimise either noise or crosstalk, but not both. Finally, the noise and crosstalk models are connected to a receiver model, where the bit-error-rate (BER) performance of OTDM systems is evaluated. The BER performances of the NOLM and TOAD demultiplexing are compared using the optimised device parameters. It is found that TOAD has a slightly better BER performance compared with NOLM for lower baseband bit rate (i.e. a larger number of OTDM channels for an aggregate bit rate).

TABLE OF CONTENTS

	Page
GLOSSARY OF ABBREVIATIONS	i
GLOSSARY OF SYMBOLS	iii
LIST OF FIGURES	viii
LIST OF TABLES	xiii
ACKNOWLEDGEMENTS	xv
DECLARATION	xvi
CHAPTER ONE - INTRODUCTION	
1.1 Introduction	1
1.2 Aims and Objectives	3
1.3 Original Contributions	3
1.4 Publications	4
CHAPTER TWO – LITERATURE REVIEW: WDM AND OTDM	
2.1 Introduction	5
2.2 Historical Background	6
2.3 Essential Components for WDM Transmission / Network	10
2.4 Essential Components for OTDM Systems	13
2.5 Technological Challenges of Long-haul High Capacity WDM Transmission	16
2.6 Technological Challenges of long-haul High Capacity OTDM Transmission	22
2.7 The Future	26
CHAPTER THREE – NONLINEAR FIBRE OPTICS	
3.1 Introduction	29
3.2 Pulse Propagation in Optical Fibre	30
3.2.1 Nonlinear Schrödinger equation	30
3.2.2 Beam Propagation Method	33
3.2.3 Pulse deformation	35
3.3 Optical Soliton	37
3.3.1 Optical Soliton at the anomalous dispersion wavelength	37
3.3.2 Optical soliton at zero dispersion wavelength	43
3.3.3 Soliton interaction	45
3.4 Cross Phase Modulation	48
3.4.1 Optical Kerr effect	49
3.4.2 The effect of XPM on polarisation-maintaining fibre	53
3.5 Stimulated Raman scattering	55
3.6 Four Wave Mixing	57
3.7 Summary	59
CHAPTER FOUR – SEMICONDUCTOR LASER AMPLIFIER	
4.1 Introduction	60
4.2 Operation Principles	61
4.3 Rate Equations	65
4.4 Light Propagation inside a SLA	70
4.4.1 Gain Spectrum	70
4.4.2 Unsaturated and saturated gain	72
4.4.3 SPM and XPM in SLA	73
4.4.4 Fast gain recovery in subpicosecond pulse	76
4.5 Summary	82

CHAPTER FIVE – MATHEMATICAL MODEL FOR NONLINEAR OPTICAL LOOP MIRROR DEMULTIPLEXER

5.1	Introduction	83
5.2	Operation Principles	83
5.3	Mathematical Model	87
5.3.1	Assumptions of the model	87
5.3.2	Peak transmittance of the switching window	90
5.3.3	Width of soliton switching window	99
5.3.4	Soliton switching profile	107
5.4	Verification of the Model	112
5.5	Summary	119

CHAPTER SIX – NOISE AND CROSSTALK ANALYSIS FOR THE NONLINEAR OPTICAL LOOP MIRROR DEMULTIPLEXER

6.1	Introduction	120
6.2	Noise and Crosstalk in NOLM demultiplexing	120
6.2.1	Relating intensity noise	120
6.2.2	NOLM residual crosstalk	122
6.2.3	Neighbour channel crosstalk	125
6.3	Crosstalk and Noise Analysis	125
6.3.1	Simulation results of NOLM relative intensity noise	126
6.3.2	Simulation results of NOLM residual crosstalk	129
6.3.3	Simulation results of neighbour channel crosstalk	131
6.3.4	Tradeoff between noise and crosstalk in NOLM demultiplexing	135
6.4	Summary	137

CHAPTER SEVEN - NOISE AND CROSSTALK ANALYSIS OF THE TERHERTZ OPTICAL ASYMMETRIC DEMULTIPLEXER USING A COMPUTER MODEL

7.1	Introduction	138
7.2	Operation Principles	138
7.3	TOAD Model	140
7.3.1	Switching window equation for TOAD	140
7.3.2	SLA model	141
7.3.3	TOAD switching window	146
7.3.4	Optimisation of switching energy	149
7.3.5	Limitation on signal intensity	152
7.4	Crosstalk and Noise Analysis	154
7.4.1	TOAD relative intensity noise	156
7.4.2	TOAD crosstalk	158
7.4.3	Tradeoff between noise and crosstalk in TOAD demultiplexing	165
7.5	Summary	168

CHAPTER EIGHT - BIT ERROR RATE PERFORMANCE OF NOLM AND TOAD DEMULTIPLEXER

8.1	Introduction	169
8.2	Gordon-Haus Jitter and Relative Intensity Noise	170
8.2.1	Equations for Gordon-Haus jitter	170
8.2.2	Simulation results	172
8.3	Receiver Model	175
8.4	BER Analysis	181
8.4.1	Simulation results for 100 Gb/s demultiplexing	183
8.4.1.1	100 Gb/s demultiplexing (10 OTDM channels)	183
8.4.1.2	100 Gb/s demultiplexing (100 OTDM channels)	192
8.4.2	Simulation results for 300 Gb/s demultiplexing	195

8.4.2.1	300 Gb/s demultiplexing (30 OTDM channels)	195
8.4.2.2	300 Gb/s demultiplexing (300 OTDM channels)	198
8.5	Summary	201
CHAPTER NINE – CONCLUSIONS AND FURTHER WORKS		
9.1	Conclusions	202
9.1	Conclusions	205
REFERENCES		207
APPENDIX		220

GLOSSARY OF ABBREVIATIONS

3R	Retiming, Reshaping and Regenerating
ADM	Add Drop Multiplexer
ANSI	American National Standards Institute
ASE	Amplified Spontaneous Emission
AWG	Arrayed-Waveguide Grating
BER	Bit Error Rate
BPF	Band Pass Filter
BPM	Beam Propagation Method
C-Band	Conventional Band
CCW	Counter Clockwise
CW	Clockwise
DBF-LD	Double Feedback Laser Diode
DSF	Dispersion Shifted Fibre
EDFA	Erbium-doped Fibre Amplifier
FDM	Frequency Division Multiplexing
FP-SLA	Fabry-Perot SLA
FWM	Four Wave Mixing
FWHM	Full Width Half Maximum
I/O	Input / Output
L-Band	Long-wavelength Band
MZI	Mach-Zehnder Interferometer
NOLM	Nonlinear Optical Loop Mirror
NSE	Nonlinear Schrödinger Equation
NXT	Neighbour Channel Crosstalk

OPC	Optical Phase Conjugation
OTDM	Optical Time Division Multiplexing
PC	Polarisation Controller
PDH	Plesiochronous Digital Hierarchy
PM	Polarisation-maintaining
PSTN	Public Switch Telephone Network
RIN	Relative Intensity Noise
RMS	Root-Mean-Square
RXT	Residual Crosstalk
SGS	Self-Gain Saturation
SLA	Semiconductor Laser Amplifier
SDH	Synchronous Digital Hierarchy
SHB	Spectral Hole Burning
SONET	Synchronous Optical Network
SPM	Self-Phase Modulation
SRS	Stimulated Raman Scattering
SSMF	Standard Single-Mode Fibre
STDM	Statistical Time Division Multiplexing
TDM	Time Division Multiplexing
TOAD	Terahertz Optical Asymmetric Demultiplexer
TPA	Two Photons Absorption
TW-SLA	Travelling Wave SLA
WDM	Wavelength Division Multiplexing
XGS	Cross Gain Saturation
XPM	Cross Phase Modulation

GLOSSARY OF SYMBOLS

Symbol	Definition
β_2	First-order dispersion coefficient
ε	Relative permittivity (dielectric constant)
ε_0	Vacuum permittivity
$\chi^{(j)}$	j^{th} order electric susceptibility
P	Polarisation vector
E	Electric field
ω	Optical frequency
λ	Optical wavelength
$A(z,t)$	Slowly varying envelope of an optical wave
k	Propagation constant
k_L	Linear part of propagation constant
N	Refractive index
c	Speed of light
γ	Fibre nonlinear coefficient
P	Optical power
P_o	Peak optical power of a pulse
V_g	Group velocity
τ	Time reference of a pulse / switching profile
α	Loss coefficient
T_{FWHM}	FWHM width of the NOLM control pulse
N	Soliton order
z_o	Soliton period
ΔT	Separation time between two pulses

L_S	Length of the merging cycle of two solitons due to soliton interaction
L_T	Transmission distance of optical pulses
I	Light intensity
B_F	Degree of modal birefringence
L_B	Beat length of birefringence
E_p	Photon energy
h	Planck's constant
g_R	Raman-gain coefficient
A_{eff}	Effective cross section area of a fibre cable
T_{sp}	Spontaneous life-time
r_{in}	Reflectivity of the input facet of an SLA
r_{out}	Reflectivity of the output facet of an SLA
N	Carrier density
N_o	Transparent carrier density
N_{th}	Carrier density of lasing threshold
I_c	Electrical current
q	Electron charge
V_{SLA}	Volume of the active medium of an SLA
A_{SLA}	Cross-section area of an SLA
L_{SLA}	Length of the SLA
R_{sp}	Spontaneous emission
Γ	Confinement factor
g	Differential gain of an SLA
g_p	Peak differential gain of the gain spectrum of an SLA
$\Delta\lambda_g$	Spectral width of the differential gain of an SLA

a	Gain coefficient of an SLA
α_{SLA}	Photon loss coefficient of an SLA
ϕ	Optical phase
$\Delta\phi$	Phase difference between CW and CCW signal pulses
$\Delta\phi_p$	Peak phase change of NOLM's signal pulses
α_{LEF}	Linewidth enhancement factor
T_x	Transmittance of a NOLM switching window
T_w	Walk-off time between control and signal pulses
L	Length of the NOLM's fibre loop
P_{avg}	Averaged optical power for the walk-off portion of a NOLM's control pulse
P_{RAMAN}	Raman threshold power
W	Width of transmission window of NOLM demultiplexer
$S(t)$	Normalised power profile of an optical pulse
$p(t)$	Probability function of Gaussian shape
RMS_{jitter}	RMS timing jitter of signal pulses
RIN_{NOLM}	NOLM relative intensity noise
RIN_{TOAD}	TOAD relative intensity noise
RXT_{NOLM}	NOLM residual crosstalk
RXT_{TOAD}	TOAD residual crosstalk
NXT_{NOLM}	NOLM neighbour channel crosstalk
NXT_{TOAD}	TOAD neighbour channel crosstalk
M_{TDM}	Number of OTDM channels
T_b	Bit duration of an OTDM time slot
E_c	Control pulse energy

f_c	Repetition rate of NOLM's control pulses
$TOAD_W$	TOAD switching window
G_o	Initial gain of an SLA
G_{CW}	CW gain of signal pulses in TOAD
G_{CCW}	CCW gain of signal pulses in TOAD
T_{asy}	Asymmetric arrival time of TOAD (the CW pulse reaches the SLA T_{asy} ahead of the CCW pulse)
R_G	Optimal gain ratio between CW and CCW pulses for maximum TOAD switching gain
E_{sat}	Saturation energy of an SLA
E_{CTRL}	Optimised control pulse energy for TOAD
E_{max}	Maximum signal energy for TOAD demultiplexing for avoiding the perturbation of the SLA properties
L_{tot}	Total transmission length of a OTDM system
N_{ph}	Number of photons per unit energy
ΔL	Separation length between two amplifiers
R_b	Data rate of the demultiplexed signal
R	Responsivity of the photo-detector
L_f	Loss due to the optical filter
η_{DEMUX}	Switching ratio of the target pulse energy
η_{in}	Input coupling efficiencies of the optical amplifier
η_{out}	Output coupling efficiencies of the optical amplifier
$H_T(\omega)$	Overall transfer function of the optical receiver
B_e	Electrical bandwidth
B_o	Optical bandwidth
K	Boltzman constant

T_k	Temperature in Kelvin
R_L	Load resistance of the photo-detector
$\overline{i_a^2}$	Power spectral density of the electrical input noise current
N_{sp}	Population inversion factor of the optical pre-amplifier

LIST OF FIGURES

Number	Title	Page
2.1	Signal composition of T1 link.	7
2.2	Block diagram for point-to-point WDM transmission.	10
2.3	WDM demultiplexing using splitter and optical filters.	12
2.4	The block diagram of a typical OTDM transmission system.	13
2.5	OTDM Multiplexing.	15
2.6	Dispersion compensation fibre cables.	23
3.1	Beam propagation method.	33
3.2	Propagation of a broadened pulse.	35
3.3	Propagation of a compressed pulse.	36
3.4	Propagation of fundamental soliton.	38
3.5	Propagation of second order soliton.	39
3.6	Transformation from a Gaussian pulse to a fundamental soliton.	41
3.7	Frequency spectrum of a hyperbolic secant pulse propagating at zero-dispersion wavelength.	43
3.8	Pulse merging cycle due to the attractive force of soliton interaction.	45
3.9	The repulsive force of soliton interaction.	47
4.1	Light amplification in a FP-/TW- type SLA.	60
4.2a	Spontaneous emission.	61
4.2b	Stimulated absorption.	61
4.2c	Stimulated emission.	61
4.3	Internal gain spectrum for different carrier densities.	71
4.4	Internal gain Vs. input power for various I_c .	73
4.5	Response of carrier density in the active region of a SLA to the input pulse intensity.	77

4.6a	Gain dynamics of an SLA for 500 fs pump pulse.	78
4.6b	Gain dynamics of an SLA for 2 ps pump pulse.	78
4.7	Normised probe traces of an SLA for femtosecond pump pulses at various wavelengths.	80
5.1	Block diagram of NOLM demultiplexer.	83
5.2	Phase diagram of E_{cw} and E_{ccw} .	84
5.3	T_{FWHM} Vs. $T_w L$ calculated from (5.13) and (5.17) for $L = 3$ km.	93
5.4	T_{FWHM} Vs. $T_w L$ calculated from (5.13) and (5.17) for $L = 6$ km.	95
5.5	Soliton peak power Vs. the total walk-off time, calculated from (3.23), (5.13) and (5.17), for different values of β_2 .	96
5.6	A typical soliton switching window (the control pulse walks over the signal pulse).	98
5.7	Soliton window width at $F_{tx} = 0.1$ Vs. the total walk-off time for different values of β_2 .	101
5.8	Soliton window width at $F_{tx} = 0.3$ Vs. the total walk-off time for different values of β_2 .	103
5.9	Soliton window width at $F_{tx} = 0.5$ Vs. the total walk-off time for different values of β_2 .	103
5.10	The change of soliton pulse width during propagation.	108
5.11	Soliton switching profile ($\alpha=0$) for different values of the walk-off time.	109
5.12	Soliton switching profile ($\alpha = 0.5$ dB/km) for different values of the walk-off time.	110
5.13	Verification of (5.34).	115
6.1	Transformation from timing jitter noise to relative intensity noise.	119
6.2	NOLM residual crosstalk.	120
6.3	NOLM relative intensity noise Vs. the total walk-off time for FWHM signal pulse with $\tau = 1$ ps.	126, 127
6.4	NOLM residual crosstalk Vs. the total walk-off time.	131
6.5	NOLM neighbour channel crosstalk Vs. the total walk-off time.	132

6.6	Tradeoff between noise and crosstalk.	134
7.1	Configuration of a typical TOAD.	136
7.2	SLA model.	139
7.3	Dynamics of carrier density inside the active region of an SLA.	141
7.4a	G_{CW} and G_{CCW} Vs. time ($T_{asy} = 0$ ps).	144
7.4b	TOAD switching window ($T_{asy} = 0$ ps).	144
7.5a	G_{CW} and G_{CCW} Vs. time ($T_{asy} = 2$ ps).	144
7.5b	TOAD switching window ($T_{asy} = 2$ ps).	144
7.6a	G_{CW} and G_{CCW} Vs. time for different values of switching energy.	148
7.6b	TOAD switching window for different values of switching energy.	148
7.7	Maximum signal energy E_{max} Vs. the initial gain G_o .	150
7.8	TOAD residual crosstalk.	152
7.9	TOAD relative intensity noise versus the SLA asymmetry.	154
7.10	RXT_{TOAD} and NXT_{TOAD} Vs. the SLA asymmetry T_{asy} .	156
7.11	RXT_{TOAD} Vs. T_{asy} .	157
7.12	RXT_{TOAD} and NXT_{TOAD} Vs. T_{asy} .	158
7.13	TOAD crosstalk versus SLA asymmetry at total bit rate = 100 Gbps.	159
7.14	TOAD crosstalk versus SLA asymmetry at total bit rate = 200 Gbps.	159
7.15	TOAD crosstalk versus SLA asymmetry at total bit rate = 300 Gbps.	159
7.16	RXT_{TOAD} and NXT_{TOAD} Vs. T_{asy} at total bit rate = 100 Gb/s.	160
7.17	RXT_{TOAD} Vs. T_{asy} at total bit rate = 300 Gb/s.	161
7.18	RXT_{TOAD} and NXT_{TOAD} Vs. T_{asy} for different values of duty cycle.	162
7.19	RIN_{TOAD} and TOAD crosstalk Vs. SLA asymmetry at total bit rate = 100 Gbps for different values of L_{SLA} .	163
7.20	RIN_{TOAD} and TOAD crosstalk Vs. SLA asymmetry at total bit rate = 200 Gbps for different values of L_{SLA} .	163

8.1	RMS_{jitter} versus ΔL for different values of FWHM soliton width.	170
8.2	RMS_{jitter} versus L_{tot} for different values of FWHM soliton width.	171
8.3	RIN_{NOLM} versus total the walk-off time.	172
8.4	Block diagram for the receiver model.	173
8.5	BER versus the average received optical power for baseline bit rate 10 Gb/s.	179
8.6	BER versus the average received optical power for baseline bit rate 1 Gb/s.	179
8.7	NOLM relative intensity noise versus the total walk-off time for different values of L and β_2 .	182
8.8	NOLM crosstalk versus the total walk-off time for different values of L and β_2 .	183
8.9	RIN_{NOLM} and RXT_{NOLM} versus the total walk-off time for $\beta_2 = -5$ ps ² /km and $L = 1$ km.	184
8.10	η_{DEMUX} versus the total walk-off time for $\beta_2 = -3$ ps ² /km, $L = 1$ km.	185
8.11	TOAD energy switching ratio versus the SLA asymmetry for different values of SLA length.	186
8.12	TOAD power penalty versus the SLA asymmetry for 100 Gb/s demultiplexing (10 channels).	188
8.13	TOAD power penalty versus the SLA asymmetry for 100 Gb/s demultiplexing (10 channels).	189
8.14	BER versus the average received optical power for 100 Gb/s (10 channels) optimised NOLM and TOAD demultiplexing.	189
8.15	TOAD power penalty versus the SLA asymmetry for 100 Gb/s demultiplexing (100 channels).	191
8.16	BER versus the average received optical power for 100 Gb/s (100 channels) optimised NOLM and TOAD demultiplexing.	192
8.17	TOAD power penalty versus the SLA asymmetry for 300 Gb/s demultiplexing (30 channels).	194
8.18	BER versus the average received optical power for 300 Gb/s (30 channels) optimised NOLM and TOAD demultiplexing.	194

8.19	NOLM crosstalk versus the total walk-off time for 300 Gb/s demultiplexing.	196
8.20	TOAD power penalty versus the SLA asymmetry for 300 Gb/s demultiplexing (300 channels).	197
8.21	BER versus the average received optical power for 300 Gb/s (30 channels) optimised NOLM and TOAD demultiplexing.	198

LIST OF TABLES

Number	Title	Page
2.1	North American and ITU's PDH hierarchies	7
2.2	SONET/SDH signal hierarchies	8
3.1	Simulation parameters for pulse broadening	34
3.2	Simulation parameters for pulse compression	35
3.3	Simulation parameters for soliton propagation	37
3.4	Simulation parameters for Fig. 3.6	41
3.5	Simulation parameters for Fig. 3.8	45
5.1	Simulation parameters for (5.34)	109
5.2	Verification of (5.13) and (5.17)	111
5.3	Verification of (5.21) and (5.26) for $F_{tx} = 0.1$	113
5.4	Verification of (5.21) and (5.26) for $F_{tx} = 0.5$	114
5.5	Simulations parameters for Fig. 5.13	115
6.1	Tradeoff between noise and crosstalk in NOLM demultiplexing	133
7.1	Simulation parameters for Fig. 7.3	140
7.2	Simulation parameters for Fig. 7.4a	143
7.3	Simulation parameters for Fig. 7.6	149
7.4	Noise and crosstalk simulations of TOAD	153
7.5	Simulation parameters for Figs. 7.9a – 7.9d	153
8.1	Parameters of the NOLM simulations in Chapter 8	171
8.2	Parameters of the receiver model	178
8.3	NOLM parameters for minimum power penalty for 100 Gb/s demultiplexing (10 channels)	185
8.4	NOLM parameters for minimum power penalty for 100 Gb/s demultiplexing (100 channels)	190

8.5	NOLM parameters for minimum power penalty for 300 Gb/s demultiplexing (30 channels)	193
8.6	Optimised NOLM parameters for minimum power penalty for 300 Gb/s demultiplexing (300 channels).	195

ACKNOWLEDGEMENTS

Looking back to the past four years, pursuing for a PhD was tantamount to a host of intellectual, financial and sentimental challenges to me. I am of great pleasure to have this opportunity to thank a number of people and organisations for helping me get through this difficult and challenging period. The Overseas Research Students Award Scheme (ORSAS) from the UK government financially supported this PhD project. I owe the completion of my PhD to three people in the Optical Communication Research Group. The first person is of course my supervisor, Professor Ghassemlooy, who has been giving me inspiring guidance since I was his undergraduate student nearly five years ago. The second person I would like to thank is Dr Graham Swift, who generously handed me over tons of materials and references to kick-start my PhD project. I would also like to thank Mr Alfred Decker, an exchanged student from Austria, who held numerous stimulating technical discussions with me in the third year of my PhD.

I am grateful to the support and encouragement of many friends I met in Sheffield, especially Nicholas, Chun Kit, Ellick and Sarah. The care and understanding from my mother and sisters in Hong Kong sheltered my heart whenever I needed to take a break from the uphill struggle. Finally, I would like to thank Tammy for her patience and love. The past four years are especially memorable to us. We first met at the beginning of my PhD study and got married in my final year of PhD.

DECLARATION

I hereby declare that this thesis is entirely my own work and has not been submitted in support of an application of another degree or qualification of this or any other university, institute of learning or industrial organisation.

Signature : 

Name : Chin Ying CHEUNG

Date : 15 July 2002

CHAPTER ONE - INTRODUCTION

1.1 Introduction

Fibre-based optical communication systems are widely used in long-haul high-capacity transmission of voice and data. The first generation of fibre-based systems was for point-to-point applications, where electrical technologies were used to perform more complex operations, such as multiplexing, demultiplexing, switching, etc. The latest developments of fibre-based systems are the introduction of all-optical devices to perform functions that were previously carried out electrically [1]. The obvious advantage of this approach is to bypass the intermediate electrical-to-optical and optical-to-electrical conversions at the transmitting and receiving ends respectively of the communications systems.

The optical time division demultiplexer is an essential element of the future all-optical networks. Its function is the direct extraction of one or more time-multiplexed channels from a high-capacity optical data stream, without the need for the conversion from optical to electrical domain beforehand. For a receiver system employing electrical time division demultiplexer, the high-capacity optical signal is first converted to electrical form by an optical detector. Then an electrical time division demultiplexer is used to extract the target channel(s) from the OTDM signal. Current optical receivers can handle signal capacity as high as 20 Gb/s [2]. Nevertheless, the capacity of optical time multiplexed signal could be up to hundreds of G-bits per second. Steadily improved electrical technology cannot match the enormous demand for transmission bandwidth. The bandwidth limitation of receiver systems can be overcome by employing all-optical time division demultiplexers, where the target channel is extracted from the OTDM signal in optical domain for subsequent electrical processing

Besides OTDM, wavelength division multiplexing (WDM) is another important multiplexing scheme for carrying high-speed optical data. A technical and historical review for OTDM and WDM will be given in Chapter 2. The objective of this PhD study is the investigation of the noise and crosstalk characteristics of two types of all-optical time division demultiplexers, namely, nonlinear optical loop mirror and terahertz optical asymmetric demultiplexer. The operation principles of NOLM and TOAD demultiplexers are based on the nonlinear properties of optical fibre and semiconductor laser amplifier (SLA), respectively. The theoretical backgrounds of nonlinear fibre optics and SLA will be given in Chapters 3 and 4, respectively. A new mathematical model for NOLM demultiplexing will be described in Chapter 5. One of the objectives of this model is to maximise the amplitude of NOLM's transmission window. Based on this mathematical model, a noise and crosstalk analysis of NOLM demultiplexer will be presented in Chapter 6. A new mathematical model for maximising the amplitude of TOAD's transmission window will be described in Chapter 7. Also found in Chapter 7 is the noise and crosstalk analysis of TOAD demultiplexer. Finally, the bit-error-rate performances of NOLM and TOAD demultiplexers will be compared in Chapter 8. Conclusions and suggestions of further works will be found in Chapters 9 and 10, respectively.

1.2 Aims and Objectives

- Analyse the noise and crosstalk characteristics of nonlinear optical loop mirror demultiplexer
- Analyse the noise and crosstalk characteristics of terahertz optical asymmetric demultiplexer
- Compare the bit-error-rate performances of nonlinear optical loop mirror and terahertz optical asymmetric demultiplexers.

1.3 Original Contributions

- Optimisation of device parameters for maximising peak transmittance of the NOLM switching window (Section 5.3.2).
- Development of a new analytical equation for calculating the width of NOLM switching window (Section 5.3.3).
- Development of a new convolution approach for calculating the profile of NOLM switching window (Section 5.3.4).
- Development of an equation for evaluating the residual crosstalk of NOLM demultiplexer (Section 6.2.2).
- Analysis of relative intensity noise, residual crosstalk and neighbour channel crosstalk in NOLM demultiplexing (Section 6.3).
- Optimisation of switching energy of TOAD demultiplexer for maximising the peak transmittance of switching window (Section 7.3.3).
- Analysis of relative intensity noise, residual crosstalk and neighbour channel crosstalk in TOAD demultiplexing (Section 7.4).
- Optimisation of device parameters of TOAD for minimising the power penalty in 100 Gb/s and 300 Gb/s demultiplexing (Sections 8.4.1 and 8.4.2).
- Clarification of Gordon-Haus Jitter for the special case of distributed amplification (Section 8.2.1).
- Bit-error-rate comparisons of NOLM and TOAD for 100 Gb/s and 300 Gb/s demultiplexing (Sections 8.4.1 and 8.4.2).

1.4 Publications

This research project has so far led to publications listed below:

C.Y.Cheung, G.Swift, and Z.Ghassemlooy, 'An analysis of the effect of Gordon-Haus jitter on non-linear optical loop mirror (NOLM) demultiplexing', SPIE Photonics East, Boston USA, v 4216, 6-8 November 2000, pp. 85-94.

G.Swift, Z.Ghassemlooy, C.Y.Cheung, and A.Decker, 'Analysis of optical time division multiplexed transmission', Proceedings of SPIE (2000), conference code 56961, 27-28 Jan 2000, pp.100-108

C.Y.Cheung, Z.Ghassemlooy, and G.Swift, 'Mathematical modelling and BER analysis of 100 Gb/s NOLM demultiplexer using a soliton as a control pulse', IEE Proceedings Optoelectronics, Vol. 147, No. 4, August 1999, pp.245-250.

C.Y.Cheung, Z.Ghassemlooy, and G.Swift, 'Bit-error-rate analysis for a 100 byte/s nonlinear optical loop mirror demultiplexer employing soliton control and signal pulses', Optics Letters, Vol.24, No.24, 15 Dec 1999.

C.Y.Cheung, Z.Ghassemlooy, and G.Swift, 'Minimizing power penalty of 100 Gb/s NOLM demultiplexer employing optical soliton control pulse', SPIE Photonics East, Boston. USA, v 3847, 19-22 Sep 1999, pp.148-157.

C.Y.Cheung, and Z.Ghassemlooy, 'Modelling of NOLM demultiplexers employing optical soliton control pulse', Microwave and Optical Technology Letters, Vol.21, No.3, 5 May 1999, pp.205-208.

C.Y.Cheung, and Z.Ghassemlooy, 'Modelling of NOLM demultiplexers operating with soliton control pulse', Colloquium on Optical Solitons, London, IEE, 4 Feb 1999, pp.12/1-12/6.

CHAPTER TWO - LITERATURE REVIEW: WDM AND OTDM

2.1 Introduction

Two techniques to exploit and unleash the potentially huge transmission capacity in fibre optics communications are wavelength division multiplexing and optical time division multiplexing. In WDM, a number of discrete optical frequencies are allocated for the transmission of different data channels. An aggregate huge transmission capacity is achieved by simultaneously transmitting all wavelength channels. On the contrary, OTDM uses only one optical wavelength to transmit data stream of extremely high bit rate, which is formed by time-multiplexing data channels of lower bit rate via bit, byte or data block interleaving. The bit rate of the OTDM data stream is too high ($> 100\text{Gbit/s}$) to be processed electrically. Therefore, the multiplexing and demultiplexing operations need to be carried out in optical domain using all-optical processing technologies [1], [4].

The spectral width of an optical signal around a central wavelength is dependent on the data transmission rate and the carrier linewidth of the light source. An ideal light source with high purity of the optical frequency will produce a transform-limited signal. In this case, the frequency spectrum of the data channel is solely determined by the Fourier-transform of the signal envelope. The spectral width of OTDM signal is generally larger than that of individual WDM channels as OTDM data stream operate at a much higher data rate. The transmission bit rate of OTDM systems can be as high as 1 Tbit/s [155], compared to the bit rates of 2.5-40 Gbit/s per wavelength channel in typical WDM systems [6]-[8], [156].

This chapter gives a comprehensive review of WDM and OTDM. Historical developments of the two multiplexing schemes and their electrical predecessors – frequency division multiplexing (FDM) and time division multiplexing (TDM) are described in Section 2.2.

Sections 2.3 and 2.4 describe the technologies required to realise WDM and OTDM systems. They include tunable laser, optical filter, all-optical time division demultiplexer, etc. The technological challenges and limitations of WDM and OTDM systems are elucidated in Sections 2.5 and 2.6. The concluding section of this chapter predicts the future development of WDM and OTDM. Researchers and industrial analysts overwhelmingly hold a view that WDM, rather than OTDM, will play a vital role in future telecommunication networks [5]-[8]. The main reason for that is the availability of off-the-shelf WDM devices. WDM systems can be realized by passive optical devices, which are readily available in the market. Nevertheless, OTDM systems require active optical devices that are still being developed in laboratories. The author will give his opinion about the future development of the two seemingly competing multiplexing schemes.

2.2 Historical Background

At the early stage of the telecommunication history, voice and data were transmitted separately through the telephone and telegraph networks. Early public switched telephone networks (PSTN) employed FDM to transmit up to 60 analogue voice channels simultaneously [9]. AT&T pioneered digitising of voice traffic with the introduction of digital T1 transmission link in 1960s. The main reason of switching from analogue to digital transmission was the inherent higher immunity against noise in digital communication systems [10]. An important characteristic of T1 transmission is its capability to accommodate voice, video and other data formats into a 1.544 Mb/s digital data stream using TDM. Fig. 2.1 shows a possible composition of a T1 signal, where “bursty” input data streams are combined into a constant bit rate signal using statistical time division multiplexing (STDM) before being time-multiplexed to the T1 signal. STDM dynamically allocates time slots to active terminals for avoiding the transmission link being idle when a terminal has nothing to send [11].

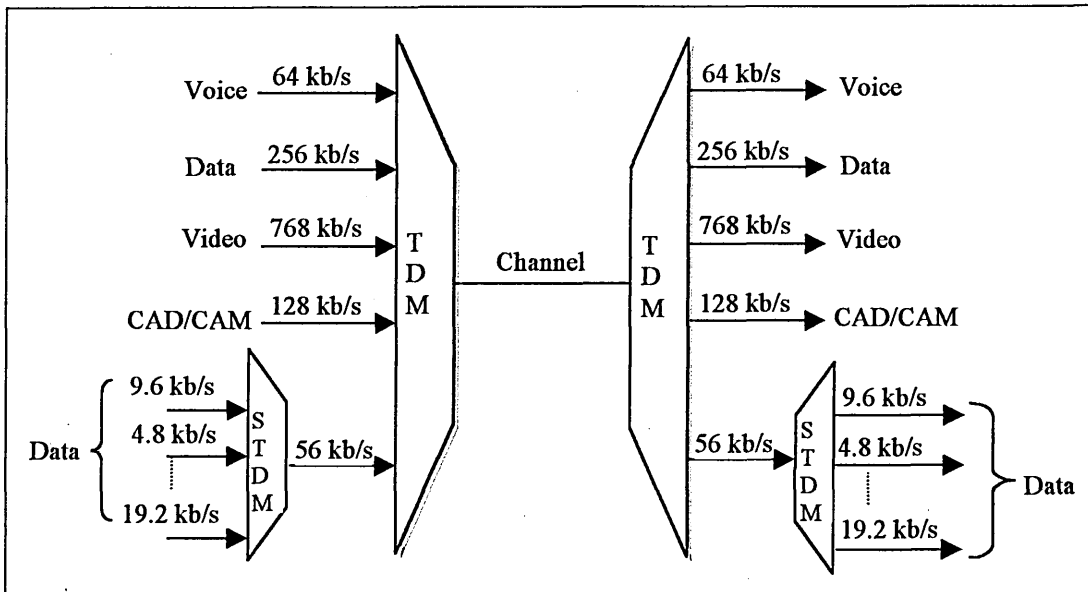


Fig. 2.1. An example of signal composition of T1 link.

The signal carried by a T1 link is called DS1. A DS1 signal can be further demultiplexed to 24 DS0 signals, each with 64 kb/s. Multiple DS1 signals can also be multiplexed up to various levels of higher bit rate signals (DS2, DS3 and DS4). Five levels of TDM signals (DS0 – DS4) forms a digital hierarchy that is retrospectively called plesiochronous digital hierarchy (PDH). The AT&T PDH is used in the U.S. and Canada. International Telecommunication Union (ITU) had developed a similar digital hierarchy with levels of data rate different from the North American standard. Table 2.1 lists all signal levels of the North American and ITU's PDHs [11].

Table 2.1: North American and ITU's PDH hierarchies			
North American PDH		ITU's PDH	
Designation	Data Rate (Mb/s)	Designation	Data Rate (Mb/s)
DS-1	1.544	E1	2.048
DS-2	6.312	E2	8.448
DS-3	44.736	E3	34.368
DS-4	274.176	E4	139.264

The multiplexing scheme used in the PDH is called asynchronous TDM due to the fact that individual network nodes run their own independent clock. These clocks are not synchronised with each other. At all levels of multiplexing the lower bit rate signals are

individually rate adjusted via bit stuffing to match the clock rate of the higher level signals [10]. With extra bits stuffed, a particular low-level signal is not directly accessible from a higher-level signal. The original stream must be fully demultiplexed even if only one low-level signal needs to be accessed. A new digital hierarchy called synchronous optical network (SONET) was standardised by the American National Standards Institute (ANSI) aiming at providing a synchronous TDM service with many other attractive features over PDH [11]. A compatible version called synchronous digital hierarchy (SDH) was published by ITU in 1996 [11]. Table 2.2 shows the SONET and SDH signal hierarchies. SONET and SDH were designed to take advantage of the high-speed digital transmission capacity of optical fibre cable. The highest bit rate supported by SONET/SDH was 10 Gbit/s.

SONET Designation	SDH Designation	Data Rate (Mb/s)
STS-1/OC-1		51.84
STS-3/OC-3	STM-1	155.52
STS-9/OC-9		150.336
STS-12/OC-12	STM-4	662.08
STS-18/OC-18		933.12
STS-24/OC-24		1244.16
STS-36/OC-36		1866.24
STS-48/OC-48	STM-16	2488.32
STS-96/OC-96		4876.64
STS-192/OC-192	STM-64	9953.28

[**Notations: STS-n (synchronous transport signal) is electrical signal in SONET
 OC-n (optical carrier) is optical signal in SONET
 STM-n stands for synchronous transport module in SDH **]

The ever-increasing aggregate TDM bit rate achieved by the advancements of digital technology would have been more than enough to satisfy the steady growth rate of voice traffic. However, due to the explosive growth of the Internet and other bandwidth demanding multimedia applications since early 1990's, long-haul telecommunication traffic has been increasingly being dominated by data, not voice [7]. The STM-16 (2.5

Gbit/s) available in the market since 1991 cannot cope with the explosive growth of the data traffic. The traditional approach to solve this bandwidth shortage problem is to keep increasing the aggregate TDM bit rate. The bit rate requirement of hundreds of Gbit/s for future telecommunication systems spurred the research development of OTDM so as to overcome the bottleneck of limited electrical bandwidth in TDM. Another approach to solve this bandwidth shortage problem is to employ WDM to transmit multiple wavelength channels simultaneously. Currently the telecommunication industry favours WDM rather than OTDM [7], [8] because of lower cost and more rapid implementation. There are at least two factors that inhibited the deployment of OTDM systems. The first is the limitation of existing fibre cables. It is necessary to use dispersion shifted fibre (DSF) or employ dispersion compensation techniques [12], [13] for transmitting ultra-high OTDM bit rate. However, the cost of replacing all existing fibre cables with DSF or dispersion compensation fibre in a short period of time is too high to be an economically viable solution. The bandwidth shortage problem must be solved very quickly because the existing fibre cables were inadequate to cope with the short-term need of the telecommunication industry in mid 1990's. The second obstacle for the deployment of OTDM systems is the need to develop all-optical processing devices to switch digital signals in optical domain. Although some progress has already been made in realising all-optical processing such as optical buffer, multiplexing, demultiplexing, signal regeneration, etc [14]-[18], most of the all-optical devices are bulky and the technology is not mature enough to enable the production of compact and reliable opto-electronic chips/devices. On the contrary, WDM is already reaching an advanced stage of development as it can be realised using commercially available components. The breakthrough of widespread WDM deployment is the development of erbium-doped fibre amplifier (EDFA) [7]. This technology makes the long-haul WDM transmission economically viable by replacing the

expensive 3R (retiming, reshaping and regenerating) electrical repeaters with wide bandwidth optical amplifiers.

The essential components to realise WDM and OTDM networks will be described in the following two sections. The discussion of the development of WDM and OTDM will be continued in the concluding section of this chapter.

2.3 Essential Components for WDM Transmission/Network

Figure 2.2 shows the block diagram of point-to-point WDM transmission. A number of light sources of different carrier frequencies are individually modulated by electrical signals. The frequency spectrum of individual wavelength signals should ideally be as narrow as possible (i.e. transform-limited) in order to minimize the crosstalk between the wavelength channels. It is possible to obtain a laser carrier linewidth as narrow as 4 MHz / 250 MHz by externally / directly modulating the optical wave generated from the double-feedback laser diode (DBF-LD) [19]. The typical bit rate of individual wavelength channels is about 2.5 Gbit/s. A transform-limited signal for such a bit rate is attainable using current laser technology. In WDM implementation, it is desirable to use wavelength tunable lasers for a flexible network design. The wavelength tuning can be carried out by mechanical, electrical, acousto-optical and electro-optical methods [20].

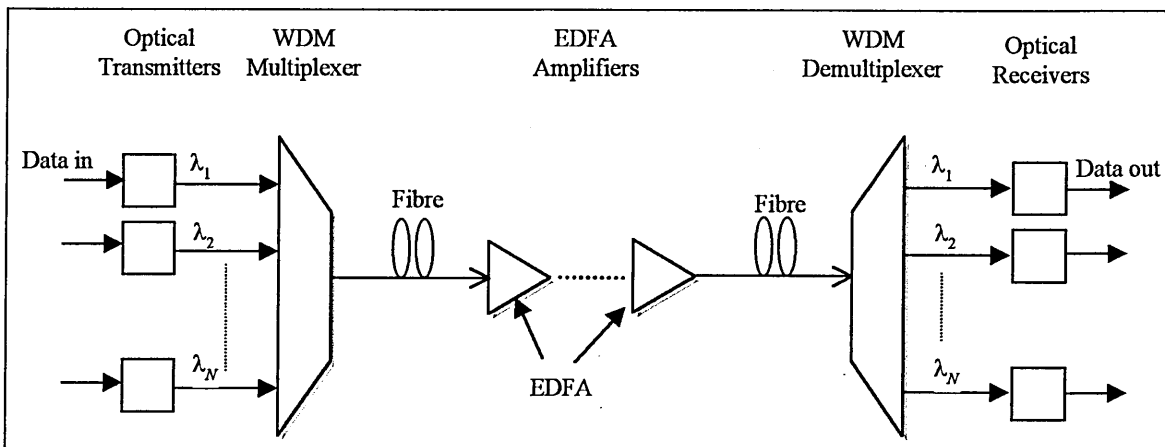


Fig. 2.2. Block diagram for point-to-point WDM transmission.

The N wavelength channels in Fig. 2.2 are combined by a WDM multiplexer to produce a high capacity optical signal. Multiplexing can be achieved by simply passing the multiple wavelength channels into an N -to-1 fibre coupler. The disadvantage of using this method is the high loss incurred. The insertion loss (dB) of the coupler increases with the total number of wavelengths, as represented in the equation below [21].

$$Loss = 10 \log_{10} (NumOfChannels). \quad (2.1)$$

According to (2.1), the insertion loss of a 10-to-1 coupler is 10 dB. The dependence of the insertion loss on the number of multiplexing wavelength channels affects the scalability of a WDM system. Using WDM multiplexers based on arrayed-waveguide grating (AWG) can solve this problem. An AWG multiplexer is composed of an arrayed-waveguide grating, input-output waveguides and focusing slab waveguides [22]. The arrayed waveguide has a numerical aperture larger than the input-output waveguides for minimising the coupling loss. Y.Inoue, *et-al* reported an insertion loss of only 3 dB using AWG multiplexer [23]. The loss is fairly independent of the number of wavelength channels.

Optical amplifiers are required to compensate the fibre loss in long-haul transmission systems. The amplifier spacing is a compromise between cost and system performance. In the project of Transatlantic Telephone (TAT)-12/13, 133 optical amplifiers were installed along the distance of 5913 km between the Rhode Island, U.S. and Lands Ends, England [24]. EDFA is a principle choice of optical amplifiers for long-haul transmission as it offers high gain, large saturated output power and wide bandwidth [25]. The characteristic of wide bandwidth is especially important for WDM transmission because of the multi-wavelength nature of the signal. WDM transmission of 100 channels \times 10 Gb/s using EDFA with 20 nm flat gain spectrum was reported in Ref. 26.

At the receiving end, the WDM signal is demultiplexed to different wavelength signals for data detection. The simplest form of WDM demultiplexer consists of a 1-to- N splitter and N optical filters (Fig. 2.3). Individual wavelengths are selected by passing the signal to an optical filter. In system design of WDM, the filter passband characteristic and its roll-off slope must be considered to ensure minimum crosstalk. Three types of filter commonly used for WDM are fixed interference filter, tunable Fabry-Perot filter and grating based filter [21].

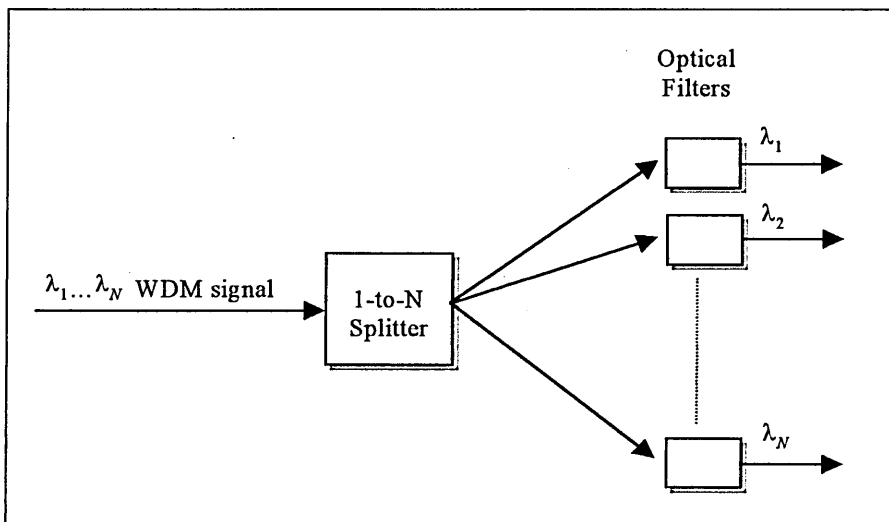


Fig. 2.3. WDM demultiplexing using splitter and optical filters.

WDM demultiplexing can also be carried out using grating-based devices such as array-waveguide grating demultiplexer [22]. The fact that AWG can perform both multiplexing and demultiplexing makes it a good candidate as an add-drop multiplexer (ADM). Multiple wavelength channels can be dropped and added at the same time using optical feedback loop connecting to the AWG [27].

In point-to-point implementation, WDM is only involved in data transmission between two network nodes and plays no role in switching/routing. At each network node, the received WDM signal must undergo full demultiplexing and optical-electrical-optical conversion, allowing the electrical SDH/SONET network equipment to perform the rest of network

functionality. This inevitably causes delay of data delivery. Among the various solutions proposed to remedy this problem [28]-[30], wavelength routing [28] is the most technically viable approach for high speed switching under the current technology. In a wavelength routing network, a virtual circuit between the source and target network nodes is established based on wavelength assigned for the intermediate links. Due to the limited number of WDM channels available in each transmission link (the reason will be explained in Section 2.5), an important feature of large-scale WDM network is the ability to dynamically assign wavelength within an optical virtual circuit. Different wavelengths could be used in the intermediate links along any path of the virtual circuit. The change of wavelength of a signal is carried out all-optically by wavelength converter without the need of optical-electrical-optical conversion. The techniques adopted by most all-optical wavelength converters exploit the nonlinear optics phenomenon in fibre cable [28], or in semiconductor laser amplifier (SLA) [28], [31].

2.4 Essential Components for OTDM Systems

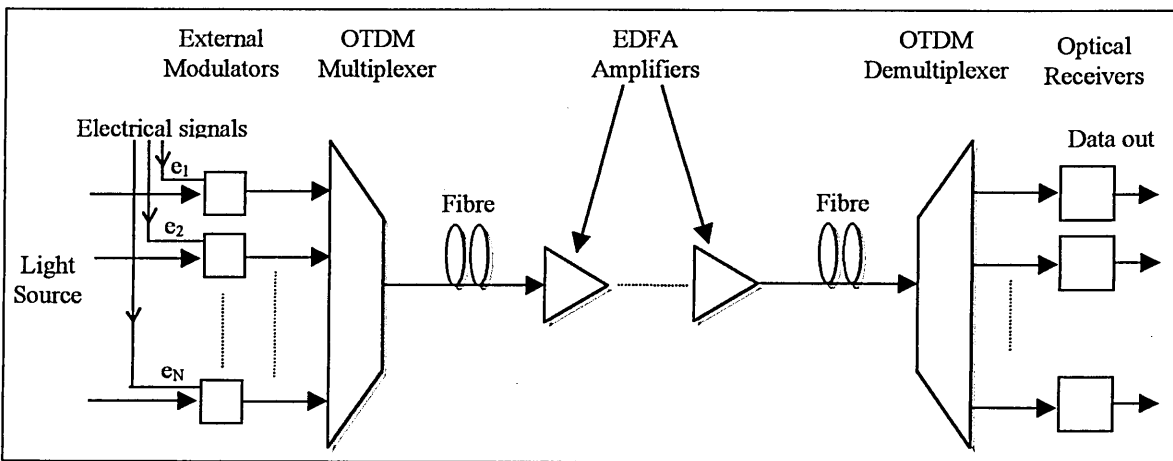


Fig. 2.4. The block diagram of a typical OTDM transmission system.

Figure 2.4 shows the block diagram of a typical OTDM transmission system. Only one light source is shown in the diagram due to the single wavelength nature of OTDM system.

The types of light source widely employed in OTDM experiments include the continuous

optical wave generated from DFB laser and the repetitive optical pulses generated from the active mode locked (ML) Nd:YAG / Nd:YLF laser [32]-[34]. As shown in Fig. 2.4, the light generated by the laser is split to reach N external modulators, which are driven by N electrical signals respectively. External modulation is preferred in OTDM system as it can achieve narrow carrier linewidth, whereby reducing timing jitter of the transmitted pulses [19].

The optical pulses coming out from the external modulators may need to be compressed in order to support the high bit rate required in high capacity OTDM transmission. Pulse compression can be performed by frequency-chirping the optical pulses and then passing them through an anomalous dispersive medium. The key of this approach is to create a linear frequency chirp across the optical pulse from the leading edge to the trailing side. Ideally, the midpoint of the linear-frequency chirp should be right at the central part of the pulse. The nonlinear medium responsible for the creation of such linear frequency chirp over the optical pulse can be either a fibre cable [35] or a SLA [36]. When a frequency-chirped pulse passes through a dispersive medium, different parts of the pulse would travel at different velocities due to the temporal variation of frequency. If the trailing edge travels faster than the leading edge, the result would be pulse compression. The dispersive medium can be a fibre-grating [35] or a dispersive fibre cable.

After pulse compression, the N input signals in Fig. 2.4 are multiplexed into a high capacity OTDM signal. The simplest conceptual description of the multiplexing process is a set of delay lines with various lengths (Fig. 2.5). With the propagation delay imposed by the delay lines, the optical pulses of each input signal would be positioned at its corresponding time slot in the context of the aggregate OTDM signal. The technology that

can implement stable OTDM multiplexing is the Mach-Zehnder interferometer-based planar lightwave circuit (PLC) [37].

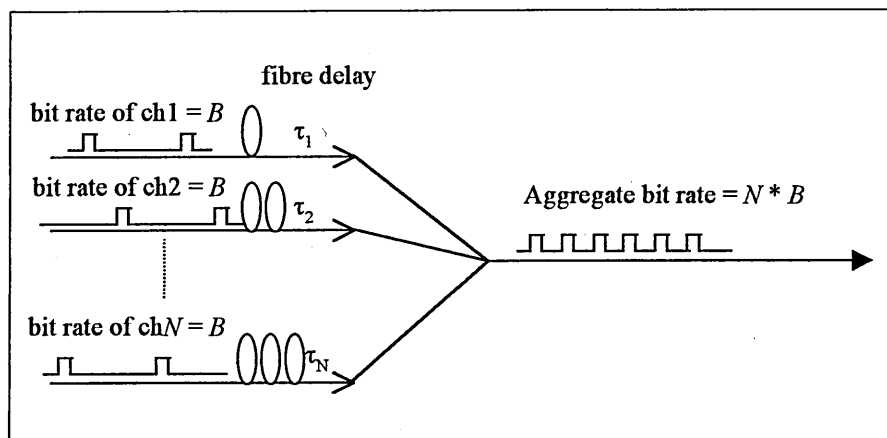


Fig. 2.5. OTDM multiplexing.

In long-haul OTDM transmission, the quality of high speed OTDM signal deteriorates as the propagation distance increases. Although employing 3R electrical repeaters can mitigate this problem, the high cost involved prohibits it from being a financially viable solution to signal degradation [7]. In fact, one of the reasons for the rapid deployment of WDM transmission in early 1996 is to avoid the expensive electrical repeaters in TDM system. A cost efficient solution to this problem is all-optical signal regenerator. An all-optical signal regenerator could be based on nonlinear polarisation rotation in fibre as a decision gate [38], semiconductor integrated – Mach-Zehnder interferometer (MZI) [18] or semiconductor based nonlinear interferometer [39].

At the receiving end, the OTDM signal is demultiplexed back to OTDM channels of slower bit rates. There have been a number of designs proposed for all-optical time division demultiplexing, for example, nonlinear optical loop mirror [16], terahertz optical asymmetric demultiplexer [17] and four wave mixing (FWM) in a SLA [40]. Another essential components for OTDM network is add-drop multiplexer, which allows the adding and dropping of any OTDM channel simultaneously [41].

2.5 Technological Challenges of Long-haul High Capacity WDM Transmission

In WDM, the increase of transmission capacity is achieved by adding more WDM channels to the system. The spectral width of the low-loss spectral region in a dispersion-shifted-fibre (DSF) is around 200 nm [42]. To estimate how many STM-64 (10 Gbit/s) signals could be accommodated in the third transmission window, the following assumptions are made: (i) the baseband spectrum of the signal is twice the Nyquist bandwidth, and (ii) a guard band equivalent to the baseband spectrum is assigned to each WDM channel. Based on the above assumptions, the maximum number of channels to be accommodated by the 200 nm window is 1250. The potential capacity of WDM transmission is $1250 \times 10 \text{ Gbit/s} = 12.5 \text{ Tb/s}$.

Nevertheless, under the current technology, many factors limit the total number of channels of a WDM system. The first is the bandwidth limitation of optical amplifier. EDFA is widely used for loss compensation because of its broad bandwidth and high gain [25]. In EDFA, light amplification is achieved by creating the population inversion of electron levels through injecting a pump laser power into the active medium (fibre). The resultant gain spectrum is dependent on the pump wavelength. Early research of EDFA was focused on the conventional band (C-band) amplification at around 1550nm. C. G. Atkins, *et-al*, reported 3dB bandwidth of 35 nm in C-band EDFA [43]. The reported 3dB gain spectrum had a sharp peak and dip (3dB) profile followed by a 20 nm flat line. The gain variation along optical frequency leads to insufficient optical power in some WDM channels and too much optical power in some other WDM channels. Both cases are detrimental to the WDM transmission. In a transmission link with hundreds of EDFAs, complete power extinction can occur to some channels at the system output, due to insufficient gain compensation of the amplifier chain. On the other hand, too much optical power will strengthen the undesirable nonlinear effects such as self-phase modulation

(SPM), cross-phase modulation (XPM), four-wave mixing, etc. Details are presented in Chapter 3. Gain flattening is required to avoid the above problems. Many techniques have been proposed to equalise the gain spectrum [25], for example, using all-fibre acousto-optic tunable filter after the EDFA amplification can keep the gain variation under 0.6 dB within a C-band 37 nm bandwidth [44].

For further broadening the EDFA bandwidth, multiple pump wavelengths could be used simultaneously to amplify WDM channels at both C-band (1550 nm) and long wavelength band (L-band) (i.e. 1580 nm) [45]. Using this method, it is possible to obtain gain-flattened bandwidth of 50 nm. The latest research trend of optical amplifiers is to investigate alternative technologies for widening gain bandwidth even further. The Raman amplifier is a promising candidate for realising broadband amplification beyond 80 nm [46-47]. The widest bandwidth of Raman amplification reported in the literature is 100 nm [46]. Twelve wavelengths pumping ranging from 1405 nm to 1510 nm, generated by a WDM laser diode unit, were used to obtain the broadband amplification. However, considering the 200 nm low-loss region in DSF, there is still much room for improvement in terms of bandwidth broadening of amplification. Using the two assumptions laid out in the first paragraph of this section, the aggregate capacity of WDM transmission under the restriction of current optical amplifier technology is 6.25 Tb/s, i.e. half the full potential of 12.5 Tb/s. Another technological challenge in optical amplification is the commercialisation of Raman amplifier. The key factor is to drive down the cost per unit bandwidth while maintaining stable operation.

Besides amplification bandwidth, another factor that fundamentally limits the number of channels accommodated in a WDM system is fibre nonlinearity. Intensity interference and channel crosstalk between multiple WDM channels due to the nonlinear response in fibre

cable grows with the propagation distance. The need to allocate extra channel spacing for maintaining a certain level of bit-error-rate limits the number of accommodated WDM channels. The simplest approach of suppressing the effects of fibre nonlinearity is to keep the light intensity of the WDM signal sufficiently small. However, the corresponding decrease of signal-to-noise signal is also detrimental to the communication system. Therefore, it is vital to design the WDM system in a way that reduces the negative impact of fibre nonlinearity.

The major nonlinear phenomena that affect the performance of WDM systems are four-wave-mixing, stimulated Raman scattering (SRS) and cross phase modulation [42], [48]. This section focuses on the effects of these nonlinear phenomena on WDM transmission. A detailed mathematical and physical description of FWM, SRS, XPM and other nonlinear phenomena in optical fibre will be given in Chapter 3. FWM is caused by the nonlinear interaction between optical power at different wavelengths in a fibre cable [35]. Its direct result is the transfer of optical energy from existing frequency components to new frequency components. Severe crosstalk and signal distortion would occur if the newly created frequency components overlap with some of the wavelength channels of the WDM signal. The signal distortion is the result of beating between the WDM optical waves and the FWM generated signal waves within the spectrum of a WDM channel [49]. The BER performance of a WDM system will be degraded if the bandwidth of the optical receiver is wide enough to detect both the WDM signal term and the FWM beating terms. Furthermore, the power loss of the WDM channels due to the FWM effect will also decrease the SNR of those channels.

SRS transfers optical energy from a shorter wavelength to a range of longer wavelengths. The optical wave that loses energy in the process is called pump wave. The optical wave

that gains energy in the process is called Stokes wave. The rate of energy transfer per unit length increases with the pump intensity, Stokes intensity and a wavelength-dependent parameter called Raman gain coefficient [35]. The energy gain of the Stokes wavelengths is determined by the spectrum of the Raman gain coefficient. In a two-wavelength WDM system, optical energy is transferred from the shorter wavelength to the longer wavelength results in channel crosstalk. The situation is more complicated for the systems with more than two WDM channels. Some wavelength channels will lose optical energy to the longer wavelength channels and at the same time gain optical energy from the shorter wavelength channels. The amount of energy transfer is also dependent on the bit pattern because the SRS is significant only if the Stokes intensity is higher than a certain level (i.e. SRS occurs in marked bits only). The energy transfer mechanism described about occurs in multi-wavelength signals. Nevertheless, SRS will also affect single-wavelength signals of high bit rate. Since the spectral width of an optical pulse is the inverse of its pulse width in time domain, ultra-short pulses for supporting high bit rate would have huge spectral width. In high bit rate systems, the spectral width of individual pulses is so large that the optical energy is transferred from the shorter wavelength to the longer wavelength by SRS. As a result, the central frequency of the ultra-short pulses would be shifted downward by the energy transfer mechanism of SRS [132]. The equation of SRS threshold will be given in Chapter 3.

XPM in WDM transmission systems modulates optical phase across the pulse envelope in individual wavelength channels because of the nonlinear response of the refractive index to the total optical power of other wavelength channels. For example, in an N wavelengths system, the optical phase of each channel will be modulated by the optical power of the other $N-1$ wavelength channels. The amount of phase change caused by XPM increases with the number of wavelength channels and the optical power of individual channels.

Current optical receivers are based on direct detection, which is insensitive to the XPM-induced phase fluctuation. Nevertheless, the instantaneous phase modulation broadens the spectral profile of the optical pulse. The phase fluctuation due to XPM will eventually be transformed into pulse distortion and intensity interference [50], [51], thus limiting the transmission distance of the WDM system. The randomness of bit patterns of WDM channels exacerbates the problem. It is because the XPM experienced by an optical pulse at a WDM channel depends on the number of co-propagating optical pulses at other WDM channels.

Several strategies are currently used to alleviate the problems of fibre nonlinearity in WDM systems [42], [48]. Allocating extra channel spacing can avoid overlapping between the generated FWM wavelengths and the existing wavelength channels. The new wavelengths generated in the FWM process are dependent on the wavelengths of the co-propagating WDM channels. The mathematical function for calculating the FWM wavelengths from the existing wavelengths will be given in Chapter 3. For serving the purposes of this chapter, it is adequate to indicate that the FWM wavelengths are generally not fixed in regular spacing in the frequency spectrum. Therefore, allocating WDM channels in unequal spacing can avoid the overlapping between the FWM wavelengths and the existing WDM channels. It has been reported that the propagation distance of a WDM system with a bit rate 8×10 Gbit/s using unequal channel spacing is 30 km longer than the same system using equal spacing [52]. However, the optical power loss in some WDM channels due to the transfer of energy to the FWM wavelengths is inevitable even if unequal channel spacing is employed. The other disadvantage of using unequal channel spacing is its inefficiency to accommodate high transmission capacity.

The prerequisite physical condition for producing significant FWM effect is phase matching between optical waves of different wavelengths [35]. This condition is met when the WDM channels are in the region of zero-dispersion wavelength [35]. FWM is less significant in WDM systems employing non-zero dispersion fibre cables such as standard single-mode fibre (SSMF). Furthermore, in a non-zero dispersion fibre, the walk-off between optical pulses of different WDM channels shortens the effective co-propagation distance between optical pulses, thus suppressing both FWM and XPM. The walk-off effect is the result of the velocity differences between optical pulse trains of different wavelengths. The amount of walk-off time increases with the channel spacing. Theoretical and experimental results show that XPM is reduced significantly for channel spacing ≥ 0.8 nm [50].

The group velocity of an optical wave depends on the magnitude of the first-order dispersion coefficient (β_2). In a non-zero dispersion fibre, β_2 is a function of optical wavelength. The difference in β_2 at two optical wavelengths results in the walk-off effect. However, for a pair of β_2 with opposite signs (i.e. positive and negative values), the optical waves of two wavelengths will have the same group velocity as long as the two wavelengths have the same magnitude of β_2 . In such cases, the walk-off time between optical waves at two WDM channels would be equal to zero. A simple way to avoid this situation is to use the wavelength range of positive or negative β_2 , not both. This means further restriction over the usage of frequency spectrum. There is no effective scheme to reduce the SRS effect on WDM systems because of the ultra-wide bandwidth of SRS [35]. The most practical approach is to keep the light intensity small, at the expense of the decreased signal-to-noise ratio.

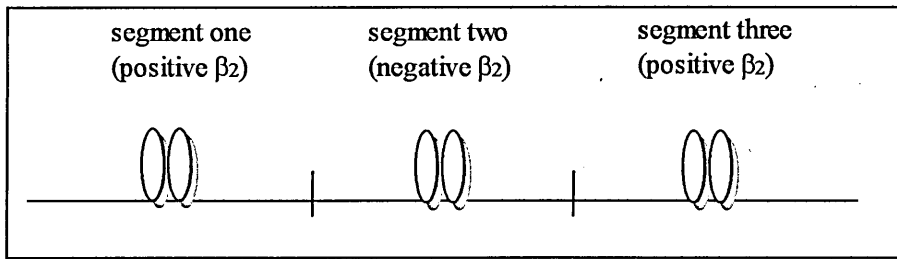
Channel crosstalk in WDM systems is introduced not only by the fundamental effects mentioned above, but also by the WDM system components described in Section 2.3. Currently, the most popular choice of channel spacing in WDM systems is 0.8 nm (100 GHz spacing). The transmission of 3.08 Tb/s (77×42.7 Gbit/s) WDM signal 1200 km was achieved in an experiment reported by Y. Yamada, *et-al* [155]. Good system design for reducing WDM crosstalk is required to attain a transmission capacity higher than 1 Tb/s.

2.6 Technological Challenges of Long-Haul High Capacity OTDM Transmission

Pulse width in pico-seconds and even femto-seconds is used in high capacity OTDM transmission. Such ultra-short pulses are vulnerable to chromatic dispersion due to their wide frequency spectrum. In addition, optical transmitter [19] and in-line optical amplifiers [53] deteriorate the BER performance of OTDM systems by introducing timing jitter to the ultra-short pulses. At the receiving end, the demultiplexing of the high capacity data stream is based on the time slots assigned to individual OTDM channels. Severe crosstalk occurs if the timing jitter of optical pulses is larger than the width of the time slot. The major challenges of designing and implementing high capacity OTDM systems are to minimize the two detrimental effects mentioned above, namely chromatic dispersion and timing jitter. The strength of the two effects increases with transmission distance. The rest of this section is dedicated to a review of the technologies and strategies currently employed for reducing the impacts of chromatic dispersion and timing jitters in long-haul high capacity OTDM systems.

Within the low loss wavelength region (1550 nm) of standard single mode fibre, the first order dispersion coefficient is about $-17 \text{ ps}^2/\text{nm}/\text{km}$. It is possible to use dispersion shifted fibre for achieving low fibre loss and zero β_2 . However, fibre nonlinearity in zero β_2 fibre would result in severe pulse distortion, thus limiting both the transmission distance and bit

rate [54]. A number of techniques can be used to compensate chromatic dispersion in high capacity optical transmission systems [12]. One approach is to propagate optical pulses in a series of fibre segments connected alternatively with positive and negative values of β_2 , as



shown in Fig. 2.6. The positive β_2 implies that optical components with longer wavelength propagate faster than those with shorter wavelength [35]. The optical pulse disperses somewhat at the end of segment one due to the velocity difference between frequency components. On the contrary, the negative β_2 implies that optical components with longer wavelength propagate slower than those with shorter wavelength. The dispersed pulse is restored to its original width at the end of segment two due to the fact that positive and negative values of β_2 in segment one and two are cancelled out each other.

Fig. 2.6. Dispersion compensation fibre cables

Pre-chirping optical pulses at the transmitting end can delay the impairments of chromatic dispersion [12]. The pre-chirping creates an increasing optical frequency along pulse profile from the trailing edge to the leading edge. If a pre-chirped pulse propagates in an optical fibre with negative β_2 , the long wavelength components in the leading edge would slip through the entire pulse backward to the trailing edge. Similarly, the trailing edge of the pulse would slip forward to the leading edge. The swapping between the leading and trailing edge components makes the pulse immune to dispersion for a certain propagation distance. However, dispersion will begin to occur when the pulses reach the distance where the swapping between the leading and trailing edges has completed. This dispersion

compensation method is effective only for relatively short distance propagation (< 200 km) [12].

Another approach to tackle dispersion is optical phase conjugation (OPC). The phase conjugation reverses the optical spectrum of the signal in a way that optical components with longer wavelength are converted to shorter wavelength and vice versa. The pulse shape is unchanged in the process. The phase conjugation can be carried out at the mid point of the total propagation distance. The optical pulse disperses in the first half of the propagation. The phase conjugator inverts the frequency components of the pulse at the midpoint. The second half of the propagation restores the pulses back to its original width.

A non-system-invasive approach to solve the dispersion problem is optical soliton. By finding a delicate balance between dispersion coefficient and fibre nonlinearity, pulse shape of a soliton can be maintained regardless of the propagation distance [35]. Chapter 3 will give a more detailed description about the theory of soliton. Experiments show that, with soliton control scheme, the transmission distance of soliton pulses can be as long as 20,000 km [55] and even unlimited [32].

The most daunting challenge to soliton transmission is the timing jitter of the propagating soliton pulses. A soliton needs a certain level of peak optical power to sustain its undistorted shape during propagation. Fibre loss is compensated by periodically placing optical amplifiers along the fibre link for maintaining the peak power required in soliton transmission. The perturbation of the soliton waves by amplified spontaneous emission (ASE) generated in the amplification process causes root-mean-square (RMS) central optical frequency jitter among individual soliton pulses [53]. The frequency jitter will be transformed to timing jitter as the soliton pulses propagate along the fibre link. The timing jitter increases with ASE and propagation distance. The accumulated timing jitter in a long

fibre link with many optical amplifiers would result in severe OTDM crosstalk when the signal is demultiplexed at the receiving end of the transmission.

Since the RMS frequency jitter of soliton pulses increases with ASE, timing jitter can be reduced somewhat by using an optical filter to limit the amount of wide bandwidth ASE at the amplifier output. Under this jitter-reduction scheme, optical power at the wings of the soliton spectrum would be lost due to the finite bandwidth of the optical filter. After an optical signal passes through a number of optical filters in a long transmission distance, the accumulated loss in soliton power due to the filters may become so large that the optical power of the pulse is no longer adequate for maintaining soliton propagation. The amplifiers should have extra gain to compensate for the soliton power loss due to optical filters. Nevertheless, the extra gain creates another problem -- it amplifies the background optical power between soliton pulses. In the situation without extra gain (i.e. the amplifier gain is exactly equal to the fibre loss), such background power would be attenuated by the fibre loss. With amplifier gain larger than the fibre loss, the background optical power may eventually destroy the soliton transmission when it grows to become comparable to the soliton power [56]. Nonlinear gain can be employed to amplify the high intensity soliton pulses and to suppress the low intensity background instability [57]. Alternatively, the background instability from the extra gain could be eliminated by sliding the central frequency of the optical filters along the transmission distance [58]. This technique makes use of the fact that a soliton pulse will shift its central frequency as it propagates in a fibre cable [35]. Therefore only the soliton pulses can follow the frequency sliding filters and the spectrum of background power will not be amplified throughout the propagation.

Some of the dispersion compensation techniques described earlier this section can reduce the timing jitter between soliton pulses without the need of implementing schemes to

suppress the central frequency jitter. Timing jitter occurs when a train of frequency-jittered solitons propagates a certain distance of fibre cable, due to the velocity difference between adjacent soliton pulses. Therefore, it is possible to employ some dispersion compensation techniques to reverse the process of timing jitter. For example, optical phase conjugation (OPC) at an optimum point along the transmission link or at the end of the transmission link for post-transmission compensation could be used to undo the timing jitter caused by the frequency jitter of soliton pulses [59]. Besides timing jitter, another problem that limits the bit rate and transmission distance of soliton transmission is soliton interaction [60], which will be described in detail in Chapter 3. Soliton interaction induces attraction and repulsion forces between adjacent soliton pulses during the propagation. Controlling the relative phase [35] or amplitude [35], [61] between soliton pulses can weaken the soliton interaction forces.

It is difficult to realise high capacity OTDM system for long-haul transmission because of the problems described above. The highest bit rate of OTDM transmission system reported in the literature is 1.28 Tbit/s [155]. However, the transmission distance was only 70 km. E. Yoshida, *et-al* demonstrated a 320 Gbit/s OTDM transmission over 120 km using dispersion compensation fibre [62]. The highest bit-rate-distance product under the current technology is 89.6 Tb.km/s.

2.7 The Future

Major telecommunication carriers around the world have chosen WDM as a multiplexing scheme for delivering high capacity data transmission since mid 1990's. On the research front, the most advanced WDM system is capable of transmitting 3.08 Tbit/s (77 channels \times 42.7 Gbit/s) data over 1200 km [155], while the best OTDM system can only transmit 1 Tbit/s (128 channels \times 10 Gbit/s) data over 70 km [156]. In short to medium term, WDM is

a preferred multiplexing scheme to meet the huge demand of ever-increasing bandwidth-hungry applications. Nevertheless, one major fundamental weakness of a WDM system is its inefficient use of transmission bandwidth. In a WDM system, a significant portion of frequency spectrum is allocated for the guard bands. At the current stage of WDM research, there is still room in the frequency spectrum for increasing the number of WDM channels through technology improvement. In the future, given the finite low-loss bandwidth of fibre, the WDM development may reach a state where fibre bandwidth is used up and therefore is incapable of accommodating more WDM channels. There will be a need to use the fibre bandwidth more efficiently. Although OTDM is a multiplexing scheme that can efficiently utilize fibre bandwidth, the problems associated with ultra-high data rate transmission described in the last section pose formidable difficulties to the implementation of OTDM system. There probably exists a fundamental limitation of bit-rate-distant product in OTDM transmission. This means that it may not be possible to increase OTDM bit rate beyond some point. The future optical communication system could combine the ideas of WDM and OTDM for delivering long-haul high capacity data transmission, i.e. OTDM-level bit rate for each WDM channel. In fact, an attempt has been made by S. Kawanishi, *et-al* to demonstrate the possibility of this combination [63]. A 3 Tb/s ($160 \text{ Gbit/s} \times 19 \text{ WDM channels}$) optical signal has been successfully transmitted over 40 km in this experiment. Each 160 Gbit/s WDM channel is composed of $10 \text{ Gbit/s} \times 16 \text{ OTDM channels}$. WDM and OTDM can complement each other in such hybrid system. Currently an imbalance of research resources is overwhelmingly focused on the WDM-related technologies due to the wide spread use of WDM transmission. It is also important to intensify the development of OTDM technologies. All-optical time division demultiplexer is an essential building block of an OTDM system. The aim of this thesis is to provide a thorough analysis of the noise and crosstalk characteristics of two all-optical

time division demultiplexing devices, namely, nonlinear optical loop mirror and terahertz optical asymmetric demultiplexer.

CHAPTER THREE - NONLINEAR FIBRE OPTICS

3.1 Introduction

The propagation of light in vacuum behaves as a high speed shifting of a sinusoidal electromagnetic wave. In a non-vacuum medium, the propagation of light is a function of a time-and-frequency-dependent polarisation vector, which is induced from the physical interaction between the electric fields and the materials of the medium. If the response of a medium to the optical wave is linear, then the simplest form of the resultant polarisation vector (P) will be a linear function given as:

$$P(z, t) = \kappa \cdot E(z, t), \quad (3.1)$$

where $E(z, t)$ is the electric field interacting with the medium, and κ is a constant value representing the response of the medium.

If fibre material had a linear response as represented by (3.1), fibre optic communication systems would be free from all the troubles of fibre nonlinearities described in Chapter 2. Instead of a constant value, the material response (i.e. κ in (3.1)) of fibre material is in some way dependent on the electric field of the light. The most general form of the induced polarisation vector is [35]:

$$P = \epsilon_0 \left[\chi^{(1)} \cdot E + \chi^{(2)} \cdot E^2 + \chi^{(3)} \cdot E^3 + \dots \right], \quad (3.2)$$

where ϵ_0 is the vacuum permittivity and $\chi^{(j)}$ ($j = 1, 2, \dots$) is the j^{th} order electric susceptibility.

The electric susceptibilities in (3.2) are dependent on the wavelength of the propagating light. The response of fibre material to a propagating wave is nonlinear due to the existence of $\chi^{(j)}$ ($j \geq 2$). The nonlinear response of the fibre material and the interaction between nonlinearly induced polarisation vectors of multiple co-propagating electromagnetic waves

lead to a number of fascinating nonlinear phenomena such as self-phase modulation, cross-phase modulation, four wave mixing and stimulated Raman scattering.

Nonlinear fibre optics is playing an important role in today's fibre optics communication systems. Better understanding of the nonlinear behaviours of optical signals is essential for the development of viable engineering solutions that alleviate the undesirable nonlinear effect, and in some cases exploit those nonlinear effects in order to realize a wide range of all-optical devices such as switching, demultiplexing, wavelength conversion and amplification [1], [16], [46], [64]. This Chapter covers some of the important areas of nonlinear fibre optics, with special attention given to the ones that are relevant to the analysis of the two all-optical devices: NOLM and TOAD. The organisation of this chapter is as follows. Pulse propagation in optical fibre will be described mathematically in Section 3.2. The rest of this chapter will be devoted to the five important nonlinear fibre phenomena, which are SPM, XPM, optical soliton, FWM and SRS.

3.2 Pulse Propagation in Optical Fibre

3.2.1 Nonlinear Schrödinger equation

The one-dimensional electric field $E(z,t)$ of an optical pulse propagating in optical fibre cable can be represented mathematically as:

$$E(z,t) = A(z,t) \cdot \exp[i(\omega_0 t - k_0 z)], \quad (3.3)$$

where $A(z,t)$ is the slow-varying envelope of the wave, ω_0 is the central frequency of the optical pulse, $k_0 = n(\omega_0)\omega_0/c$ is the propagation constant at ω_0 , n is the wavelength-dependent refractive index, and c is the speed of light in vacuum.

In a dispersive nonlinear medium such as optical fibre, the propagation constant is dependent on wavelength and light intensity given as:

$$k(\omega) = k_L(\omega) + \gamma \cdot P, \quad (3.4)$$

where $k(\omega)$ is the effective propagation constant, k_L is the linear part of $k(\omega)$, γ is the nonlinear coefficient, and P is the optical power of the propagating pulse. The wavelength dependence of $k_L(\omega)$ can be expressed as a Taylor's series [25]:

$$k_L(\omega) = k_o + (\omega - \omega_o) \cdot \frac{\partial k(\omega_o)}{\partial \omega} + \frac{(\omega - \omega_o)^2}{2} \cdot \frac{\partial^2 k(\omega_o)}{\partial \omega^2} + \dots \quad (3.5)$$

If (3.5) is approximated by ignoring the higher order terms and then substituted into (3.4), we will have :

$$\Delta k = \Delta \omega \cdot \frac{\partial k(\omega_o)}{\partial \omega} + \frac{\Delta \omega^2}{2} \cdot \frac{\partial^2 k(\omega_o)}{\partial \omega^2} + \gamma \cdot P, \quad (3.6)$$

where $\Delta k = k(\omega) - k_o$, and $\Delta \omega = \omega - \omega_o$.

The Fourier transform pair for $A(z, t)$ in (3.3) is:

$$A(\Delta k, \Delta \omega) = \iint A(z, t) \cdot \exp(-i\Delta k z) \cdot \exp(i\Delta \omega t) dz dt, \quad (3.7)$$

$$A(z, t) = \frac{1}{(2\pi)^2} \iint A(\Delta k, \Delta \omega) \cdot \exp(i\Delta k z) \cdot \exp(-i\Delta \omega t) d\Delta k d\Delta \omega. \quad (3.8)$$

Differentiating (3.8) with respect to z and t results in (3.9) and (3.10), respectively:

$$\frac{\partial A(z, t)}{\partial z} = i\Delta k \cdot A(z, t). \quad (3.9)$$

$$\frac{\partial A(z, t)}{\partial t} = -i\Delta \omega \cdot A(z, t). \quad (3.10)$$

Differentiating (3.10) with respect to t gives:

$$\frac{\partial^2 A(z, t)}{\partial t^2} = -\Delta \omega^2 \cdot A(z, t). \quad (3.11)$$

Equations 3.6, 3.9, 3.10 and 3.11 can be combined into:

$$i \frac{\partial A(z, t)}{\partial z} + i \frac{1}{V_g} \cdot \frac{\partial A(z, t)}{\partial t} - \frac{1}{2} \cdot \frac{\partial^2 k(\omega_o)}{\partial \omega^2} \cdot \frac{\partial^2 A(z, t)}{\partial t^2} + \gamma \cdot P \cdot A(z, t) = 0,$$

$$\text{where } \frac{1}{V_g} = \frac{\partial k(\omega_o)}{\partial \omega}. \quad (3.12)$$

V_g is the group velocity of the pulse. The first two partial differential terms can be transformed to an ordinary differential term as shown in the following equation:

$$i \frac{dA(z,t)}{dz} - \frac{1}{2} \cdot \frac{\partial^2 k(\omega_o)}{\partial \omega^2} \cdot \frac{\partial^2 A(z,t)}{\partial t^2} + \gamma \cdot P \cdot A(z,t) = 0. \quad (3.13)$$

The first term in (3.13) is interpreted as the ordinary distance derivative as seen by an observer moving with the velocity V_g . It is useful to transform $A(z,t)$ in (3.13) to an amplitude profile $A(z,\tau)$, which is in the function of a frame of reference τ moving at the group velocity V_g . τ is commonly known as the time reference to the profile of a propagating pulse. Then (3.13) becomes:

$$i \frac{\partial A(z,\tau)}{\partial z} + \frac{i\alpha}{2} - \frac{\beta_2}{2} \cdot \frac{\partial^2 A(z,\tau)}{\partial \tau^2} + \gamma \cdot |A(z,\tau)|^2 \cdot A(z,\tau) = 0, \quad (3.14)$$

where $\tau = t - z/V_g$ and α is the power loss coefficient to account for fibre loss. β_2 in (3.14) represents the second order frequency derivative in (3.13), it is also called first order dispersion coefficient as mentioned in Chapter 2. $A(z,\tau)$ in (3.14) is normalised with the optical power ($|A|^2 = P$). Equation 3.14 is called Nonlinear Schrödinger Equation (NSE) when $\alpha = 0$. It governs the evolution of amplitude profile of a pulse propagating in a dispersive nonlinear medium. The third term of the equation represents the first order dispersion, and the last term of the equation takes into account the nonlinear effect of the optical fibre.

3.2.2 Beam Propagation Method (BPM)

Equation 3.14 is a nonlinear partial differential equation, therefore cannot be solved analytically. BPM is a numerical approach that is widely used to solve the NSE [35], [65], [66]. The procedures for solving the NSE using BPM are described in this subsection. All simulations of optical pulse propagation in fibre cable presented in this thesis are calculated using BPM. The source code of the Matlab program for implementing BPM is shown in the Appendix. The source code was written by the Author.

Referring back to (3.14), dispersion (3rd term) and nonlinearity (4th term) act together to change the optical field throughout the length of the fibre cable. Since both dispersion and nonlinearity are dependent on the optical field and the optical field itself is also dependent on these two terms, the dispersion and nonlinearity terms are inter-dependent. BPM yields an approximate solution for the NSE by assuming that in propagating the optical field over a small distance, the dispersive and nonlinear effects can be treated as acting independently on the optical field. Therefore, (3.14) can be rewritten as:

$$\frac{\partial A(z, \tau)}{\partial z} = (\hat{D} + \hat{N}(A(z, \tau)))A(z, \tau), \quad (3.15)$$

where

$$\hat{D} = -i \frac{\beta_2}{2} \cdot \frac{\partial^2}{\partial \tau^2} - \frac{\alpha}{2}, \quad (3.16)$$

$$\hat{N}(A(z, \tau)) = i\gamma \cdot |A(z, \tau)|^2. \quad (3.17)$$

In (3.15), (3.16), and (3.17), \hat{D} is the dispersion operator which takes the dispersion and loss into account and $\hat{N}(A(z, \tau))$ is the nonlinearity operator. In BPM, the whole propagation distance is split into a large number of segments as shown in Fig. 3.1. At distance z , the optical field profile $A(z, \tau)$ propagates a small distance of $\Delta z/2$ with dispersion and loss only. When the pulse reaches the point $z+(\Delta z/2)$, the nonlinearity effect between distance z and $z+\Delta z$ is taken into account and the optical field profile changes

accordingly. Then the pulse propagates the remaining $\Delta z/2$ with dispersion and loss only. The accuracy of this approach depends on the resolutions of the segments. Given a fixed propagation length, increasing the number of segments would increase the accuracy of BPM.

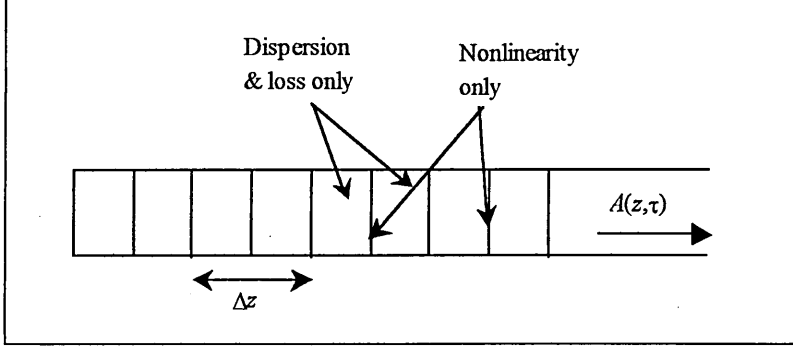


Fig. 3.1. Beam propagation method.

For separating the effects of dispersion and nonlinearity, (3.15) is broken down into the following two equations:

$$A(z + (\Delta z / 2), \tau) = \exp(\hat{D} \cdot (\Delta z / 2)) \cdot A(z, \tau), \quad (3.18)$$

$$A(z + \Delta z, \tau) = \exp(\hat{N}(A(z + (\Delta z / 2), \tau)) \cdot \Delta z) \cdot A(z, \tau). \quad (3.19)$$

Equation 3.16 cannot be directly substituted into (3.18) as \hat{D} is a differential operator, not a mathematical expression. In order to solve this problem, \hat{D} is rewritten by replacing the differential operator $\partial/\partial \tau$ with $i\omega$ [67]. Then (3.16) becomes:

$$\hat{D} = i \frac{\beta_2}{2} \cdot \omega^2 - \frac{\alpha}{2}. \quad (3.20)$$

Using (3.17) to (3.20), we can present Fig. 3.1 mathematically as:

$$A(z + \Delta z, \tau) = F^{-1}(F(F^{-1}(F(A(z, \tau)) \cdot \exp(\hat{D} \cdot \Delta z / 2)) \cdot \exp(\hat{N}(F^{-1}(\exp(\hat{D} \cdot \Delta z / 2) \cdot F(A(z, \tau)))) \cdot \Delta z)) \cdot \exp(\hat{D} \cdot \Delta z / 2)) \quad (3.21)$$

$F()$ and $F^{-1}()$ in (3.21) represent Fourier-transform and inverse-Fourier-transform, respectively. Equation 3.21 is used to calculate the change of amplitude profile of a

propagating pulse over a small distance Δz . The calculated profile at $z+\Delta z$ can be substituted back into (3.21) for calculating the amplitude profile at $z+2\Delta z$. This loop of calculations continues for the rest of the segments. By using this method, we can obtain the evolution of the amplitude profile of an optical pulse over the whole propagation length.

3.2.3 Pulse deformation

The shape of an optical pulse propagating in a fibre cable generally changes with the propagation distance due to the interplay between dispersion and nonlinearity. The evolution of the amplitude profile of a propagating pulse can be obtained by solving (3.14) with BPM. This section shows how nonlinearity and dispersion deform the profile of a propagating pulse. Two cases are considered in the computer simulations, which are obtained by solving (3.14) with the beam propagation method described in the previous section. The amplitude of the optical field is normalised in such a way that the square of its absolute value is equal to the optical power.

Case I: *Pulse broadening*

Parameters	Values
FWHM pulse width	5 ps
β_2	8 ps ² /km
γ	2 W ⁻¹ km ⁻¹ for monomode fibre
Peak pulse power	620 mW
Pulse shape	Gaussian
Propagation distance	3 km
α	0 dB
Time resolution	128 points
Distance resolution	1500 points

The simulation result for pulse propagation using parameters listed in Table 3.1 is shown in Fig. 3.2. Fig. 3.2 shows that the peak power of the pulse is getting lower and the width of the pulse is getting wider as the propagation distance increases. The pulse broadening is due to dispersion and nonlinearity. Dispersion is a pulse widening effect, which is

originated from the velocity differences between various frequency components of the pulse. The nonlinearity creates a linear frequency chirp with positive gradient across the central part of a Gaussian pulse [35]. This is due to the optical power dependence of the effective propagation constant (see (3.4)). The variation of the effective propagation constant across the optical power profile modulates the phase of the optical wave. The resultant frequency chirp will lead to pulse broadening as different wavelength components across the pulse profile travel at different speed. It is also shown in Fig.3.2 that the rate of pulse broadening is high for the first 1 km of propagation, but decreases gradually as the pulse propagates further. This is because the dispersion and nonlinearity terms in (3.14) become less significant for a pulse with lower intensity and broadened width [35].

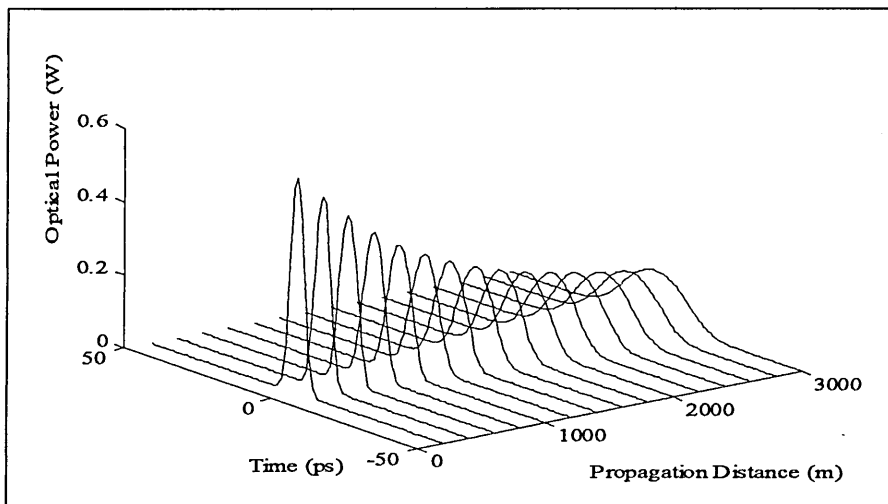


Fig. 3.2. Propagation of a broadened pulse.

Case II: Pulse compression

Table 3.2: Simulation Parameters for Case II	
Parameters	Values
FWHM pulse width	5 ps
β_2	-3 ps ² /km
γ	2 W ⁻¹ km ⁻¹
Peak pulse power	500 mW
Pulse shape	Gaussian
Propagation distance	3 km
α	0 dB
Time resolution	128 points
Distance resolution	1500 points

The simulation result for pulse propagation using parameters listed in Table 3.2 is shown in Fig. 3.3. Here the evolution of pulse profile is opposite to that of Fig. 3.1. The pulse compression shown in Fig 3.3 is due to the frequency chirp induced by nonlinearity. The fibre nonlinearity creates a linear frequency chirp across the optical pulse profile. A linear frequency chirp of a positive gradient under a negative β_2 leads to pulse compression. This is exactly the pulse compression effect described in Section 2.4.

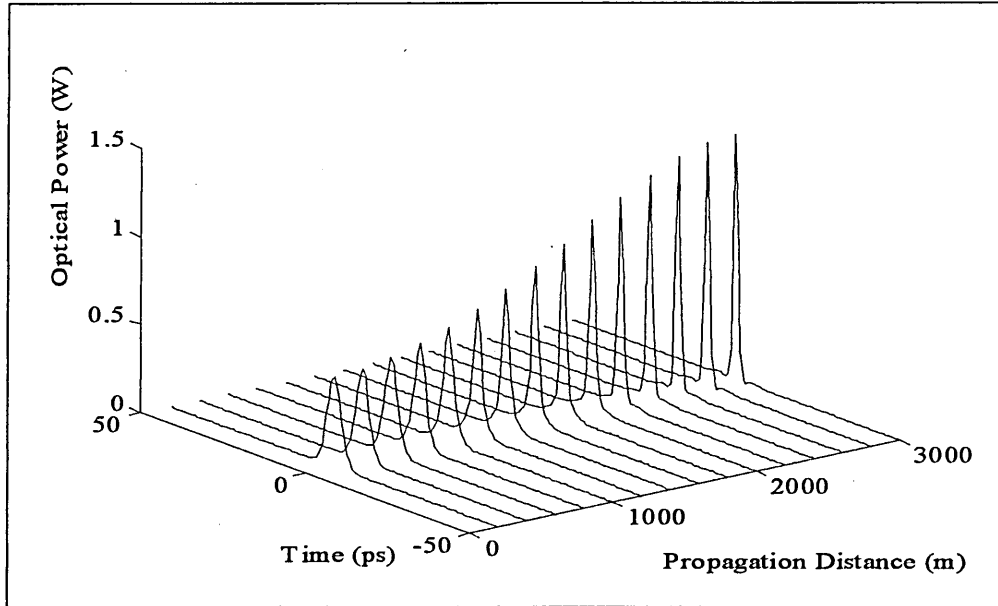


Fig. 3.3. Propagation of a compressed pulse.

3.3 Optical Soliton

3.3.1 Optical Soliton at the anomalous dispersion wavelength

Generally, numerical approaches are needed to approximate a solution for the NSE. In 1972, Zakharov and Shabat applied the inverse scattering method to exactly solve the NSE under some special conditions [68]. The inverse scattering method leads to a set of analytical solutions for a propagating pulse provided that the initial amplitude profile of the pulse at $z = 0$ satisfies the following general equation.

$$A(0, \tau) = N \operatorname{sech} \left(\frac{1.763 \cdot \tau}{T_{FWHM}} \right), \quad (3.22)$$

where T_{FWHM} is the full width half maximum of the optical power profile, and N is an integer associated with the soliton order. Equation 3.22 is normalised in such a way that the peak amplitude is equal to 1 for $N = 1$. The soliton order is related to the other propagation parameters by the following equation:

$$N^2 = \frac{\gamma \cdot P_o \cdot T_{FWHM}^2}{3.11 \cdot |\beta_2|}, \quad (3.23)$$

where P_o is the peak optical power of the soliton pulse, and β_2 must be anomalous.

Equation 3.22 represents a fundamental soliton for $N = 1$. A fundamental soliton can maintain its pulse shape profile regardless of the propagation distance. This unique feature is the result of a delicate balance between SPM and dispersion in the anomalous dispersion region.

Computer simulation for soliton propagation using BPM is shown in Fig. 3.4. Parameters used in the simulation (Table 3.3) meet the condition set in (3.23).

Parameters	Values
FWHM pulse width	5 ps
β_2	-8.04 ps ² /km
γ	2 W ⁻¹ km ⁻¹
Peak pulse power	500 mW
Pulse shape	Soliton
Propagation distance	3 km
α	0 dB
Time resolution	128 points
Distance resolution	1500 points

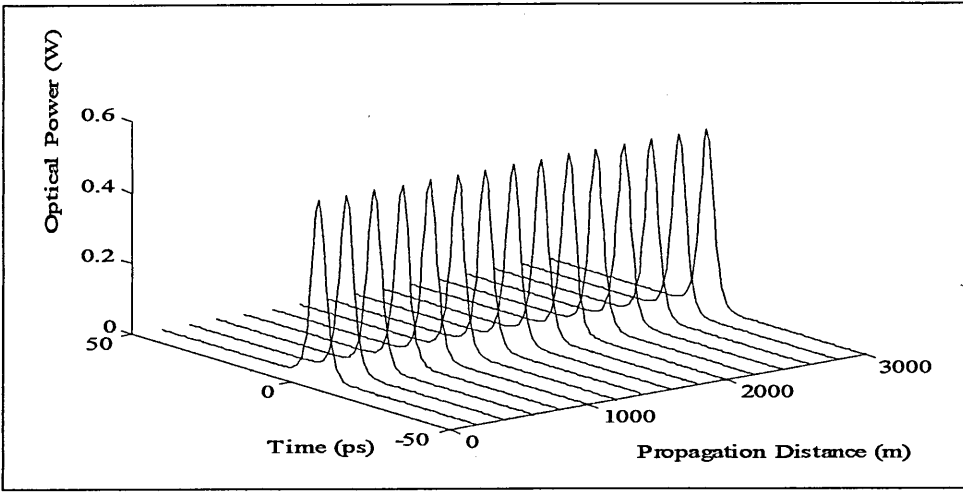


Fig. 3.4. Soliton propagation.

Parameters of a standard single mode fibre at wavelength 1550 nm are $\gamma = 2\text{W}^{-1}\text{km}^{-1}$, and $\beta_2 = -17\text{ps}^2/\text{km}$. According to (3.23), the peak power required to support propagation of 5 ps fundamental soliton for a standard single mode fibre is 1 W. Using dispersion-shifted fibre (DSF) with smaller $|\beta_2|$ can reduce the soliton peak power. For example, the soliton peak power for $\beta_2 = -1\text{ps}^2/\text{km}$ and $T_{FWHM} = 5\text{ps}$ is 62 mW.

The propagation of higher order soliton ($N > 1$ in (3.23)) behaves very differently from the propagation of fundamental soliton. The mathematical expression for the propagation of a second order soliton ($N = 2$) is given as [35]:

$$A(z, \tau) = \frac{4 \cdot \left[\cosh\left(3 \cdot \frac{1.763 \cdot \tau}{T_{FWHM}}\right) + 3 \cdot \exp(i \cdot 4 \cdot \xi) \cdot \cosh\left(\frac{1.763 \cdot \tau}{T_{FWHM}}\right) \right] \cdot \exp(i \cdot \xi / 2)}{\left[\cosh\left(4 \cdot \frac{1.763 \cdot \tau}{T_{FWHM}}\right) + 4 \cdot \cosh\left(2 \cdot \frac{1.763 \cdot \tau}{T_{FWHM}}\right) + 3 \cdot \cos(4 \cdot \xi) \right]}, \quad [3.24]$$

$$\text{where } \xi = \frac{z \cdot 3.11 \cdot |\beta_2|}{T_{FWHM}^2}. \quad [3.25]$$

Figure 3.5 shows the evolution of a propagating second order soliton pulse calculated by (3.24). The simulation parameters are $T_{FWHM} = 5\text{ps}$, $\beta_2 = -10\text{ps}^2/\text{km}$, $\gamma = 2\text{W}^{-1}\text{km}^{-1}$, and $\alpha = 0$. The initial amplitude shape of any order of soliton pulse is a hyperbolic secant function.

Therefore initial optical power profile of the second order soliton pulse shown in Fig. 3.5 is also a hyperbolic secant square shape. The pulse is compressed to a higher peak and narrower width at the initial stage of the propagation. A small second peak appears at a distance around 400 m, and the pulse is restored to its original shape at 1265 m. If the propagation distance is extended beyond 1265 m, the pulse shape evolution cycle shown in Fig. 3.5 will repeat itself every 1265 m. Unlike the fundamental soliton, which has an undistorted shape for any propagation distance, the pulse shape of higher order soliton changes periodically with a cycle governed by the mathematical function corresponding to the soliton order. The pulse propagation cycle of the second order soliton is governed by (3.24). Similarly, all other high order solitons ($N > 2$) have their own mathematical functions for calculating their evolution cycles of pulse propagation.

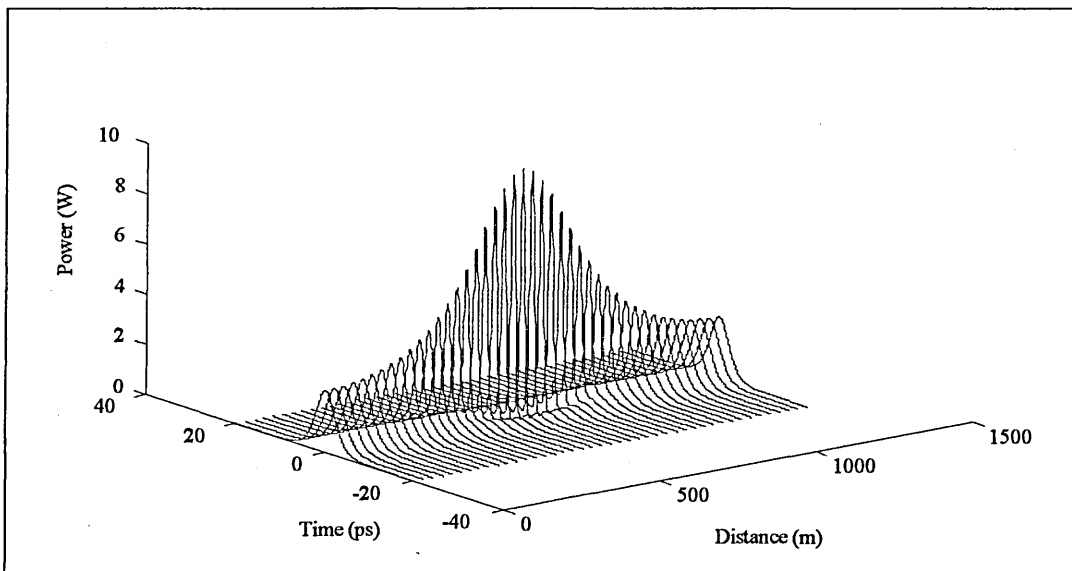


Fig. 3.5. Pulse propagation for second order soliton.

The distance for one cycle of pulse evolution is called soliton period. The soliton period for the second order soliton shown in Fig. 3.5 is 1265 m. The equation for calculating soliton period (z_o) is [35]:

$$z_o = \frac{0.161 \cdot \pi \cdot T_{FWHM}^2}{|\beta_2|} \quad (3.26)$$

Equations 3.22 and 3.23 must be satisfied for soliton propagation. It requires a strict control of the shape and peak power of an optical pulse. Practically it is very difficult to generate optical pulses with an exact shape of hyperbolic secant square as required in (3.23). The soliton discussion so far would merely be a theoretical analysis for mathematicians if the conditions constituting a soliton pulse set by (3.22) and (3.23) must be precisely met in the optical transmitter. It turns out that a soliton can still be formed even if the shape of a pulse is initially deviated from the ideal shape of hyperbolic secant square, provided that the pulse has sufficient peak power. If the peak power of a pulse is equivalent to $0.5 < N < 1.5$ in (3.23), the pulse will adjust its shape and width to transform itself to the shape and width of fundamental soliton after a certain propagation distance. The non-soliton part of the pulse energy will be dispersed away in the process. If the peak power of a pulse is equivalent to $1.5 < N < 2.5$ in (3.23), the pulse will transform itself to a second order soliton. The same applies to all higher order solitons. Figure 3.6 shows the transformation of an optical pulse from a Gaussian shape to a soliton shape. The propagating pulse is in the transformation process during the first half of the propagation. The pulse shape is then kept constant after being transformed to fundamental soliton. This simulation is obtained by solving the NSE with BPM. The simulation parameters for Fig. 3.6 are listed in Table 3.4.

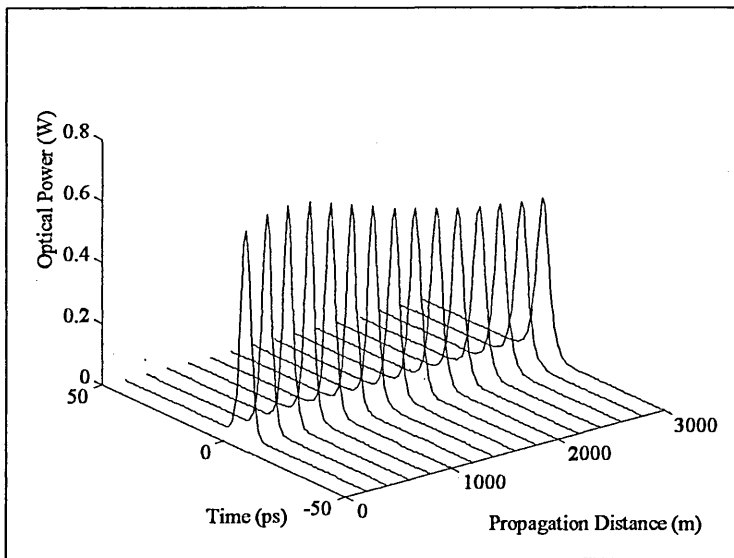


Fig. 3.6. Transformation from a Gaussian pulse to a fundamental soliton.

Table 3.4: Simulation parameters	
Parameters	Values
FWHM Pulse Width	5 ps
β_2	-10 ps ² /km
γ	2 W ⁻¹ km ⁻¹
Peak Pulse Power	650 mW (change to 622 mW for the fundamental soliton)
Initial Pulse Shape	Gaussian (final pulse shape is fundamental soliton)
Propagation Distance	3 km
α	0 dB
Time Resolution	128 points
Distance Resolution	1500 points

Theoretically the propagation of fundamental soliton is free of distortion for any propagation distance. In reality, fibre loss limits the propagation distance of soliton systems since soliton needs sufficient optical power to have the required nonlinearity balanced against dispersion. According to (3.23), the pulse width of a propagating soliton will increase as its peak power decreases due to fibre loss. It is necessary to use optical amplifier to maintain the peak power level of the soliton pulses as mentioned in Section 2.6.

3.3.2 Optical soliton at zero dispersion wavelength

Optical soliton in the anomalous dispersion region is the effect of a delicate balance between fibre nonlinearity and the first order dispersion coefficient. In standard fibre, the first order dispersion coefficient dominates over higher orders dispersion coefficients. In dispersion-shifted fibre, where β_2 for the operating wavelength region is zero, dispersion would exist in the form of higher order dispersion coefficients. Since the dispersion of NSE (i.e. (3.14)) has only the first order dispersion coefficient term, the term of higher order dispersion coefficient needs to be included for dispersion-shifted fibre. If the fibre loss is ignored, the modified propagation equation becomes [35]:

$$i \frac{\partial A(z, \tau)}{\partial z} - i \frac{\beta_3}{6} \cdot \frac{\partial^3 A(z, \tau)}{\partial \tau^3} + \gamma \cdot |A(z, \tau)|^2 \cdot A(z, \tau) = 0, \quad (3.27)$$

where β_3 is the second order dispersion coefficient.

Figure 3.7 shows the change of frequency spectrum of a hyperbolic secant pulse propagating at the zero-dispersion wavelength [35]. The spectrum of a soliton-shape pulse initially centres at the zero dispersion wavelength (dashed line in Fig. 3.7). After a certain propagation distance, the pulse spectrum will be split into two spectral peaks (solid lines in Fig. 3.7) due to the self phase modulation effect [35]. The two peaks are in positive and negative β_2 regions, respectively. The spectral peak in anomalous β_2 will form a soliton as the negative value of β_2 balances against the fibre nonlinearity. The part of pulse energy in the positive β_2 will disperse away because of the dispersion effect. The soliton peak power in the anomalous β_3 region is related to other system parameters as:

$$N^2 = \frac{\gamma \cdot P_o \cdot T_{FWHM}^3}{5.48 \cdot |\beta_3|}. \quad (3.28)$$

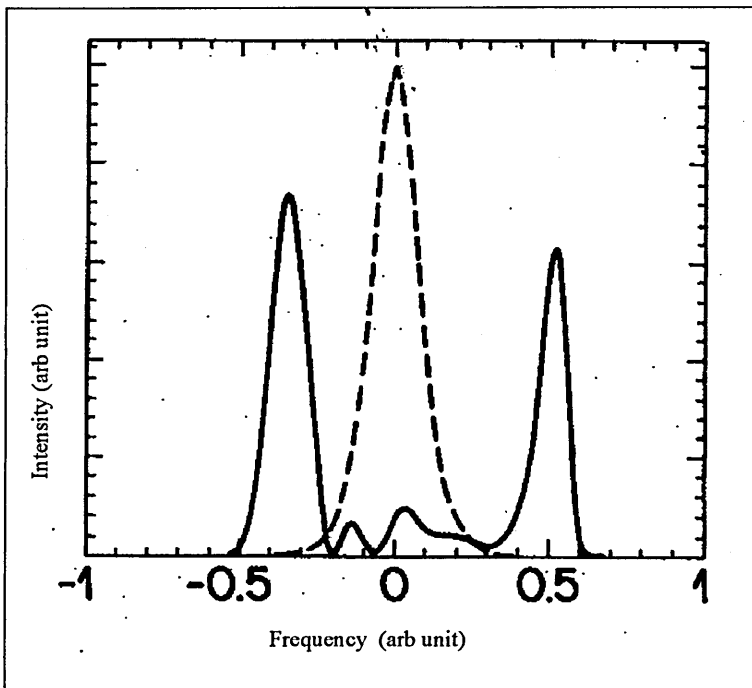


Fig. 3.7. Frequency spectrum of a hyperbolic secant pulse propagating at zero-dispersion wavelength.

In general, the reason for using zero-dispersion wavelength in fibre optics communication is to suppress the dispersion effect and avoid the merger between two adjacent pulses in a long distance transmission. Nevertheless, this argument is invalid for soliton transmission since there is no dispersion problem in soliton systems. The advantage of transmitting soliton pulse at zero dispersion wavelength is the reduction of the peak power required to support soliton propagation. For the same value of N , lower peak power is required in (3.28) than in (3.23). However, the formation of soliton at zero dispersion wavelength requires a long propagation distance in order to get rid of the dispersing positive β_2 part of the pulse energy. The dispersing part of the pulse energy may interfere with the adjacent pulses in the process of soliton formation if the duty cycle of the signal is not sufficiently small.

3.3.3 Soliton interaction

Soliton interaction refers to the attractive and repulsive forces between two adjacent solitons. Two adjacent solitons may move closer/apart during propagation, depending on the separation time, their relative phase and amplitude. For two solitons with the same amplitude, the attractive force between them is at maximum when they are in-phase (no phase difference) and the repulsive force between them is at maximum when they are anti-phase (phase difference = π) [60]. The forces of soliton interaction increase when the separation time between the two solitons decreases. Soliton interaction has a devastating effect on OTDM transmission as it may result in a complete dislocation of the pulses from their corresponding time slots. The attractive forces between two solitons may also lead to a merger between the two.

The equation for the time domain profile of two adjacent in-phase fundamental solitons at $z = 0$ is given as:

$$A(0, \tau) = \operatorname{sech} \left[\frac{1.763 \cdot \left(\tau - \frac{\Delta T}{2} \right)}{T_{FWHM}} \right] + \operatorname{sech} \left[\frac{1.763 \cdot \left(\tau + \frac{\Delta T}{2} \right)}{T_{FWHM}} \right], \quad (3.29)$$

where ΔT is the time separation between the peaks of the two soliton pulses.

Equation 3.29 is substituted into (3.14) and then solved by BPM. The results are shown in Fig. 3.8, and the simulation parameters are listed in Table 3.5.

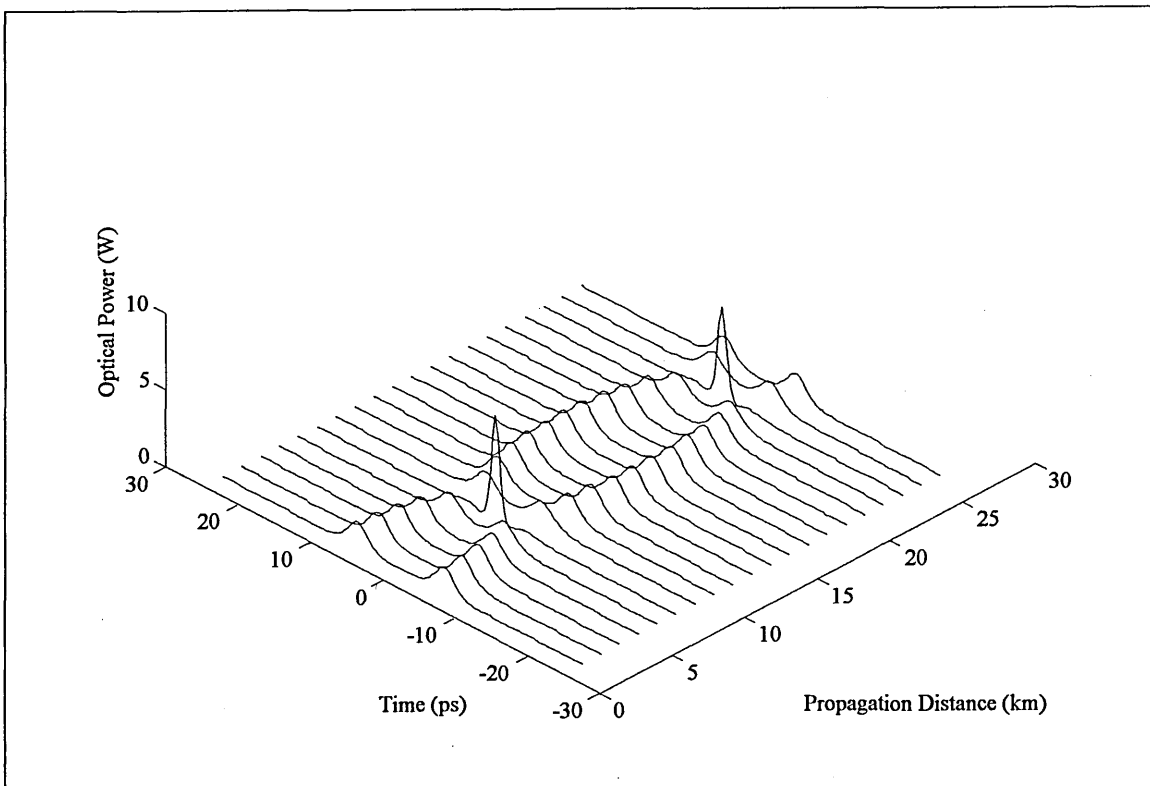


Fig. 3.8. Pulse merging cycle due to the attractive force of soliton interaction.

Table 3.5: Simulation parameters

Parameters	Values
FWHM pulse width	3 ps
β_2	-10 ps ² /km
γ	2 W ⁻¹ km ⁻¹
Peak pulse power	1.73 mW
Initial pulse phase	A pair of fundamental solitons (in-phase)
Separation time of the soliton pair	12ps (between the peaks of the solitons)
Propagation distance	26 km
α	0 dB
Time resolution	128 points
Distance resolution	13,000 points

As can be seen from Fig. 3.8, initially the two solitons are separated by about 10 ps. As the propagation distance increases, the two pulses get closer by the attractive force of soliton interaction until they completely merge at around the propagation distance of 7.5 km. Beyond this point, the two pulses diverge away from each other as they propagate further. At around propagation distance of 15 km, the two pulses start to converge, once again merging completely at around 22 km. The evolution of two initially in-phase solitons will

follow a pattern of pulse merging cycle similar to the one shown in Fig. 3.8. The length of the pulse merging cycle (L_S) depends on the separation time between the two solitons and is given as [35]:

$$L_S = \frac{\pi \cdot \sinh\left(\frac{1.763 \cdot \Delta T}{T_{FWHM}}\right) \cdot \cosh\left(\frac{0.882 \cdot \Delta T}{T_{FWHM}}\right) \cdot T_{FWHM}^2}{3.11 \cdot |\beta_2| \cdot \left[\frac{1.763 \cdot \Delta T}{T_{FWHM}} + \sinh\left(\frac{1.763 \cdot \Delta T}{T_{FWHM}}\right) \right]} \quad (3.30)$$

In Fig. 3.8, the two successively propagating solitons merge into one provided that the initial phase difference between them is zero. However, if the initial phase difference between two solitons is π , then the repulsive force of soliton interaction will drive them apart. The equation representing two successively propagating solitons with phase difference π is:

$$A(0, \tau) = \sec h \left[\frac{1.763 \cdot \left(\tau - \Delta T/2\right)}{T_{FWHM}} \right] + \sec h \left[\frac{1.763 \cdot \left(\tau + \Delta T/2\right)}{T_{FWHM}} \right] e^{i\pi} \quad (3.31)$$

Equation 3.31 is substituted into (3.14) and then solved by BPM using the same simulation parameters in Table 3.5. The results are shown in Fig. 3.9, which illustrates that two solitons are driven apart as they propagate along the fibre.

One way to avoid soliton interaction is to increase the soliton separation time. The soliton interaction is insignificant if the soliton separation time meets the following condition [35].

$$\Delta T \gg 1.13 \cdot T_{FWHM} \cdot \log\left(\frac{L_T}{z_0}\right), \quad (3.32)$$

where L_T is the transmission distance, and z_0 is the soliton period (see (3.26)).

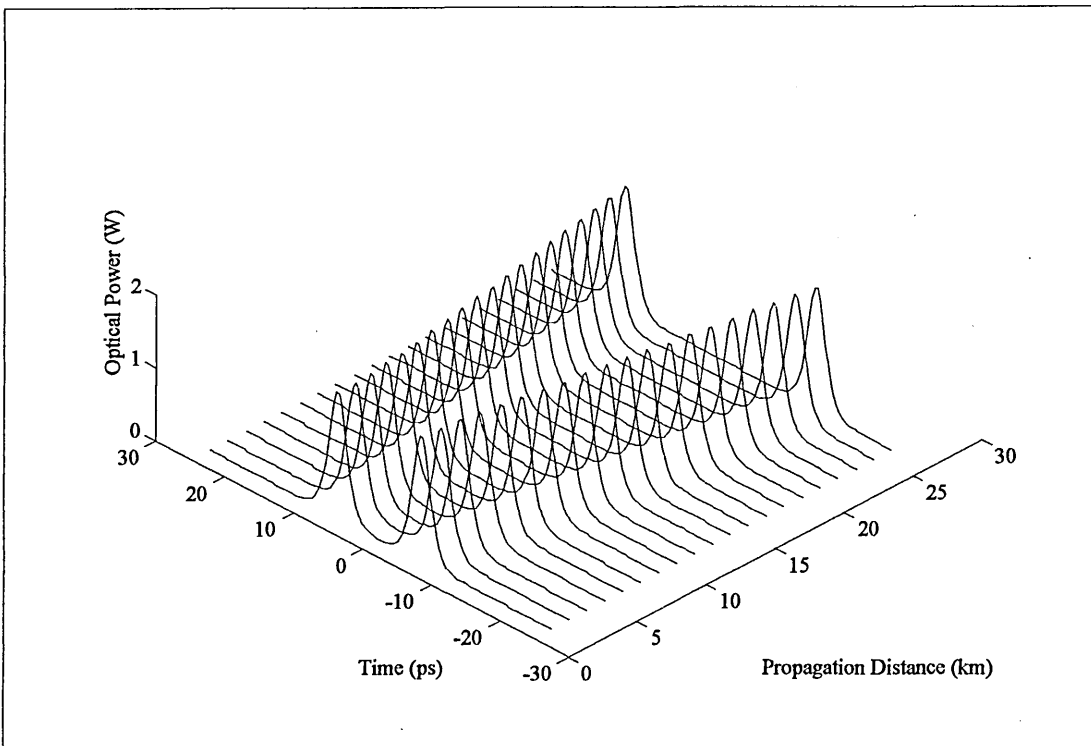


Fig. 3.9. The repulsive force of soliton interaction.

The overall impact of soliton interaction on an optical signal also depends on the bit pattern of the signal. If all bits are ones and the phase relationship between neighbouring pulses is the same, the soliton interaction will have no overall effect on the optical signal. For any pulse in the pulse train, the attractive/repulsive force by its preceding pulse will be cancelled out by the attractive/repulsive by its successive pulse. However, for real signal with random characteristics, the situation is more complicated. Employing coding schemes for a soliton train can reduce the impact of soliton interaction by making the mark and space more evenly distributed.

3.4 Cross Phase Modulation

Equation 3.14 represents the propagation of an optical wave. For the co-propagation of multiple optical waves with different wavelengths or polarisations, (3.14) needs to be modified to include additional fibre nonlinearity terms. In (3.4), the fibre nonlinearity is represented by the nonlinear coefficient term γ . XPM occurs due to the fact that the

effective refractive index of an optical wave depends not only on its optical power but also on the optical power of other co-propagating waves. The dependence of the effective refractive index on optical power and the resultant modulation of optical phase will be discussed in Section 3.4.1. Section 3.4.2 describes the XPM effect on the polarisation-maintaining (PM) fibre.

3.4.1 Optical Kerr effect

The electric field of a linearly polarised continuous optical wave can be expressed in trigonometric form as:

$$E = A \cos(\omega_o t), \quad (3.33)$$

where A is the slow-varying envelope (it is a constant value for a continuous wave), and ω_o is the central frequency of the optical wave. In order to simplify (3.33), the distant variable z is omitted for the consideration of only one observing point along the fibre cable. Equation 3.33 neatly represents a propagating optical wave. However, for the cases of multiple co-propagating optical waves, it is tedious and mathematically cumbersome to perform multiplication and division among trigonometric expressions. It is a common practice to represent (3.33) in exponential terms as:

$$E = \frac{1}{2} A \exp(i\omega_o t) + \frac{1}{2} A^* \exp(-i\omega_o t), \quad (3.34)$$

where A^* is the complex conjugate of A .

The electric field of two continuous optical waves of different wavelengths co-propagating in a fibre cable is:

$$E(t) = \frac{1}{2} A_1 \exp(i\omega_1 t) + \frac{1}{2} A_1^* \exp(-i\omega_1 t) + \frac{1}{2} A_2 \exp(i\omega_2 t) + \frac{1}{2} A_2^* \exp(-i\omega_2 t), \quad (3.35)$$

where A_1 and A_2 are the slow-varying amplitude profiles of the electric fields, and ω_1 and ω_2 are the central frequencies of the two optical waves. Equation 3.35 is in scalar form, with the assumption that the two optical waves are polarised on the same plane.

The electric fields interact with the susceptibilities of the fibre material to induce polarisation (see (3.2)). Mathematically it is equivalent to substituting (3.35) into (3.2). The first order susceptibility in (3.2) represents the linear response of the material. Only the third order susceptibility is considered in this sub-section as it is the one contributing to the XPM phenomenon. Substituting (3.35) into the third susceptibility term in (3.2) gives:

$$P_{NL}(t) = \frac{1}{2} \cdot [P_{NL}(\omega_1) \cdot \exp(i\omega_1 t) + P_{NL}(\omega_2) \cdot \exp(i\omega_2 t)] + \dots \quad (3.36)$$

where

$$P_{NL}(\omega_1) = \frac{3\epsilon_0 \chi_{xxxx}^{(3)}}{4} \cdot (|A_1|^2 + 2 \cdot |A_2|^2) \cdot A_1, \quad (3.37)$$

$$P_{NL}(\omega_2) = \frac{3\epsilon_0 \chi_{xxxx}^{(3)}}{4} \cdot (|A_2|^2 + 2 \cdot |A_1|^2) \cdot A_2. \quad (3.38)$$

Only the terms relevant to SPM and XPM are shown here. Equations 3.37 and 3.38 represent the nonlinear polarisations of frequencies ω_1 and ω_2 , respectively. The third order susceptibility $\chi^{(3)}$ is in a tensor structure with components responsible for different combinations of polarised planes of the two optical waves. As the two optical waves are assumed to be linearly polarised on the same plane, only one component of $\chi^{(3)}$ (i.e. $\chi_{xxxx}^{(3)}$) is included in (3.37) and (3.38). As shown in (3.37) and (3.38), the nonlinear polarisation of an optical wave depends not only on the light intensity of that wave but also on the light intensity of its co-propagating wave. If (3.35) is extended to N co-propagating waves, the nonlinear polarisation of each wave will have N nonlinear terms. The first and second terms of (3.37)-(3.38) lead to SPM and XPM, respectively. The contribution of

XPM terms to the nonlinear polarisation is twice as effective than that of the SPM term, as shown in (3.37) and (3.38).

An electric field is related to its induced polarisation by:

$$\mathbf{P} = \epsilon_0 \cdot \epsilon \cdot \mathbf{E}, \quad (3.39)$$

where ϵ is the dielectric constant (or relative permittivity). The dielectric constant consists of linear part and nonlinear part for taking into account the linear and nonlinear dependence of the induced polarisation. The linear and nonlinear parts of the dielectric constant for ω_1 in (3.35) are given in (3.40) and (3.41), respectively.

$$\epsilon_L = 1 + \chi^{(1)}. \quad (3.40)$$

$$\epsilon_{NL} = \frac{3}{4} \chi_{xxxx}^{(3)} \cdot (|A_1|^2 + 2 \cdot |A_2|^2). \quad (3.41)$$

ϵ_{NL} may be different for individual co-propagating optical waves as XPM is twice effective as SPM, as shown in (3.41) and (3.37)-(3.38). The dielectric constant can be related to the refractive index by the following equation [35].

$$\epsilon_L + \epsilon_{NL} = (n + \Delta n)^2, \quad (3.42)$$

where n is the linear part of the refractive index, and Δn is the change of refractive index due to fibre nonlinearity. Here, the fibre loss term is neglected since it is very small compared to other terms. Given the approximation $\Delta n \ll n$, (3.42) can be rearranged to solve Δn as:

$$\Delta n = n_2 \cdot (|A_1|^2 + 2 \cdot |A_2|^2), \quad (3.43)$$

where

$$n_2 = \frac{3}{8 \cdot n} \text{Re}(\chi_{xxxx}^{(3)}). \quad (3.44)$$

n_2 is called nonlinear-index coefficient [35].

According to (3.3), the phase of a propagating optical wave is described by the following equation:

$$\phi(z, t) = \omega_o t - \frac{2 \cdot \pi \cdot n_{eff}}{\lambda_o} \cdot z, \quad (3.45)$$

where ω_o is the central frequency of the optical wave, λ_o is the central wavelength of the optical wave, and n_{eff} is the effective index of refraction, which consists of linear and nonlinear parts, as was stated previously. The phase shift experienced by a particular point of the envelope profile is distance dependent, as given by:

$$\phi(z) = \frac{2 \cdot \pi \cdot n_{eff}}{\lambda_o} \cdot z. \quad (3.46)$$

The phase change of A_i due to fibre nonlinearity can be calculated by replacing n_{eff} in (3.46) with Δn in (3.43). The result is:

$$\phi_{NL} = \frac{2 \cdot \pi \cdot z \cdot n_2}{\lambda_o} \cdot (|A_1|^2 + 2 \cdot |A_2|^2). \quad (3.47)$$

$|A_i|^2$ is normalised to be the light intensity. Then (3.47) becomes:

$$\phi_{NL} = \frac{2 \cdot \pi \cdot z \cdot n_2}{\lambda_o \cdot A_{eff}} \cdot (I_1 + 2 \cdot I_2), \quad (3.48)$$

where A_{eff} is the effective cross-section area of the fibre cable, and I_1 and I_2 are the light intensities of the optical waves.

According to (3.48), the phase changes due to SPM and XPM for propagation distance L are:

$$\phi_{SPM} = \gamma \cdot P_1 \cdot L, \quad (3.49)$$

$$\phi_{XPM} = 2 \cdot \gamma \cdot P_2 \cdot L, \quad (3.50)$$

where P_1 and P_2 are the optical power of the co-propagating optical waves, and γ is the nonlinear coefficient given by:

$$\gamma = \frac{2 \cdot \pi \cdot n_2}{\lambda_o \cdot A_{eff}}. \quad (3.51)$$

Equation 3.50 plays a very important role in the mathematical model presented in Chapter 5.

The description of XPM so far is focused on the effect of two or more co-propagating optical waves linearly polarised on the same plane. It is shown in Ref. 35 that XPM is at its maximum when the two co-propagating waves are linearly co-polarised, and at its minimum when the two co-propagating waves are orthogonally polarised. The orthogonal case is about 1/3 as effective as the linearly co-polarised case.

3.4.2 The effect of XPM on polarisation-maintaining fibre

Single mode fibre cable supports two principal axes (x and y) of polarisation. The overall polarisation of the light is dependent on the relative strength of its electric fields polarised in x - and y -axes. In an isotropic medium (i.e. the effective refractive index experienced by an optical wave is the same regardless of the polarisation), the refractive indices of x - and y -axes will have the same value. Therefore, the overall polarisation of the light will be kept constant as the light propagates in such a medium. Fibre material is an anisotropic medium, which means that the two principal axes have different refractive indices, namely n_x and n_y . The difference of refractive indices leads to a velocity difference between the two orthogonally polarised modes. The velocity difference periodically changes the relative phase difference of the x - and y - polarisations. If an incident light propagates in both principal axes, its overall polarisation state will experience cycles of change the same as the relative phase difference does. The strength of this effect is quantified by a parameter called the degree of modal birefringence (B_F), which is given as [35]:

$$B_F = |n_x - n_y|. \quad (3.52)$$

A propagating light wave in fibre cable, initially 45° linearly-polarised against both x - and y -axes, will experience a cycle of polarisation evolution: linearly-polarised \rightarrow circularly-polarised \rightarrow elliptically-polarised \rightarrow linearly-polarised with 180° out of phase \rightarrow circularly-polarised \rightarrow elliptically-polarised \rightarrow linearly-polarised. The fibre length for a complete evolution cycle to occur is called beat length (L_B), which is related to B_F by [35]:

$$L_B = \frac{\lambda}{B_F}. \quad (3.53)$$

If the incident light is polarised with one of the principal axes in an anisotropic medium, its polarisation state will not change as it propagates. Typical optical communication systems employ direct detection in optical receivers. Therefore it is not necessary to maintain the polarisation state of the propagating signal. Nevertheless, in some all-optical devices, it is important to maintain polarisation state of the processed signal. Both types of all-optical demultiplexers analysed in this thesis require a constant polarisation state for optical signal circulating inside the devices for efficient operation. However, inevitable variations in fibre geometry and composition lead to coupling of energy from one polarisation to the other. One way to overcome this problem is to deliberately introduce a large amount of modal birefringence into the fibre in order to make the small and irregular perturbations negligible. This type of fibre is called polarisation-maintaining (PM) fibre. B_F in PM cable must satisfy the following equation for maintaining the polarisation state of the propagating signals [69].

$$B_F \geq \lambda / 1mm. \quad (3.54)$$

According to (3.52), a large of amount of modal birefringence is required to maintain a sufficient difference between n_x and n_y . The principal axes supporting faster and slower light propagation are called fast and slow axes, respectively. The refractive index of the

fast axis is smaller than that of the slow axis. If two co-propagating optical waves with high intensity are polarised in the same principal axis, the effective index of refraction is equal to the refractive index of that axis (x or y) plus the nonlinear refractive index induced by fibre nonlinearity. The difference between n_x and n_y decreases if the co-propagating optical waves are polarised in the fast axis. This will make B_F smaller and may eventually destroy the properties of PM fibre if B_F is too small to satisfy (3.54). Polarising the co-propagating optical waves in slow axis can avoid this problem. The other way to avoid this problem is to introduce sufficiently high degree of birefringence into the PM fibre for compensating the nonlinear refractive index induced by SPM and XPM [35].

3.5 Stimulated Raman Scattering

Stimulated Raman scattering is a nonlinear process that transfers photons from higher frequency components to lower frequency components. The energy of a photon is represented by:

$$E_p = hf, \quad (3.55)$$

where E_p is the photon energy, h is the plank's constant, and f is the optical frequency. The energy difference due to the transfer of a photon from high frequency component to low frequency component in SRS will change the vibrational state of the molecules of the fibre material for energy conservation. The origin of SRS is the imaginary part of the third order susceptibility of the fibre material. The optical waves at the lower frequency component that gains optical power in the process is called the Stokes wave. The optical wave that gives up optical energy is called the pump wave. The growth of a Stokes wave is given as [35]:

$$\frac{dI_s}{dz} = g_R \cdot I_p \cdot I_s, \quad (3.56)$$

where I_S is the Stokes intensity, I_P is the pump intensity, and g_R is the Raman-gain coefficient. g_R lies on a gain spectrum with a wide frequency range (up to 40 THz). This feature makes SRS a promising candidate as an optical amplifier (see Section 2.5). The g_R spectrum depends on the pump wavelength. Equation 3.56 requires a co-propagating Stokes wave for SRS to occur. In practice, SRS exists even if there is no co-propagating Stokes wave to begin with. A high intensity pump wave will generate a spectrum g_R of weak intensity. This process is called spontaneous Raman scattering. Then the newly generated weak Stokes wave can act as I_S in (3.56) to initiate the SRS.

Equation 3.56 represents the SRS in continuous pump and Stokes waves. For the case of co-propagating pump and Stokes pulses, it is necessary to take into account the chromatic dispersion, SPM and XPM. Two interactive propagating equations for the pump and Stokes waves need to be considered for evaluating the nonlinear effects mentioned above. Each of the two propagating equations are similar to (3.14) with inclusion of the SRS and XPM. The coupled propagation equations for the pump and Stokes waves are given as:

$$\left. \begin{aligned} i \frac{\partial A_p(z, \tau)}{\partial z} + \frac{i\alpha}{2} - \frac{\beta_{2p}}{2} \cdot \frac{\partial^2 A_p(z, \tau)}{\partial \tau^2} + \gamma \cdot \left(|A_p(z, \tau)|^2 + 2 \cdot |A_s(z, \tau)| \right) \cdot A_p(z, \tau) + \\ i \frac{\omega_p}{\omega_s} \cdot \frac{g_R}{A_{eff}} \cdot |A_s(z, \tau)|^2 \cdot A_p(z, \tau) = 0 \end{aligned} \right\} \quad (3.57)$$

$$\left. \begin{aligned} i \frac{\partial A_s(z, \tau)}{\partial z} + \frac{i\alpha}{2} - \frac{\beta_{2s}}{2} \cdot \frac{\partial^2 A_s(z, \tau)}{\partial \tau^2} + \gamma \cdot \left(|A_s(z, \tau)|^2 + 2 \cdot |A_p(z, \tau)| \right) \cdot A_s(z, \tau) - \\ i \frac{g_R}{A_{eff}} \cdot |A_i(z, \tau)|^2 \cdot A_s(z, \tau) = 0 \end{aligned} \right\} \quad (3.58)$$

where A_P and A_S are the pulse envelopes of the pump and Stokes waves, respectively, β_{2P} and β_{2S} are the first order dispersion coefficients of the pump and Stokes waves, and ω_P and ω_S are the frequencies of the pump and Stokes waves, respectively. The SRS terms in (3.57) and (3.58) are in opposite signs because the pump wave loses energy and the Stokes

wave gains energy. The effective cross section area of the fibre (A_{eff}) is included in the SRS terms to convert the optical power ($|A_i(z, \tau)|^2$) to the signal intensity in (3.56). In (3.57), the Raman gain coefficient is multiplied by the frequency ratio of ω_P/ω_S , reflecting the fact that the pump wave has larger photon energy than the Stokes wave. In general, (3.57) and (3.58) should be solved numerically to evaluate the SRS effect on the co-propagating pump and Stokes pulses. When most of the energy of the pump wave has been transferred to the Stokes wave, the Stokes wave may have sufficient intensity to transfer its own energy to a down-shifted frequency component through a second order SRS process.

3.6 Four Wave Mixing

Four wave mixing is a nonlinear process that generates new frequency components from existing frequency components [35]. It is so named because FWM involves four optical waves, including the existing and newly generated optical waves. For presenting the mathematical origin of FWM, the propagation of three optical waves in a fibre is considered first. It can be represented by:

$$E(t) = \frac{1}{2}A_1 \exp[i(\omega_1 t - k_1 z)] + \frac{1}{2}A_1^* \exp[-i(\omega_1 t - k_1 z)] + \frac{1}{2}A_2 \exp[i(\omega_2 t - k_2 z)] + \frac{1}{2}A_2^* \exp[-i(\omega_2 t - k_2 z)] + \frac{1}{2}A_3 \exp[i(\omega_3 t - k_3 z)] + \frac{1}{2}A_3^* \exp[-i(\omega_3 t - k_3 z)] \quad (3.59)$$

where A_i is the slow-varying amplitudes of electric fields of the optical waves, ω_i is the frequencies of the optical waves, and k_i is the propagation constant of the optical waves ($i = 1, 2, 3$). The nonlinear response of the polarisation can be evaluated by substituting (3.59) into the third order susceptibility term in (3.2). As the third order susceptibility term in (3.2) involves $E(t)^3$, the terms of the resultant polarisation consist of terms with different permutations of A_1, A_2, A_3 and their conjugates. The terms $|A_1|^2$, $|A_2|^2$ and $|A_3|^2$ representing SPM and XPM were described Section 3.4. The other terms of the resultant

polarisation are for FWM. Two of the FWM terms of the nonlinear polarisation are given as:

$$P_{FWM} = \frac{6 \cdot \epsilon_0 \cdot \chi_{xxxx}^{(3)}}{4} \left\{ \begin{aligned} &A_1 A_2 A_3 \exp[i((\omega_1 + \omega_2 + \omega_3)t - (k_1 + k_2 + k_3)z)] + \\ &A_1^2 A_2^* \exp[i((2\omega_1 - \omega_2)t - (2k_1 - k_2)z)] + \dots \end{aligned} \right\}. \quad (3.60)$$

There are many FWM terms similar to (3.60). Each term represents the annihilation of photons of existing frequency components and the creation of photons of newly generated FWM components. The annihilation and creation of photons at different frequencies can occur in a great variety of forms. An example is given below for the first FWM polarisation terms of (3.60). A new frequency component created from the first term of (3.60) is represented as:

$$E_{FWM} = E_4 \exp[i(\omega_4 t - k_4 z)], \quad (3.61)$$

where

$$E_4 = E_1 \cdot E_2 \cdot E_3, \quad (3.62)$$

$$\omega_4 = \omega_1 + \omega_2 + \omega_3, \quad (3.63)$$

$$k_4 = k_1 + k_2 + k_3, \quad (3.64)$$

A phase matching condition of (3.64) is required for the creation of the new FWM wave.

Equation 3.65 shows the three contributions to phase mismatch Δk in FWM.

$$\Delta k = \Delta k_W + \Delta k_M + \Delta k_{NL}, \quad (3.65)$$

where Δk_W is the phase mismatch due to waveguide dispersion, Δk_M is the phase mismatch due to material dispersion, and Δk_{NL} is the phase mismatch due to fibre nonlinearity. The phase matching condition is satisfied if Δk is equal to zero. The waveguide dispersions of different frequency components are nearly the same in single mode fibre. Δk_{NL} can be ignored if the intensities of all co-propagating optical waves are the same. Δk_M is very close to zero if all the optical waves are transmitted within the zero-dispersion wavelength region. Therefore, FWM will have most significant impact on the transmission systems

employing dispersion shifted fibre with a flat zero-dispersion wavelength region. The effect of FWM on such systems and the methods to alleviate the problem were described in Chapter 2.

3.7 Summary

Theories of nonlinear fibre optics have been introduced in this chapter. The topics discussed include nonlinear Schrödinger equation, beam propagation method, optical soliton, self phase modulation, cross phase modulation, stimulated Raman scattering and four wave mixing.

CHAPTER FOUR - SEMICONDUCTOR LASER AMPLIFIER

4.1 Introduction

A major function of the semiconductor laser amplifier is to amplify optical signals without the need of optical-electrical-optical conversion. There are two types of SLA: Fabry-Perot (FP) and travelling wave (TW). The only difference between them is the level of reflectivity on the two facets at the longitudinal ends of the SLA (details can be referred in Section 4.2). Anti-reflection coating is added to the facets in the TW-type SLA in order to allow the input optical power to pass straight through the SLA without encountering any internal feedback. FP-type SLA, like a semiconductor laser, does not have anti-reflection materials coated on the surface of its facets. One of the all-optical demultiplexers being analysed in this thesis (i.e. TOAD) employs TW-type SLA. This chapter will give a general description of the properties of TW-type SLA. For the sake of simplified abbreviation, the term SLA used for the rest of this thesis refers to TW-type SLA unless it is explicitly specified otherwise.

SLA was expected to play a very important role in the future optical communication systems as in-line amplification for boosting attenuated optical signals and pre-detection amplification for enhancing system sensitivity [70]-[72]. However, the uses of SLA as lumped amplifiers and preamplifiers have been less significant since the introduction of EDFA in 1989. This is because EDFA is widely regarded as a better technology compared with SLA in terms of noise figure, polarisation insensitivity and saturation output power for optical amplification at wavelength 1550nm [73]-[74]. Although EDFA has replaced SLA for linear amplification in long-haul optical systems, SLA still finds many other applications in optical communication systems. One of those is the exploitation of amplifier's nonlinearity in all-optical processing. This chapter covers both the linear and

nonlinear properties of SLA. The operation principles of SLA are described in Section 4.2. Section 4.3 describes the rate equations, which are a set of mathematical functions for evaluating the carrier and photon densities inside a SLA. The linear and nonlinear characteristics of light propagating through a SLA are described in Section 4.4. Section 4.4 will also describe the gain and phase dynamics of ultra-short pulse's amplification.

4.2 Operation Principles

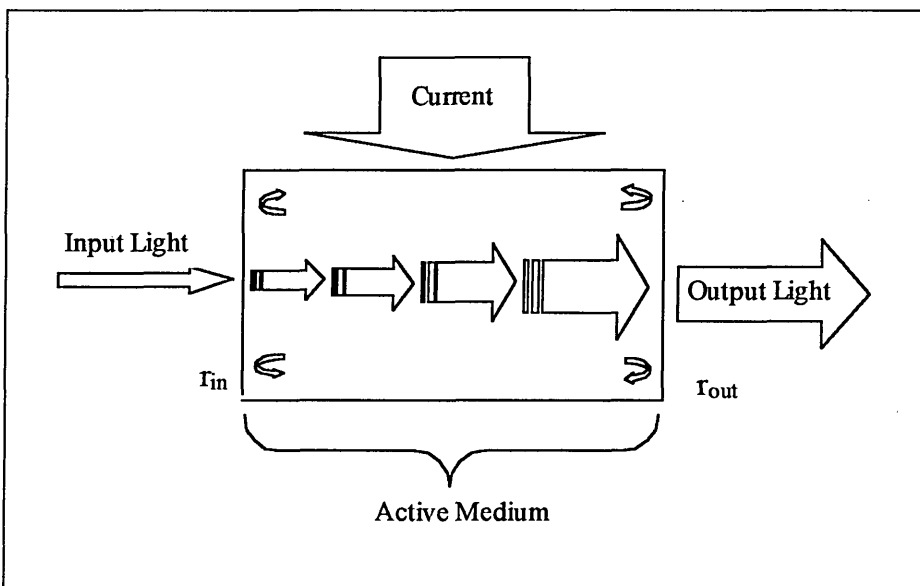


Fig. 4.1. Light amplification in a FP-/TW- type SLA.

Figure 4.1 shows the light amplification process inside a FP-/TW- type SLA. The input light enters into the active medium through the left facet of the amplifier. It then gets amplification by stimulated emission inside the active medium. This amplification mechanism will be explained later in this section. Finally, the amplified light emerges at the output through the right facet of the amplifier.

The three physical processes governing the creation and annihilation of photons inside the active medium are (i) spontaneous emission, (ii) stimulated absorption and (iii) stimulated emission. These processes are illustrated in Figs. 4.2a, 4.2b and 4.2c, respectively.

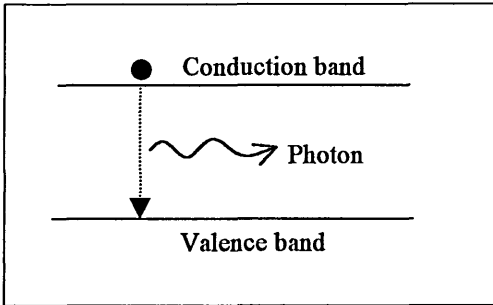


Fig. 4.2a. Spontaneous Emission.

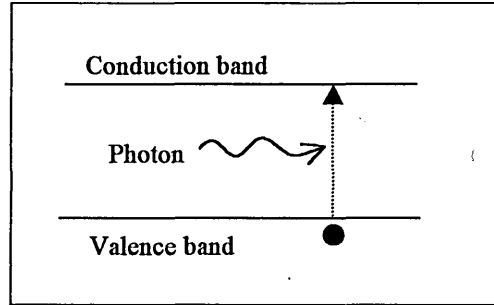


Fig. 4.2b. Stimulated Absorption

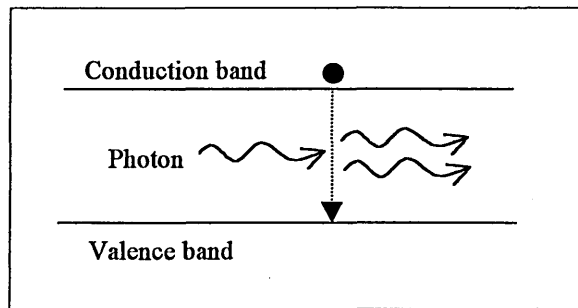


Fig. 4.2c. Stimulated Emission.

In spontaneous emission (Fig. 4.2a), an electron at a higher energy-state (conduction band) is dropped to a lower energy-state (valence band). The energy difference leads to the creation of a new photon or the generation of heat/vibration. The strength of spontaneous emission is quantified by a parameter called spontaneous life-time (T_{sp}), which is dependent on energy bands. Shorter T_{sp} means stronger spontaneous emission (i.e. more excited electrons drop to lower energy level by releasing photons). The newly created photons will radiate at random phase and direction. In stimulated absorption (Fig. 4.2b), an incident photon interacts with an electron at the valence band. The results are the annihilation of the incident photon and the lifting of the electron from the valence band to the conduction band. The energy difference between the valence and conduction band is equal to the energy of the annihilated photon for energy conservation. In stimulated emission (Fig. 4.2c), an incident photon interacts with an excited electron to release two identical photons with the same phase, frequency and propagation constant. The energy-

state of the excited electron will drop from its original position (conduction band) to the valence band in the process.

The input light to the amplifier participates in the stimulated emission process as shown by Fig. 4.2c. Each of the incident photons will interact with an excited electron to generate another identical photon. The result will be light amplification. The photons generated by spontaneous emission will not be part of the amplification process as they radiate in random phase and direction. A small number of them will propagate within the signal waveguide and eventually become amplifier noise. Stimulated absorption acts as a loss mechanism to the amplified light. High efficiency of light amplification requires the occurrence of stimulated emission to be maximised and the occurrence of stimulated absorption and spontaneous emission to be minimised. The three processes compete with each other inside the active medium. The probability of stimulated emission increases with the incident photons and the electron density at the conduction band. The probability of spontaneous emission increases with the electron density at the conduction band. The probability of occurrence for stimulated absorption increases with the incident photons and the electron density at the valence band. With no externally supplied current, electron density at the valence band is much higher than that at the conduction band at room temperature, according to the Fermi-Dirac function [75]. Therefore light amplification will not occur under this condition. In order to create a condition in which the electron density at the conduction band is higher than that at the valence band, the amplifier needs to be biased with a certain amount of electrical current. The bias current supplies a large number of excited electrons to the active medium to create the condition of population inversion of electrons for the stimulated emission to occur.

The labels r_{in} and r_{out} in Fig. 4.1 represent the reflectivity of the input and output facets respectively. As outlined in Section 4.1, facet reflectivity is the parameter that differentiates between FP and TW types of SLA. Antireflection coatings are added on the surface of the facets of TW-type amplifier to make r_{in} and r_{out} negligible, thus allowing the input light to pass straight through the active medium to the output facet. In practice, even with the best antireflection coatings, there is still some residual reflectivity on both facets. A SLA is regarded as near travelling wave (NTW) type as long as it satisfies the following equation [72]:

$$G_S \cdot \sqrt{r_{in} \cdot r_{out}} \leq 0.17, \quad (4.1)$$

where G_S is the single pass gain of the amplifier. In this thesis, a SLA is defined as TW type as long as it satisfies (4.1). In FP-type amplifier, the input light is reflected by the facets and oscillates within the active medium. The total signal gain increases with the number of oscillations until the carrier density is depleted to a point where the increase of photons due to stimulated emission is cancelled out by the mechanism of photon loss, thus inhibiting the signal from further growth [76]. The gain at the steady state represents the internal optical gain provided by the FP-SLA to the input signal.

TW-type SLA has many advantages over FP-type SLA in linear amplification, including wider bandwidth, low sensitivity to signal polarisation, larger saturated output power and tolerance to temperature and bias current fluctuation. The amplification characteristics of TW-type SLA will be discussed in detail in Section 4.4. FP-type SLA has a narrower bandwidth as the reflectivity on the two facets only allows the amplification of an envelope of discrete longitudinal modes. Each longitudinal mode has a narrow spectral width. This effect is similar to the oscillation of discrete longitudinal modes in semiconductor laser diode [76]. On the contrary, an ideal TW-type SLA with zero reflectivity on both facets will have a continual gain. On the other hand, the FP-type SLA has some advantages over

the TW type. Firstly it required a smaller bias current to support the high output gain. With the oscillation of multi-pass gain, the FP-type SLA requires lower carrier density to attain high internal gain. Secondly it introduces less amplifier noise due to its narrower bandwidth.

4.3 Rate Equations

The prerequisite data required for the analysis of light propagation in a SLA are the variation of carrier and photon densities in temporal and spatial domains. Once the dynamics of the carrier and photon densities across the SLA length during the time period of light propagation are known, it is possible to predict the responses of a SLA to the input light. Rate equations are two mathematical functions which govern the interaction between photon and carrier densities inside an active medium. The characteristics of SLA response to an incident light have been studied by many researchers using various mathematical models [77]-[85]. Most models are based on these rate equations.

There are a number of slightly different forms of rate equations reported in the literature. This section will first describe a number of these and highlight the subtle differences between them. The particular rate equations used in this thesis and the reasons for their selection will be given at the end of this section.

The factors that contribute to the changes of carrier density inside the SLA over time are best described by the following partial differential equation.

$$\frac{\partial N}{\partial t} = \frac{I_c}{q \cdot V_{SLA}} - R_{sp} - \frac{\Gamma \cdot g \cdot I_{sig}}{E_p}, \quad (4.2)$$

where N is the carrier density, I_c is the electrical current, q is the electron charge, V_{SLA} is the volume of the active medium, R_{sp} is the spontaneous emission, Γ is the confinement factor, I_{sig} is the signal intensity, g is the differential gain (i.e. gain per unit length) and E_p

is the photon energy. The bias current, represented by the first term of (4.2), supplies excited electrons to the active medium, and it is assumed to be independent of the spatial position within the active medium. Variations in carrier density over the cross-section due to current diffusion from the top to the bottom of the active region (see Fig.4.1) are ignored. This is justified because the thickness of the active region is generally smaller than the diffusion length [86]. R_{sp} represents the loss of excited electrons by spontaneous emission. The last term in (4.2) represents the loss of excited electrons by stimulated emission. The confinement factor Γ is the ratio between the cross-section area of the active region and the transverse area of the optical waveguide. Since the transverse area of the optical waveguide is generally larger than the cross-section area of the active region, not all optical power of the propagating pulse interacts with the active medium. The confinement factor included in the stimulated emission term reflects the fact that only the portion of optical waveguide overlapping with the cross-section area participates in the stimulated emission process. The signal intensity increases with the propagation length inside the SLA because of the amplification process. Therefore, the carrier density varies with the longitudinal position of the SLA. Equation 4.2 is the partial differential equation that describes this change of carrier density in terms of time and longitudinal distance.

The gain g in (4.2) depends on the signal wavelength and the carrier density [87]. The peak gain g_p of the gain spectrum at carrier density N is given as [87]:

$$g_p = a \cdot (N - N_o), \quad (4.3)$$

where a is the gain coefficient and N_o is the transparent carrier density. There will be neither gain nor loss if the carrier density is at the transparent level. The gain spectrum and its peak wavelength are different for different values of carrier density. If the input light has a wide bandwidth, a wavelength integration of stimulated emission could be used to

replace the third term in (4.2) for higher accuracy of the rate equation [78]. However, this approach requires much more computation time.

The rate of change of light intensity inside the SLA can be heuristically represented by:

$$\frac{dI_{sig}}{dz} = \Gamma \cdot g \cdot I_{sig} - \alpha_{SLA} \cdot I_{sig}, \quad (4.4)$$

where α_{SLA} is the photon loss coefficient. Equation 4.4 is a total differential equation that describes the change of light intensity over propagation distance while the optical signal is travelling inside the SLA. α_{SLA} in (4.4) is equivalent to the term of photon lifetime in [80] and the terms α_a and α_c in [78]. This loss term could be neglected to reduce calculation time if the carrier density is high. Equation 4.3 shows that the differential gain is directly proportional to N and it becomes the dominant term in (4.4) for large N . Equation 4.4 does not include the gain of light intensity from spontaneous emission. The R_{sp} term in (4.2) will generate photons radiating at random direction and phase. Only a very small portion of this random-phase light propagates along the signal waveguide contributing a negligible number of photons. However, the spontaneously emitted photons in the signal waveguide get amplified through stimulated emission. The resultant amplified spontaneous emission (ASE) is a major noise source of optical amplifier. Spontaneous emission increases with the bias current (see (4.2)). Adams, *et-al* [78] show that ASE has negligible impact on the rate equation if the current density is below 1500 A/cm^2 . In order to be consistent with the rate equation of carrier density (see (4.2)), the spontaneous emission term is not included in (4.4). However, for the analysis of concatenated effect of lumped SLAs, it is necessary to include the ASE term in the rate equation because the accumulated ASE of serially connected SLAs is significant. In this analysis, since only a single SLA is required in the application of TOAD (see Chapter 7), the spontaneous emission term is not included in (4.4).

Equations 4.2 and 4.4 are used to calculate the rate of change of carrier density and light intensity inside the SLA. There are some discrepancies in the literature regarding the confinement factor used in the stimulated emission terms of the rate equations. As in (4.2) and (4.4), references [72], [78], [88] include the confinement factor in the rate equations of both carrier density and light intensity. Some other models (e.g. [80], [82]) include the confinement factor only in the rate equation of light intensity, but not in the rate equation of carrier density, i.e.:

$$\frac{\partial N}{\partial t} = \frac{I_c}{q \cdot V_{SLA}} - R_{sp} - \frac{g \cdot I_{sig}}{E_p}, \quad (4.5)$$

$$\frac{dI_{sig}}{dz} = \Gamma \cdot g \cdot I_{sig} - \alpha_{SLA} \cdot I_{sig}. \quad (4.6)$$

The strength of I_{sig} is quantified by the amount of optical power per unit area transverse to the propagation direction. In the carrier density rate equation, there is no need to include the confinement factor into the stimulated emission term since I_{sig} itself already represents the strength of light within the cross-section area of the active region.

The newly generated photons inside the active region due to stimulated emission cannot be confined within the cross-section area of that region since the transverse area of the signal waveguide is larger than the cross-section area of the active region. The newly generated photons will eventually ‘disperse’ over the transverse dimensions of the signal waveguide. It is necessary to include the confinement factor in the stimulated emission term of (4.6) in order to take into account the effect of the resultant reduction of I_{sig} . Therefore, it is more accurate to use the rate equations (4.5) and (4.6) to describe the rate of change in carrier density and signal intensity inside the active region.

Some mathematical models (e.g. [77], [85]) adopt the unit of optical power P_{sig} instead of light intensity in the rate equations, which are given as:

$$\frac{\partial N}{\partial t} = \frac{I_c}{q \cdot V_{SLA}} - R_{sp} - \frac{\Gamma \cdot g \cdot P_{sig}}{A_{SLA} \cdot E_p}, \quad (4.7)$$

$$\frac{dP_{sig}}{dz} = \Gamma \cdot g \cdot P_{sig} - \alpha_{SLA} \cdot P_{sig}, \quad (4.8)$$

where P_{sig} is the total optical power in the transverse waveguide, A_{SLA} is the cross-section area of the SLA. Unlike (4.5) and (4.6), the confinement factor is included in both the rate equations in order to prevent the optical power outside the active region from interacting with the carrier density.

There are two mathematical definitions in the literature for the spontaneous emission term R_{sp} of rate equations. A simple definition is given in [78], [80], [82] as:

$$R_{sp} = \frac{N}{T_{sp}}, \quad (4.9)$$

A more complex definition is given in [77], [89] as:

$$R_{sp} = A \cdot N + B \cdot N^2 + C \cdot N^3, \quad (4.10)$$

where T_{sp} is the spontaneous emission time, A is the surface and defect recombination coefficient, B is the radiative recombination coefficient and C is the Auger recombination coefficient.

Most mathematical models use (4.9) to predict SLA performance because of its simplicity. T_{sp} can be obtained by comparing the experimental results with (4.9). Equation 4.10 contains the terms of radiative and nonradiative recombination. B is responsible for radiative recombination and the other two coefficients are responsible for nonradiative recombination. More accurate simulation results can be obtained by including only the radiative part of (4.10) for the rate equation of signal power and including the whole equation of (4.10) for the rate equation of carrier density [89]. This is because only the radiative part of the spontaneous emission contributes to the creation of new photons. The

SLA model adopted in this thesis will use the simpler definition (i.e. (4.9)) to evaluate R_{sp} for three reasons. Firstly, the aim of the SLA model is to calculate the gain and phase dynamics of the SLA for evaluating the TOAD switching window (see Chapter 7). The spontaneously generated photons have insignificant effect on the overall gain dynamics of the SLA. Secondly, using T_{sp} as a parameter to evaluate the gain recovery time is consistent with the common practice in the current literature. Thirdly, (4.9) requires less computation resources since it has fewer terms.

The rate equations used in this thesis are:

$$\frac{\partial N}{\partial t} = \frac{I_c}{q \cdot V_{SLA}} - \frac{N}{T_{sp}} - \frac{\Gamma \cdot g \cdot P^+}{A_{SLA} \cdot E_p}, \quad (4.11)$$

$$\frac{dP^+}{dz} = \Gamma \cdot g \cdot P^+. \quad (4.12)$$

where P^+ is the optical power propagating in the direction of the signal waveguide. The photon loss term is excluded from (4.12) because it is dominated by the stimulated emission. Equation 4.12 is subject to the following boundary condition.

$$P^+ = P_{sig}, \quad \text{at } z=0. \quad (4.13)$$

4.4 Light Propagation Inside an SLA

4.4.1 Gain spectrum

The gain spectrum of a SLA is dependent on carrier density and temperature [87]. This subsection describes the characteristics of the gain spectrum for different carrier densities at constant temperature.

The spectral curve of differential gain depends upon the semiconductor material and can be obtained by experimental measurement [87]. The spectral curve of differential gain used here follows the empirical formula defined in [83] and is given as:

$$g(\lambda) = g_p - a \cdot N \cdot \left(\frac{\lambda - \lambda_p}{\Delta\lambda_g} \right)^2, \quad (4.14)$$

where g_p , a and N has been defined in (4.3), λ_p is the peak wavelength and $\Delta\lambda_g$ is the spectral width of the differential gain. The peak of the differential gain spectrum is at λ_p . The spectral curve of differential gain in (4.14) does not represent the internal gain spectrum of the SLA. The internal gain is defined as the ratio between the amplified output power and the input power to the SLA, and is given as:

$$G = \exp(\Gamma \cdot g \cdot L_{SLA}), \quad (4.15)$$

where G is the internal gain and L_{SLA} is the length of the SLA.

Equation 4.15 is obtained by integrating (4.12) with respect to SLA length. It is assumed in (4.15) that the input power is not large enough to cause spatial variation of carrier density along the longitudinal dimension of the SLA.

The peak wavelength λ_p shifts to a lower value as the carrier density increases [87]. This can be modeled by the following equation [83]:

$$\lambda_p = \lambda_o + \left(1 - \frac{N}{N_{th}} \right) \cdot b, \quad (4.16)$$

where λ_o and b are constants and N_{th} is the carrier density of lasing threshold. The threshold carrier density depends on the reflectivity of the facets. The lasing threshold in TW-type SLA is larger than in FP-type as there is no oscillation of optical signal inside the amplifier. Fig. 4.3 plots the internal gain spectrum of various carrier densities using (4.14), (4.15) and (4.16). The simulation parameters are $a = 5.5 \times 10^{-20} \text{ m}^2$, $N_o = 1 \times 10^{24} \text{ m}^{-3}$, $N_{th} = 2.66 \times 10^{24} \text{ m}^{-3}$, $\lambda_o = 1.45 \text{ }\mu\text{m}$, $b = 106.4 \text{ nm}$, $\Delta\lambda_g = 75 \text{ nm}$, $\Gamma = 0.3$ and $L_{SLA} = 300 \text{ }\mu\text{m}$. It is shown that the the internal gain curve shifts to a lower wavelength as the carrier density increases. The peak gain increases with the carrier density, as has been indicated in (4.3).

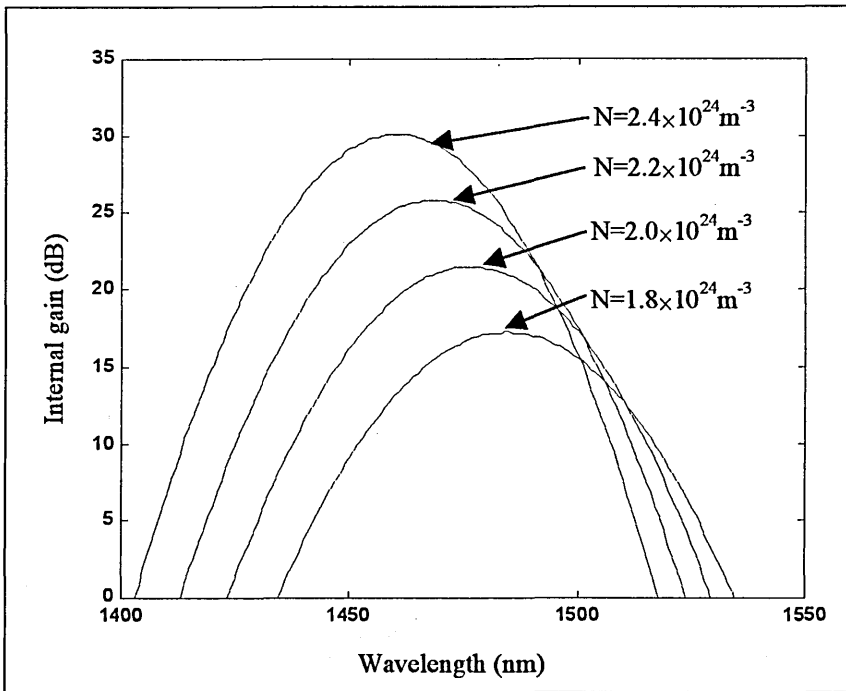


Fig. 4.3. Internal gain spectrum for different carrier densities.

4.4.2 Unsaturated and saturated gain

The carrier density is directly proportional to the bias current when there is no input optical power, as shown in (4.11). If P^+ in (4.11) are set to zero and the bias current is constant, then (4.11) is reduced to:

$$N = \frac{I_c \cdot T_{sp}}{q \cdot V_{SLA}} \quad (4.17)$$

The carrier density is in equilibrium state when biased by a constant current. The time derivative of N is equal to zero under this condition. Equation 4.17 shows that the carrier density increases with the bias current. However, when input optical power enters into the SLA for amplification, the stimulated emission (the last term in (4.11)) will deplete the carrier density. This leads to a decrease of differential gain (see (4.3)). Therefore increasing the input power will saturate the internal gain. The saturation effect limits the dynamic range of the amplification. The saturated gain corresponds to the 3 dB reduction of internal gain from its unsaturated peak value. The saturated input power is defined as the input power at the saturated gain. In a SLA, it is desirable to have high-unsaturated gain

and high saturated input power for achieving large amplification and wide dynamic range. Nevertheless, there is always a compromise between gain and saturated input power in any SLA. The mathematical model developed by Adams, *et-al* [78] shows the tradeoff between unsaturated gain and saturated input power, which is given as:

$$P_{in} = \frac{E_p \cdot V_{SLA}}{(G-1)} \cdot \left[\frac{I_c}{q \cdot V_{SLA}} - \frac{N_o}{T_{sp}} - \frac{\ln(G)}{a \cdot \Gamma \cdot L_{SLA} \cdot T_{sp}} \right], \quad (4.18)$$

where P_{in} is the input optical power. The other variables have been defined in previous equations. Fig. 4.4 shows the internal gain with respect to P_{in} for different values of bias current. As can be seen, the plots display a threshold effect above which the internal gain drops rapidly. It also shows that the saturated input power decreases as the unsaturated gain increases. The simulation parameters are $E_p = 1.36 \times 10^{-19}$ J, $V_{SLA} = 9 \times 10^{-17}$ m³, $N_o = 1 \times 10^{24}$ m⁻³, $T_{sp} = 4$ ns, $a = 5 \times 10^{-20}$ m², $\Gamma = 0.5$, $L_{SLA} = 300$ μ m.

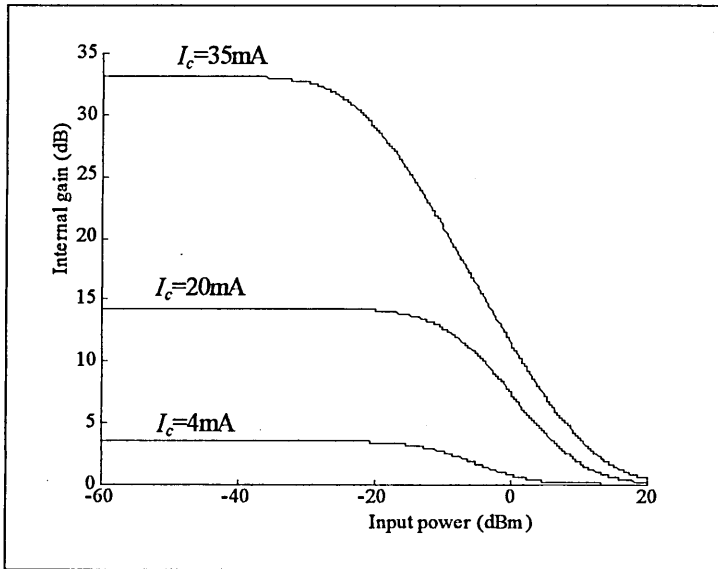


Fig. 4.4. Internal gain Vs. input power for various I_c .

4.4.3 SPM and XPM in SLA

The refractive index in the active region of a semiconductor laser is a function of carrier density [90]. Since the carrier density inside the active region decreases with the increase of input light intensity, the phase change of an optical signal propagating inside a SLA is

nonlinear. SPM and XPM in a SLA refer to the phase modulations of an optical signal by the optical signal itself and its co-propagating signal(s), respectively. SPM and XPM effects in SLA are different from those in fibre cable. Firstly, the strengths of SPM and XPM in a SLA are much stronger than their counterparts in fibre cable. The SLA length as short as hundreds of micrometer can produce a significant amount of phase shift to the input signals. Secondly, unlike phase nonlinearity in fibre cable, SPM and XPM in SLA are usually accompanied with gain modulation due to the fact that the change of carrier density modulates both the phase and gain of an input signal. One of the all-optical time division demultiplexers being analysed in this thesis (TOAD) exploits the XPM effect in SLA. Part of the mathematical model for TOAD demultiplexing presented in Chapter 7 is based on the theories introduced in this subsection.

Refractive index inside the active region of a SLA generally decreases with the increase of carrier density. An important parameter that quantifies the strength of SPM and XPM in SLA is the derivative of refractive index with respect to carrier density. According to the experimental measurements carried out by J.Manning, *et-al* [90] for seventeen semiconductor lasers from various vendors, the derivative of refractive index with respect to carrier density is $-(1.2 \pm 0.2) \times 10^{-26} \text{ m}^3$ for AlGaAs lasers and $-(2.8 \pm 0.6) \times 10^{-26} \text{ m}^3$ for 1.3 μm InGaAsP lasers. It was found that there is a linear relationship between carrier density and refractive index at bias current near the lasing threshold [90]. A number of mathematical models for investigating the nonlinear characteristics of refractive index in SLA were reported in the literature [77]-[79], [83], [86], [91]. The most commonly used value for the derivative of refractive index with respect to carrier density in these models is $-(2.8 \pm 0.6) \times 10^{-26} \text{ m}^3$. The nonlinear refractive index can be calculated from the following equation [83

$$n = n_o - 2.8 \times 10^{-26} \cdot N, \quad (4.19)$$

where n is the refractive index taking into account the change of carrier density, n_o is the carrier-independent contribution to the refractive index and N is the carrier density in the unit of m^{-3} . Equation 4.19 assumes that the mathematical relation between the refractive index and the carrier density is linear and constant for all values of N .

Another commonly used parameter for quantifying the SPM and XPM effects in SLA is the linewidth enhancement factor. References [79], [86], [91] use the following expression to calculate the phase modulation of an amplified signal in a SLA.

$$\frac{\partial \phi}{\partial z} = -\frac{1}{2} \alpha_{LEF} \cdot g, \quad (4.20)$$

where ϕ is the phase of the signal pulse at a temporal point of the pulse profile, α_{LEF} is the linewidth enhancement factor and g is the differential gain. z in (4.20) is related to the reference frame of the pulse profile τ by $\tau = t - z/V_g$ where V_g is the light velocity inside the active region. Equation 4.20 can be used to calculate the phase change of an optical pulse due to nonlinearity of the refractive index. It is a partial differentiation equation for calculating the optical phase at a fixed temporal point, τ , against the longitudinal dimension of the SLA. Combining (4.19) and (4.20) will obtain the mathematical relation between α_{LEF} and the carrier density derivative of the refractive index as follows [79]:

$$\alpha_{LEF} = -\frac{dn}{dN} \cdot \frac{4\pi}{\lambda_o \cdot a}, \quad (4.21)$$

where λ_o is the central wavelength of the input signal and a is the gain coefficient in (4.3).

A high intensity input signal decreases the carrier density inside the active region by stimulated emission. The decrease in carrier density leads to a decrease in optical gain and an increase of refractive index. Therefore, SPM in SLA always co-exists with self gain saturation (SGS). The situation would be more complicated for the case of two input

signals. In that case, each signal will experience SPM, XPM, SGS and cross gain saturation (XGS). The total change of refractive index caused by SPM and XPM is the same for the two signals. Nevertheless, the two signals may have different levels of gain depletion, which is caused by SGS and XGS. The reason for the gain difference is the wavelength dependence of the differential gain (see Fig. 4.3). The magnitude of the gain difference is dependent on the wavelength gap between the two signals.

4.4.4 Fast gain recovery in subpicosecond pulse

Figure 4.5 shows a typical response of carrier density dynamics to an input pulse over a long time frame that covers (i) the time before the pulse arrives, (ii) the time duration in which the pulse passes through the SLA, (iii) the period after the pulse passes through the SLA. The SLA gain is constant before the pulse arrives. Under the equilibrium conditions in which no external optical power is coupled into the active region and the bias current is constant, the carrier density in the active region of a SLA is a constant value. In this state, the bias current and the spontaneous time determine the carrier density, as indicated by (4.17). The carrier density begins to deplete when a high intensity optical signal passes through the SLA. The light intensity of the input pulse fuels the stimulated emission process (see (4.12)), which results in a decrease of carrier density across the duration of the central peak of the input pulse, as shown in the region (ii) of Fig. 4.5. The carrier density is at its minimum near the end of the falling edge of the pulse profile. After the pulse has completely passed through the SLA, the depleted gain recovers slowly and steadily back to the level of the equilibrium state, as shown in Fig. 4.5.

The rate of recovery of carrier density decreases as N increases, as can be seen in the change of gradient of the N curve in the region (iii) of Fig. 4.5. The constant pump rate of excited electrons from the bias current is much higher than the spontaneous emission rate

when N is small. As a result, the rate of increase of carrier density (the gradient of the N curve) is large at the beginning of the region (iii) (see Fig. 4.5). The gap between the pump rate and the spontaneous emission rate becomes narrower as N increases in the recovery process. It leads to a decrease of recovery rate of carrier density. This is reflected in Fig. 4.5 by the relatively flat curve at the end of the region (iii).

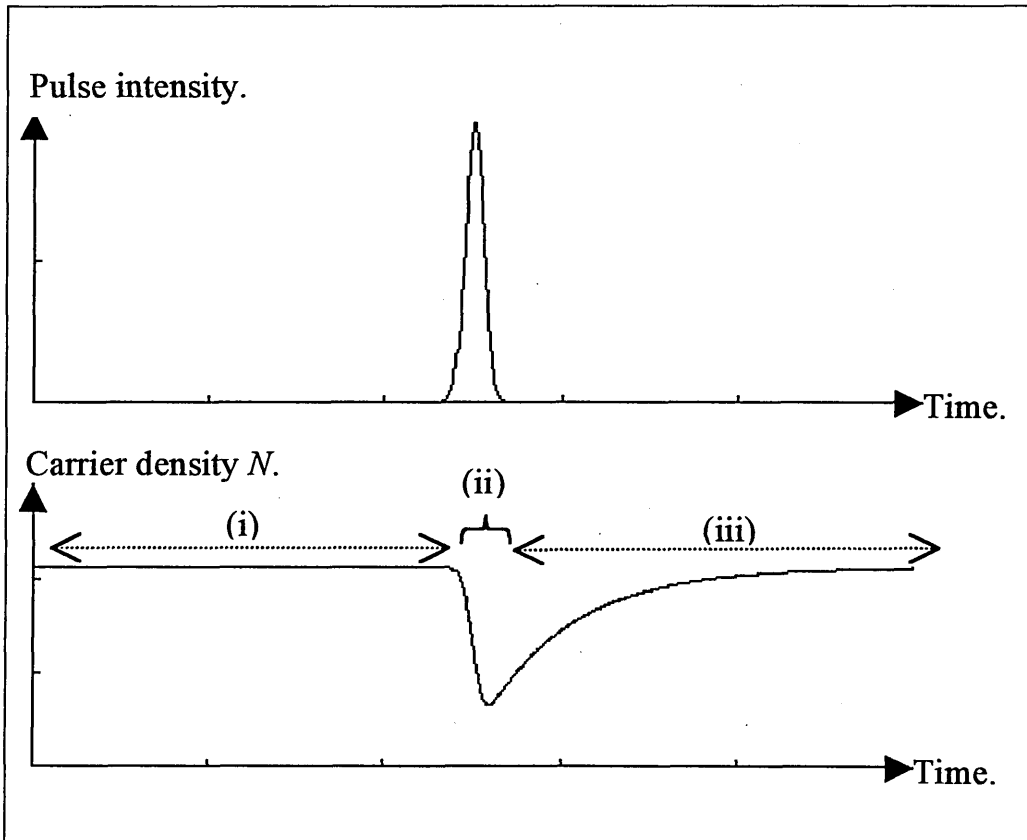


Fig. 4.5. Response of carrier density in the active region to the input pulse intensity.

The time required for a full recovery of carrier density is proportional to the spontaneous lifetime T_{sp} . A smaller T_{sp} means lower initial carrier density at the equilibrium state (see (4.17)), thus shorter recovery time is required to reach the initial state.

The response of carrier density to input pulse shown in Fig.4.5 is caused by the interaction between carrier density and photon density inside the active region of the SLA, which can be well explained by the rate equations. However, if the high intensity input pulse is

shorter than 1 ps, the SLA will have gain dynamics completely different from the one shown in Fig. 4.5. Since the mid 1980's, many researchers have been experimentally and theoretically studying the characteristics of gain and phase dynamics of sub-picosecond pulse propagating through SLA [92]-[102]. This subsection will give a brief review about the experimental and theoretical studies of subpicosecond dynamics of SLA.

Figure 4.6 shows the normalised gain responses of an AlGaAs/GaAs SLA for input pulse widths of 500 fs (Fig. 4.6a) and 2 ps (Fig. 4.6b) [95]. The results were obtained from the pump-probe experiments reported in [95]. The x-axes in Fig. 4.6 represent the time delay of the low intensity probe pulse with respect to the high intensity pump. Fig. 4.6a displays an instant depletion of the probe gain near the zero time delay and a partial recovery of the gain from time delay 0 ps to 1.5 ps. The fast partial recovery is followed by a slow recovery of gain, which corresponds to the gain recovery in Fig. 4.5. It should be noted that the time scales of Fig. 4.6 are so small that the slow gain recovery looks like a flat line. The probe gain will eventually recover to its initial value, as in the case of Fig.4.5. The probe gain in Fig. 4.6b initially depletes to the level of the partial recovered gain in Fig. 4.6a. Then the depleted gain begins the slow recovery process. Figs. 4.6a and 4.6b show that there is a deep gain depletion and a fast recovery component in the SLA gain dynamics for subpicosecond input pulse. Results of the pump-probe experiments carried out in GaAlAs and InGaAsP SLAs show similar characteristics [92], [94].

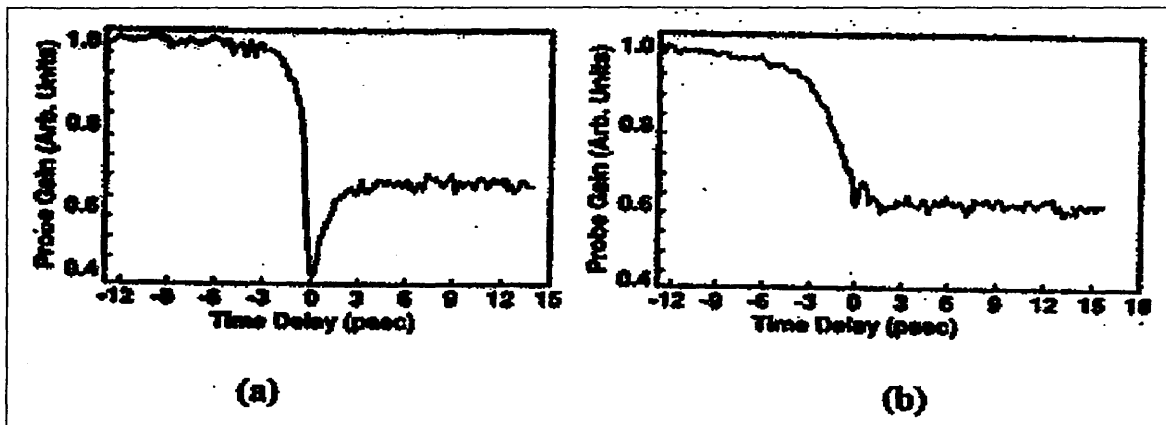


Fig. 4.6. (a) gain dynamics for 500 fs pump pulse; and (b) gain dynamics for 2 ps pump pulse from [95].

A number of possible physical effects may lead to the deep depletion and fast partial recovery shown in Fig.4.6a. The majority of researchers believe that the gain dynamics of femtosecond input pulses are largely caused by carrier heating in the active region of the SLA [92]-[100]. If a high intensity input pulse with a wavelength equivalent to the bandgap energy of the atomic system enters the SLA, the electrons near the bandgap will drop to combine with the hole in valence band by stimulated emission. The conduction band generally has a large number of intraband energy levels. The electrons are ‘hotter’ in higher intraband levels. The removal of the ‘cooler’ electrons near the bandgap by stimulated emission increases the temperature of the carriers. Another factor that causes carrier heating is the free carrier absorption, which is a kind of photon loss mechanism inside the active region [103]. The process of photon annihilation heat up the carriers. Since the gain coefficient is temperature dependent, the change of temperature affects the gain curve of the atomic system [87]. This leads to the deeper depletion of probe gain in Fig. 4.6a (comparing to Fig. 4.6b). The temperature of the ‘heated’ carriers will drop back to the equilibrium value in a short relaxation time via phonon emission. The quick return to the equilibrium temperature leads to the fast partial recovery of gain in Fig. 4.6a. The carrier dynamics caused by carrier heating are only visible in subpicosecond input pulse as the relaxation time of carrier heating is less than 1 ps. The rising rate of carrier temperature

increases with the rising edge of the pulse. In the case of longer pulse, the rising rate of carrier temperature is so slow that the short relaxation time of carrier heating has 'cooled' the carrier well before the carrier heating becomes significant. Moreover, given the same pulse energy, the shorter pulse will have higher peak power. Therefore the carrier heating effect will be more pronounced in femtosecond pulses.

Some researchers believe that, besides carrier heating, spectral hole burning (SHB) and two photon absorption (TPA) may also play a role in the gain dynamics of femtosecond pulses propagating in SLA [94], [96]-[99]. J.Mark, *et-at* [97] interpreted their pump-probe experimental results by the physical effects of carrier heating, SHB and TPA. Figure 4.7 shows the normalised probe transmission versus pump-probe delay time obtained from experimental measurements [97]. The probe transmission response in Fig. 4.7 represents the pump wavelengths of 1533 nm (the lowest curve), 1528 nm, 1523 nm, 1518 nm, 1513 nm, 1508 nm, 1503 nm, 1498 nm, 1493 nm, 1488 nm (the highest curve). The range of wavelengths used in the experiments covered the gain, transparent and absorption regions of the gain spectrum. At wavelengths above (below) the transparent point, the pump pulse experiences gain (absorption), and therefore decreases (increases) the carrier density inside the active region. The curves in Fig. 4.7 show a rapid variation of probe transmission before they settle to the transmission levels that reflect the carrier densities of their corresponding wavelengths after the pump pulses passed the SLA. The settled probe transmission will slowly return to the initial equilibrium level in the time scale of spontaneous lifetime. J.Mark, *et-al*, attributed the rapid variation of probe transmission at various pump wavelengths to carrier heating, SHB and TPA [97]. The relatively slow (700-800 fs) increase of transmission seen in all traces were attributed to carrier heating effects. The transient increase of gain in the absorption region and the rapidly recovering gain saturation in the gain region were attributed to SHB. The small negative component

opposing the effect of SHB in the absorption region close to the transparent wavelength was attributed to TPA.

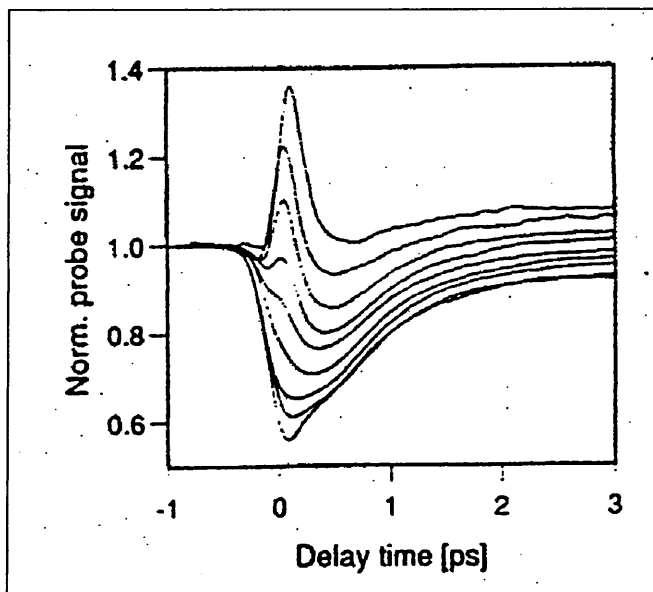


Fig. 4.7. Normalised probe traces for femtosecond pump pulses at various wavelengths.

The fast variation of gain induces phase change of the probe pulse. Phase measurements by pump-probe experiments using femtosecond pump pulse revealed that there is an additional ultrafast phase dynamics on top of the gain-induced phase change [96], [98]. There is still no scientific explanation for that ultrafast component so far.

Since the physical effects behind the gain dynamics of femtosecond pulses in SLA have not been fully understood, most mathematical models for femtosecond pulse dynamics are based on some phenomenological parameters to simulate the experimental results [93]-[94], [96]-[97], [100], [102]. For example, in [96], two relaxation time constants are defined to simulate the fast gain recovery caused by carrier heating. The values of the parameters in these phenomenological models were determined by fitting the experimental results with the assumed mathematical equations.

4.5 Summary

A comprehensive review of TW-type semiconductor laser amplifier has been presented in this chapter. Section 4.2 described the operation principles of such devices. The rate equations for mathematical modelling of SLA were discussed and some inconsistencies found in the literature regarding the confinement factor in the rate equations were clarified. Finally, the characteristics of SLA amplification were described and explained in Section 4.4.

CHAPTER FIVE - MATHEMATICAL MODEL FOR NONLINEAR OPTICAL LOOP MIRROR DEMULTIPLEXER

5.1 Introduction

A mathematical model for optimising and simulating the demultiplexing operations of NOLM demultiplexer is described in this chapter. The proposed model will be employed for the noise and crosstalk analysis of NOLM demultiplexer in chapter 6. This chapter is organised as follows. Section 5.2 describes the operation principles of NOLM demultiplexer. The mathematical model is presented and verified in Sections 5.3 and 5.4, respectively.

5.2 Operation Principles

N. J. Doran and D. Wood [104] first proposed using NOLM as an optical switching device in 1988. Optical switching in the proposed device was solely dependent on the light intensity of the input signal [104]-[106]. Therefore it was not suitable for all-optical time division demultiplexing. An improved design of NOLM switching was introduced by K. J. Blow, *et-al* in 1990, which allowed the NOLM to be operated in a dual-wavelength mode for extracting an OTDM channel from an aggregated high-capacity OTDM data stream [107]. The demultiplexing mechanism will be illustrated later in this section. Since 1990 many researchers have been studying NOLM based demultiplexers theoretically and experimentally [108]-[122]. The NOLM demultiplexer to be analysed in this thesis is based on the two-wavelength mode, which was first proposed in [107].

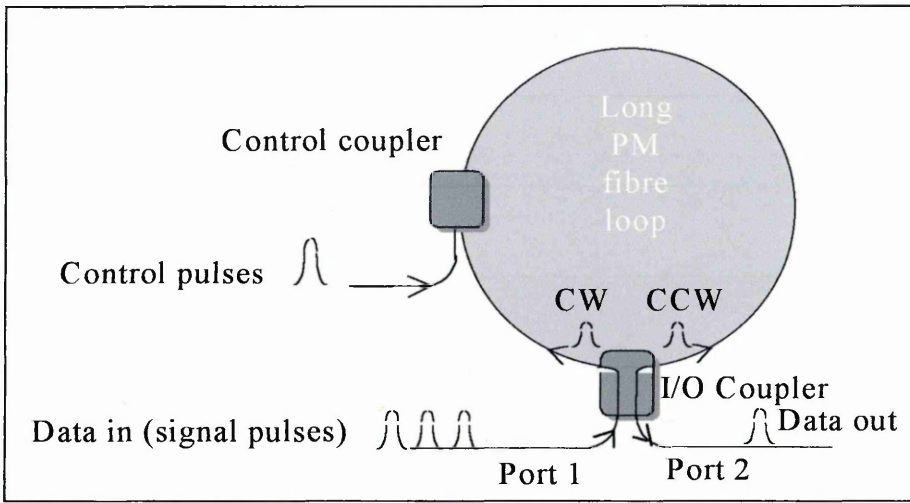


Fig. 5.1. Block diagram of NOLM demultiplexer.

Figure 5.1 shows a typical block diagram of NOLM demultiplexer. A fibre loop mirror is constructed by connecting two ends of a long fibre to an I/O coupler. As can be seen in Fig. 5.1, a high capacity optical OTDM signal is divided by the I/O coupler into two signal streams of equal intensity. The two divided signals propagate in clockwise (CW) and counter-clockwise (CCW) directions, respectively. The I/O coupler is a directional coupler with 50% coupling coefficient. The incoming pulses are coupled across the I/O coupler according to the coupler transfer matrix [123]. The equation relating the electric fields of the input and output ports of the I/O coupler is given as [123]:

$$\begin{bmatrix} E_{CW} \\ E_{CCW} \end{bmatrix} = \sqrt{1-\alpha_c} \begin{bmatrix} 1 & i \\ \frac{1}{\sqrt{2}} & \frac{i}{\sqrt{2}} \\ i & 1 \\ \frac{i}{\sqrt{2}} & \frac{1}{\sqrt{2}} \end{bmatrix} \begin{bmatrix} E_{in} \\ 0 \end{bmatrix}, \quad (5.1)$$

where E_m is the input electric field, E_{CW} is the coupled CW electric field, E_{CCW} is the coupled CCW electric field, and α_c is the coupling loss. The bottom element of the vector for input electric fields is zero because the optical power only enters one of the input ports. The same magnitude for all elements in the transfer matrix means that E_m is split into E_{CW} and E_{CCW} with equal amplitude. E_m is generally a complex number and therefore can be expressed as $x + iy$, where x and y are its real and imaginary parts, respectively. The

complex phase of E_{CW} and E_{CCW} in (5.1) can be represented graphically as shown in Fig.

5.2. It is note that E_{CCW} has a $\pi/2$ phase lag with respect to E_{CW} .

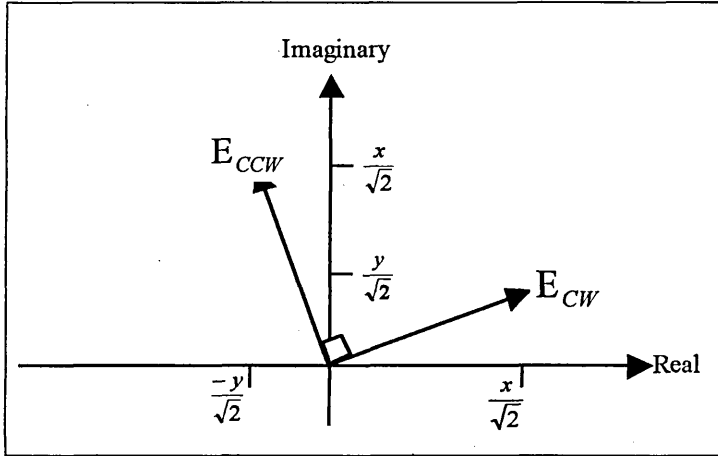


Fig. 5.2. Phase diagram of E_{CW} and E_{CCW} .

E_{CW} and E_{CCW} propagate along the polarisation-maintaining fibre loop in counter-clockwise directions. After the whole propagation of the fibre loop, the two split pulses reach the I/O coupler at the same time. An equation similar to (5.1) for the coupling of E_{CW} and E_{CCW} is given as:

$$\begin{bmatrix} E_{back} \\ E_{forward} \end{bmatrix} = \sqrt{1-\alpha_C} \begin{bmatrix} \frac{1}{\sqrt{2}} & \frac{i}{\sqrt{2}} \\ \frac{i}{\sqrt{2}} & \frac{1}{\sqrt{2}} \end{bmatrix} \begin{bmatrix} E_{CCW} \\ E_{CW} \end{bmatrix}, \quad (5.2)$$

where E_{back} is the optical field coupling back to port 1, and $E_{forward}$ is the optical field at port 2. Equation 5.2 can be further broken down into two equations:

$$E_{forward} = \sqrt{1-\alpha_C} \cdot \left(\frac{iE_{CCW}}{\sqrt{2}} + \frac{E_{CW}}{\sqrt{2}} \right), \quad (5.2a)$$

$$E_{back} = \sqrt{1-\alpha_C} \cdot \left(\frac{E_{CCW}}{\sqrt{2}} + \frac{iE_{CW}}{\sqrt{2}} \right). \quad (5.2b)$$

The phase of E_{CCW} still lags E_{CW} by $\pi/2$ after a circulation of the fibre loop. A further $\pi/2$ phase delay introduced in (5.2a) makes E_{CCW} completely out of phase with respect to

E_{CW} , E_{CW} and E_{CCW} in (5.2a) cancel out each other, thus making $E_{forward}$ equal to zero.

On the contrary, the in-phase sum of E_{CW} and E_{CCW} in (5.2b) results in complete energy transfer to E_{back} . As a result, the entire signal is reflected back to the input port of the demultiplexer.

The above scenario assumes that there is no control pulse pumped into the fibre loop. In a NOLM demultiplexer, a train of control pulses synchronised with the CW pulses of the target OTDM channel are coupled into the fibre loop through the control coupler (see Fig. 5.1). The control pulses, propagating in the CW direction, will co-propagate with the CW pulses of the target channel. XPM effect induced by the co-propagating control pulses changes the phase of the CW pulses (but not the CCW pulses). Therefore, after propagating a whole fibre loop, a phase difference is created between CW and CCW pulses of the target channel. A close examination of (5.1), (5.2a) and (5.2b) reveals that pulse energy of target channel would be completely transferred to $E_{forward}$ (see (5.2a)) if the phase difference created by XPM is equal to π . The demultiplexing operation of NOLM demultiplexer can be carried out by aligning the high intensity control pulses with the CW pulses of the target channel. Due to the weak nonlinearity of the fibre material, a long loop of fibre cable (several kilometres) is required to achieve a reasonable phase change. Since the wavelength of the control pulses is different from that of the signal pulses, an optical filter can be used at the output port (port 2) to block the control pulse energy.

5.3 Mathematical Model

The objectives of the mathematical model presented in this section are:

- 1) Optimising system parameters for maximising peak transmittance of the NOLM switching window;
- 2) Calculating the width of the NOLM switching window;
- 3) Evaluating the shape of the NOLM window.

Each of these will be described in detail in separate subsections. Assumptions made in the mathematical model are outlined in Section 5.3.1.

5.3.1 Assumptions of the model

Assumptions made for the mathematical model include:

1. The I/O and control couplers in Fig. 5.1 are assumed to respond ideally and consistently to the input OTDM signal and the control pulse stream. The ideal responses of the I/O coupler are to have 50% coupling ratio and induce a $\pi/2$ phase lag in the cross-waveguide with respect to the straight-waveguide, as has been described in the previous section. The response of the control coupler should ideally have a coupling ratio 100% for the control pulse and 0% for the signal pulse. The coupling ratio of a fused tapered coupler generally depends on the wavelength of the input light [124]-[128]. Therefore, the I/O and control couplers used in the NOLM configuration should be tailored for the wavelengths of the control and signal pulses. If the wavelengths of the control and signal pulses are changed for performance optimisation (see Chapter 6), a different set of I/O and control couplers should be used for keeping the ideal responses of the couplers. Alternatively, wavelength-flattened fused coupler [129] could be used in the NOLM demultiplexer. A tiny deviation from the coupling ratio of 50:50 in the I/O coupler would result in a small amount of crosstalk at the

output port of the NOLM demultiplexer [65]. This kind of crosstalk is ignored in the NOLM model by the assumption of ideal coupler.

2. The type of fibre used in the loop mirror: The demultiplexing operation in NOLM demultiplexer is attributed to the XPM effect, which is caused by the high intensity of the control pulse. As discussed in Chapter 3, the XPM strength depends on the relative state of polarisation between the two co-propagating pulse streams. Maximum XPM can be achieved only if the pulse streams have the same state of polarisation. Polarisation maintaining (PM) fibre is assumed for the fibre loop (see Fig. 5.1) for maximising the XPM effect. The input OTDM signal and the control pulse stream should have their state of polarisation aligned in one of the principle axis of the PM fibre by polarisation controllers (PC). If the control and signal pulses are not polarized on the same plane, additional optical power of control pulse would be required in order to achieve adequate XPM for the demultiplexing operation.
3. Shape of control pulse: As illustrated in Chapter 3, an optical pulse will change its shape during propagation. The shape evolution of a propagating pulse depends on many factors, such as pulse intensity, pulse width, pulse shape, first order dispersion coefficient β_2 , fibre nonlinearity, etc. In order to simulate the operations of NOLM demultiplexing, the effect of XPM on the CW signal pulses must be correctly calculated. In general, numerical methods are required to evaluate the change of pulse profile during propagation. For simplifying the numerical analysis of NOLM demultiplexing, the temporal intensity profile of the propagating control pulse is assumed to have a constant shape. As discussed in Section 3.3, the pulse shape of a propagating soliton is unchanged due to a delicate balance between dispersion and fibre nonlinearity. In the NOLM model, the control pulse is assumed to be fundamental

soliton. In practice, it is not possible for the intensity profile of the control pulse to remain unchanged even though soliton is employed. It is because the loss mechanism in fibre reduces the optical power of the propagating pulse. The decrease of optical power of the control pulse during propagation will be catered for in the mathematical model, provided that the control pulse profile remains in soliton shape. However, if the loss of optical power is so much that (3.23) is no longer satisfied, the simulation results of the mathematical model will be invalid since the soliton shape of control pulse cannot sustain in that case.

Employing soliton control pulse has other advantages apart from simplifying numerical calculation. These advantages are discussed below by highlighting the disadvantages of employing non-soliton control pulses. If a dispersing control pulse is used, the pulse intensity will be getting lower and the pulse profile will be getting wider as the propagation distance increases. The ever-decreasing intensity weakens the XPM effect on the CW signal pulses. Additional control pulse energy is required for maintaining the strength of XPM. The result is a less efficient switching. The problem of weak XPM can be solved by employing a control pulse with ever-sharpening pulse profile during propagation, as shown in Fig. 3.3. However, the ever-sharpening pulse profile creates another problem. The switching ratio of the demultiplexing window is proportional to the accumulated XPM experienced by the signal pulse. The strength of XPM profile within the target time slot varies with the control pulse shape. An ever-changing pulse shape during propagation would create an irregular switching window, which is detrimental to NOLM demultiplexing. An irregular switching window may lead to pulse distortion and incomplete switching of the target signal pulses [120]. Moreover, it also deteriorates the noise and crosstalk performance of the NOLM system. Details are given in Chapter 6.

5.3.2 Peak transmittance of the switching window

The equation for NOLM switching is given as [65]:

$$T_x = 1 - \cos^2\left(\frac{\Delta\phi}{2}\right), \quad (5.3)$$

where T_x is the transmittance of the switching window, and $\Delta\phi$ is the phase difference between CW and CCW signal pulses. The phase difference is due to the XPM-induced phase change of CW pulses. Since XPM is proportional to the optical power of the propagating control pulses (see (3.50)), the temporal phase-change profile $\Delta\phi(t)$ is dependent on the intensity profile of the control pulse and the velocity difference between control and signal pulses. If the control pulse propagates faster or slower than the signal pulse, the temporal profile of the signal pulse at the target time slot would co-propagate with a sliding control pulse profile. The control pulse may eventually ‘walk-off’ the signal pulse if propagation length is large enough. The walk-off time is in the unit of picosecond per unit length. The combined effect of the control pulse profile and the walk-off time creates a phase-change profile, which will be transformed into the switching profile, according to (5.3). If there is no phase difference ($\Delta\phi = 0$), T_x in (5.3) would become zero. The transmittance is 100% when the phase difference is equal to π . However, if the phase difference is too large (i.e. $> \pi$), T_x would drop from its maximum value. Therefore, device parameters of NOLM demultiplexer should be optimised to make the peak phase-change equal to π .

$\Delta\phi$ can be derived from (3.50). Taking into account the walk-off of the control pulse, the XPM-induced phase change is given as:

$$\Delta\phi(\tau) = 2 \cdot \gamma \cdot \int_0^L P(\tau - T_w \cdot z) dz, \quad (5.4)$$

where $\Delta\phi(\tau)$ is the phase-change profile within the target time slot, γ is the fibre nonlinear coefficient, $P(\tau)$ is the optical power profile of the control pulse, T_w is the walk-off time per unit length, and L is the length of the fibre loop. Equation 5.4 assumes that the control pulse has a higher velocity than the signal pulse.

The distance integral in (5.4) covers the portion of the control pulse that contributes XPM effect at one temporary point of the phase-change window. The temporal length of that portion of control pulse is equivalent to the total walk-off time ($T_w L$). Instead of integrating the walk-off portion of the control pulse profile for calculating the contribution of XPM to a particular point of the switching profile, it is mathematically more convenient to model that temporal portion of the optical power profile as an averaged constant. Then (5.4) can be rewritten as:

$$\Delta\phi(\tau) = 2 \cdot \gamma \cdot P_{avg}(\tau) \cdot L, \quad (5.5)$$

where P_{avg} is the averaged optical power for the walk-off portion of control pulse that contributes XPM to a temporal point of the switching profile. P_{avg} can be calculated from:

$$P_{avg} = \frac{\int_0^{T_w L} P(\tau - t) dt}{T_w \cdot L}, \quad (5.6)$$

where t is the sliding time unit of the control pulse profile due to the walk-off effect, and τ represents a temporal point of the switching profile. Combining (5.5) and (5.6) leads to:

$$\Delta\phi(\tau) = \frac{2 \cdot \gamma}{T_w} \int_0^{T_w L} P(\tau - t) dt. \quad (5.7)$$

$\Delta\phi(\tau)$ would be at its peak value if the time integral of (5.7) is at maximum. This condition is met only if the control pulse is positioned at the mid-point of the total walk-off time. Referring to (5.6), this condition is equivalent to ($\tau = T_w L/2$). At peak phase-change, (5.7) becomes:

$$\Delta\phi_p = \frac{2 \cdot \gamma}{T_w} \int_0^{T_w L} P\left(\frac{T_w L}{2} - t\right) dt, \quad (5.8)$$

where $\Delta\phi_p$ is the peak phase-change. Equation 5.8 can be rewritten as:

$$\Delta\phi_p = \frac{2 \cdot \gamma}{T_w} \int_{-T_w L/2}^{T_w L/2} P(t) dt. \quad (5.9)$$

Since the control pulse is assumed to be a fundamental soliton in this mathematical model, $P(t)$ can be replaced by the soliton pulse profile. The optical power profile of a fundamental soliton is given by:

$$P(t) = P_o \cdot \text{sech}^2\left(\frac{1.763t}{T_{FWHM}}\right), \quad (5.10)$$

where P_o is the peak power of the soliton pulse, and T_{FWHM} is the full width half maximum of the optical power profile. The square of hyperbolic secant function in (5.10) is obtained by squaring (3.22) and setting $N = 1$ for the fundamental soliton.

Combining (5.9) and (5.10) gives:

$$\Delta\phi_p = \frac{2 \cdot \gamma \cdot P_o}{T_w} \int_{-T_w L/2}^{T_w L/2} \text{sech}^2\left(\frac{1.763t}{T_{FWHM}}\right) dt. \quad (5.11)$$

The integral form in (5.11) can be solved by standard integral function [130]. The peak phase-change is π for 100% transmittance. Then (5.11) is transformed into:

$$\pi \cdot T_w = \frac{4 \cdot \gamma \cdot P_o \cdot T_{FWHM}}{1.763} \tanh\left(\frac{1.763 \cdot T_w \cdot L}{2 \cdot T_{FWHM}}\right). \quad (5.12)$$

P_o in (5.12) is the soliton peak power. When it is replaced by the peak power equation for fundamental soliton (3.23), then (5.12) becomes:

$$\pi \cdot T_w \cdot T_{FWHM} = 7.052 \cdot |\beta_2| \tanh\left(\frac{0.8815 \cdot T_w \cdot L}{T_{FWHM}}\right), \quad (5.13)$$

where β_2 is the first order dispersion coefficient.

The peak transmittance of the NOLM demultiplexer will be 100% if (5.13) is satisfied. This equation can be used to optimise T_{FWHM} and T_w for 100% switching at the peak of the demultiplexing window. In (5.13), it is assumed that fibre loop is loss free. Nevertheless, in NOLM demultiplexers, where a long length of fibre cable is used, it is necessary to include fibre loss α in the analysis. Peak power of the control pulse decreases as the propagation length increases. Therefore, the constant value of distance-dependent peak power in (5.12) should be replaced by the effective peak power, which gives the average value of the decreasing peak power over the whole propagation distance. The decrease of peak power due to fibre loss is given as:

$$P(z) = P_o \exp(-\alpha z), \quad (5.14)$$

where z is the propagation distance.

From (5.14), the average value of decreasing peak power over the whole propagation distance is given as:

$$P_{o-eff} = \frac{1}{L} \int_0^L P_o \exp(-\alpha z) dz, \quad (5.15)$$

where P_{o-eff} is the average peak power. Solving the integral of (5.15) gives:

$$P_{o-eff} = \frac{P_o}{\alpha L} (1 - \exp(-\alpha L)). \quad (5.16)$$

For taking into account the fibre loss, P_o in (5.12) should be substituted by P_{o-eff} in (5.16).

Following the same mathematical treatment from (5.12) to (5.13), (5.16) becomes:

$$\pi \cdot T_w \cdot L \cdot \alpha \cdot T_{FWHM} \approx 7.052 \cdot (1 - \exp(-\alpha L)) \cdot |\beta_2| \cdot \tanh\left(\frac{0.8815 \cdot T_w \cdot L}{T_{FWHM}}\right). \quad (5.17)$$

According to the soliton peak power equation (3.23), the soliton pulse width increases as the peak power decreases. The other two parameters (β_2 and γ) in (3.23) are independent of

optical power. Equation 5.17 is only an approximation as it assumes that the soliton control pulse has a constant profile throughout the whole propagation distance. Nevertheless, it will be shown in Section 5.4 that the accuracy of (5.17) is sufficient for most situations.

The peak transmittance of switching window can be maximised by solving (5.13) for loss-free fibre and solving (5.17) for lossless fibre. Equations 5.13 and 5.17 are solved using the Newton-Raphson method [131] and the results are plotted in Fig. 5.3. The fibre nonlinear coefficient used in the simulation is $2W^{-1}\text{km}^{-1}$ -- a typical value of single mode fibre [87]. The optimisation of T_{FWHM} versus T_wL for 100% switching is shown in Fig. 5.3. Fig. 5.3 shows that T_{FWHM} decreases as the total walk-off time increases. The increased walk-off time will shorten the interactive time between CW signal pulses and the central part of the control pulses, thus resulting in a reduction of the phase difference between CW and CCW signal pulses. The soliton control pulse requires narrower width for higher peak power (see (3.23)), in order to compensate the reduction of phase-change. Therefore, T_{FWHM} in Fig. 5.3 is decreased for maintaining $\Delta\phi_p = \pi$ when the walk-off time increases.

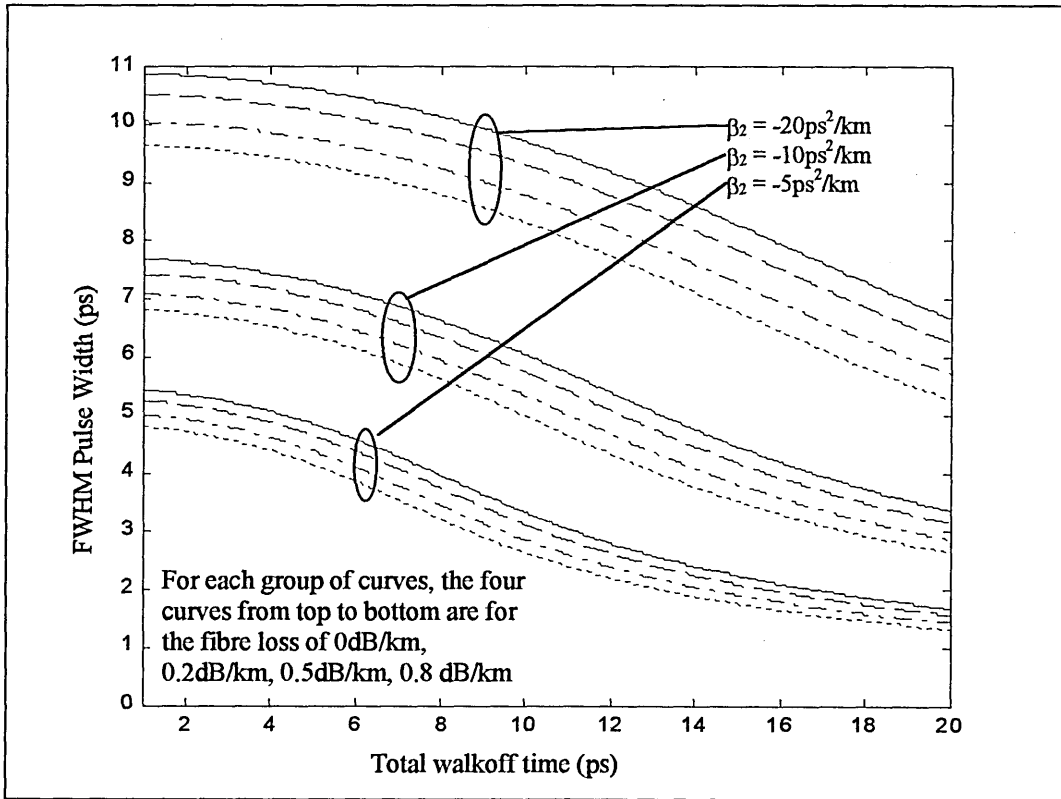


Fig. 5.3. T_{FWHM} Vs. $T_w L$ calculated from (5.13) and (5.17) for $L = 3$ km.

Another characteristic shown in Fig. 5.3 is the increase of T_{FWHM} with $|\beta_2|$. This is because the peak power of an optical soliton pulse is directly proportional to $|\beta_2|$ and inversely proportional to T_{FWHM}^2 (see (3.23)). In order to maintain a certain level of soliton peak power for 100% switching, a narrower pulse width should be used to replenish the decreased peak power due to a smaller value of $|\beta_2|$.

With fibre loss taken into account, the optical power of the control pulse gradually decreases as the propagation distance increases; therefore the phase change caused by XPM is also reduced. As shown in Fig. 5.3, the control pulse width is decreased for compensating the loss of phase change due to fibre loss.

Figure 5.3 shows the optimisation of control pulse width and total walk-off time for $L = 3$ km. Figure 5.4 shows the optimization for the same set of parameters as Fig. 5.3 except that L is equal to 6 km instead of 3 km. It is shown by comparing Figs. 5.3 and 5.4 that the

optimised values of control pulse width are larger for longer fibre loop. It is because lower soliton power is required when the interactive distance for XPM is longer. Figure 5.4 also displays a more contrast difference of optimised values of T_{FWHM} for different fibre loss. This reflects the fact that fibre loss has more influence over the soliton power in longer propagation distance.

According to (3.23), a soliton pulse needs higher power to support a shorter pulse width. Nevertheless, a high intensity optical pulse propagating over a long distance will induce stimulated Raman scattering (see Chapter 3). SRS is a nonlinear process that transfers photons from higher frequency components to lower frequency components. In order to avoid the transfer of optical energy from the high intensity control pulse to the co-propagating CW signal pulse, the control pulse should have a longer wavelength than the signal pulse. Otherwise, the resultant unequal intensity of CW and CCW signal pulse will induce demultiplexing crosstalk [65]. Even if the control pulse has a longer wavelength than the signal pulse, the Raman effect of transferring optical energy from the control pulse to lower frequency components can still occur for very high intensity control pulses due to spontaneous Raman scattering (see Chapter 3). Under the assumption of Lorentzian Raman-gain spectrum, the threshold pump power that will lead to significant transfer of optical power to initially absent Stokes wave is given as [31]:

$$P_{RAMAN} \approx \frac{16 \cdot A_{eff}}{g_R \cdot L_{eff}}, \quad (5.18)$$

where P_{RAMAN} is the Raman threshold, A_{eff} is the effective fibre core area, g_R is the Raman gain coefficient, and L_{eff} is the effective interactive length taking into account the fibre loss.

The effective interactive length is given as [35]:

$$L_{eff} = \frac{1 - \exp(-\alpha \cdot L)}{\alpha}, \quad (5.19)$$

where α is the fibre loss, and L is the propagation length.

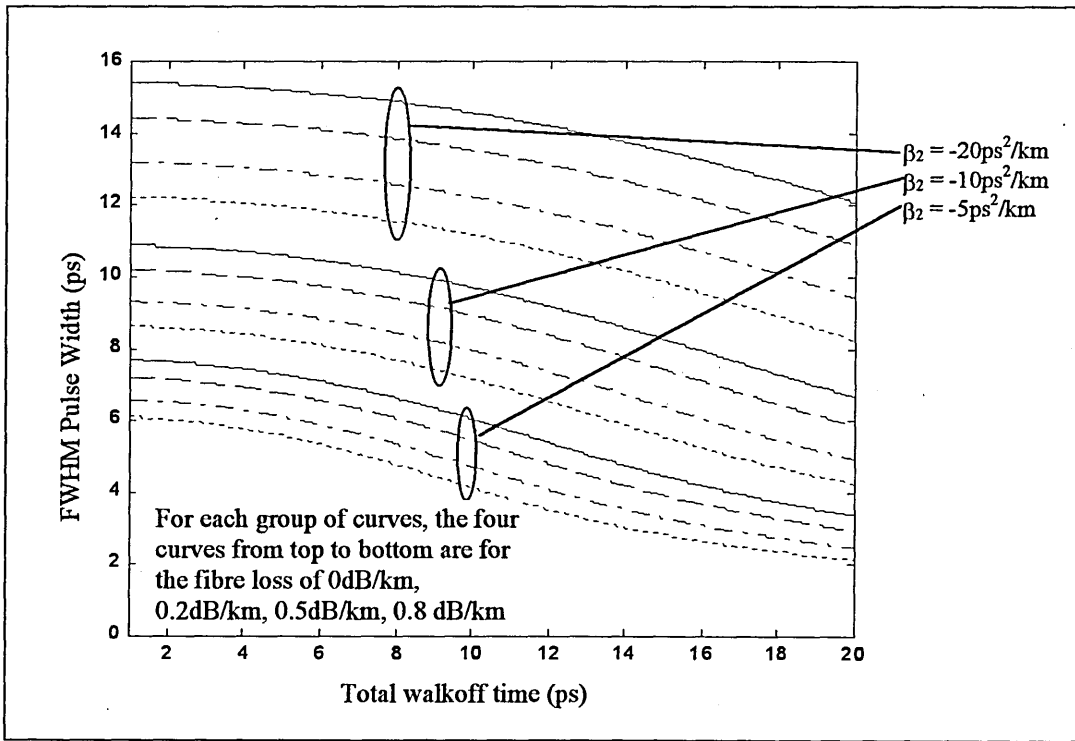


Fig. 5.4. T_{FWHM} Vs. $T_w L$ calculated from (5.13) and (5.17) for $L = 6$ km.

Figure 5.5 plots the peak power of soliton control pulse Vs. total walk-off time by solving (3.23), (5.13), and (5.17). The optimised values of T_{FWHM} , calculated from (5.13) and (5.17), are substituted into (3.23). The parameters used are $L = 3$ km, $\gamma = 2 \text{ W}^{-1} \text{ km}^{-1}$.

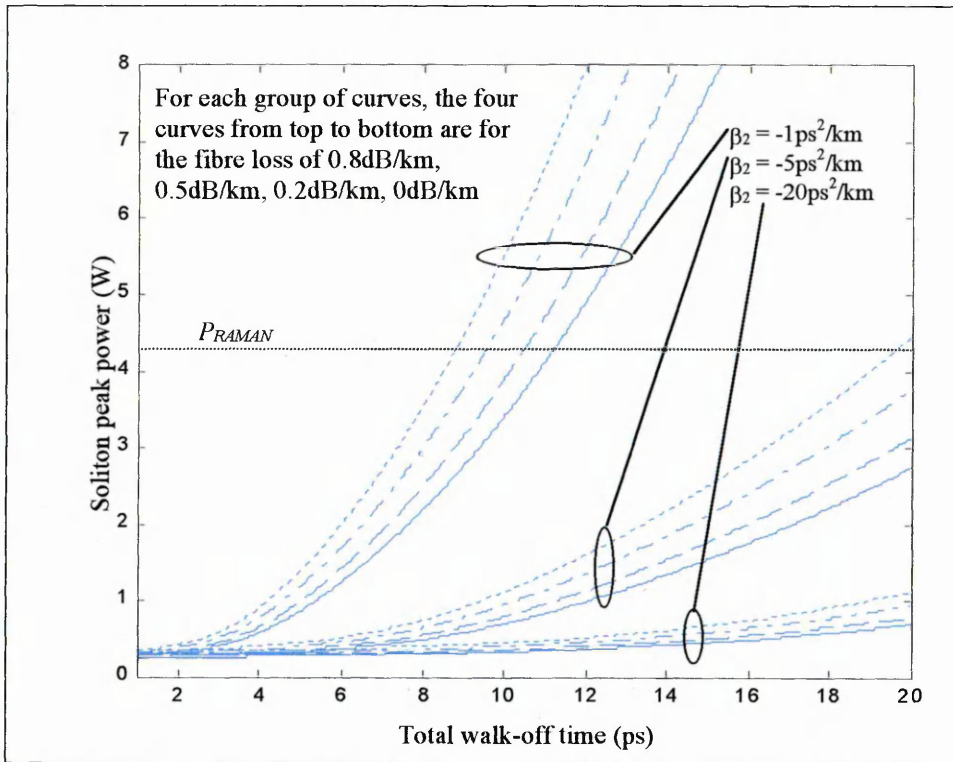


Fig. 5.5. Soliton peak power Vs. the total walk-off time, calculated from (3.23), (5.13) and (5.17), for different values of β_2 .

Figure 5.5 shows that optimised peak power of soliton control pulse increases with total walk-off time and fibre loss but decreases with $|\beta_2|$. The horizontal dashed line in Fig. 5.5 represents the threshold Raman power calculated from (5.18). The Raman gain coefficient, the effective fibre core area and the fibre loss are assumed to be 6.67×10^{-14} m/W, $50 \mu\text{m}^2$ and 0.2 dB/km, respectively. The calculated Raman threshold is 4.27 W. Figure 5.5 shows that, for smaller $|\beta_2|$, the optimised soliton peak power reaches the Raman threshold at a smaller total walk-off time. The Raman threshold imposes an upper limit of the total walk-off time for different values of $|\beta_2|$ and fibre loss. The details of what impact the Raman effect would make on NOLM demultiplexing will be elaborated in Chapter 9.

The Raman threshold in (5.18) represents the optical power level that will stimulate the Raman effect for initially absent Stokes wave. Another factor that affects the strength of the Raman effect in soliton system is the width of a soliton pulse. Raman effect causes a

continuous downshift of the mean frequency of subpicosecond soliton pulses propagating in optical fibre [132]. The frequency spectrum of ultra-short soliton is so wide that some lower frequency components of the pulse can be acting as Stokes waves for the SRS to occur. Therefore, the energy of higher frequency components of a soliton pulse is continuously transferred to the lower frequency components. The result would be a continuous downshift of central frequency as the soliton pulse propagates. J. P. Gordon [132] developed an equation for evaluating the frequency shift of soliton pulse and it is given by:

$$\frac{dv_o}{dz} (THz / km) = \frac{0.0436}{T_{FWHM}^2}, \quad (5.20)$$

where v_o is the central frequency of the soliton pulse. The frequency-shift of the control pulse will change the walk-off time between control and signal pulses. As the mathematical model does not include the Raman term, the simulation results of this model are invalid for ultrashort control pulse. The control pulse width for the simulation of NOLM demultiplexing is restricted to ≥ 1 ps in order to avoid the effect of soliton self-frequency shifting.

5.3.3 Width of soliton switching window

The conventional definition of window width is FWHM. Nevertheless, in this mathematical model, a more flexible and general definition of window width is adopted. The inset of Fig. 5.6 shows a typical shape of a soliton switching window. The window width W is defined as the period of time in which the normalised transmittance of the switching window is varied within a range set by a predefined variable F_{tx} as shown in Fig. 5.6. If $F_{tx} = 0.5$, W is equivalent to FWHM width.

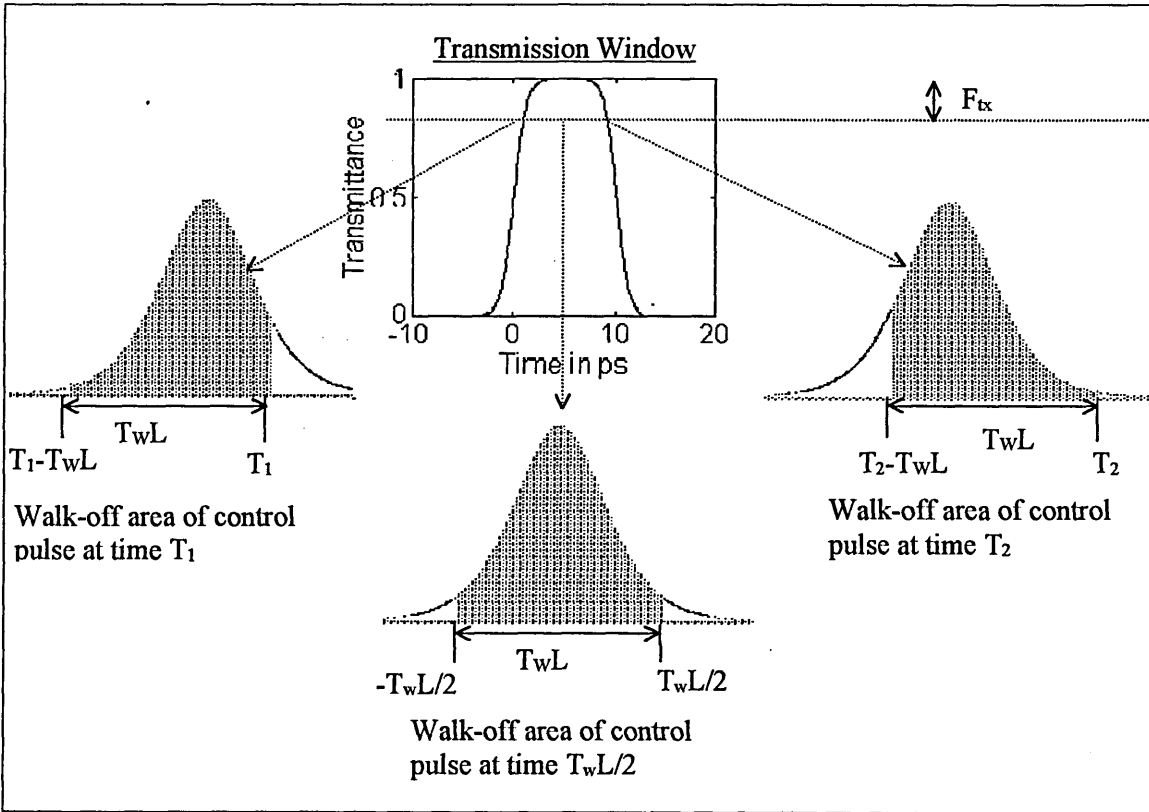


Fig. 5.6. A typical soliton switching window (the control pulse walks over the signal pulse).

In Fig. 5.6, the shaded areas represent the portion of the control pulse profile walking through the signal pulse. At time T_1 the transmittance level just reaches the threshold level set by F_{tx} . From T_1 to T_2 it remains above the threshold level and it reaches the peak value at time $T_wL/2$. The transmittance drops below the threshold level after T_2 . By comparing the shaded areas at T_1 , $T_wL/2$, and T_2 in Fig. 5.6, the shaded areas at T_1 (T_2) is just left (right) shift with $(T_wL/2) - T_1$ and $T_2 - (T_wL/2)$, respectively from the symmetric walk-off region at $T_wL/2$. $T_2 - (T_wL/2)$ is equal to $(T_wL/2) - T_1$ due to the symmetrical shape of the soliton pulse. Figure 5.6 assumes a constant control pulse shape throughout the whole propagation so that the XPM at any temporal point within the switching window is proportional to the integral of the walk-off portion of the soliton pulse profile. This implies that the change of optical power profile due to fibre loss is ignored. Then W can be expressed as:

$$W = 2(T_wL/2 - T_1) = 2(T_2 - T_wL/2) = 2|(T_wL/2) - T_1|, \quad (5.21)$$

where $T_i = T_1$ or T_2 , T_1 and T_2 are defined in Fig. 5.6.

Using (5.3), the XPM-induced phase-change at the level of F_{tx} is given as:

$$\Delta\phi(F_{tx}) = 2 \cdot \cos^{-1}(\sqrt{F_{tx}}). \quad (5.22)$$

And the XPM at F_{tx} is related to the power profile of the control pulse given as (see (5.11)):

$$\Delta\phi(F_{tx}) = \frac{2 \cdot \gamma \cdot P_o}{T_w} \int_{T_i - T_w L}^{T_i} \sec h^2 \left(\frac{1.763 \cdot \tau}{T_{FWHM}} \right) d\tau. \quad (5.23)$$

T_{FWHM} in (5.23) represents the FWHM width of the control pulse.

Combining (5.22) and (5.23) results in:

$$2 \cdot \cos^{-1}(\sqrt{F_{tx}}) = \frac{2 \cdot \gamma \cdot P_o}{T_w} \int_{T_i - T_w L}^{T_i} \sec h^2 \left(\frac{1.763 \cdot \tau}{T_{FWHM}} \right) d\tau. \quad (5.24)$$

Referring back to (5.11), the peak transmittance equation is given as:

$$\pi = \frac{2 \cdot \gamma \cdot P_o}{T_w} \int_{-T_w L/2}^{T_w L/2} \sec h^2 \left(\frac{1.763 \cdot \tau}{T_{FWHM}} \right) d\tau. \quad (5.25)$$

After dividing (5.24) by (5.25) and solving the time integral, we will have:

$$4 \cdot \cos^{-1}(\sqrt{F_{tx}}) \cdot \tanh(0.8815 T_w \cdot L / T_{FWHM}) / \pi = \tanh[1.763 \cdot T_i / T_{FWHM}] - \tanh[1.763 \cdot (T_i - T_w \cdot L) / T_{FWHM}] \quad (5.26)$$

Equation 5.26 yields two solutions of T_i , one is T_1 and the other one is T_2 . Window width can then be calculated by substituting either of the solutions in (5.26) into (5.21). Equation 5.21 holds true no matter which one of the solutions of T_i is used in the substitution. The perfect symmetrical shape of soliton switching window shown in Fig. 5.6 can be attained only if the fibre cable is loss-free. Therefore, the limitation of (5.21) and (5.26) is the assumption of loss-free fibre. As the equation of 100 % peak transmittance is included in the window width equation, (5.21) and (5.26) can only be used in conjunction with (5.13) and (5.17).

Window width at $F_{tx} = 0.1$ versus total walk-off time, calculated from (5.21) and (5.26) for different values of β_2 , are shown in Fig. 5.7. T_{FWHM} and $T_w L$ in (5.21) and (5.26) are calculated from (5.13) for 100 % peak transmittance of the soliton switching window. The fibre length is assumed to be 3 km. Figure 5.7 illustrates a threshold walk-off level W_{th} below which the variation of W is relatively flat and above which a substantial increase of W is observed. The threshold level increases with $|\beta_2|$. The threshold characteristics of window width can be explained as follows. The two main factors that determine the width of a soliton switching window are control pulse width and the total walk-off time. Two general cases are considered here. Firstly, when the control pulse width \gg total walk-off time, the window width is largely proportional to the control pulse width and is virtually independent of the total walk-off time. Secondly, when total walk-off time \gg control pulse width, the window width is largely proportional to the total walk-off time. All the four curves in Fig. 5.7 are flat for small $|\beta_2|$, since the window width is independent of the total walk-off time when control pulse width \gg total walk-off time. The total walk-off time becomes an overwhelming factor for determining the window width when the walk-off time is larger than the threshold value, as shown in Fig. 5.7.

Referring to Fig. 5.3, which plots the FWHM pulse width Vs. the total walk-off time, the optimised control pulse width decreases as $|\beta_2|$ decreases. A similar characteristic can be found in the small walk-off time region of Fig. 5.7, where a decrease of $|\beta_2|$ results in a decrease of window width. It is because the window width in small walk-off time is largely determined by the control pulse width. It is also shown in Fig. 5.7 that the threshold point W_{th} is reached at a smaller total walk-off time for a decrease of $|\beta_2|$. In the case of a

decreased $|\beta_2|$, the walk-off time has a greater influence on the window width due to the decreased control pulse width.

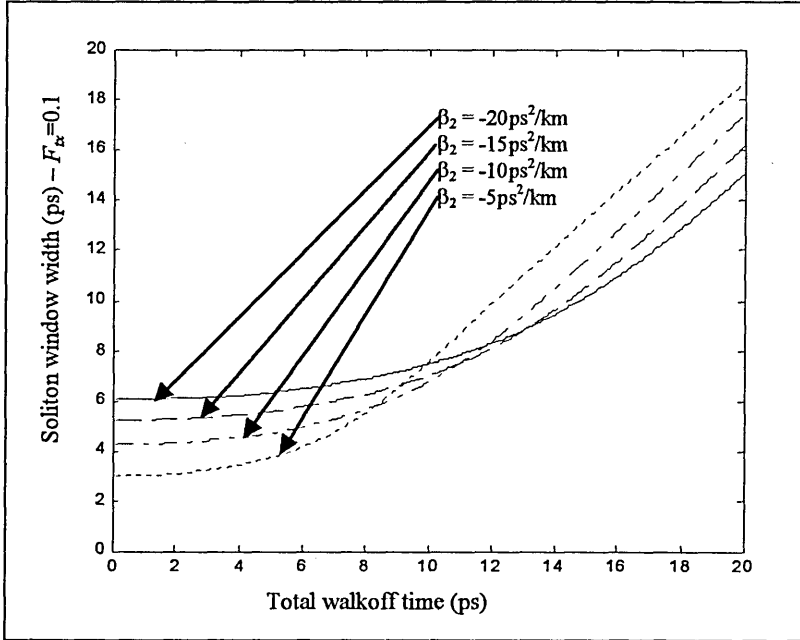


Fig. 5.7. Soliton window width at $F_{tx} = 0.1$ Vs. the total walk-off time for different values of β_2 .

In the post-threshold region of the total walk-off time, the four curves in Fig. 5.7 look like having the same gradient but being vertically shifted against each other. The window width is wider for smaller $|\beta_2|$ and the vertical gaps between the curves are independent of the further increase of the total walk-off time, as shown in Fig. 5.7. It was mentioned in the previous paragraph that the optimised control pulse width increases with $|\beta_2|$. The steepness of the rising and falling edges of the switching window in large walk-off time is dependent on the width of the control pulse. A control pulse with impulse characteristics will result in a square shape of the switching window. Ideally, the width of the square-shape window is equal to the total walk-off time. The rising/falling time of the switching window increases with the control pulse width. The window width in Fig. 5.7 is defined as the period of time in which the normalised transmittance of the switching window is varied

between 0.9 to 1 (i.e. $F_{tx} = 0.1$ in Fig. 5.6). For large walk-off time, a larger $|\beta_2|$ leads to a wider control pulse (see Fig. 5.3). The window width narrows due to the slower rising/falling time of the switching window. Therefore, the window width in the post-threshold region of total walk-off time increases as $|\beta_2|$ decreases.

For comparison purpose, window width versus the total walk-off time for $F_{tx} = 0.3$ and 0.5 are plotted in Figs. 5.8 and 5.9, respectively. The other simulation parameters are the same as those for Fig. 5.7. It is shown by comparing Figs. 5.7 and 5.8 that, in the post-threshold region of walk-off time, the differences in window width among various $|\beta_2|$ are smaller for the window width at $F_{tx} = 0.3$ than at $F_{tx} = 0.1$. By extending the window width definition from 90 % - 100 % to 70 % - 100 % of transmittance variation, a portion of window width of larger rising/falling time originally excluded from $F_{tx} = 0.1$ is included in $F_{tx} = 0.3$. Therefore, the differences in window width among the curves in Fig. 5.8 are smaller than those in Fig. 5.7. In Fig. 5.9, the differences in window width for different values of $|\beta_2|$ in the post-threshold region of the walk-off time are further reduced to become close to zero.

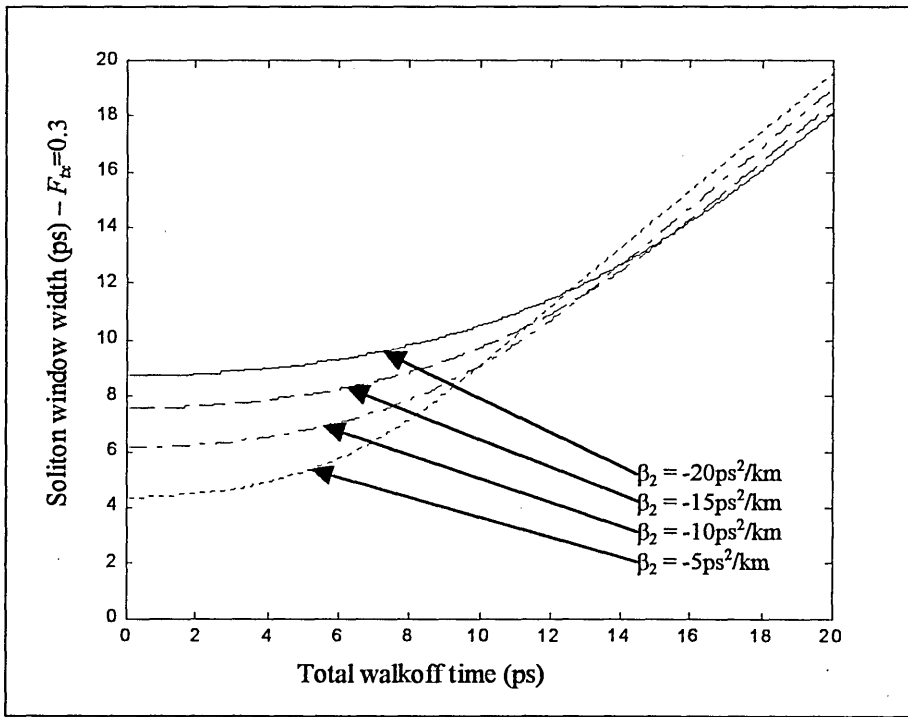


Fig. 5.8. Soliton window width at $F_{tx} = 0.3$ Vs. the total walk-off time for different values of β_2 .

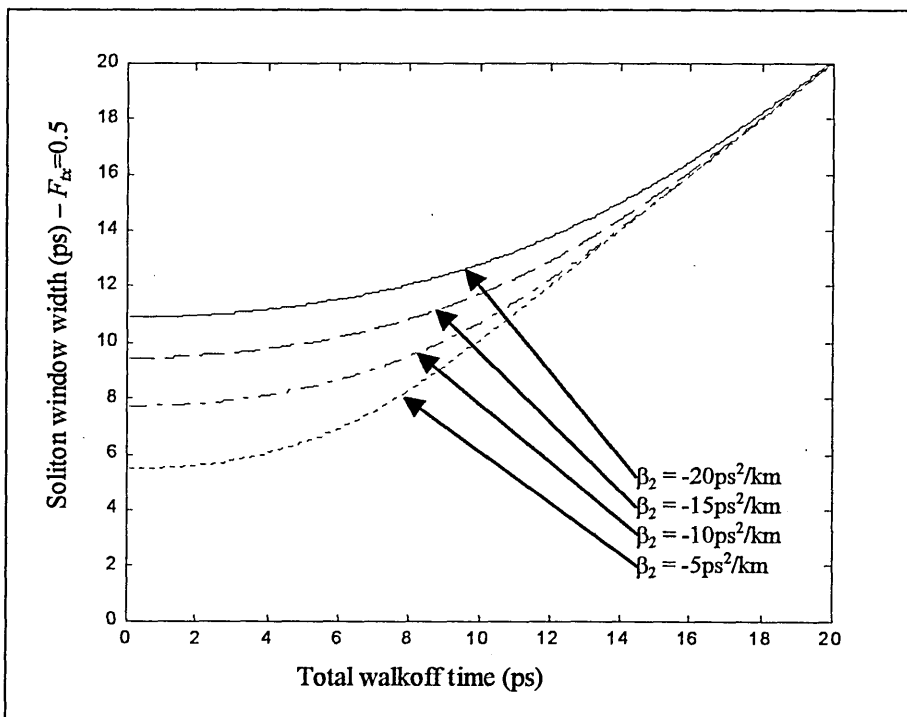


Fig. 5.9. Soliton window width at $F_{tx} = 0.5$ Vs. the total walk-off time for different values of β_2 .

The most common definition of window width is FWHM (i.e. $F_{tx} = 0.5$). Nevertheless, FWHM window width is not necessarily the best definition to evaluate system performance in some situations. For instance, FWHM window width is not a good indicator to assess the completeness of switching of target pulse energy from the input port to the output port of the NOLM demultiplexer. The four values of $|\beta_2|$ in Fig. 5.9 will lead to the same FWHM window width when the total walk-off time is equal to 20ps. But it is wrong to assume that the amount of the target pulse energy being switched to the output port is the same for the four cases. In fact, the slow rising/falling time of switching window in larger $|\beta_2|$ will cause incomplete switching of the rising and falling edges of the target pulse if the target pulse width is comparable to the window width [122]. Figure 5.7 clearly shows that, using the definition of $F_{tx} = 0.1$, the difference in window width between the cases of $\beta_2 = -5\text{ps}^2/\text{km}$ and $-20\text{ps}^2/\text{km}$ is as large as 4ps. The wider window width allows more energy of the target pulse to be switched. The window width at $F_{tx} = 0.1$ is a better definition to assess the completeness of switching of target signal pulse in this case. At $F_{tx} = 0.1$, the two important parameters for controlling the width of a soliton switching window are β_2 and the total walk-off time (see Fig. 5.7). To create a wider switching window, a smaller value of $|\beta_2|$ should be used if the total walk-off time is below the threshold level, and a larger value of $|\beta_2|$ should be used if the total walk-off time is above the threshold level. The width of soliton switching window has great implications in noise and crosstalk performance of NOLM demultiplexer, which will be thoroughly analysed in Chapter 6.

5.3.4 Soliton switching profile

Assuming that the control pulse propagates faster than the signal pulse, the phase-change profile for the target signal pulse is given as:

$$\Delta\phi(t) = \frac{2 \cdot \gamma \cdot P_o}{T_w} \int_{t-T_w L}^t \operatorname{sech}^2\left(\frac{1.763 \cdot \tau}{T_{FWHM}}\right) d\tau. \quad (5.27)$$

Equation 5.27 is derived in a similar way to (5.11) and (5.23). The switching profile can be obtained by substituting (5.27) into the transmittance equation (5.3). The function of switching profile is given as:

$$T_x(t) = 1 - \cos^2 \left[\frac{\gamma \cdot P_o}{T_w} \int_{t-T_w L}^t \operatorname{sech}^2\left(\frac{1.763 \cdot \tau}{T_{FWHM}}\right) d\tau \right], \quad (5.28)$$

where $T_x(t)$ is the switching profile.

Equations 5.27 and 5.28 assume that the soliton power remains the same during the entire propagation. For taking the fibre loss into account, the constant peak power in (5.28) should be replaced by a distance-dependent effective peak power, which decreases with propagation length. Then the switching profile for varying soliton peak power is given as:

$$T_x(t) = 1 - \cos^2 \left[\frac{\gamma \cdot P_o}{T_w} \int_{t-T_w L}^t \exp\left(\frac{-\alpha \cdot (t - \tau)}{T_w}\right) \cdot \operatorname{sech}^2\left(\frac{1.763 \cdot \tau}{T_{FWHM}}\right) d\tau \right], \quad (5.29)$$

where α is the fibre loss per unit length. Since the control pulse propagates faster than the signal pulse, the XPM-induced switching profile perceived by the target signal pulse is caused by the intensity profile of a forwardly sliding control pulse. At any temporal point t of the switching profile, the signal pulse has experienced the sliding control pulse profile from t to $t - T_w L$, where $T_w L$ is the total walk-off time. The propagation distance of the control pulse increases from zero to L as the signal pulse experiences the sliding control pulse profile from t to $t - T_w L$. The peak power of the control pulse decreases with the propagation distance as:

$$P(z) = P_o \exp(-\alpha z), \quad (5.30)$$

where P_o is the initial peak soliton power, and $P(z)$ is the peak soliton power at length z . The exponential term in (5.29) accounts for the decrease of soliton peak power from $z = 0$ to L as the signal pulse experiences the sliding control profile. The variable τ in (5.29) slides from t to $t - T_w L$. Substituting $\tau = t$ and $\tau = t - T_w L$ into (5.29) represent initial soliton peak power and the decreased soliton peak power at $z = L$, respectively.

Equation 5.29 assumes that the normalised soliton pulse profile remains unchanged during propagation despite its peak power decreasing with propagation distance. However, according to the soliton peak power equation (3.23), the soliton pulse width increases as its peak power decreases. The mathematical relation between the soliton pulse width and the soliton peak power can be obtained by combining (3.23) and (5.30). The result is given as:

$$T_{FWHM}(z) = \sqrt{\frac{3.1 \cdot |\beta_2|}{\gamma \cdot P_o \cdot \exp(-\alpha z)}}. \quad (5.31)$$

For taking into account the distant-dependence of the soliton pulse width, T_{FWHM} in (5.29) should be replaced by (5.31). Substituting (5.31) into (5.29) gives:

$$T_x(t) = 1 - \cos^2 \left[\frac{\gamma \cdot P_o}{T_w} \int_{t-T_w L}^t \exp\left(\frac{-\alpha \cdot (t - \tau)}{T_w}\right) \cdot \sec^2 \left(\tau \cdot \sqrt{\frac{\gamma \cdot P_o \cdot \exp(-\alpha z)}{|\beta_2|}} \right) d\tau \right]. \quad (5.32)$$

The exponential term inside the hyperbolic secant function decreases with propagation distance due to the fibre loss. Similar to the exponential term in (5.29), this distance-dependent exponential term should be transformed into a walk-off-time-dependent exponential in order to be compatible with τ for integration. The equation for soliton switching profile after the transformation is given as:

$$T_x(t) = 1 - \cos^2 \left[\frac{\gamma \cdot P_o}{T_w} \int_{t-T_w L}^t \exp\left(\frac{-\alpha \cdot (t-\tau)}{T_w}\right) \cdot \operatorname{sech}^2 \left(\tau \cdot \exp\left(\frac{-\alpha \cdot (t-\tau)}{2 \cdot T_w}\right) \cdot \sqrt{\frac{\gamma \cdot P_o}{|\beta_2|}} \right) d\tau \right] \quad (5.33)$$

Equation 5.33 will be reduced to (5.29) if $\alpha = 0$. There is no analytical solution for the integral inside the cosine-square in (5.33). For any discrete temporal point of soliton switching profile, the Matlab trapezoidal numerical integration method is required for solving the integral of (5.33) [133]. This is a time-consuming and mathematically tedious process for calculating a soliton switching profile with thousands of temporal points. For calculating the crosstalk and noise of NOLM demultiplexing (details are given in Chapter 6), thousands of soliton switching profiles with various combinations of system parameters need to be evaluated. The long computation time required for calculating soliton switching window hinders the crosstalk and noise analysis. Thus, there is a need to simplify (5.33) for achieving efficient calculation while maintaining an acceptable degree of accuracy. For time resolution of 3000 points, the calculation time for (5.33) using AMD 300 MHz machine is nearly 2 hours, compared to the calculation of less than 3 seconds after the simplification.

Figure 5.10 shows a typical diagram for the changing of soliton pulse width during propagation. The exponential term inside the hyperbolic secant function in (5.33) represents the change of soliton pulse width. The calculation process can be considerably simplified by approximating the τ -dependent exponential term of changing soliton pulse width as a constant value. That means assuming a constant soliton pulse width throughout the propagation. For an ever-changing control pulse width, as shown in Fig. 5.10, an approximation is made to assume the control pulse having a constant pulse width of $z = L/2$. After this amendment, (5.33) becomes:

$$T_x(t) = 1 - \cos^2 \left[\frac{\gamma \cdot P_o}{T_w} \int_{t-T_w L}^t \exp\left(\frac{-\alpha \cdot (t-\tau)}{T_w}\right) \cdot \text{sech}^2 \left(\tau \cdot \exp\left(\frac{-\alpha \cdot L}{4}\right) \cdot \sqrt{\frac{\gamma \cdot P_o}{|\beta_2|}} \right) d\tau \right]. \quad (5.34)$$

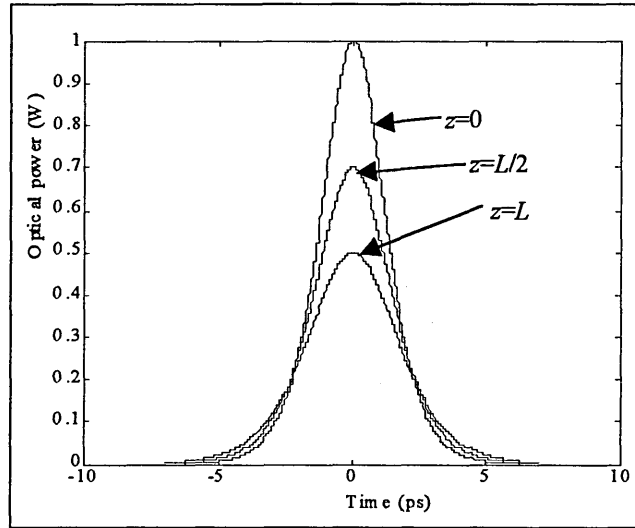


Fig. 5.10. The change of soliton pulse width during propagation.

The form of the integral in (5.34) is equivalent to the convolution between the t -dependent exponential function of a limited range and the hyperbolic-secant-square function. The most efficient way of solving (5.34) using Matlab is to use the convolution multiplication function [133]. Instead of repeatedly solving (5.33) for every temporal point of the soliton switching profile, a complete soliton profile can be obtained by evaluating the convolution function in (5.34) only once.

Equation 5.34 is solved for $\alpha = 0$ and the results are shown in Fig. 5.11. The three soliton switching profiles in Fig. 5.11 represent $T_w = 1$ ps/km, $T_w = 2.5$ ps/km and $T_w = 4$ ps/km, respectively. The simulation parameters used are listed in Table 5.1. It is shown in Fig. 5.11 that a switching profile becomes wider and its transmittance becomes lower for larger values of walk-off time. The switching profile is wider because the interactive time of XPM within the target time slot is lengthened by the larger walk-off time. Larger walk-off time also results in lower transmittance because the peak of the control pulse passes more quickly through the CW signal pulse.

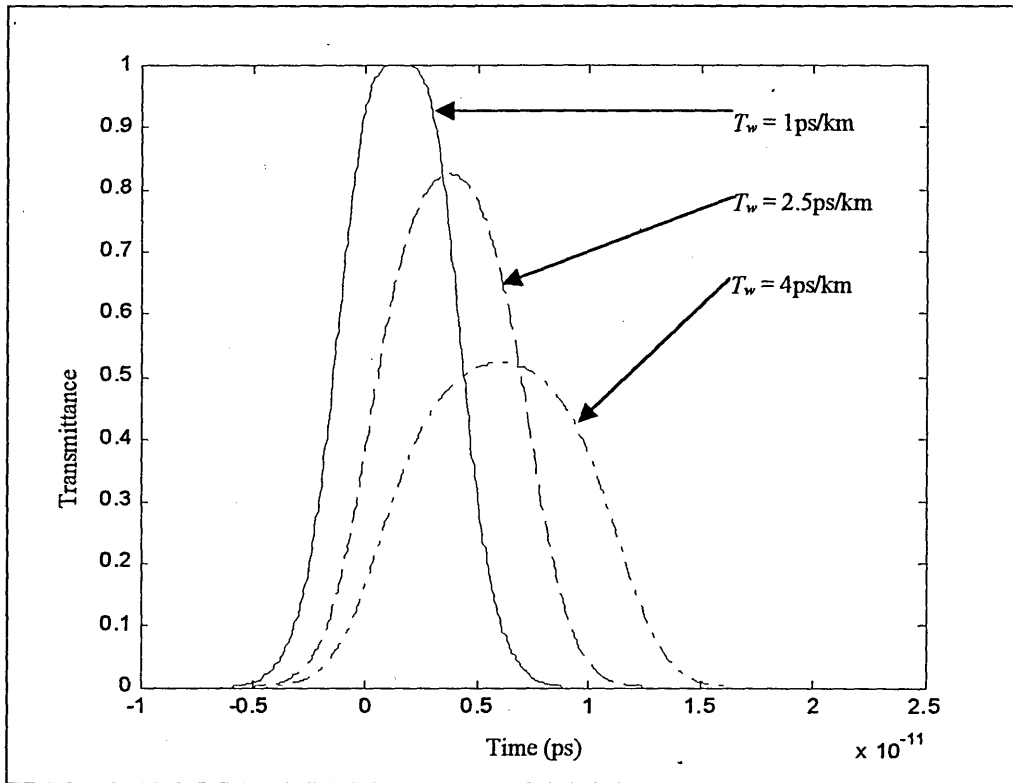


Fig. 5.11. Soliton switching profile ($\alpha=0$) for different values of the walk-off time.

Table 5.1: Simulation parameters for (5.34)

Parameters	Values
Fibre nonlinear coefficient γ	$2 \text{ W}^{-1}\text{km}^{-1}$
Soliton peak power P_o	280 mW
First order dispersion parameter β_2	$-5 \text{ ps}^{-2}/\text{km}$
Fibre length L	3 km

The soliton switching profiles for $\alpha = 0.5\text{dB/km}$ obtained from (5.34) are shown in Fig. 5.12. The other simulation parameters are the same as those in Fig. 5.11 (see Table 5.1). All the three switching profiles in Fig. 5.11 have lower transmittance than their counterparts in Fig. 5.12, due to the decreased soliton peak power by the fibre loss.

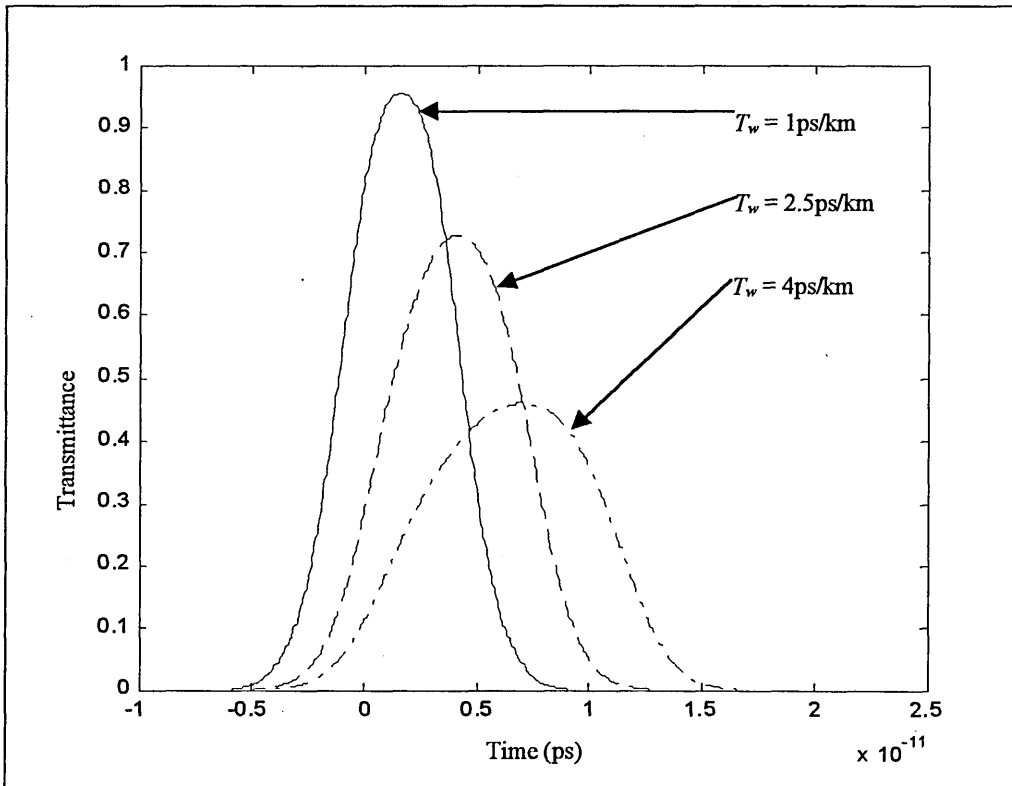


Fig. 5.12. Soliton switching profile ($\alpha = 0.5\text{dB/km}$) for different values of the walk-off time.

5.4 Verification of the Model

The mathematical model presented in this chapter was verified by numerically solving the nonlinear schrödinger equation using the beam propagation method. BPM is a widely adopted method for the simulation of pulse propagation and has been validated experimentally [156]. The derivation of NSE and a full description of BPM can be found in Chapter 3. For a given set of simulation parameters (e.g. Tables 3.1-3.3), solving NSE with BPM produces the simulation results for the evolution of the optical power profile of a propagating pulse. A few examples of pulse profile evolution for different sets of parameters were given in Figs. 3.2-3.4. Since the XPM-induced phase-change of the CW signal pulse is dependent on the optical power of the co-propagating control pulse, the accumulated phase-change profile for the whole fibre loop can be calculated from substituting the simulation results of the BPM into the XPM equation (3.50). In order to take the walk-off time into account, the control pulse profile is continually shifted against

the fixed target time slot as the propagation length increases. The continually shifted control pulse profile is substituted into (3.50) for calculating the accumulated phase-change profile. Finally, the phase-change profile is substituted into (5.3) to obtain the soliton switching profile. Simulating NOLM operations using BPM requires much more computing resources than the computer model presented in this chapter. The soliton switching profiles simulated by the BPM are compared with the simulation results of the computer model for verification. All simulations in this section assume that the fibre nonlinear coefficient $\gamma = 2 \text{ W}^{-1} \text{ km}^{-1}$. The equations of the model to be verified in this section are (5.13), (5.17), (5.21), (5.26) and (5.34).

Equations 5.13 and 5.17 are the optimisation equations for 100% peak transmittance of soliton switching window. Device parameters optimised by (5.13) and (5.17) are used to calculate the soliton switching profiles using BPM, the results are shown in Table 5.2.

System parameters optimised by (5.13) and (5.17)					Peak transmittance Calculated from BPM (%)
α (dB/km)	L (km)	β_2 (ps ² /km)	T_w (ps/km)	T_{FWHM} (ps)	
0	3	5	1	5.23	100
0	3	5	2.5	4.14	100
0	3	5	4	2.8	99.99
0	3	10	1	7.55	100
0	3	10	2.5	6.76	100
0	3	10	4	5.4	100
0	6	5	1	7.1	100
0	6	5	2.5	4.47	100
0	6	5	4	2.81	100
0	6	10	1	10.47	100
0	6	10	2.5	8.27	100
0	6	10	4	5.61	100
0.2	3	5	1	5.05	99.95
0.2	3	5	2.5	3.92	100
0.2	3	5	4	2.62	99.8
0.2	3	10	1	7.3	99.94
0.2	3	10	2.5	6.47	99.99
0.2	3	10	4	5.09	99.98
0.2	6	5	1	6.56	99.94
0.2	6	5	2.5	3.93	99.53

0.2	6	5	4	2.46	97.64
0.2	6	10	1	9.74	99.88
0.2	6	10	2.5	7.43	99.97
0.2	6	10	4	4.92	98.98
0.5	3	5	1	4.8	99.61
0.5	3	5	2.5	3.63	98.82
0.5	3	5	4	2.39	96.85
0.5	3	10	1	6.95	99.62
0.5	3	10	2.5	6.09	99.31
0.5	3	10	4	4.68	98.35
0.5	6	5	1	5.89	99.72
0.5	6	5	2.5	3.29	93.26
0.5	6	5	4	2.06	83.19
0.5	6	10	1	8.83	99.28
0.5	6	10	2.5	6.38	99
0.5	6	10	4	4.12	90.13

The column of peak transmittance in Table 5.2 refers to the transmittance at the peak phase-change of the soliton switching window calculated from BPM. The peak transmittance should be ideally 100 % as (5.13) and (5.17) are used to optimise device parameters for maximising the peak transmittance. Table 5.2 shows that the mathematical model agrees very well with BPM except when the fibre loss is large and the fibre length is long. For the typical fibre loss of 0.2dB/km, Table 5.2 shows that (5.13) and (5.17) can produce accurate simulation results

For the verification of the window width equations (5.21) and (5.26), Table 5.3 compares the simulation results calculated from the mathematical model and the BPM for window width of $F_{tx} = 0.1$.

System parameters optimised by (5.13) and (5.17)					Window width		
α (dB/km)	L (km)	β_2 (ps ² /km)	T_w (ps/km)	T_{FWHM} (ps)	(5.21) & (5.26) (ps)	BPM (ps)	Diff. (%)
0	3	-5	1	5.23	3.24	3.25	0.3
0	3	-5	3	3.65	6.44	6.41	0.4
0	3	-10	1	7.55	4.42	4.43	0.2
0	3	-10	3	6.35	6.13	6.12	0.2
0	6	-5	1	7.1	4.96	4.95	0.2
0	6	-5	3	3.74	15.13	15.13	0
0	6	-10	1	10.47	6.49	6.49	0
0	6	-10	3	7.29	12.87	12.89	0.2
0.2	3	-5	1	5.05	3.15	3.1	1.6
0.2	3	-5	3	3.43	6.53	6.36	2.6
0.2	3	-10	1	7.3	4.29	4.22	1.6
0.2	3	-10	3	6.05	6.1	5.99	0.2
0.2	6	-5	1	6.56	4.75	4.61	2.9%
0.2	6	-5	3	3.28	15.48	14.6	5.7
0.2	6	-10	1	9.74	6.14	5.97	2.8
0.2	6	-10	3	6.46	13.28	12.49	6%
0.5	3	-5	1	4.8	3.03	2.89	4.6
0.5	3	-5	3	3.15	6.69	6.11	8.7
0.5	3	-10	1	6.95	4.11	3.93	4.4
0.5	3	-10	3	5.65	6.07	5.73	5.6
0.5	6	-5	1	5.89	4.51	4.09	9.3
0.5	6	-5	3	2.75	15.89	12.6	20.7
0.5	6	-10	1	8.83	5.71	5.23	8.4
0.5	6	-10	3	5.46	13.89	11.32	18.5

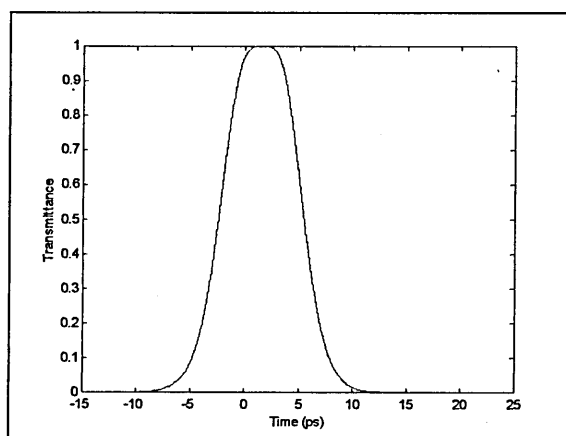
Table 5.3 shows that the simulation results obtained from the mathematical model and the BPM agree very well for $\alpha = 0$ dB/km and $\alpha = 0.2$ dB/km. However, discrepancies as large as 20.7 % for large fibre loss and long fibre length can be observed. Part of the reason of the large discrepancies is the inadequate accuracy of (5.13) and (5.17) when the fibre loss is large. For the comparisons of the accuracy of the window width equations for different values of F_{tx} , Table 5.4 lists the simulations results calculated from the mathematical model and the BPM for $F_{tx} = 0.5$ (FWHM window width). Table 5.4 shows that the window width equations have higher accuracy when F_{tx} is larger.

System parameters optimised by (5.13) and (5.17)					Window width		
α (dB/km)	L (km)	β_2 (ps ² /km)	T_w (ps/km)	T_{FWHM} (ps)	(5.21) & (5.26) (ps)	BPM (ps)	Diff. (%)
0	3	-5	1	5.23	5.76	5.77	0.2
0	3	-5	3	3.65	9.1	9.11	0.1
0	3	-10	1	7.55	7.92	7.93	0.1
0	3	-10	3	6.35	10.03	10.03	0
0	6	-5	1	7.1	8.64	8.64	0
0	6	-5	3	3.74	18	18.02	0.1
0	6	-10	1	10.47	11.53	15.54	0.1
0	6	-10	3	7.29	18.21	18.23	0.1
0.2	3	-5	1	5.05	5.6	5.62	0.4
0.2	3	-5	3	3.43	9.08	9.04	0.4
0.2	3	-10	1	7.3	7.68	7.71	0.4
0.2	3	-10	3	6.05	9.88	9.86	0.2
0.2	6	-5	1	6.56	8.22	8.24	0.2
0.2	6	-5	3	3.28	18	17.84	0.3
0.2	6	-10	1	9.74	10.88	10.95	0.6
0.2	6	-10	3	6.46	18.11	17.86	1.4
0.5	3	-5	1	4.8	5.38	5.4	0.4
0.5	3	-5	3	3.15	9.05	8.85	2.2
0.5	3	-10	1	6.95	7.35	7.4	0.7
0.5	3	-10	3	5.65	9.7	9.56	1.4
0.5	6	-5	1	5.89	7.73	7.61	1.6
0.5	6	-5	3	2.75	18	17.1	5
0.5	6	-10	1	8.83	10.08	10.09	0.1
0.5	6	-10	3	5.46	18.04	16.86	6.5

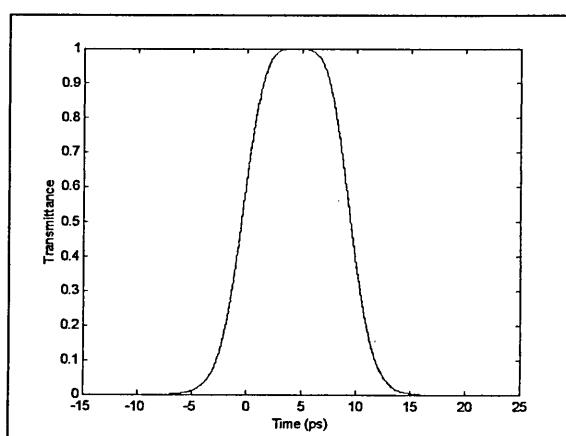
For the verification of the soliton switching profile equation (5.34), Fig. 5.13 show the simulation results obtained from (5.34) and the BPM. The solid and dashed lines in Figs. 5.13a – 5.13l represent the soliton profile calculated from (5.34) and the BPM, respectively. Table 5.5 lists the simulation parameters for Fig. 5.13. Only the solid curves are visible in Figs. 5.13a - 5.13d as the soliton switching profiles calculated from (5.34) and BPM fit perfectly at $\alpha = 0$. Although there are small deviations between the solid and dashed profiles in Figs. 5.13e - 5.13l ($\alpha = 0.2\text{dB/km}$), the simulation results of (5.34) generally agree quite well with those of BPM.

Table 5.5: Simulations parameters for Fig. 5.13						
Figure	System parameters optimised by (5.13) and (5.17)					
	α (dB/km)	L (km)	β_2 (ps^2/km)	T_w (ps/km)	T_{FWHM} (ps)	P_o at $z = 0$ (mW)
5.13a	0	3	-10	1	7.55	273
5.13b	0	3	-10	3	6.35	386
5.13c	0	6	-5	1	7.1	154
5.13d	0	6	-5	3	3.74	556
5.13e	0.2	3	-5	1	5.05	305
5.13f	0.2	3	-5	3	3.43	661
5.13g	0.2	3	-10	1	7.3	292
5.13h	0.2	3	-10	3	6.05	435
5.13i	0.2	6	-5	1	6.56	181
5.13j	0.2	6	-5	3	3.28	723
5.13k	0.2	6	-10	1	9.74	164
5.13l	0.2	6	-10	3	6.46	373

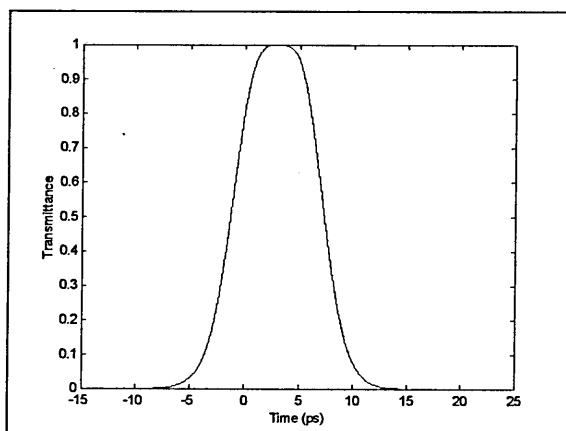
Note: the following graphs show the verification of (5.34)



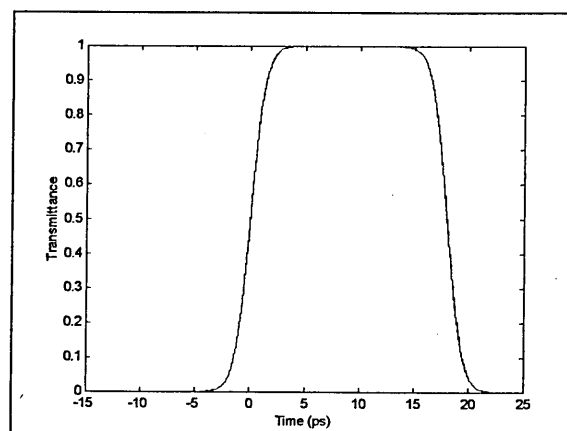
(a)



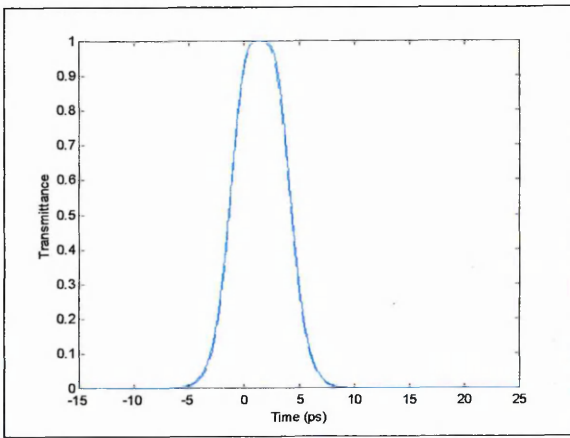
(b)



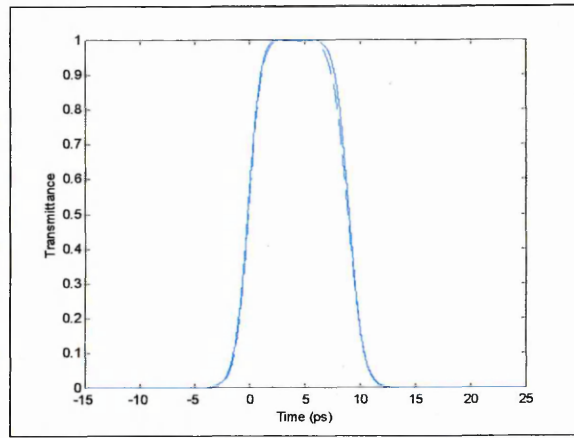
(c)



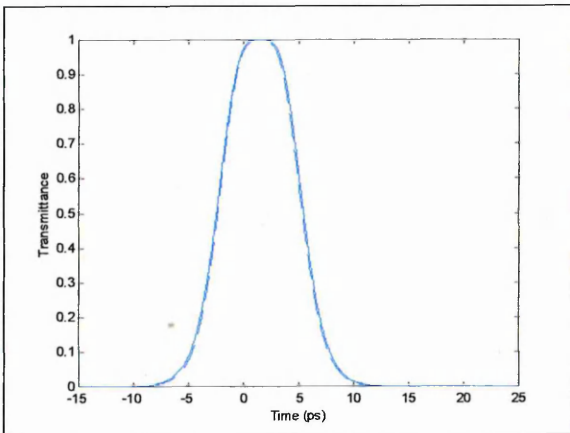
(d)



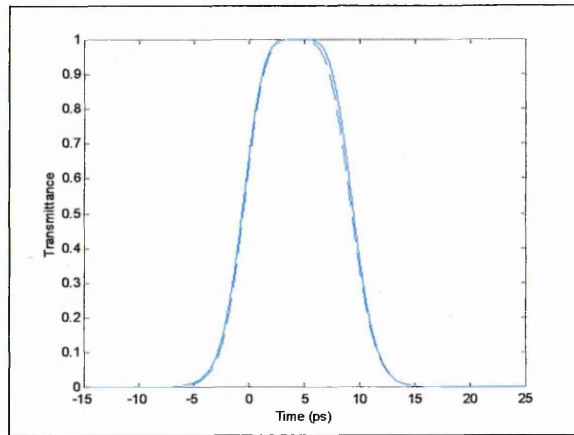
(e)



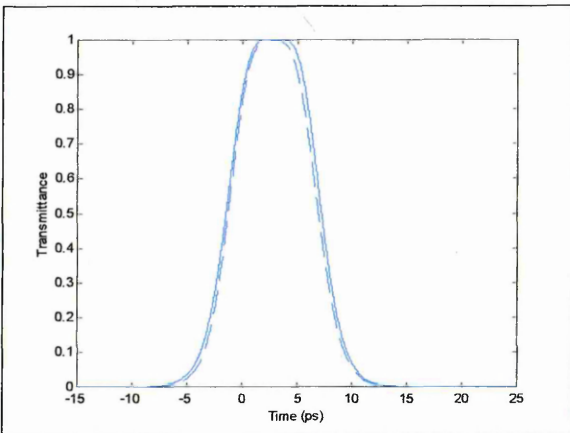
(f)



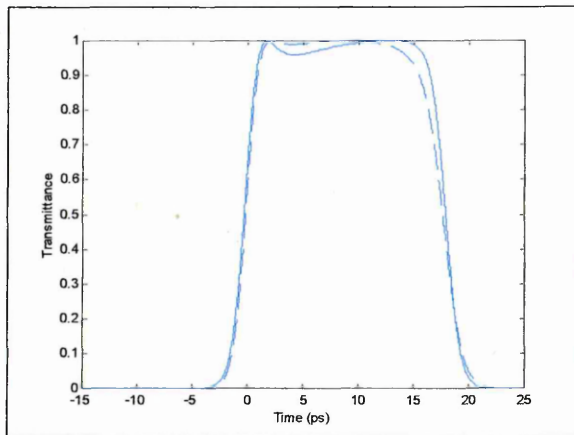
(g)



(h)



(i)



(j)

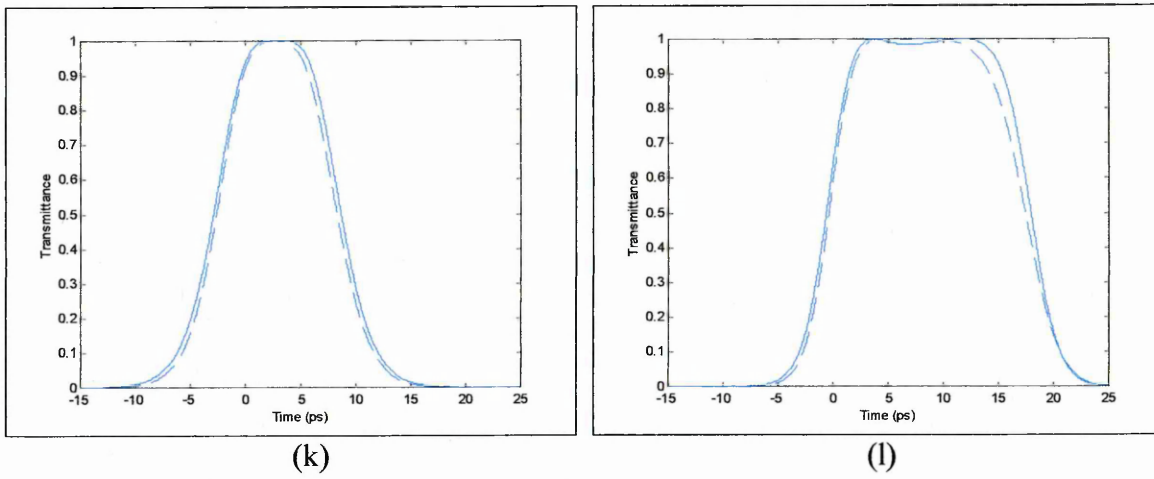


Fig. 5.13 Verification of (5.34).

5.5 Summary

A new mathematical model for optimising and simulating the demultiplexing operations of NOLM demultiplexer has been presented. By using this model, device parameters of NOLM demultiplexer can be optimised for maximising the peak transmittance of the NOLM switching window. This model can also be employed to calculate the window width and window profile of NOLM demultiplexing. The simulation results obtained by this model were compared with those calculated from solving NSE with BPM. According to the verification, the simulation results from the proposed computer model agree with those from BPM for fibre loss up to 0.2 dB/km.

CHAPTER SIX - NOISE AND CROSSTALK ANALYSIS FOR THE NONLINEAR OPTICAL LOOP MIRROR DEMULTIPLEXER

6.1 Introduction

An analysis of noise and crosstalk characteristics of NOLM demultiplexer is presented in this chapter. The noise and crosstalk model used in the analysis was partly derived from the mathematical models reported in Refs. 65 and 111. The input parameters of the noise and crosstalk model are obtained from the simulation results of the NOLM model described in Chapter 5. The organisation of this chapter is as follows. The origins of the noise and crosstalk associated with the NOLM demultiplexer are described in Section 6.2. The simulation results of the noise and crosstalk model are presented and analysed in Section 6.3.

6.2 Noise and Crosstalk in NOLM demultiplexing

6.2.1 Relating intensity noise

A major problem of high-speed long haul soliton transmission systems is the timing jitter of soliton pulses. The timing jitter could be introduced by the optical transmitter [19], optical amplifier [53], and soliton interaction [134]. Figure 6.1 shows a typical NOLM switching window and signal pulses with timing jitter. Ideally the target signal pulse should appear at the middle of the switching window, however, as it can be seen from Fig. 6.1, the signal pulses do not always arrive at the centre of the switching window. The arrival time of the jittered signal pulses can be statistically described by a Gaussian function, with a root-mean-square timing jitter RMS_{jitter} in the unit of picosecond. Because of the non-square shape of the switching window (see Fig. 6.1), the intensity profile of the demultiplexed signal pulse is varied according to the temporal location of the target pulse. The energy of the demultiplexed pulse is at maximum when the target pulse is located at

the centre of the switching window. Since the temporal position of the target pulses has the characteristics of Gaussian noise, the timing jitter noise associated with the target pulses is transformed to the intensity noise through the switching window. The intensity fluctuation of the demultiplexed pulses depends on the shape of the NOLM switching profile. One of the reasons for employing soliton control pulse is to attain a relatively flat-top switching profile in order to reduce the NOLM intensity noise caused by the timing jitter.

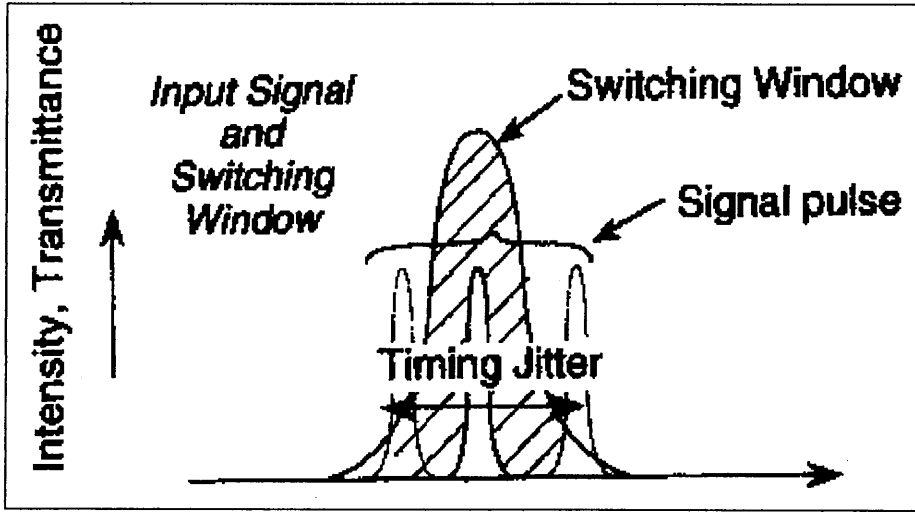


Fig. 6.1. The transformation from timing jitter noise to relative intensity noise.

Assuming the mean arrival time of the target signal pulses is at the centre of the NOLM switching profile, the mathematical function for calculating the relative intensity noise induced by the timing jitter of the signal pulses is given as [65]:

$$RIN_{NOLM} = \frac{\int_{-\infty}^{\infty} w^2(t) \cdot p(t) dt - \left[\int_{-\infty}^{\infty} w(t) \cdot p(t) dt \right]^2}{\left[\int_{-\infty}^{\infty} w(t) \cdot p(t) dt \right]^2}, \quad (6.1)$$

where $w(t) = \int_{-\infty}^{\infty} T_x(t') \cdot S(t'-t) dt'$, $p(t)$ is the probability distribution of the arrival time of signal pulse versus NOLM switching profile, $T_x(t')$ is the NOLM switching profile, and $S(t')$ is the normalised power profile of the target pulses. $p(t)$ is a Gaussian distribution with a root-mean-square timing jitters RMS_{jitter} . The mean arrival time of the signal pulse is

located at the central point of FWHM NOLM switching profile (i.e. the central pulse in Fig. 6.1). On the right side of (6.1), the numerator represents the variance of the demultiplexed energy of the target pulses, and the denominator represents the square of the mean demultiplexed energy of the target pulses. $T_x(t')$ can be obtained from the switching profile equation (5.34).

6.2.2 NOLM residual crosstalk

The counter-clockwise pulses in Fig. 5.1 encounter a large number of clockwise control pulses during the propagation of a whole fibre loop, as shown in Fig. 6.2. Although the CCW signal pulses do not co-propagate with the control pulses, they still experience a small amount of XPM because of the large number of control pulses they meet during the propagation. The residual XPM experienced by the CCW pulses will manipulate itself to become residual crosstalk.

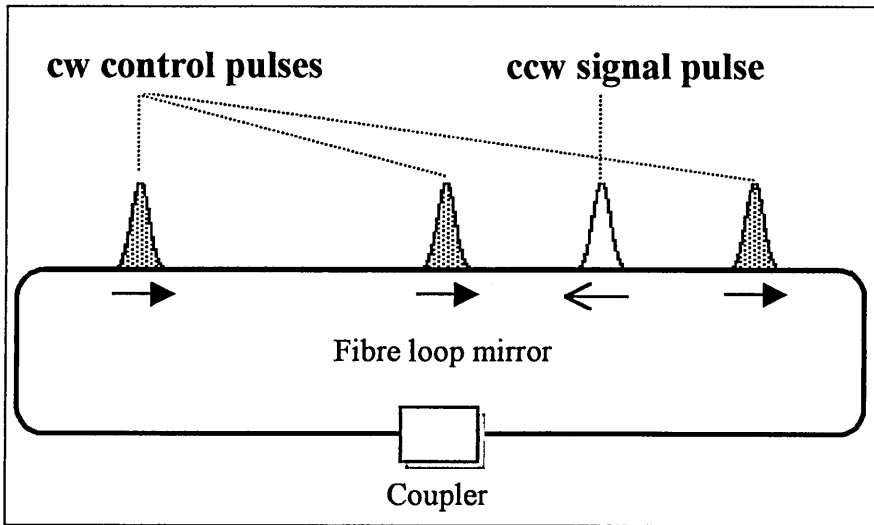


Fig. 6.2. NOLM residual crosstalk.

Assuming the peak transmittance of the NOLM switching window to be optimised by (5.13) or (5.17), the NOLM residual crosstalk can be heuristically represented by the following equation:

$$RXT_{NOLM} = \frac{M_{TDM} - 1}{2} \cdot \frac{1 - \cos^2\left(\frac{\Delta\phi_{CCW}}{2}\right)}{1 - \cos^2\left(\frac{(\pi - \Delta\phi_{CCW})}{2}\right)}, \quad (6.2)$$

where M_{TDM} is the total number of OTDM channels, and $\Delta\phi_{CCW}$ is the phase-change of CCW signal pulses due to the residual XPM. The number of non-target channels ($M_{TDM} - 1$) is divided by two for assuming that the both mark and space in the signal pulses have equal probabilities of occurrence. The numerator and denominator of the rightmost term in (6.2) represent the residual transmittance of a non-target channel and the peak transmittance of the target channel, respectively. The peak transmittance of the target channel is not exactly equal to π , because residual phase-change has not been considered in the derivation of the maximised peak transmittance equations ((5.13) and (5.17)) in Chapter 5.

Equation 6.2 can be simplified using the trigonometric theorem, which is given as:

$$RXT_{NOLM} = \frac{M_{TDM} - 1}{2} \cdot \tan^2\left(\frac{\Delta\phi_{CCW}}{2}\right). \quad (6.3)$$

The XPM-induced phase-change of the CCW pulses for a single encounter of counter-propagating control pulse $\Delta\phi_{CCW-one}$ is given as [111]:

$$\Delta\phi_{CCW-one} = \frac{\gamma \cdot E_c \cdot c}{n}, \quad (6.4)$$

where γ is the nonlinear fibre coefficient, E_c is the control pulse energy, c is the speed of light in vacuum, and n is the effective index of the fibre core. Since the number of control pulses met by a CCW signal pulse is $2nLf_c/c$, where f_c is the repetitive rate of the control pulse, and L is the fibre length [111]. The total phase-change experienced by a CCW signal pulse is given as:

$$\Delta\phi_{CCW} = 2 \cdot \gamma \cdot E_c \cdot L \cdot f_c. \quad (6.5)$$

Because of the fibre loss, the control pulse energy E_c decreases as the propagation distance increases. The control pulse energy experienced by a CCW signal pulse depends on the spatial position of the fibre loop where the control pulse and the CCW pulse meet. To take into account the fibre loss, E_c in (6.5) should be replaced by average control pulse energy over the fibre length. The modified expression is given as:

$$\Delta\phi_{CCW} = \frac{2 \cdot \gamma \cdot E_c \cdot f_c \cdot (1 - \exp(-\alpha L))}{\alpha}, \quad (6.6)$$

where α is the fibre loss.

The energy of a soliton control pulse is the integral of the soliton power profile (5.10) and is given as:

$$E_c = 1.134 \cdot P_o \cdot T_{FWHM}, \quad (6.7)$$

where P_o is the soliton peak power, and T_{FWHM} is the FWHM soliton pulse width.

Equation 6.6 is substituted with (6.7) and becomes:

$$\Delta\phi_{CCW} = \frac{2.268 \cdot \gamma \cdot f_c \cdot P_o \cdot T_{FWHM} \cdot (1 - \exp(-\alpha L))}{\alpha}. \quad (6.8)$$

The number of variables in (6.8) can be reduced by replacing P_o with the soliton peak power equation (3.23). The result is:

$$\Delta\phi_{CCW} = \frac{7.052 \cdot f_c \cdot |\beta_2| \cdot (1 - \exp(-\alpha L))}{T_{FWHM} \cdot \alpha}, \quad (6.9)$$

where β_2 is the first order dispersion coefficient.

The NOLM residual crosstalk can be calculated by substituting (6.9) into (6.3), which is given as:

$$RXT_{NOLM} = \frac{M_{TDM} - 1}{2} \cdot \tan^2 \left[\frac{3.526 \cdot f_c \cdot |\beta_2| \cdot (1 - \exp(-\alpha L))}{T_{FWHM} \cdot \alpha} \right]. \quad (6.10)$$

Equation 6.10 is used to calculate NOLM residual crosstalk in Section 6.3.2.

6.2.3 Neighbour channel crosstalk

Neighbour channel crosstalk (NXT_{NOLM}) is due to demultiplexing of adjacent non-target channels appearing at the output port of the NOLM, which can be represented mathematically as:

$$NXT_{NOLM} = \frac{\int_{-T_b/2}^{T_b/2} T_x(t) \cdot S(t + T_b) dt + \int_{-T_b/2}^{T_b/2} T_x(t) \cdot S(t - T_b) dt}{2 \cdot \int_{-T_b/2}^{T_b/2} T_x(t) \cdot S(t) dt}, \quad (6.11)$$

where T_b is the duration of an OTDM time slot. In (6.11), the signal pulse profile $S(t)$ is located at the centre of the FWHM NOLM switching profile. The factor 2 in the denominator assumes that the probabilities of occurrence for mark and space are the same.

6.3 Crosstalk and Noise Analysis

Simulation results from the mathematical models presented in Chapter 5 and Section 6.2 are presented analysed in this section. The device parameters of the NOLM switching profile used in the crosstalk and noise analysis is optimised using (5.17) for maximising the peak transmittance of the soliton switching window. The switching profile equation (5.34) of the NOLM model is used for evaluating the switching profile. The fibre loss and nonlinearity used are 0.2 dB and $2 \text{ W}^{-1}\text{km}^{-1}$, respectively. It has been shown in Section 5.4 that the accuracy of (5.17) is adequate for fibre loss up to 0.2 dB.

In the analysis, the signal pulse is assumed to be in soliton shape. The normalised signal pulse profile rather than actual power profile is used for the calculations, as the noise and crosstalk described in Section 6.2 do not depend on the signal power. The analyses for relative intensity noise, residual crosstalk and neighbour channel crosstalk are presented in Sections 6.3.1, 6.3.2 and 6.3.3, respectively. The tradeoffs between the noise and crosstalk are discussed in Section 6.3.4.

6.3.1 Simulation results of NOLM relative intensity noise

Optimised values of the control pulse width T_{FWHM} and the total walkoff time are substituted into (5.34) for calculating NOLM switching profiles. The NOLM switching profiles are then substituted into (6.1) for calculating NOLM relative intensity noise. The results obtained are shown as follows.

Figure 6.3a shows the NOLM relative intensity noise versus the total walkoff time for $\beta_2 = -20 \text{ ps}^2/\text{km}$, $-10 \text{ ps}^2/\text{km}$ and $-5 \text{ ps}^2/\text{km}$. The other simulation parameters are FWHM signal pulse width = 1 ps, $RMS_{jitter} = 1 \text{ ps}$, and fibre length $L = 3 \text{ km}$. As can be seen from Fig. 6.3a, RIN_{NOLM} for $\beta_2 = -20 \text{ ps}^2/\text{km}$ is almost independent of the total walk-off time. The dependence of RIN_{NOLM} on the walk-off time increases as $|\beta_2|$ decreases. For $\beta_2 = -5 \text{ ps}^2/\text{km}$, RIN_{NOLM} decreases from -20 dB to -25.5 dB as the total walk-off time increases from 1 ps to 9 ps. This is due to the widening of the switching window by increasing the walk-off time. The RIN_{NOLM} curve for $\beta_2 = -10 \text{ ps}^2/\text{km}$ displays similar characteristics, but with a smaller scale of variation in RIN_{NOLM} . The two curves of RIN_{TOAD} for $\beta_2 = -10 \text{ ps}^2/\text{km}$ and $-5 \text{ ps}^2/\text{km}$ show a threshold walk-off time (9 ps), beyond which the RIN_{NOLM} stops decreasing and remains at a steady value (-25.7 dB) for the further increase of walk-off time. The NOLM relative intensity noise is insensitive to the total walk-off time after the walk-off threshold. The NOLM relative intensity noise for $\beta_2 = -20 \text{ ps}^2/\text{km}$ has similar threshold characteristics, but its scale of variation in RIN_{NOLM} is too small to be visible in Fig. 6.3a.

Figure 6.3b shows the RIN_{NOLM} versus the total walk-off time for the same parameters as Fig.6.3a except that $L = 6 \text{ km}$. The RIN_{NOLM} curves in Fig. 6.3b display a walk-off threshold characteristic similar to the one in Fig. 6.3a. The walk-off threshold for both figures is the same (i.e. 9 ps). For $\beta_2 = -5 \text{ ps}^2/\text{km}$ ($-10 \text{ ps}^2/\text{km}$) and total walk-off time = 1

ps, increasing the length of the fibre loop from 3 km to 6 km can reduce RIN_{NOLM} by 4 dB (1.5 dB). The influence of fibre length on RIN_{NOLM} decreases as the total walk-off time increases. The NOLM relative intensity noise is insensitive to the fibre length for the total-off time $>$ the walk-off threshold.

Figures 6.3c and 6.3d plot the RIN_{NOLM} versus the total walk-off time using the same parameters as Figs. 6.3a and 6.3b, respectively, except that RMS_{jitter} is 3 ps instead of 1 ps. The NOLM relative intensity noise in Figs. 6.3c and 6.3d is larger than those in Figs. 6.3a and 6.3b because of the larger root-mean-square jitter of the signal pulses. The threshold characteristic of the total walk-off time can also be observed in Figs. 6.3c and 6.3d. By increasing RMS_{jitter} , the walk-off threshold is increased from 9 ps in Figs. 6.3a and 6.3b to 20 ps in Figs. 6.3c and 6.3d. The value of RIN_{NOLM} after the walk-off threshold is the same (i.e. -25.7 dB) for Figs. 6.3a – 6.3d.

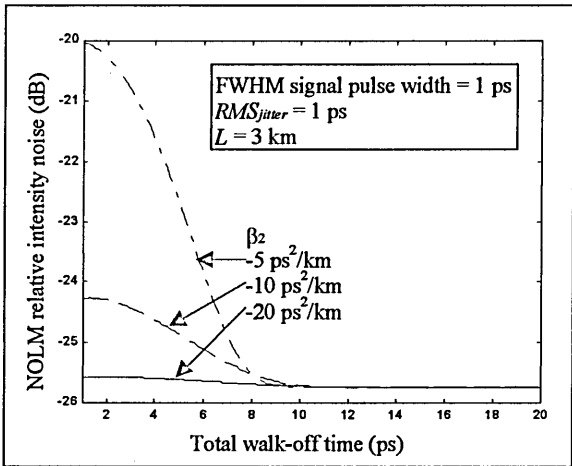


Fig. 6.3 a

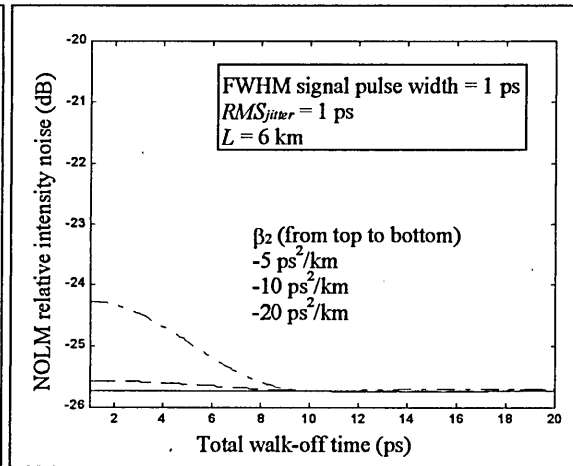


Fig. 6.3 b

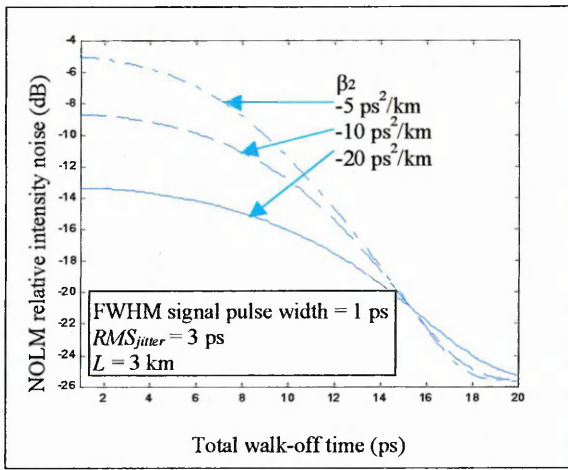


Fig. 6.3 c

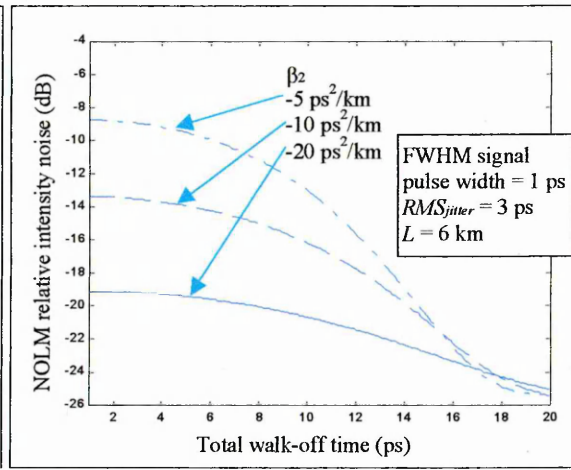
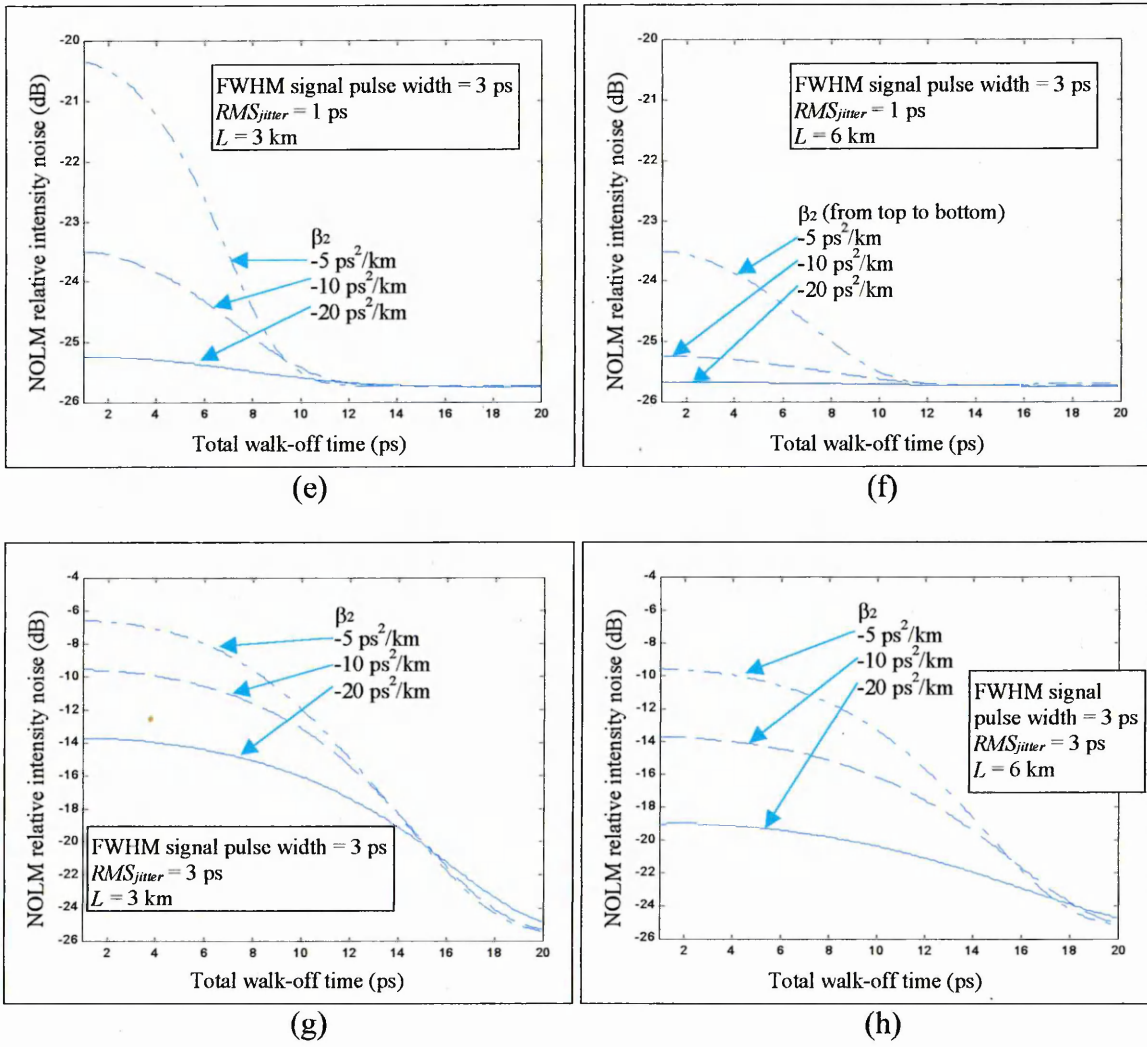


Fig. 6.3 d

Figs. 6.3a – 6.3d. NOLM relative intensity noise Vs. the total walk-off time for FWHM signal pulse with = 1 ps.

For high capacity OTDM systems, it is important to investigate how the duty cycle of optical pulses affects the noise performance of all-optical demultiplexers. Decreasing the duty cycle of the OTDM signal is intuitively believed to result in an improvement of bit-error-rate performance. This is due to the smaller neighbour channel crosstalk in narrower signal pulses. Figures 6.3e - 6.3h show RIN_{NOLM} versus the total walk-off time using the same parameters as Figs. 6.3a - 6.3d, respectively, except that FWHM signal pulse width is 3 ps. The profiles shown in Figs. 6.3a - 6.3d are very similar to those in Figs. 6.3e - 6.3h except for a slight increase of the walk-off threshold for FWHM signal pulse width = 3 ps in Figs. 6.3e and 6.3f. The differences of noise performance between various duty cycles are so tiny that they hardly have any noticeable effect on the power penalty of the demultiplexer.



Figs. 6.3e-6.3h. NOLM relative intensity noise Vs. the total walk-off time for FWHM signal pulse width = 3 ps.

6.3.2 Simulation results of NOLM residual crosstalk

For calculating the NOLM residual crosstalk, device parameters optimised by (5.17) are substituted into (6.10). The simulation results are given in this subsection. Figure 6.4a plots the NOLM residual crosstalk versus the total walk-off time for total bit rate = 100 Gb/s, $L = 3 \text{ km}$, $M_{TDM} = 10$, and different values of β_2 . In all cases, the NOLM residual crosstalk increases with total walk-off time. In NOLM demultiplexing, for compensating the loss of XPM due to an increase of the total walk-off time, the control pulse requires more power in order to maintain 100% peak transmittance of the switching window (see Chapter 5). The increase in control power leads to a larger $\Delta\phi_{CCW}$ in (6.3), thus increasing the residual

crosstalk. Also shown in Fig. 6.4a, the NOLM residual crosstalk increases with $|\beta_2|$ for small values of walk-off time. RXT_{NOLM} is less dependent on β_2 when the total walk-off time increases. The residual crosstalk is completely independent of β_2 for the total walk-off time > 14 ps. For evaluating the effect of fibre length on the NOLM residual crosstalk, Fig. 6.4b plots RXT_{NOLM} versus the total walk-off time using the same simulation parameters as in Fig. 6.4a except for $L = 6$ km. It can be observed from Figs. 6.4a and 6.4b that, for total walk-off time = 1 ps, increasing the length of the fibre loop from 3 km to 6 km will increase the residual crosstalk by 3 dB. RXT_{NOLM} becomes less dependent on L when the total walk-off time increases.

The total number of OTDM channels for Figs. 6.4a and 6.4b is 10. For total bit rate of 100 Gb/s, it amounts to 10 Gb/s per OTDM channel. Figures 6.4c and 6.4d shows the simulation results using the same parameters as Figures 6.4a and 6.4b, respectively, except for $M_{TDM} = 100$, which represents 1 Gb/s per OTDM channel. The RXT_{NOLM} curve in Fig. 6.4c (Fig. 6.4d) is downshifted approximately 10 dB against the RXT_{NOLM} curve in Fig. 6.4a (Fig. 6.4b). For any given total bit rate, the crosstalk performance can be significantly improved by increasing the number of OTDM channels. Figures 6.4e and 6.4f show the simulations results for total bit rate of 200 Gb/s. The numbers of OTDM channels used are 20 and 200, respectively. The fiber length for both figures is 3 km. As expected, the NOLM residual crosstalk increases with the total bit rate. Comparing Fig. 6.4e (Fig. 6.4f) with Fig. 6.4a (Fig. 6.4c), it can be observed that the NOLM residual crosstalk increases by 3 dB as the total bit rate increases from 100 Gb/s to 200 Gb/s.

6.3.3 Simulation results of neighbour channel crosstalk

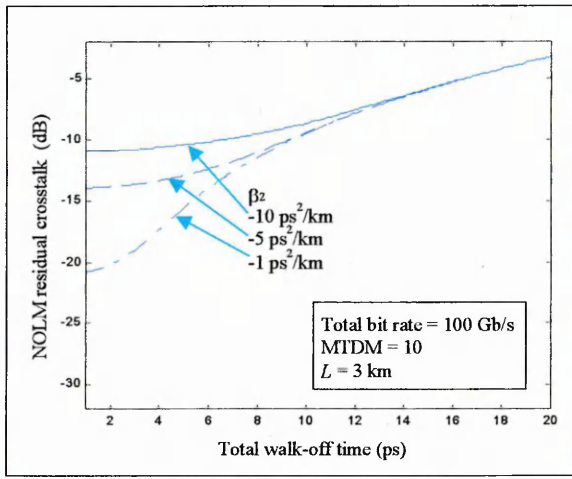
Device parameters optimised from (5.17) for 100% peak transmittance are substituted into (6.11) for calculating the neighbour channel crosstalk. The neighbour channel crosstalk depends on the duty cycle of the incoming OTDM data stream. Here, the duty cycle is defined as the ratio between the FWHM width of the data pulses and the OTDM time slot. For example, for 100 Gbps data rate, the duty cycle is equal to 0.1 if the FWHM width of signal pulse is 1 ps. The values of the duty cycle used in this subsection are 15% and 30%.

Figure 6.5a plots NOLM neighbour channel crosstalk versus the total walk-off time for aggregate bit rate = 100 Gb/s, $L = 3$ km, duty cycle = 15%, and different values of β_2 . All curves have a walk-off threshold, below which NXT_{NOLM} is independent of the total walk-off time, and above which NXT_{NOLM} increases with the total walk-off time. The increase of NXT_{NOLM} with the total walk-off time is due to the widening of NOLM switching window as a result of the increased walk-off time. NXT_{NOLM} is insensitive to the total walk-off time below the threshold level. It is also shown in Fig. 6.5a that the walk-off threshold increases with $|\beta_2|$. Since the neighbour channel crosstalk is sensitive to the window width, the characteristics of NXT_{NOLM} in Fig. 6.5a bear much similarity with the characteristics of window width in Figs. 5.7-5.9. Also shown in Fig. 6.5a, for total walk-off time of 1 ps, NXT_{NOLM} of $\beta_2 = -10$ ps²/km is 60 dB larger than that of $\beta_2 = -1$ ps²/km. The crosstalk differences among various β_2 decrease as the total walk-off time increases. The NOLM neighbour channel crosstalk becomes independent of β_2 for total walk-off time > 19 ps.

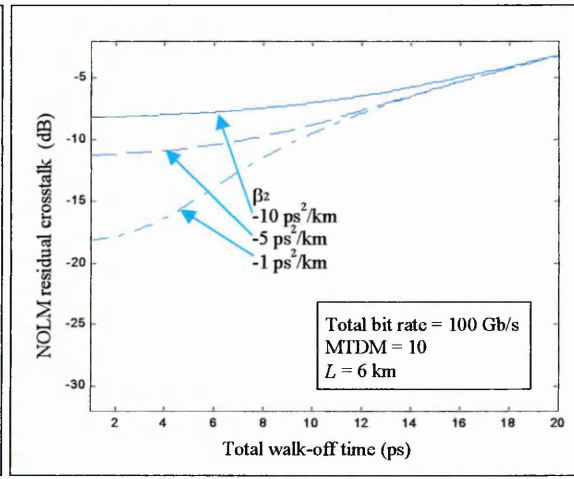
For evaluating the effect of fibre length on NOLM neighbour channel crosstalk, Fig. 6.5b plots NXT_{NOLM} versus total walk-off time using the same simulation parameters as in Fig. 6.5a except that $L = 6$ km. For small walk-off time, increasing the length of fibre loop will increase the neighbour channel crosstalk. Comparing Fig. 6.5a ($L = 3$ km) with Fig. 6.5b (L

= 6 km), at walk-off time = 1 ps, using a shorter fibre loop could reduce NXT_{NOLM} by 17 dB, 16 dB and 10 dB for $\beta_2 = -1$ ps²/km, -5 ps²/km and -10 ps²/km, respectively. The L dependence of NXT_{NOLM} decreases as total walk-off time increases, as shown in Figs. 6.5a and 6.5b.

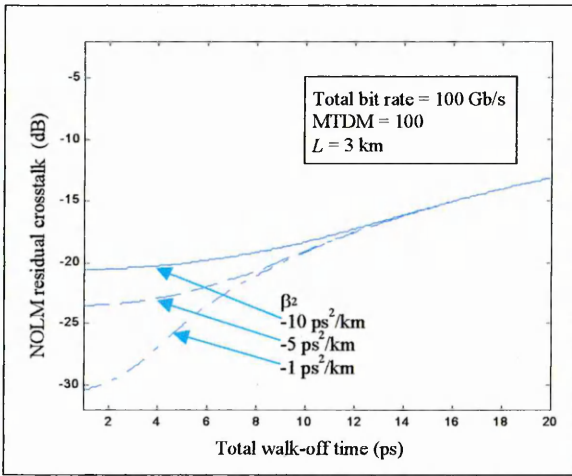
Figures 6.5c and 6.5d show the simulation results for the same parameters as Figures 6.5a and 6.5b, respectively, except that duty cycle = 30%, which corresponds to 3 ps FWHM signal pulse width. Comparing Fig. 6.5a (Fig. 6.5b) with Fig. 6.5c (Fig. 6.5d), increase duty cycle will increase NXT_{NOLM} . More energy of adjacent non-target signal pulses will be demultiplexed because of the wider pulse width in larger duty cycle. At total walk-off time = 1 ps, the differences of NXT_{NOLM} between the two duty cycles (15% and 30%) are 40 dB and 3 dB for $\beta_2 = -1$ ps²/km and -10 ps²/km, respectively. NXT_{NOLM} of the smaller $|\beta_2|$ appears to be much more sensitive to the duty cycle because of its smaller base value (-82 dB for the above parameters). Figures 6.5e and 6.5f show the simulations results of aggregate bit rate = 200 Gb/s. The other simulation parameters of Figs. 6.5e and 6.5f are the same as those of Figs. 6.5a and 6.5c respectively. Comparing Fig. 6.5a (Fig. 6.5c) and Fig. 6.5e (Fig. 6.5f), the NOLM neighbour channel crosstalk at bit rate 200 Gb/s is much higher than that at bit rate 100 Gb/s. In 200 Gb/s NOLM demultiplexing, the neighbour channel crosstalk for large walk-off time saturates at 0 dB, which indicates the same demultiplexed energy for both target and non-target pulses.



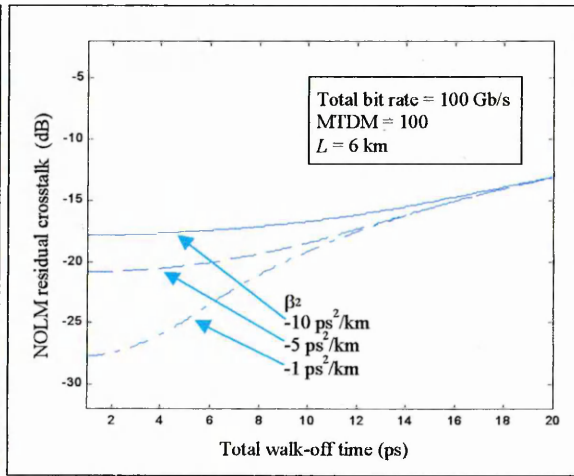
(a)



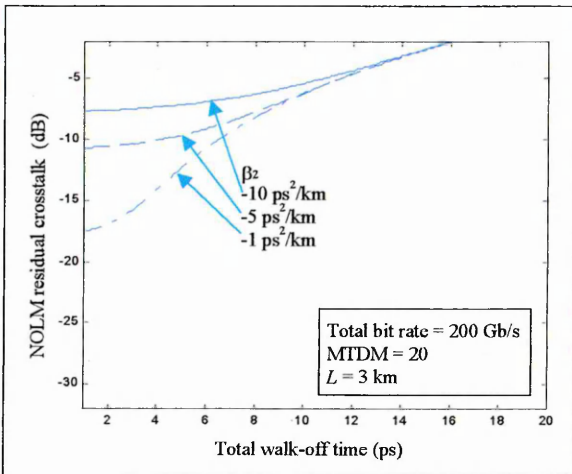
(b)



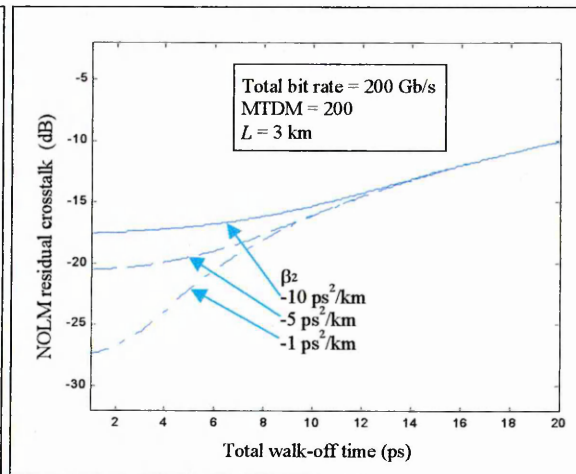
(c)



(d)

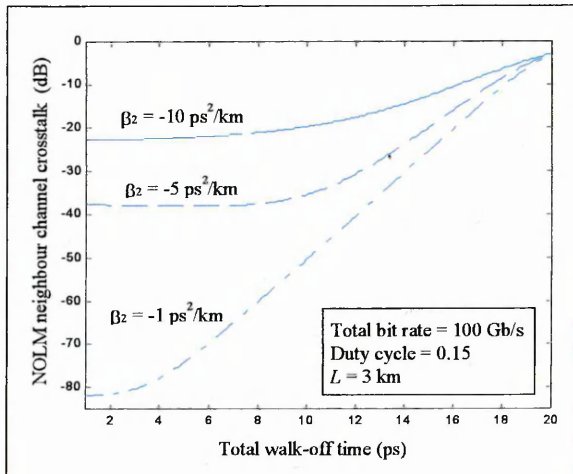


(e)

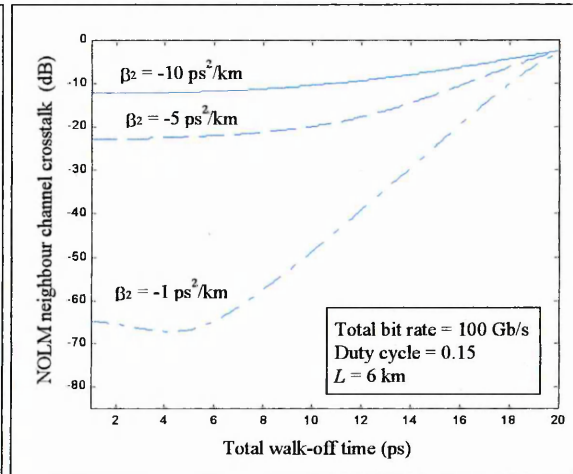


(f)

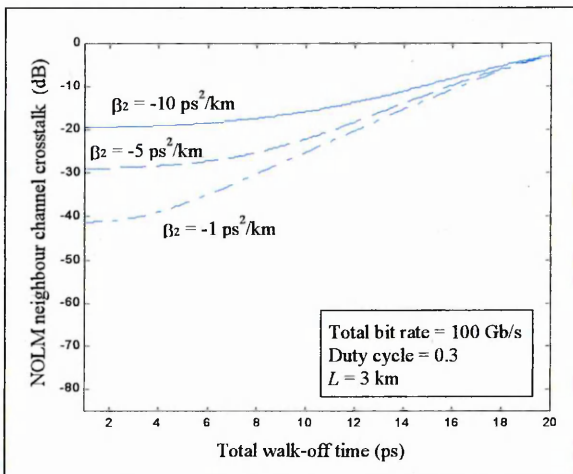
Fig. 6.4. NOLM residual crosstalk Vs. the total walk-off time.



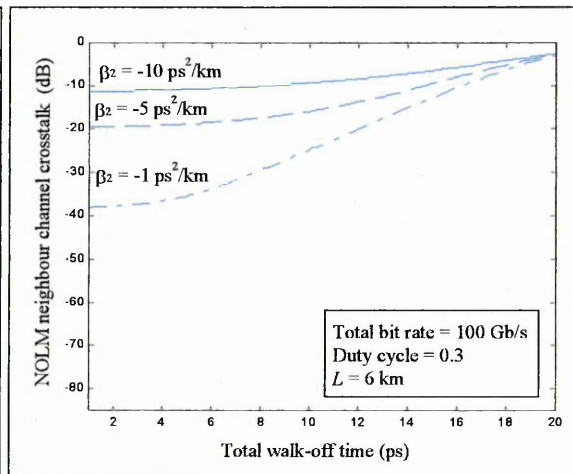
(a)



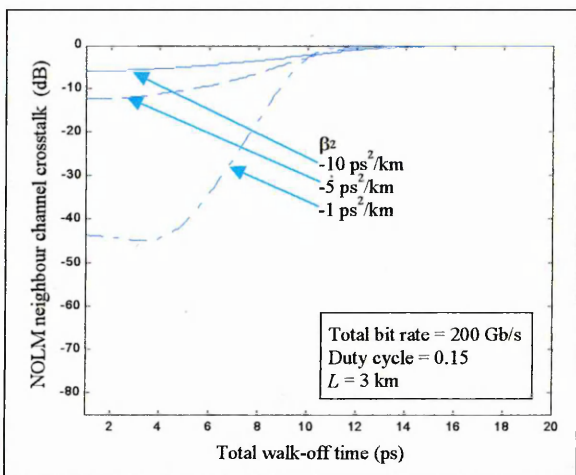
(b)



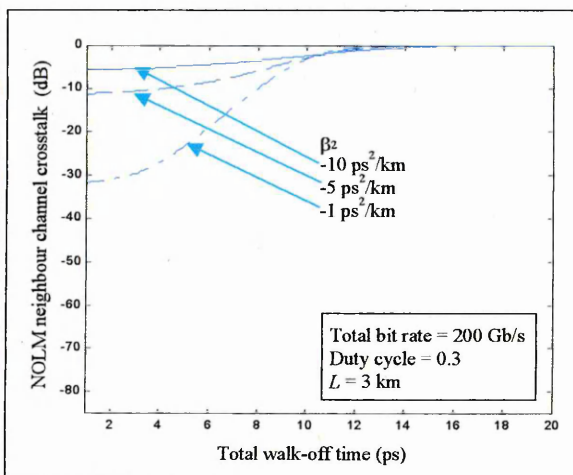
(c)



(d)



(e)



(f)

Fig. 6.5. NOLM neighbour channel crosstalk Vs. the total walk-off time.

6.3.4 Tradeoff between noise and crosstalk in NOLM demultiplexing

According to the simulation results presented in Sections 6.3.1 - 6.3.3, Table 6.1 sums up the tradeoff between noise and crosstalk in NOLM demultiplexing.

			RIN_{NOLM}	RXT_{NOLM}	NXT_{NOLM}
NOLM parameters:	$ \beta_2 $	↑ \implies	↓	↑	↑
	L	↑ \implies	↓	↑	↑
	Total walk-off	↑ \implies	↓	↑	↑
Data stream parameters:	RMS_{jitter}	↑ \implies	↑	Independent	Independent
	M_{TDM}	↑ \implies	Independent	↓	Independent
	Duty cycle	↑ \implies	Independent	Independent	↑
	Aggregate bit rate	↑ \implies	Independent	↑	↑

Table 6.1 shows that RXT_{NOLM} and NXT_{NOLM} increases/decreases with the same set of parameters. Device parameters could be optimised to minimise both RXT_{NOLM} and NXT_{NOLM} . However, Table 6.1 also shows that the variation of RIN_{NOLM} against the system parameters is in the opposite way to that of the NOLM crosstalk. Therefore, in NOLM demultiplexing, noise decreases at the expense of the increase in crosstalk and vice versa. There is a tradeoff between noise and crosstalk of NOLM demultiplexer.

Figure 6.6 plots the noise and crosstalk of NOLM demultiplexing versus total walk-off time. The NOLM and data stream parameters for the simulation are $\beta_2 = -3 \text{ ps}^2/\text{km}$, $L = 3 \text{ km}$, $RMS_{jitter} = 1 \text{ ps}$, $M_{TDM} = 100$, duty cycle = 0.1, aggregate bit rate = 100 Gb/s. Using the above parameters, RXT_{NOLM} is dominant over NXT_{NOLM} for the total walk-off time < 17 ps. RIN_{NOLM} in Fig. 6.6 drops from -16 dB to its lowest value (-25.7 dB) as walk-off time increases from 1 ps to 8 ps, and remains at its lowest value for walk-off time > 8 ps. On the other hand, RXT_{NOLM} steadily increases with total walk-off time. Figure 6.6 vindicates the general trend that the NOLM crosstalk increases with walk-off time and RIN_{NOLM} decreases with walk-off time. It can also be observed in Fig. 6.6 that, for walk-off time > 8 ps, an increase of walk-off time increases the NOLM crosstalk but does not affect RIN_{NOLM} . In

other words, a further increase of walk-off time beyond 8 ps will deteriorate the NOLM crosstalk without the benefit of the decrease of RIN_{NOLM} . It is obvious that, given the above device parameters, the walk-off time of NOLM demultiplexing should be less than 8 ps for avoiding excess RXT_{NOLM} and NXT_{NOLM} . Nevertheless, it is difficult to estimate the exact optimised value of walk-off time from the curves in Fig. 6.6 because the weighting of RXT_{NOLM} , RIN_{NOLM} and NXT_{NOLM} for the power penalty of NOLM demultiplexing is not known. A complete configuration of a receiver system must be considered in order to optimise the NOLM parameters for minimising power penalty. The optimisation of system parameters for NOLM demultiplexing will be presented in Chapter 8. It should be noted that walk-off time is not the only parameter to be optimised. Some of the parameters listed in Table 6.1 will also be considered in the optimisation.

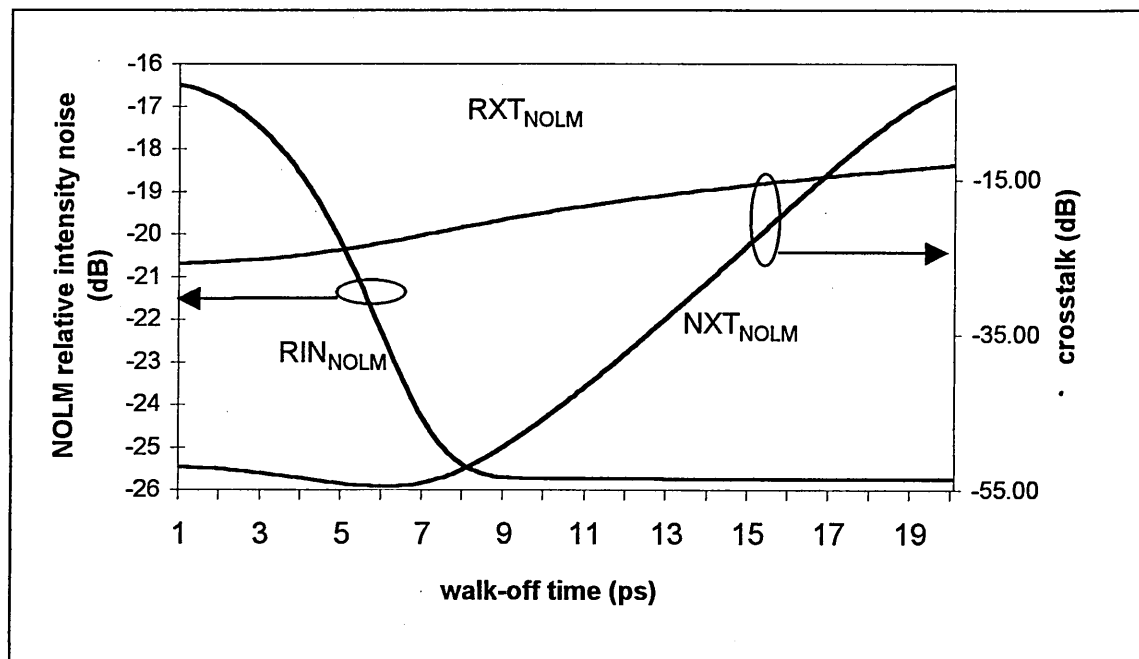


Fig. 6.6. Tradeoff between noise and crosstalk ($\beta_2 = -3 \text{ ps}^2/\text{km}$, $L = 3 \text{ km}$, $RMS_{jitter} = 1 \text{ ps}$, $M_{TDM} = 100$, duty cycle = 15%, aggregate bit rate = 100 Gb/s).

6.4 Summary

A noise and crosstalk model developed by the author has been presented in this chapter: A noise and crosstalk analysis has been carried out using the noise and crosstalk model and the NOLM model presented in Chapter 5. The noise and crosstalk associated in a NOLM demultiplexer are NOLM relative intensity noise, NOLM residual crosstalk and NOLM neighbour channel crosstalk. Simulation results show that there is a tradeoff between noise and crosstalk in NOLM demultiplexing.

CHAPTER SEVEN - NOISE AND CROSSTALK ANALYSIS OF THE TERAHERTZ OPTICAL ASYMMETRIC DEMULTIPLEXER USING A COMPUTER MODEL

7.1 Introduction

Employing semiconductor laser amplifier as a nonlinear element within a fibre loop is a principle configuration for various types of all-optical devices [135]-[148]. One of the all-optical devices using this configuration is terahertz optical asymmetric demultiplexer, which was first proposed by J. P. Sokoloff, *et-al* [17]. This chapter is dedicated to the noise and crosstalk analysis of TOAD demultiplexing using a new computer model developed by the author.

The structure of this chapter is as follows. The operation principles of TOAD are elucidated in Section 7.2. A new computer model for TOAD demultiplexing is presented in Section 7.3. This model aims at evaluating the TOAD switching window from device parameters of TOAD and optimising the switching energy for maximising the peak of TOAD window. In Section 7.4, the simulation results from the model will be fed into a noise and crosstalk model for investigating the noise and crosstalk characteristics of TOAD demultiplexer.

7.2 Operation Principles

The block diagram of a typical TOAD is shown in Fig. 7.1. A TOAD is constructed from a short loop of optical fibre (several metres), with two ends connected to an I/O coupler. A semiconductor laser amplifier (SLA) is placed asymmetrically Δx off the mid-point of the loop. The control coupler in Fig. 7.1 provides an input path for the control pulses to enter into the fibre loop. The asymmetric position of the SLA in the fibre loop could be on the same side as the control coupler, as shown in Fig. 7.1, or on the other half of the loop.

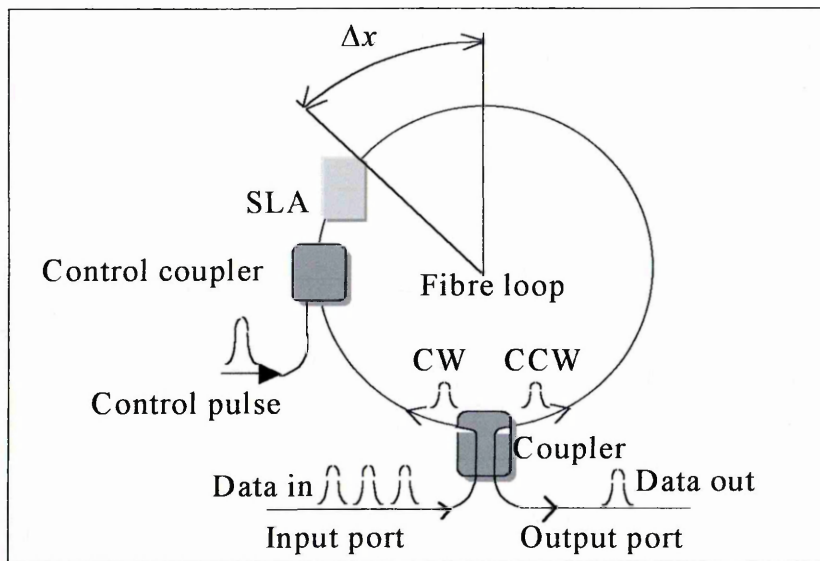


Fig. 7.1. Configuration of a typical TOAD.

The operation principles of TOAD are similar to those of NOLM demultiplexer except that the non-linear medium is the SLA instead of the fibre loop. A stream of high intensity control pulses enters the fibre loop and saturates the asymmetrically positioned SLA. The SLA gain, which is depleted by the passing of a control pulse, recovers to its unsaturated level before the arrival of the next control pulse, which will once again saturates the SLA. The SLA refractive index changes according to the periodical variation of gain dynamics due to the cross phase modulation (XPM) (see Chapter 4). As in NOLM demultiplexing, a high capacity OTDM signal is split into clockwise and counter-clockwise directions with equal intensity. The CW and CCW signal pulses pass the asymmetrically positioned SLA at different times, thus experiencing different gain and refractive index. The differences in gain and phase between the CW and CCW pulses result in the switching of an input pulse from input port to the output port, as shown in Fig. 7.1. Since the control pulse stream is synchronous with the time slot of the target channel, only the target channel will be demultiplexed to the output port.

The intensity of the signal pulses should be sufficiently low to prevent them from perturbing the carrier density of the SLA. However, in order to achieve a sufficiently large signal-to-noise ratio, high intensity signal pulses may be required in OTDM systems. It is desirable for the high intensity OTDM signals to have a wavelength outside the gain spectrum of the SLA. In this case, the demultiplexing operation is achieved solely by phase modulation, not the combination of gain and phase modulation.

7.3 TOAD Model

7.3.1 Switching window equation for TOAD

The equation for TOAD switching window is given as [147]:

$$TOAD_W(t) = \frac{1}{4} \cdot [G_{CW}(t) + G_{CCW}(t) - 2 \cdot \sqrt{G_{CW}(t) \cdot G_{CCW}(t)} \cdot \cos \Delta\phi(t)], \quad (7.1)$$

where $TOAD_W$ is the TOAD switching window, G_{CW} and G_{CCW} are the temporal gain profile of the CW and CCW pulses, respectively, and $\Delta\phi$ is the phase difference between CW and CCW pulses. Equation 7.1 assumes that the I/O coupler in Fig. 7.1 has an ideal coupling ratio of 50:50. The phase difference $\Delta\phi$ can be related to the gain ratio of CW and CCW pulses by the linewidth enhancement factor α_{LEF} [147]:

$$\frac{G_{CW}}{G_{CCW}} = \exp\left(-\frac{2 \cdot \Delta\phi}{\alpha_{LEF}}\right). \quad (7.2)$$

The phase difference obtained from (7.2) is substituted into (7.1) for the calculation of TOAD switching window.

Unlike NOLM demultiplexing, the switching ratio of TOAD window could be greater than unity. In other words, TOAD demultiplexing can provide additional gain to the target pulse. According to (7.1) and (7.2), given the linewidth enhancement factor, the TOAD switching window can be calculated from the gain profiles of the CW and CCW pulses.

The SLA model presented in the next section is used to calculate G_{CW} and G_{CCW} in (7.1) and (7.2).

7.3.2 SLA model

The SLA model presented in this chapter is modified from the one described in [88]. In Ref. 88, the confinement factor is included in the rate equations of carrier density and light intensity. However, as pointed out in Chapter 4, the confinement factor should not be included in the carrier density equation if the light intensity is used as the carrier depletion term. To remedy this error, optical power rather than light intensity is used in the rate equations of this SLA model. The rate equations for the changes of carrier and photon densities inside the active region of a SLA were given in Chapter 4 and are repeated here:

$$\frac{\partial N}{\partial t} = \frac{I_c}{q \cdot V_{SLA}} - \frac{N}{T_{sp}} - \frac{\Gamma \cdot g \cdot P^+}{A_{SLA} \cdot E_p}, \quad (7.3)$$

$$\frac{dP^+}{dz} = \Gamma \cdot g \cdot P^+, \quad (7.4)$$

where N is the carrier density, I_c is the bias current, q is the electron charge, V_{SLA} is the volume of the active region, T_{sp} is the spontaneous lifetime, A_{SLA} is the cross-sectional area of the active region, E_p is the photon energy, and P^+ is the optical power propagating in the direction of the signal waveguide. The differential gain g is given by (4.3) and repeated as below:

$$g = a \cdot (N - N_o), \quad (7.5)$$

where a is the gain coefficient, and N_o is the transparent carrier density. The differential gain in (7.5) represents the maximum level of the gain spectrum (see Chapter 4). The control and signal pulses are assumed to be in the same wavelength region where the gain spectrum is flat. Equation 7.5 represents the differential gain of the signal and control pulses.

The carrier density N and the optical power P^+ in the rate equations may vary along the length of the SLA. The rate equations are solved numerically by longitudinally breaking SLA into L_N number of segments, as shown in Fig. 7.2. The segment length is so small that N and P^+ can be approximated as spatially independent in any segment. For each segment, N and P^+ are calculated locally for a sequence of incremental time instances. For segment k at time instance t_k , N and P^+ are calculated using the following equations:

$$N(k, t_k) = N(k, t_{k-1}) + \Delta N, \quad (7.6)$$

$$P^+(k, t_k) = P^+(k-1, t_{k-1}) \cdot \exp(\Gamma \cdot g(k-1, t_{k-1}) \cdot \Delta L), \quad (7.7)$$

where

$$\Delta N = \left[\frac{I_c}{q \cdot V_{SLA}} - \frac{N(k, t_{k-1})}{T_{sp}} - \frac{\Gamma \cdot g(k, t_{k-1}) \cdot P^+(k, t_{k-1})}{A_{SLA} \cdot E_p} \right] \cdot \Delta t. \quad (7.8)$$

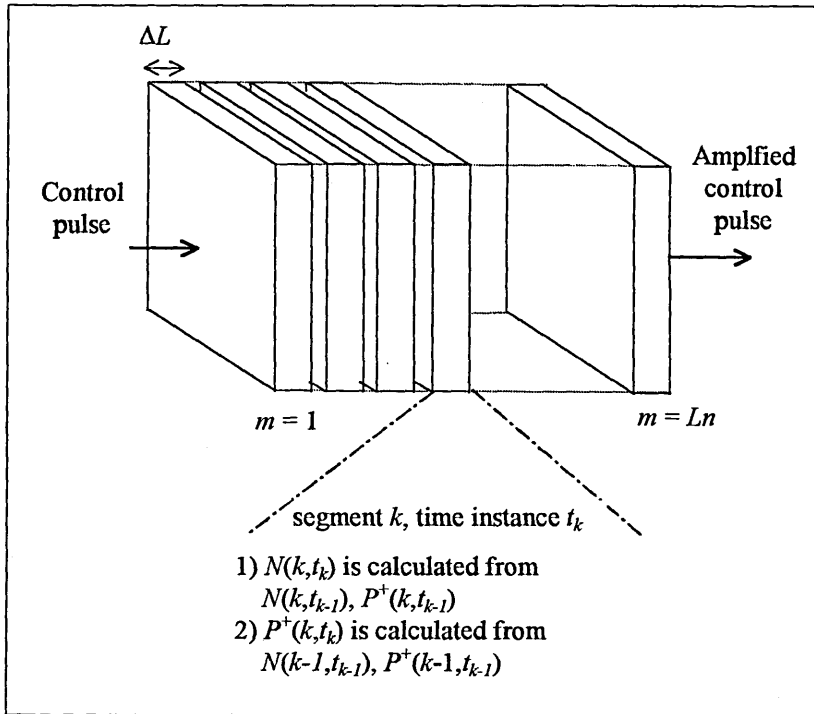


Fig. 7.2. SLA model.

Δt in (7.8) is the time increment for the numerical calculation. It is related to ΔL by $\Delta t = \Delta L / V_g$ where V_g is the group velocity of the control pulse. The rate equation of carrier

density (7.3) is a partial differential equation with time dependent variables N and P^+ . This type of equation should generally be solved by complex numerical methods [149]. In order to avoid tedious and time-consuming computation, the change of carrier density ΔN in (7.8) is treated as a time independent value. This approximation is justified if $\Delta N \ll N$. This condition is satisfied in the SLA model due to the small value of ΔL . The initial values of N can be obtained by setting the last term of (7.3) equal to zero for the equilibrium state and is given as:

$$N_i = \frac{I_c \cdot T_{sp}}{q \cdot V_{SLA}} \quad (7.9)$$

P^+ in the rate equations is zero if no control pulse enters into the SLA. A control pulse will initialise P^+ of the first segment when it enters into the SLA

Figure 7.3 is a three dimensional plot for the carrier density Vs. SLA length and time, using (7.3) and (7.4). The simulation parameters used are shown in Table 7.1. The control pulse is in Gaussian shape.

Parameters	Values
I	250 mA
V_g	$3 \times 10^8 / 3.5$
T_{sp}	100 ps
Γ	0.3
E_{ph}	0.8 eV
A	$2 \times 10^{-20} \text{ m}^2$
N_o	$1 \times 10^{24} \text{ m}^3$
A_{SLA}	$3 \times 10^{-13} \text{ m}^{-2}$
L_{SLA}	0.3 mm
total number of SLA segments	50
FWHM control pulse width	2 ps
peak power of control pulse	1 W

Each line in Fig. 7.3 represents N Vs. longitudinal position of the SLA at a particular time instance. The carrier density is independent of the longitudinal dimension of the SLA when

there is no control pulse in the SLA, as shown in the first two lines of the time axis. The carrier density at this state is given by (7.9). When the leading edge of the control pulse propagates into the first few segments of the SLA, the carrier density of those segments depletes somewhat due to the loss of excited electrons by stimulated emission. The carrier density of other segments to which the control pulse has not reached remains at the initial value. The control pulse propagates further as the time increments increase. The amplitude of control pulse power increases with the propagation distance, as indicated by (7.4). The ever-increasing optical power of control pulse depletes more excited electronics, thus decreasing the carrier density as the propagation distance and time increments increase.

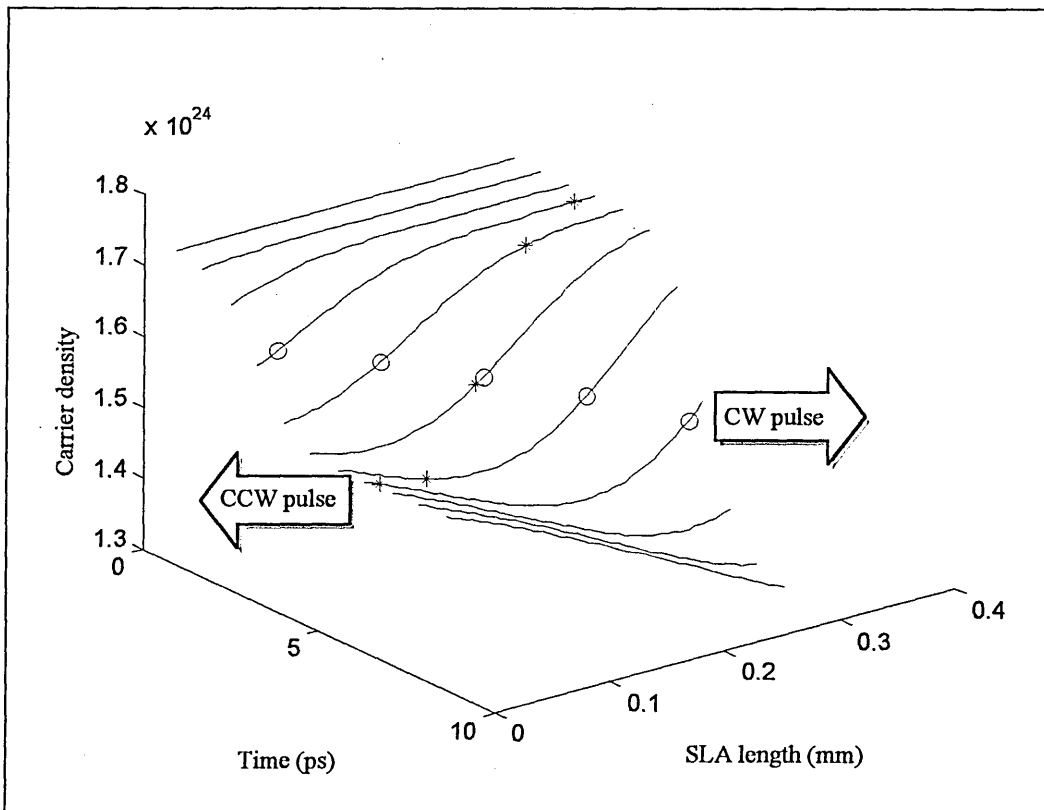


Fig. 7.3. Dynamics of carrier density inside the active region of an SLA.

The “o” symbols in Fig. 7.3 represent the carrier densities experienced by a temporal point of the CW pulse during its propagation through the SLA. The total gain of the CW pulse at that temporal point is given as:

$$G_{CW}(t) = \exp \left[\int_0^{L_{SLA}} \Gamma \cdot g \left(z, t + \frac{z}{V_g} \right) dz \right], \quad (7.10)$$

where t is the time at which the temporal point of the CW pulse enters the first segment of the SLA.

The “*” symbols in Fig. 7.3 represent the carrier densities experienced by a temporal point of the CCW pulse during its propagation through the SLA. The gain of the CCW pulse at that temporal point is given as:

$$G_{CCW}(t) = \exp \left[\int_{L_{SLA}}^0 \Gamma \cdot g \left(z, t + \frac{L_{SLA}}{V_g} - \frac{z}{V_g} \right) dz \right], \quad (7.11)$$

where t is the time at which the temporal point of the CCW pulses enters the last segment of the SLA. The CCW pulse enters the last segment first because its propagation direction is opposite to the CW pulse.

Equations 7.10 and 7.11 assume that the CW and CCW pulse reach the SLA at the same time. In other words, the SLA is assumed to be at the mid-point of the fibre loop. If the SLA is asymmetrically placed within the fibre loop, t in (7.10) and (7.11) will have different values. However, in order to substitute $G_{CW}(t)$ and $G_{CCW}(t)$ into the equation of TOAD switching window (7.1), G_{CW} and G_{CCW} need to have the same reference time. Therefore, (7.10) and (7.11) should adopt the time reference from either CW or CCW pulses. This TOAD model adopts the time reference of the CW pulse. After taking the SLA asymmetry into account, Equations 7.10 and 7.11 are transformed to the following two equations, respectively:

$$G_{CW}(t) = \exp \left[\int_0^{L_{SLA}} \Gamma \cdot g \left(z, t + \frac{z}{V_g} \right) dz \right], \quad (7.12)$$

$$G_{CCW}(t) = \exp \left[\int_{L_{SLA}}^0 \Gamma \cdot g \left(z, t + T_{asy} + \frac{L_{SLA}}{V_g} - \frac{z}{V_g} \right) dz \right], \quad (7.13)$$

where t is the time at which the temporal point of the CW pulse enters the first segment of the SLA, and T_{asy} is the asymmetric arrival time. The CW pulse reaches the SLA T_{asy} ahead of the CCW pulse. T_{asy} would be in negative value if the CCW pulse reaches the SLA first. Equations 7.12 and 7.13 assume that the control pulse is co-propagating with the CW pulse (see Fig. 7.1). Equations 7.12 and 7.13 are substituted to the switching window equations (7.1) and (7.2) for evaluating the TOAD switching profiles. The results will be shown in the next subsection.

7.3.3 TOAD switching window

Figure 7.4a shows G_{CW} and G_{CCW} Vs. time for zero asymmetry using the parameters shown in Table 7.2. The shape of the control pulse is Gaussian.

Parameters	Values
I	300 mA
V_g	$3 \times 10^8 / 3.5$
T_{sp}	100 ps
Γ	0.3
E_{ph}	0.8 eV
A	$2 \times 10^{-20} \text{ m}^2$
N_o	$1 \times 10^{24} \text{ m}^3$
A_{SLA}	$3 \times 10^{-13} \text{ m}^{-2}$
L_{SLA}	0.3 mm
α_{LEF}	4
total number of SLA segments	50
FWHM control pulse width	2 ps
peak power of control pulse	3 W
T_{asy}	0

The G_{CW} curve (solid line) in Fig. 7.4a has an initial value of 7 before the control pulse enters into the SLA. Then it drops from 7 to 1.5 by stimulated emission while the high

intensity control pulse is passing through the SLA. The fall time of G_{CW} is about 2 ps; which is equivalent to the width of the co-propagating control pulse. The G_{CCW} curve (dashed line) in Fig. 7.4a has a much slower fall time. The fall time of G_{CCW} is about (control pulse width + L_{SLA}/V_g) since it is counter-propagating against the control pulse [88].

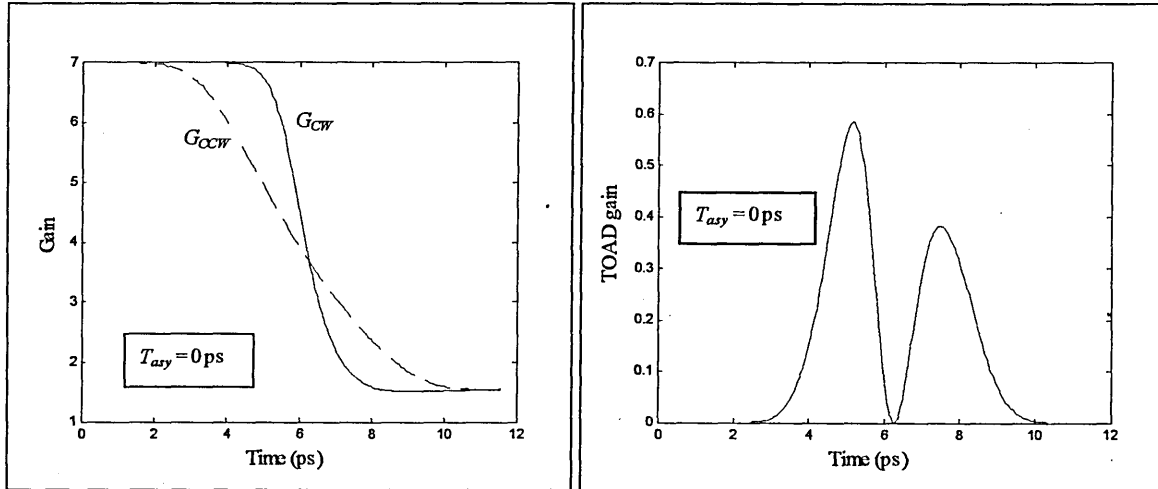


Fig. 7.4a. G_{CW} and G_{CCW} Vs. time.

Fig. 7.4b. TOAD switching window.

G_{CW} and G_{CCW} in Fig. 7.4a are substituted into (7.1) and (7.2) for simulating TOAD switching window. The result is shown in Fig. 7.4b. The central dip (TOAD gain is zero) in Fig. 7.4b corresponds to $G_{CW} = G_{CCW}$ in Fig. 7.4a.

The double peaks of the switching window displayed in Fig. 7.4b can be avoided by asymmetrically placing the SLA off the mid-point of the fibre loop. Figures. 7.5a and 7.5b show the simulation results for the gain dynamics and TOAD window using the same set of parameters as Figs. 7.4a and 7.4b except for $T_{asy} = 2$ ps.

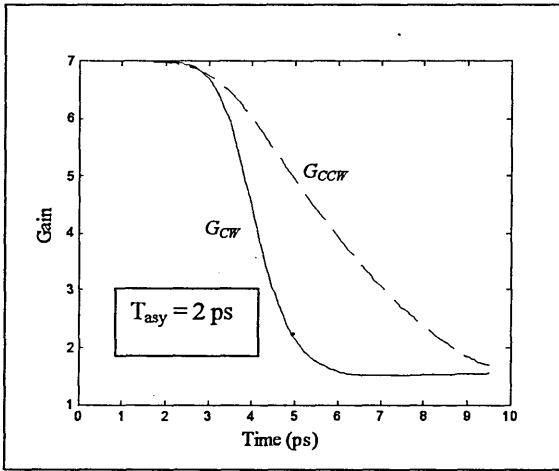


Fig. 7.5a. G_{CW} and G_{CCW} Vs time.

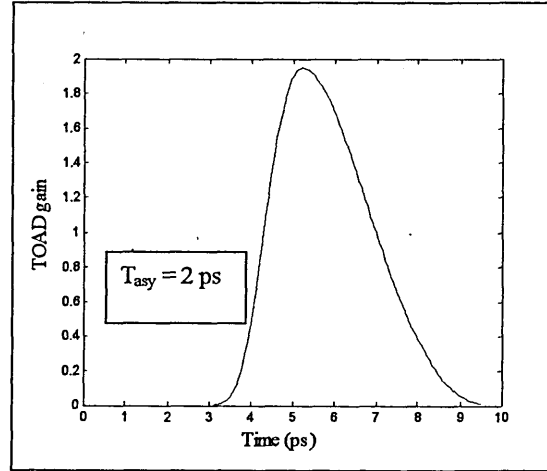


Fig. 7.5b. TOAD switching window.

Figure 7.5a shows that the G_{CW} curve is left shifted by T_{asy} against the G_{CCW} curve, thus eliminating the central dip of the TOAD window that occurs in zero asymmetry.

A single-peak TOAD window generally has a triangle shape, as shown in Fig. 7.5b. The rising and declining slopes of the triangle correspond to the fall times of G_{CW} and G_{CCW} in Fig. 7.5a, respectively. A triangle-shaped switching window is vulnerable to the demultiplexing of the non-target pulses of the neighbour channels. To demultiplex only the target pulses, a TOAD demultiplexer should ideally have a square-shaped switching window exactly covering the target time slot of the OTDM signal. The width of the ideal square-shaped switching window can be adjusted by the SLA asymmetry. Nevertheless, the ideal square-shaped window can only be obtained by the control pulse of impulse characteristics, which is impossible to be achieved in reality. The rising and declining slopes of TOAD switching profile increase with the control pulse width and SLA length, as mentioned at the beginning of this subsection. It is desirable to keep both the SLA length and control pulse width as small as possible. Nevertheless, subpico-second control pulse will result in fast and complex gain/phase dynamics of the SLA (see Chapter 4). The control pulse width for this TOAD model is assumed to be 1 ps for avoiding the sub-

picosecond effects. Different values of SLA length are used in the noise and crosstalk analysis for performance comparisons.

7.3.4 Optimisation of switching energy

The TOAD switching window is a function of G_{CW} , G_{CCW} and $\Delta\phi$, as shown in (7.1). Unlike NOLM demultiplexer, which requires phase difference = π for maximum transmittance, the optimal $\Delta\phi$ for maximum switching ratio in TOAD demultiplexer is less than π due to gain difference between CW and CCW pulses. The optimal phase difference is given as [147]:

$$\Delta\phi_{\max} = \pi - \frac{\exp\left(-\frac{\pi}{\alpha_{LEF}}\right) + 1}{\alpha_{LEF}}. \quad (7.14)$$

As $\Delta\phi$ is related to G_{CW} and G_{CCW} by (7.2), the optimal gain ratio R_G between the clockwise and counter-clockwise pulses for maximum TOAD switching gain can be obtained by substituting (7.14) into (7.2). The result is given as:

$$R_G = \exp\left[\frac{2}{\alpha_{LEF}^2} \cdot \left(\exp\left(-\frac{\pi}{\alpha_{LEF}}\right) + 1 - \pi \cdot \alpha_{LEF}\right)\right]. \quad (7.15)$$

According to (7.15), R_G is 0.25 when $\alpha_{LEF} = 4$. In order to achieve maximum switching gain at the peak of TOAD switching, the control pulse should have adequate energy to saturate the SLA from its initial gain G_o to $G_o \times R_G$, which is $G_o / 4$ in the case of $\alpha_{LEF} = 4$.

G. P. Agrawal, *et-al* [86] developed the following analytical equation for the gain saturation in a SLA by an input pulse.

$$G(E_{in}) = \exp\left\{-\ln\left[1 - \left(1 - \frac{1}{G_o}\right) \cdot \exp\left(-\frac{E_{in}}{E_{sat}}\right)\right]\right\}, \quad (7.16)$$

where E_{in} is the energy of the input pulse, $G(E_{in})$ is the saturated gain for pulse energy = E_{in} , G_o is the initial unsaturated gain, and E_{sat} is the saturation energy of the SLA. E_{sat} in (7.16) is defined as [86]:

$$E_{sat} = \frac{E_p \cdot A_{SLA}}{\Gamma \cdot \alpha} \quad (7.17)$$

All variables in (7.17) have been defined previously.

In order to attain maximum peak TOAD gain, the switching energy of the control pulse should be optimised by replacing $G(E_{in})$ in (7.16) with $G_o \times R_G$ and the result is:

$$G_o \cdot R_G = \exp \left\{ -\ln \left[1 - \left(1 - \frac{1}{G_o} \right) \cdot \exp \left(-\frac{E_{CTRL}}{E_{sat}} \right) \right] \right\}, \quad (7.18)$$

where E_{CTRL} is the optimise control pulse energy. Equation 7.18 is rearranged for calculating E_{CTRL} , which is given as:

$$E_{CTRL} = E_{sat} \cdot \ln \left(\frac{G_o \cdot R_G - R_G}{G_o \cdot R_G - 1} \right). \quad (7.19)$$

If $R_G = 1$, i.e. no gain depletion, then E_{CTRL} would be equal to zero.

Equations 7.15 and 7.19 are used to optimise switching energy of the control pulse for maximising the peak of the TOAD switching gain. An example is given below for illustrating the optimisation of switching energy. Table 7.3 lists the simulation parameters for TOAD demultiplexing. The control pulse is assumed to have a Gaussian shape, with its energy related to its power profile by the standard Gaussian equation given as:

$$P_{in}(t) = \frac{1.665 \cdot E_{in}}{T_{FWHM} \cdot \sqrt{\pi}} \cdot \exp \left(-\frac{(1.665 \cdot t)^2}{T_{FWHM}^2} \right), \quad (7.20)$$

where P_{in} is the power profile of the input Gaussian pulse, and E_{in} is the switching energy of the control pulse.

The power profile of the control pulse in (7.20) is used as the input pulse to the SLA model for calculating G_{CW} and G_{CCW} . Substituting the relevant parameters of Table 7.3 into (7.15) and (7.19), the optimal switching energy E_{CTRL} is calculated to be 2.598 pJ. Figure 7.6a plots the clockwise and counter-clockwise gains Vs. time for different values of switching energy. The solid and dashed lines represent the clockwise and counter-clockwise gains, respectively. The blue, red and green lines represent the switching energy of 1 pJ, 2.598 pJ and 25.98 pJ, respectively. All gain curves in Fig. 7.6a have the initial gain of 10 before the control pulse enters into the SLA. Because of the control pulse, the G_{CW} and G_{CCW} for $E_{in} = 1$ pJ, 2.598 pJ and 25.98 pJ are saturated to the levels of 4.5, 2.5 and 1, respectively. The saturated gains of G_{CW} and G_{CCW} decrease with switching energy, as shown in Fig. 7.6a. The clockwise and counter-clockwise gain curves in Fig. 7.6a are substituted into the TOAD switching equation (7.1) for evaluating the TOAD window. The results are shown in Fig. 7.6b. The notation of color has the same meaning as in Fig. 7.6a.

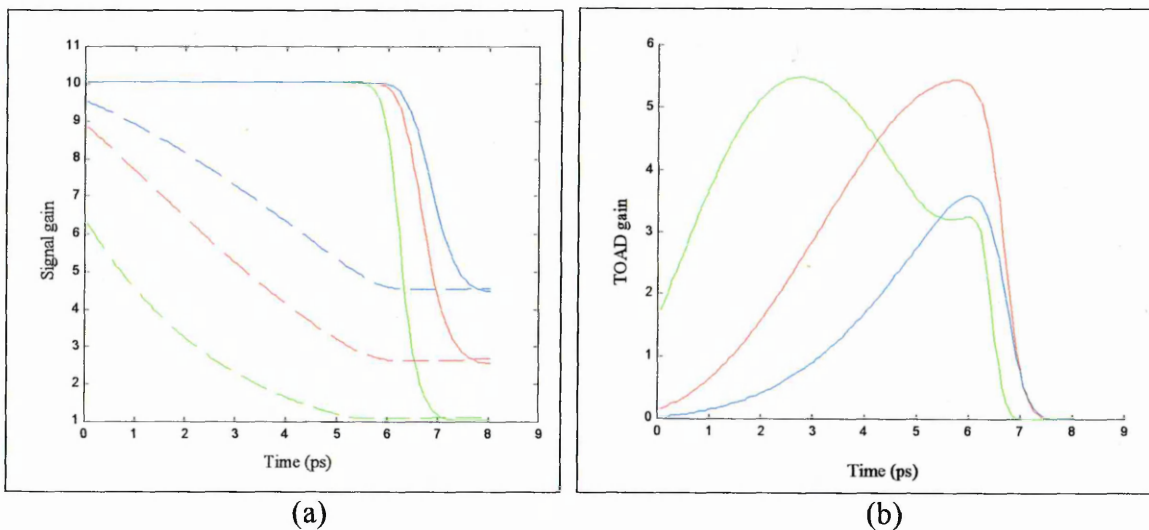


Fig. 7.6. (a) G_{CW} and G_{CCW} Vs Time. and (b) TOAD switching window

The blue, green and red curves in Fig. 7.6 represent the cases of under-saturation, over-saturation and optimised saturation of the SLA, respectively. The TOAD window of optimal switching energy (red curve in Fig. 7.6b) has a maximum TOAD gain 5.5. The

peak TOAD gain will be smaller for the switching energy below the optimal value, as shown in the blue curve of Fig. 7.6b. The green curve in Fig. 7.6b peaks at an earlier time than the red curve. By solving Eq.7.15 with $\alpha_{LEF} = 4$, the optimal gain ratio is calculated to be 0.25. It is shown by the green curves in Figs. 7.6a and 7.6b that the TOAD window in Fig. 7.6b is at its peak when the gain ratio between G_{CW} and G_{CCW} in Fig. 7.6a reaches 0.25. The TOAD gain for the green curve in Fig. 7.6b begins to drop when the excess switching energy over-saturates the SLA (i.e. $R_G > 0.25$), as shown in the dashed green line in Fig. 7.6a. The peak TOAD gain of the switching window ceases to increase when the switching energy is larger than the optimal value. It has been illustrated in the simulation results that (7.15) and (7.19) can be used to optimise the switching energy for maximising TOAD output gain.

Parameters	Values
Unsaturated gain G_o	10
Linewidth enhancement factor α_{LEF}	4
Spontaneous lifetime T_{sp}	100 ps
Confinement factor Γ	0.3
Gain coefficient a	$2 \times 10^{-20} \text{ m}^2$
Transparent carrier density N_o	$1 \times 10^{24} \text{ m}^{-3}$
Length of the amplifier L_{SLA}	0.3 mm
Cross section area of the amplifier A_{SLA}	$3 \times 10^{-13} \text{ m}^2$
Bias current I (calculated from G_o)	329 mA
Photon energy E_{ph}	0.8 eV
FWHM control pulse with T_{FWHM}	1 ps
SLA asymmetry T_{asy}	-4.5 ps
Propagation speed inside the SLA	$(3 \times 10^8 / 3.5) \text{ m/s}$
Total number of segments	50

7.3.5 Limitation on signal intensity

In the TOAD model, the CW and CCW signal pulses are assumed not to have adequate energy to influence the gain and phase dynamics of the SLA. This assumption is for avoiding the perturbation of the SLA properties by the bit patterns of the OTDM signal.

This subsection quantifies the maximum allowable signal energy in TOAD demultiplexing for satisfying this assumption.

Equation 7.16 governs the decrease of SLA gain by an input signal pulse, where E_{in} in the equation represents the signal energy. CW and CCW signal pulses are assumed to have negligible effect on the SLA if the change of the SLA gain is very small compared to the unsaturated gain. Assuming that the changes in gain of the SLA should be less than or equal to 5% after a single pass of the signal pulse through the SLA, the maximum signal energy for TOAD demultiplexing is defined as:

$$0.95 \cdot G_o = \exp \left\{ -2 \cdot \ln \left[1 - \left(1 - \frac{1}{G_o} \right) \cdot \exp \left(-\frac{E_{max}}{2 \cdot E_{sat}} \right) \right] \right\}, \quad (7.21)$$

where E_{max} is the maximum signal energy for TOAD demultiplexing. E_{max} is divided by 2 because the incoming signal pulses are split into CW and CCW pulses with equal energy.

Equation 7.22 is rearranged as follows for calculating E_{max} from other parameters.

$$E_{max} = 2 \cdot E_{sat} \cdot \ln \left(\frac{0.95 \cdot G_o - 0.95}{0.95 \cdot G_o - 1} \right). \quad (7.22)$$

Figure 7.7 plots E_{max} Vs. G_o for $A_{SLA} = 3 \times 10^{-13} \text{ m}^2$, $\Gamma = 0.3$, $a = 2 \times 10^{-20} \text{ m}^2$, and $E_p = 0.8 \text{ eV}$. It is shown that E_{max} decreases as G_o increases. A larger initial gain will increase the TOAD output gain, but at the expense of the decreased dynamic range of the OTDM signal.

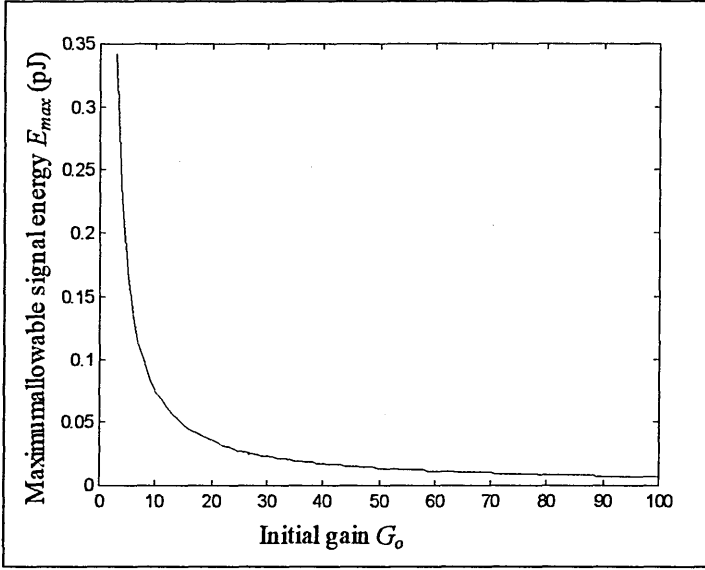


Fig. 7.7. Maximum signal energy E_{max} Vs. the initial gain G_0 .

7.4 Crosstalk and Noise Analysis

Like NOLM demultiplexing, the crosstalk and noise associated with TOAD demultiplexing are the neighbour channel crosstalk NXT_{TOAD} and residual crosstalk RXT_{TOAD} and the relative intensity noise RIN_{TOAD} . RIN_{TOAD} and NXT_{TOAD} have the same origins as in NOLM. Hence, the equations representing RIN_{TOAD} and NXT_{TOAD} can be adapted from those of RIN_{NOLM} and NXT_{NOLM} and are given as:

$$RIN_{TOAD} = \frac{\int_{-\infty}^{\infty} w^2(t) \cdot p(t) dt - \left[\int_{-\infty}^{\infty} w(t) \cdot p(t) dt \right]^2}{\left[\int_{-\infty}^{\infty} w(t) \cdot p(t) dt \right]^2}, \quad (7.23)$$

where $w(t) = \int_{-\infty}^{\infty} TOAD_W(t') \cdot S(t'-t) dt'$.

$$NXT_{TOAD} = \frac{\int_{-T_b/2}^{T_b/2} TOAD_W(t) \cdot S(t+T_b) dt + \int_{-T_b/2}^{T_b/2} TOAD_W(t) \cdot S(t-T_b) dt}{2 \cdot \int_{-T_b/2}^{T_b/2} TOAD_W(t) \cdot S(t) dt}. \quad (7.24)$$

In (7.23) and (7.24), $p(t)$ is the probability distribution of the arrival time of signal pulse Vs. TOAD switching profile, $S(t')$ is the normalised power profile of the target signal, and T_b is the duration of an OTDM time slot. $p(t)$ has a Gaussian distribution with a root-mean-square timing jitters RMS_{jitter} . $S(t)$ is located at the mid-point of the FWHM TOAD

switching profile. If TOAD window have double peaks, $S(t)$ is aligned with the peak with higher TOAD gain. The factor 2 in the denominator of (7.24) assumes that the probabilities of occurrence for mark and space are the same.

The residual crosstalk of TOAD has a different origin from its counterpart of NOLM demultiplexer. The origin of TOAD residual crosstalk is illustrated in Fig. 7.8, which shows the G_{CW} and G_{CCW} Vs. time using the simulation parameters of Table 7.3. The switching energy is 1 pJ.

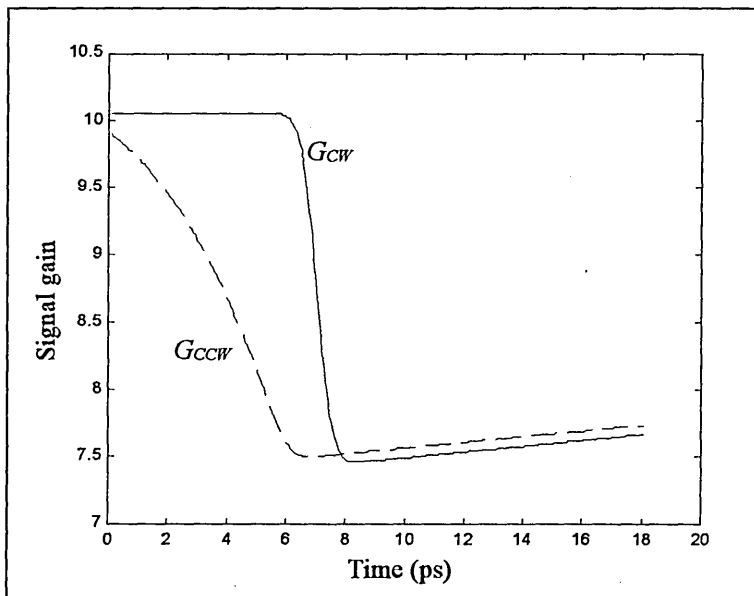


Fig. 7.8. TOAD residual crosstalk.

Figure 7.8 shows that there is a small difference between G_{CW} and G_{CCW} outside the TOAD window. That small gain difference manifests itself into TOAD residual crosstalk, according (7.1) and (7.2). The TOAD residual crosstalk is defined as:

$$RXT_{TOAD} = \frac{\sum_{r=2}^{M_{TDM}-1} \int_{(r-0.5)T_b}^{(r+0.5)T_b} TOAD_W(t) \cdot S(t-r \cdot T_b) dt}{2 \cdot \int_{-T_b/2}^{T_b/2} TOAD_W(t) \cdot S(t) dt}, \quad (7.25)$$

where M_{TDM} is the total number of OTDM channels. The crosstalk due to the two channels adjacent to the target channel is excluded from the nominator as they are defined as neighbour channel crosstalk (see (7.24)). The factor 2 in the denominator assumes that the

probabilities of occurrence for mark and space are the same. The simulation results for relative intensity noise, residual crosstalk and neighbour channel crosstalk in TOAD will be presented in Sections 7.4.1, 7.4.2 and 7.4.3, respectively.

7.4.1 TOAD relative intensity noise

The simulation results in this subsection are obtained by substituting the TOAD windows calculated from the TOAD model into the equation of TOAD relative intensity noise (7.23). The parameters for the simulations are listed in Table 7.4. Equations 7.15 and 7.19 are used to optimise the switching energy of the control pulse for maximising the TOAD gain.

Parameters	Values
Linewidth enhancement factor α_{LEF}	4
Spontaneous lifetime T_{sp}	100 ps
Confinement factor Γ	0.3
Gain coefficient a	$2 \times 10^{-20} \text{ m}^2$
Transparent carrier density N_o	$1 \times 10^{24} \text{ m}^{-3}$
Cross section area of the amplifier A_{SLA}	$3 \times 10^{-13} \text{ m}^2$
Photon energy E_{ph}	0.8 eV
FWHM control pulse with T_{FWHM}	1 ps
Propagation speed inside the SLA	$(3 \times 10^8 / 3.5) \text{ m/s}$
Total number of segments	50

Figures 7.9a – 7.9d plot RIN_{TOAD} Vs. T_{asy} for different combinations of simulation parameters, which are listed on Table 7.5. The red, green and blue lines represent $L_{SLA} = 0.5 \text{ mm}$, 0.3 mm and 0.1 mm , respectively.

Figure	Simulation parameters
Fig. 7.9a	FWHM signal pulse width = 1 ps, $RMS_{jitter} = 1 \text{ ps}$, $G_o = 5$
Fig. 7.9b	FWHM signal pulse width = 1 ps, $RMS_{jitter} = 1 \text{ ps}$, $G_o = 10$
Fig. 7.9c	FWHM signal pulse width = 3 ps, $RMS_{jitter} = 1 \text{ ps}$, $G_o = 5$
Fig. 7.9d	FWHM signal pulse width = 1 ps, $RMS_{jitter} = 3 \text{ ps}$, $G_o = 5$

It is shown in Fig. 7.9a that RIN_{TOAD} increases as the SLA asymmetry decreases and is at maximum when the SLA asymmetry is close to zero. TOAD switching window of small SLA asymmetry is sensitive to timing jitter of the signal pulses because of its double-peaks window shape, as shown in Fig. 7.4b. The double-peaks of TOAD window will gradually evolve into a single-peak as the SLA asymmetry increases (see Fig. 7.5b), Therefore, the relative intensity noise is less sensitive to timing jitter for larger SLA asymmetry. It is also shown in Fig. 7.9a that shorter (longer) SLA length will lead to larger (smaller) RIN_{TOAD} at small SLA asymmetry and smaller (larger) RIN_{TOAD} at large SLA asymmetry.

Figure 7.9b plots RIN_{TOAD} Vs. T_{asy} for the same set of parameters as Fig. 7.9a except $G_o = 10$. There is not much difference between the simulation results of Figs. 7.9a and 7.9b. Similar comparisons of simulation results for various combinations of parameters (not illustrated here) show that TOAD relative intensity noise is fairly independent of the SLA's initial gain.

For evaluating the effect of signal pulse width on RIN_{TOAD} , Fig. 7.9c plots RIN_{TOAD} Vs. T_{asy} for the same set of parameters as Fig. 7.9a except that FWHM signal pulse width is equal to 3 ps instead of 1 ps. RIN_{TOAD} is smaller for signal width = 3 ps than for signal width = 1 ps, as shown in Figs. 7.9a and 7.9c. The influence of signal width is more pronounced at small SLA asymmetry. The overall noise characteristics for various SLA lengths shown in Fig. 7.9c are similar to those of Figs. 7.9a and 7.9b.

Figure 7.9d plots RIN_{TOAD} Vs. T_{asy} for the same of parameters as in Fig. 7.9a except that RMS_{jitter} is equal to 3 ps instead of 1 ps. As intuitively predicted, RIN_{TOAD} is substantially increased due to the severe timing jitter of signal pulses.

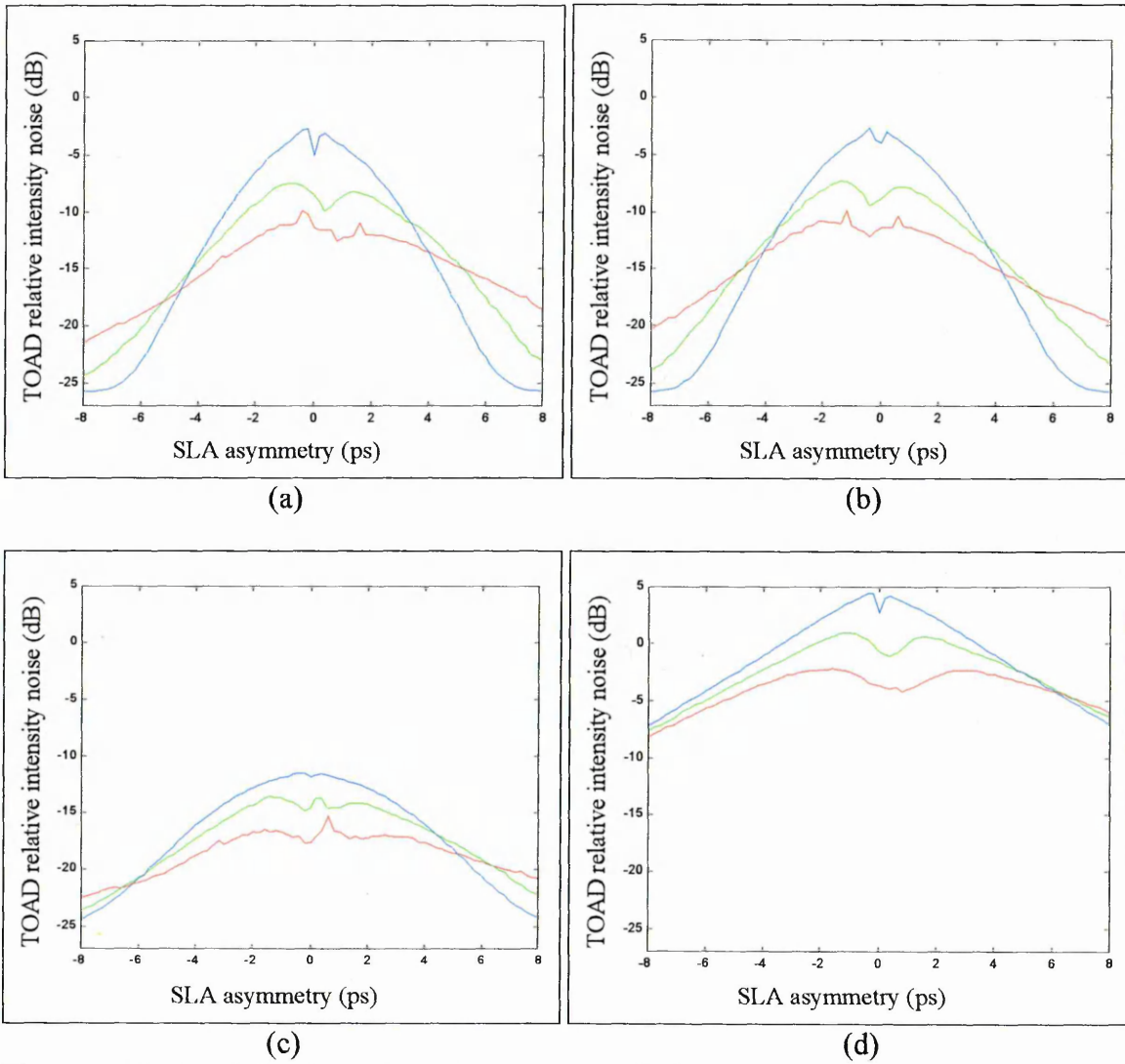


Fig. 7.9. TOAD relative intensity noise versus the SLA asymmetry (simulation parameters listed in Table 7.5)

7.4.2 TOAD crosstalk

The crosstalk for the TOAD demultiplexing were calculated by substituting the TOAD switching windows from the TOAD model into the equations of residual crosstalk (7.24) and the neighbour channel crosstalk (7.25). The parameters used in the crosstalk simulation are presented in Table 7.4.

Figure 7.10 plots RXT_{TOAD} and NXT_{TOAD} Vs. T_{asy} for 100 Gb/s demultiplexing. The simulation parameters used are $L_{SLA} = 0.3$ mm, $G_o = 5$, $M_{TDM} = 10$ and duty cycle = 0.1. The solid and dashed lines represent RXT_{TOAD} and NXT_{TOAD} , respectively. Figure 7.10

shows that both types of crosstalk have their minimum values at the near-zero SLA asymmetry, and increase as the SLA asymmetry increases in either positive or negative direction. As mentioned earlier in this chapter, the width of a TOAD window is adjusted by the SLA asymmetry. The demultiplexing of non-target pulses from neighbour channels will not occur unless the T_{asy} -induced window width is comparable to or larger than the time slot of a OTDM channel, which is 10 ps in the case of 100 Gb/s demultiplexing. Since the range of SLA asymmetry in Fig. 7.10 is not wide enough for the TOAD window to demultiplex neighbour channels, the overwhelming contribution to NXT_{TOAD} is the residual gain difference between CW and CCW pulses within the time slots of the neighbour channels. At 100 Gb/s, RXT_{TOAD} and NXT_{TOAD} display similar characteristics since they are from the same origin (i.e. residual gain/phase difference between CW and CCW pulses). RXT_{TOAD} is generally larger than NXT_{TOAD} because RXT_{TOAD} accounts for more non-target channels. The crosstalk can be minimised by setting the SLA asymmetry close to zero, as shown in Fig. 7.10.

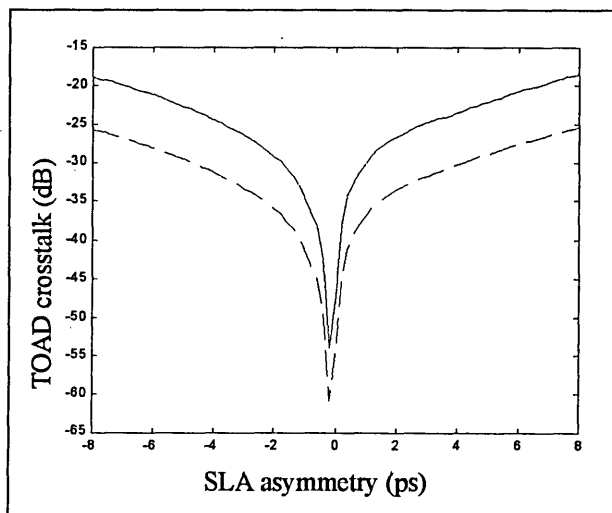


Fig. 7.10. RXT_{TOAD} and NXT_{TOAD} Vs. the SLA asymmetry T_{asy} .

Figure 7.11 plots RXT_{TOAD} Vs. T_{asy} for $L_{SLA} = 0.5$ mm, 0.3 mm and 0.1 mm. Other simulation parameters used are the same as in Fig. 7.10. The red, green and blue lines represent $L_{SLA} = 0.5$ mm, 0.3 mm and 0.1 mm, respectively. The characteristics of residual

crosstalk for the three values of L_{SLA} are similar to each other, as shown in Fig. 7.11. Simulation results for $L_{SLA} = 0.5$ mm, 0.3 mm and 0.1 mm using other combinations of parameters (not shown here) have also been carried out. It can be concluded that the change of L_{SLA} generally does not have much influence on the TOAD crosstalk. NXT_{TOAD} is not shown in Fig. 7.11 as it is dominated by RXT_{TOAD} in 100 Gb/s demultiplexing.

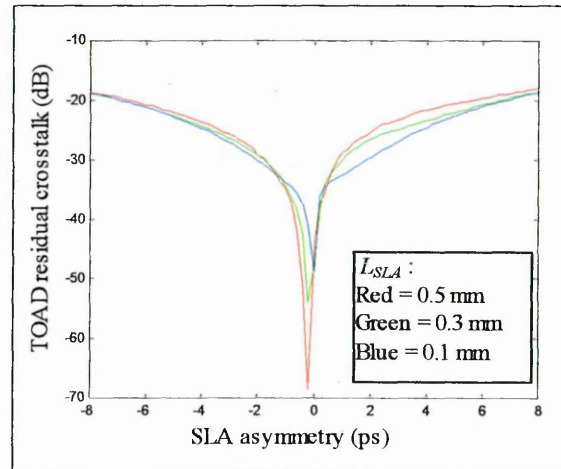


Fig. 7.11. RXT_{TOAD} Vs. T_{asy} .

Figure 7.12 plots RXT_{TOAD} and NXT_{TOAD} for $L_{SLA} = 0.5$ mm and 0.3 mm at 200 Gb/s TOAD demultiplexing with 20 OTDM channels. The solid and dashed lines represent RXT_{TOAD} and NXT_{TOAD} , respectively. The red and blue lines represent $L_{SLA} = 0.5$ mm and 0.1 mm, respectively. The crosstalk characteristics at 200 Gb/s is substantially different from those at 100 Gb/s demultiplexing. The effect of SLA length on the residual crosstalk is insignificant in 200 Gb/s demultiplexing, as shown by the similarity of the two solid lines. Nevertheless, the large vertical separation between the two dashed lines shows that the neighbour channel crosstalk is strongly dependent on the SLA length. Figure 7.12 also shows that RXT_{TOAD} (NXT_{TOAD}) dominates the TOAD crosstalk in small (long) SLA length. In order to minimise the overall crosstalk in 200 Gb/s TOAD demultiplexing, a small SLA length should be used for keeping the neighbour channel crosstalk small. The overall crosstalk can be minimised by making RXT_{TOAD} a dominant crosstalk.

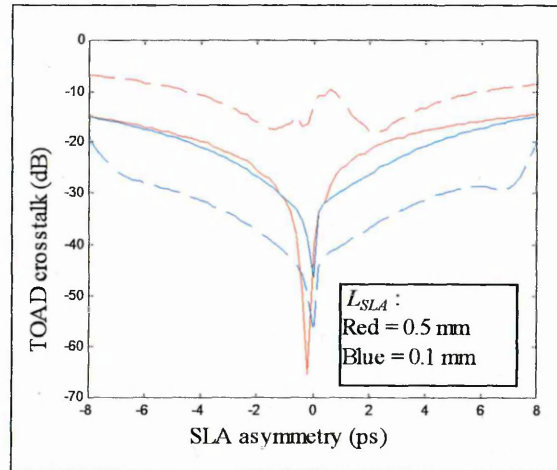


Fig. 7.12: RXT_{TOAD} and NXT_{TOAD} Vs. T_{asy} .

To sum up, the TOAD crosstalk is fairly independent of the SLA length at medium data rates (< 100 Gb/s). At high data rates (> 200 Gb/s), shorter SLA length should be used to minimize the overall crosstalk. To illustrate this point, the total crosstalk ($RXT_{TOAD} + NXT_{TOAD}$) for data rate of 100 Gb/s, 200 Gb/s and 300 Gb/s are plotted in Figs. 7.13, 7.14 and 7.15, respectively. M_{TDM} used in Figures 7.13 – 7.153 are 10, 20 and 30, respectively. Other simulation parameters used are the same as before.

Figure 7.13 shows no significant difference in crosstalk performance for different SLA lengths at 100 Gb/s TOAD demultiplexing. Figures 7.14 and 7.15 show that decreasing SLA length from 0.5 mm to 0.1 mm can greatly reduce the TOAD crosstalk for data rate > 100 Gb/s. For data rate equal to 300 Gb/s, the total crosstalk of $L_{SLA} = 0.1$ mm becomes comparable to the total crosstalk of $L_{SLA} = 0.5$ mm in large SLA asymmetry. Large SLA asymmetry should be avoided in high data rate.

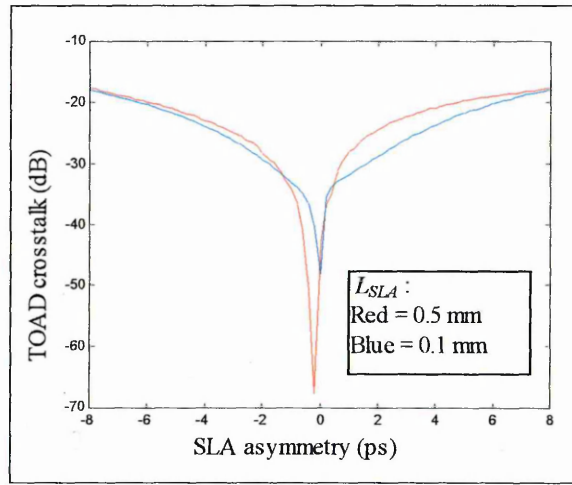


Fig. 7.13. TOAD crosstalk versus SLA asymmetry at total bit rate = 100 Gbps.

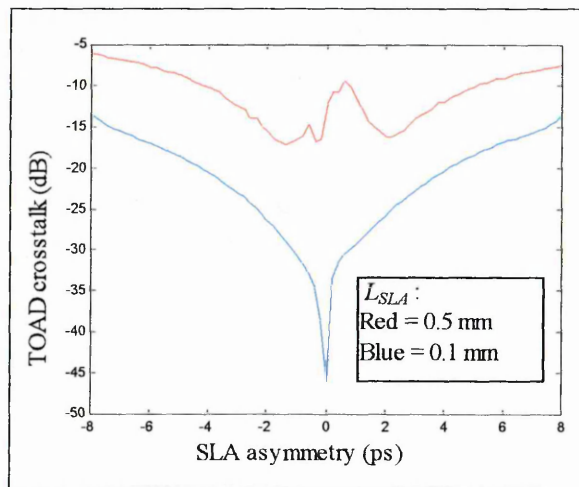


Fig. 7.14. TOAD crosstalk versus SLA asymmetry at total bit rate = 200 Gbps.

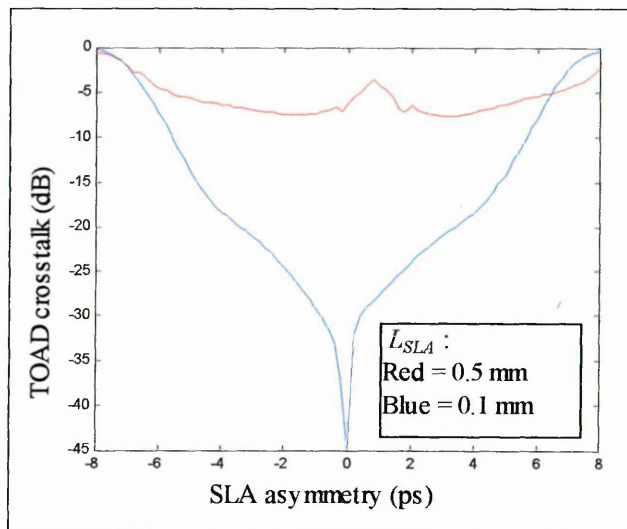


Fig. 7.15. TOAD crosstalk versus SLA asymmetry at total bit rate = 300 Gbps.

In order to assess the effect of changing G_o on the crosstalk performance, Fig. 7.16 plots RXT_{TOAD} and NXT_{TOAD} Vs. T_{asy} for different values of G_o . The simulation parameters used are $L_{SLA} = 0.3$ mm, total bit rate = 100 Gb/s, $M_{TDM} = 10$, and duty cycle = 0.1. The solid and dashed lines represent RXT_{TOAD} and NXT_{TOAD} , respectively. The red, green and blue lines represent $G_o = 5, 7.5$ and 10 , respectively. RXT_{TOAD} and NXT_{TOAD} in Fig. 7.16 have similar characteristics for various G_o (different colour). It can be inferred that changing G_o has little effect on RXT_{TOAD} and RXT_{TOAD} . Simulations using other combinations of parameters (not shown her) led to the same conclusion.

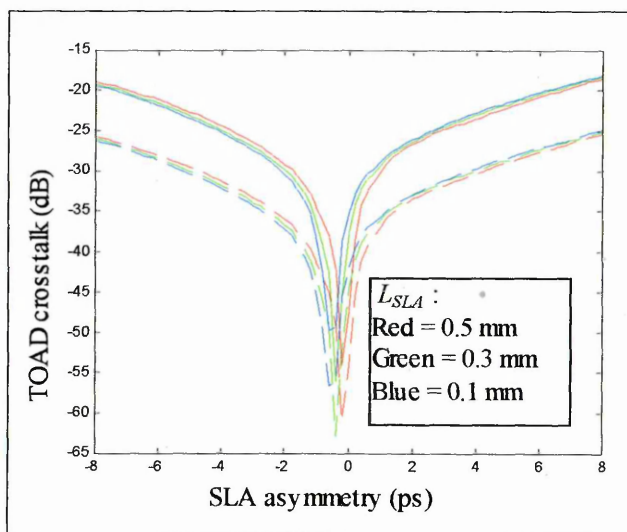


Fig. 7.16: RXT_{TOAD} and NXT_{TOAD} Vs. T_{asy} at total bit rate = 100 Gb/s.

For evaluating the effect of M_{TDM} on crosstalk performance, Fig. 7.17 plots RXT_{TOAD} Vs. T_{asy} for $M_{TDM} = 30$ and 300 at 300 Gb/s TOAD demultiplexing. The solid and dashed lines represent $M_{TDM} = 30$ and 300 , respectively. The other simulation parameters used are $G_o = 5$, $L_{SLA} = 0.3$ mm, and duty cycle = 0.1. Figure 7.17 does not include NXT_{TOAD} because the neighbour channel crosstalk is not dependent on the total number of OTDM channels, according to its mathematical definition (7.24).

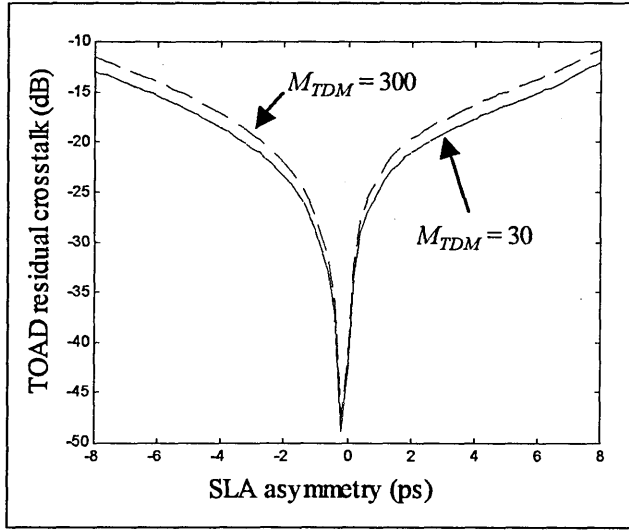


Fig. 7.17. RXT_{TOAD} Vs. T_{asy} (solid line : $M_{TDM} = 30$, dash line : $M_{TDM} = 300$).

As shown in Fig. 7.17, a substantial increase in the number of OTDM channels, from 30 to 300, results in only a slight increase in the residual crosstalk. According to the spontaneous life-time T_{sp} given in Table 7.4, the saturated G_{CW} and G_{CCW} will recover back to G_o in about 100 ps. After recovering back to G_o , G_{CW} and G_{CCW} will remain at the same value until the next control pulse saturates the SLA again. At total bit rate of 300 Gb/s, the OTDM frame periods are 100 ps and 1000 ps for $M_{TDM} = 30$ and 300, respectively. Although the number of non-target channels for $M_{TDM} = 300$ is 290 more than that for $M_{TDM} = 30$, the non-target channels outside the first 100 ps of the OTDM time frame contribute very little to the residual crosstalk.

Figure 7.18 plots RXT_{TOAD} and NXT_{TOAD} Vs. T_{asy} for illustrating the effect of changing the duty cycle on the crosstalk performance. The red and blue lines represent duty cycles of 0.1 and 0.2, respectively. The solid and dashed lines represent RXT_{TOAD} and NXT_{TOAD} , respectively. The simulation parameters used are $G_o = 5$, total bit rate = 200 Gb/s, $M_{TDM} = 20$, and $L_{SLA} = 0.3$ mm. As intuitively expected, increasing duty cycle will increase the neighbour channel crosstalk, as shown by the dashed lines in Fig. 7.18. Fig. 7.18 also

shows that the residual crosstalk is largely independent on the duty cycle. Simulations using other combinations of parameters (not shown here) confirm this finding.

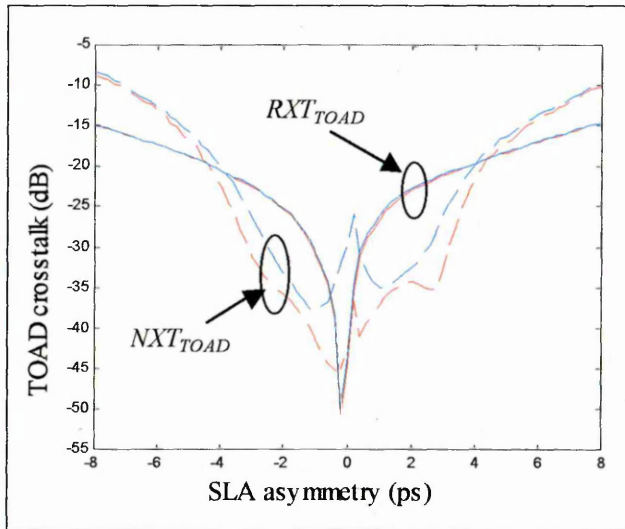


Fig. 7.18. RXT_{TOAD} and NXT_{TOAD} Vs. T_{asy} for duty cycle = 0.1 (red lines) and duty cycle = 0.2 (blue lines).

7.4.3 Tradeoff between noise and crosstalk in TOAD demultiplexing

The two device parameters that influence the noise and crosstalk performance of TOAD are L_{SLA} and T_{asy} . In TOAD demultiplexing, tradeoff between noise and crosstalk in TOAD demultiplexing appears in different forms for different bit rates. This is best illustrated by the Figs. 7.19 and 7.20.

Figures 7.19 and 7.20 plot RIN_{TOAD} and TOAD crosstalk Vs. T_{asy} for 100Gb/s and 200Gb/s demultiplexing, respectively. The bit rate of individual OTDM channels is 10 Gb/s, which makes the value of M_{TDM} equal to 10 for Fig. 7.19 and 20 for Fig. 7.20. The other parameters used are $G_o = 5$, and duty cycle = 0.1. The solid and dashed lines represent RIN_{TOAD} and TOAD crosstalk, respectively. The red and blue lines represent L_{SLA} equal to 0.5 mm and 0.1 mm, respectively. The TOAD crosstalk is calculated from $RXT_{TOAD} + NXT_{TOAD}$.

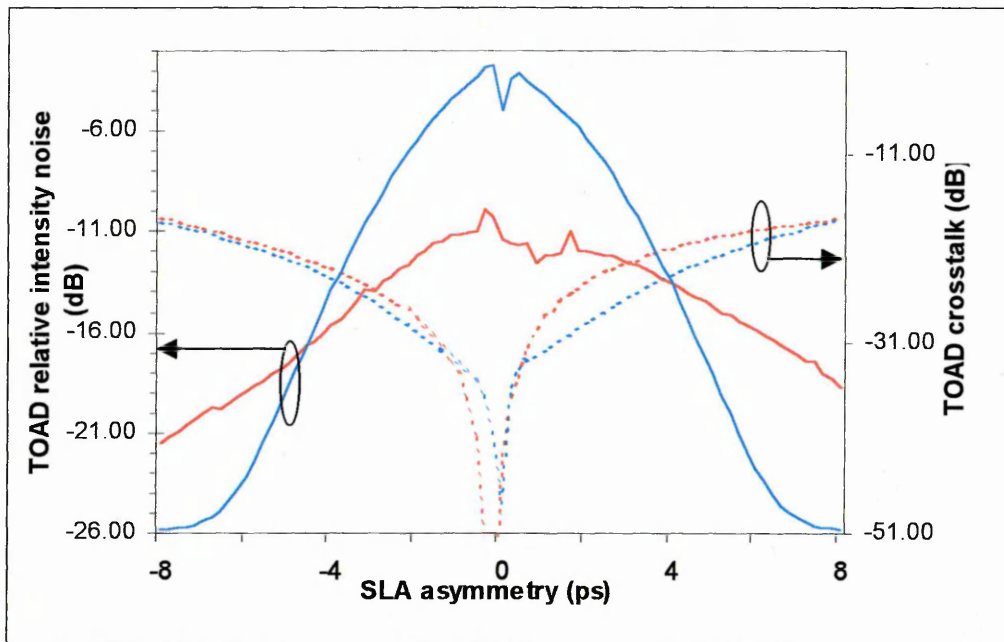


Fig. 7.19. RIN_{TOAD} and TOAD crosstalk Vs. SLA asymmetry at total bit rate = 100 Gbps for $L_{SLA} = 0.5$ mm (red lines) and 0.1 mm (blue lines).

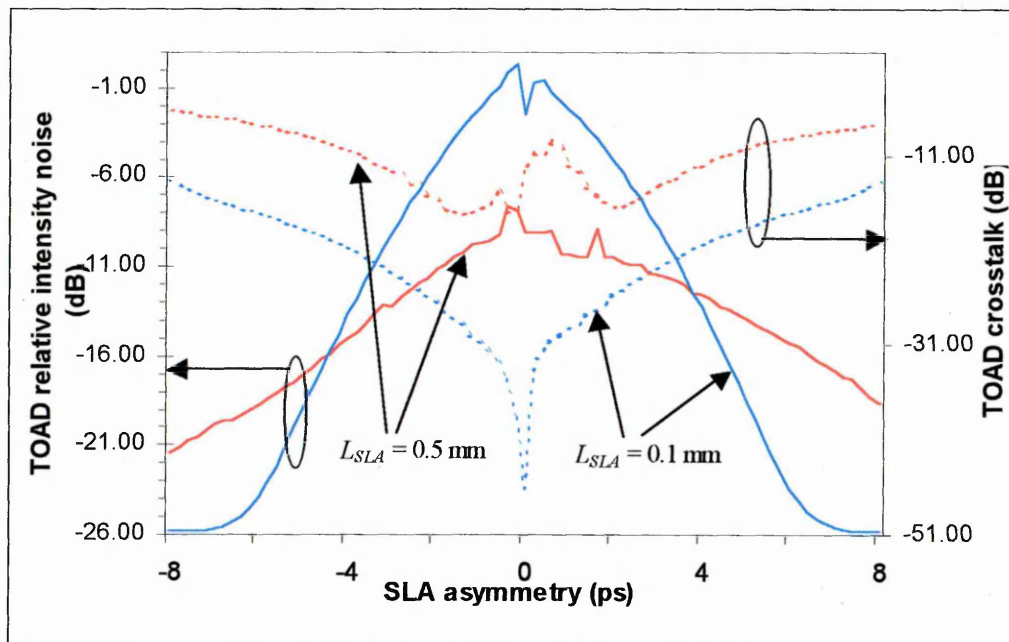


Fig. 7.20. RIN_{TOAD} and TOAD crosstalk Vs. SLA asymmetry at total bit rate = 200 Gbps for $L_{SLA} = 0.5$ mm (red lines) and 0.1 mm (blue lines).

The dashed lines in Fig. 7.19 show little dependence of TOAD crosstalk on L_{SLA} for 100 Gb/s demultiplexing. Therefore, it doesn't matter what value of L_{SLA} is used in terms of the TOAD crosstalk. Nevertheless, RIN_{TOAD} is strongly dependent on L_{SLA} , as shown by the solid lines in Fig. 7.19. Hence, in 100 Gb/s demultiplexing, what value of L_{SLA} should be

used for minimising the overall effect of crosstalk and noise is solely dependent on RIN_{TOAD} . Figure 7.19 shows that RIN_{TOAD} for $L_{SLA} = 0.1$ mm is larger in smaller SLA asymmetry and is smaller in larger SLA asymmetry. In other words, large L_{SLA} should be used in small SLA asymmetry and small L_{SLA} should be used in large SLA asymmetry. In order to obtain the optimal SLA asymmetry, other noise contributions from the optical receiver should also be taken into account for mimimising the power penalty of the TOAD. The power penalty calculations of TOAD demultiplexing will be presented in Chapter 8.

RIN_{TOAD} , RXT_{TOAD} and NXT_{TOAD} deteriorate when the total bit rate is increased. Given a fixed value of RMS_{jitter} (1 ps), increasing the total bit rate will make the pulses more vulnerable to RIN_{TOAD} because of the smaller pulse width. In addition, due to the smaller guard time between adjacent pulses in higher capacity signal, more pulse energy from the non-target neighbour channels will be demultiplexed if the total bit rate is increased. RXT_{TOAD} also increases in higher bit rate simply because the number of non-target pulses within an OTDM frame is larger. The dependence of noise and crosstalk on L_{SLA} is more complex for 200 Gb/s TOAD demultiplexing. Here, TOAD crosstalk increases with the SLA length, as shown by the dashed lines in Fig. 7.20. The noise characteristics displayed in Fig. 7.20 are similar to those in Fig. 7.19. RIN_{TOAD} at smaller L_{SLA} is larger in smaller SLA asymmetry and is smaller in larger SLA asymmetry. At small SLA asymmetry, increasing the value of L_{SLA} will decrease relative intensity noise at the expense of the increase in crosstalk. At large SLA asymmetry, increasing the value of L_{SLA} will increase both the crosstalk and noise of TOAD demultiplexing, as shown in Fig. 7.20. Therefore, for 200 Gb/s TOAD demultiplexing, small SLA length should be used in large SLA asymmetry. As for the small SLA asymmetry, the SLA length could be optimised in terms of power penalty.

7.5 Summary

A TOAD model for calculating TOAD switching window and optimising switching energy has been presented. Part of the model is derived from the SLA model of Ref. 88. The switching energy of the control pulse is optimised for maximising the peak TOAD gain of the switching window. The optimised TOAD windows are fed into a noise and crosstalk model for analysis. The noise and crosstalk associated with TOAD demultiplexer are relative intensity noise, residual crosstalk and neighbour channel crosstalk. It has been shown that different tradeoffs between noise and crosstalk exist for different data rates.

CHAPTER EIGHT - BIT ERROR RATE PERFORMANCE OF NOLM AND TOAD DEMULTIPLEXERS

8.1 Introduction

In digital communications systems, the most important criterion of evaluating system performance is the bit-error-rate. The BER performance of an OTDM system deteriorates because of the noise and crosstalk introduced by the all-optical time division demultiplexer. Thus, an ultimate design goal for NOLM and TOAD demultiplexers is to optimise device parameters for minimising BER. This chapter is concerned with the optimisation and comparison of NOLM and TOAD demultiplexers in terms of BER.

As discussed in Chapters 6 and 7, the noise and crosstalk associated with NOLM and TOAD demultiplexer are relative intensity noise, residual crosstalk and neighbour channel crosstalk. The magnitudes of noise and crosstalk vary with device parameters. For example, in NOLM demultiplexing, increasing the length of the fibre loop will reduce the relative intensity noise at the expense of an increase of residual and neighbour channel crosstalk. Similar tradeoffs in terms of noise and crosstalk exist for other device parameters for both NOLM and TOAD demultiplexers, as were described in Chapters 6 and 7. It is impossible to simultaneously minimise all the above-mentioned noise and crosstalk by simply changing device parameters. In general, a decrease of noise will result in an increase of crosstalk and vice versa. The optimal balance between crosstalk and noise will lead to a minimised BER. This can be achieved by the optimisation of device parameters.

An important factor that affects the power penalty of NOLM/TOAD demultiplexing is the relative intensity noise, which is originated from the timing jitter of OTDM signal pulses. The relative intensity noise of the demultiplexer is quantified as root-mean-square jitter RMS_{jitter} . Gordon and Haus [53] derived an analytical solution for calculating the signal

jitter (Gordon-Haus jitter) due to optical amplifiers. Based on the theoretical results from Ref. 53, Section 8.2 investigates the Gordon-Haus jitter for the special case of distributed amplification. This investigation is one of the original contributions in this PhD study. Section 8.3 describes a receiver model for the BER analysis. In Section 8.4, device parameters of NOLM and TOAD demultiplexers are optimised to minimise BER for the aggregate bit rates of 100 Gb/s and 300 Gb/s.

8.2 Gordon-Haus Jitter and Relative Intensity Noise

8.2.1 Equations for Gordon-Haus jitter

In a soliton transmission system, periodic amplification is required to compensate for the fibre loss in order to maintain the soliton peak power throughout the whole transmission length (see Chapter 3). The amplified spontaneous emission noise associated with the optical amplifiers will perturb the optical field of the amplified soliton, resulting in a random variation of the group velocity between individual soliton pulses [53]. The velocity difference between propagating pulses manifests itself into a root-mean-square timing jitter associate with the received pulses. The equation for soliton jitter due to amplifier noise was derived by Gordon and Haus and is given as [53]:

$$RMS_{jitter}^2 = \frac{(G-1) \cdot A \cdot L_{tot}^3}{9 \cdot N_{ph} \cdot \Delta L}, \quad (8.1)$$

where RMS_{jitter} is the root-mean-square jitter of soliton pulses, G is the amplifier gain, L_{tot} is the total transmission length, N_{ph} is the number of photons per unit energy, ΔL is the separation length between two amplifiers, and A is the amplitude of the soliton field. Equation 8.1 is derived from the canonical nonlinear Schrödinger equation in the soliton units of time, length and power. The soliton units are related to ordinary units as given by:

$$\beta_2 = -t_c^2 / z_c, \quad (8.2a)$$

$$\gamma = \frac{1}{z_c \cdot P_c}, \quad (8.2b)$$

where t_c , z_c and P_c are the soliton units of time, length and power, respectively. Other variables have been defined in previous chapters.

Assuming that the gain of amplifiers is adjusted to exactly compensate the fibre loss between the amplifier spacing, the amplifier gain can be represented as:

$$G = \exp(\alpha \cdot \Delta L), \quad (8.3)$$

where α is the fibre loss per unit length. Equation 8.3 is substituted into (8.1) and the result is given by:

$$RMS_{jitter}^2 = \frac{(\exp(\alpha \cdot \Delta L) - 1) \cdot A \cdot I_{tot}^3}{9 \cdot N_{ph} \cdot \Delta L}. \quad (8.4)$$

It is of practical interest to find out the optimal amplifier spacing ΔL for minimising RMS_{jitter} . The exponential term in (8.4) can be expressed in its series form given as:

$$\exp(\alpha \cdot \Delta L) = 1 + \alpha \cdot \Delta L + \frac{(\alpha \cdot \Delta L)^2}{2!} + \frac{(\alpha \cdot \Delta L)^3}{3!} + \dots \quad (8.5)$$

Substituting (8.5) into (8.4) yields:

$$RMS_{jitter}^2 = \frac{A \cdot I_{tot}^3}{9 \cdot N_{ph}} \cdot \left(\alpha + \frac{\alpha^2 \cdot \Delta L}{2!} + \frac{\alpha^3 \cdot \Delta L^2}{3!} + \dots \right) \quad (8.6)$$

According to (8.6), RMS_{jitter} would be minimum if $\Delta L = 0$. In long-haul optical communication systems, zero amplifier spacing means distributed amplification, which can be achieved by employing the fibre cable as an amplification medium. The equation of timing jitter for distributed amplification is given by:

$$RMS_{jitter}^2 = \frac{\alpha \cdot A \cdot I_{tot}^3}{9 \cdot N_{ph}}. \quad (8.7)$$

In Ref. 53, (8.7) is treated as an approximation of (8.4). Here we have shown that (8.7) represents timing jitter of distributed amplification, and (8.4) represents timing jitter of finite amplifier spacing. The simulation results from (8.4) and (8.7) are shown and analysed in the next subsection. In solving (8.4) and (8.7), the units of time, length and power should be converted to soliton units. The amplitude A used in the simulations is normalised to $P_o = |A|^2$ where P_o is the soliton peak power.

8.2.2 Simulation results

RMS_{jitter} versus ΔL calculated from (8.4) for different values of L_{tot} and FWHM soliton pulse width are shown in Fig. 8.1. Parameters used for all simulations in this subsection are $\gamma = 2 \text{ W}^{-1}\text{km}^{-1}$ and $\beta_2 = -0.5 \text{ ps}^2/\text{km}$. γ and β_2 together with soliton pulse width are used to calculate the soliton peak power, which is used to calculate A in (8.4) and (8.7). It is shown in Fig. 8.1 that RMS_{jitter} decreases with ΔL . Minimum RMS_{jitter} can be attained by distributed amplification, as shown in (8.7). RMS_{jitter} also increases with the total propagation distance. Figure 8.1 shows that RMS_{jitter} increases by about 100% for an increase of the propagation distance from 1000 km to 1500 km. Also shown in Fig. 8.1 is that increasing the signal pulse width will decrease the RMS timing jitter. For fixed values of γ and β_2 , increasing soliton pulse width will decrease the soliton peak power, thus reducing RMS_{jitter} (see (8.4) and (8.7)). If $|\beta_2|$ is decreased to maintain the same level of soliton peak power for a smaller pulse width (see (3.23)), then RMS_{jitter} would be independent of soliton pulse width.

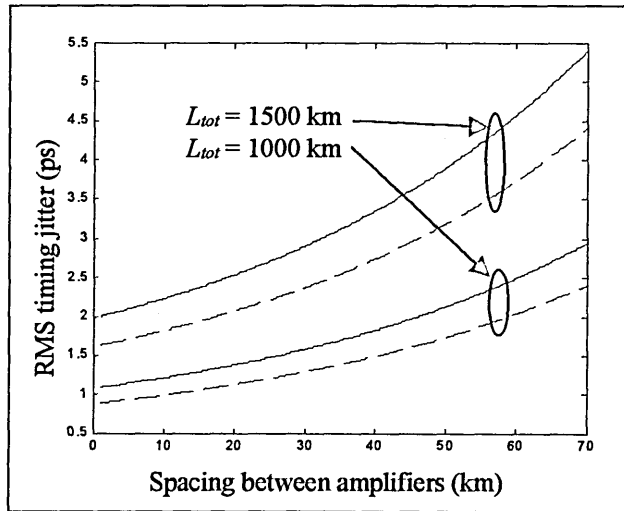


Fig. 8.1. RMS_{jitter} versus ΔL (solid lines represent FWHM soliton width = 1 ps, dashed lines represent FWHM soliton width = 1.5 ps).

Figure 8.2 shows RMS_{jitter} versus L_{tot} for various values of ΔL and signal pulse width. The simulation results for $\Delta L = 40$ km and distributed amplification are obtained from (8.4) and (8.7), respectively. Figure 8.2 shows that RMS_{jitter} increases with L_{tot} . For larger amplifier spacing, RMS_{jitter} will have a stronger dependence on L_{tot} , as illustrated by the steeper curves for $\Delta L = 40$ km. Figure 8.2 also shows that RMS_{jitter} for the distributed amplification is significantly less than that for $\Delta L = 40$ km. For example, the propagation length of 1500 m for the distributed amplification has 60% less RMS_{jitter} than the case of $\Delta L = 40$ km. In Fig. 8.2, the curves for distributed amplification represent the theoretical minimum of the RMS timing jitter induced by optical amplifiers. Nevertheless, the RMS timing jitter could be further reduced by the jitter reduction schemes discussed in Chapter 2.

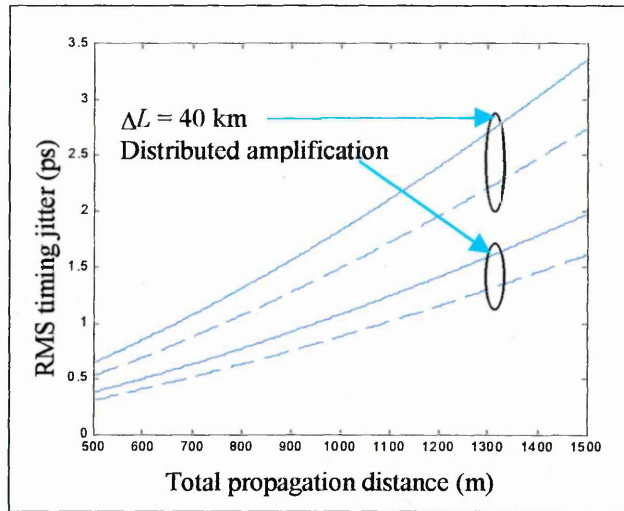


Fig. 8.2: RMS_{jitter} versus L_{tot} (solid lines represent FWHM soliton pulse width = 1 ps, dashed lines represent FWHM soliton pulse width = 1.5 ps).

Figure 8.3 shows RIN_{NOLM} versus the total walk-off time for $\Delta L = 40$ km and 0 km. The FWHM signal pulse width and the total propagation distance used in the simulation are 1 ps and 1000 km, respectively. The parameters of NOLM demultiplexers for calculating the relative intensity noise are listed in Table 8.1. The procedures for calculating RIN_{NOLM} were described in Chapter 6. The calculated RMS timing jitter for $\Delta L = 40$ km and 0 km are 1.83 ps and 0.88 ps, respectively. Figure 8.3 shows that RIN_{NOLM} for the total walk-off time of 1 ps is reduced by more than 10 dB for distributed amplification. The dependence of RIN_{NOLM} on ΔL decreases as the total walk-off time increases, as shown in Fig. 8.3. RIN_{NOLM} becomes independent of ΔL for total walk-off time > 12 ps. The other characteristics of RIN_{NOLM} shown in Fig. 8.3 were described and analysed in Chapter 6.

Table 8.1: Parameters of the NOLM demultiplexer	
Parameters	Values
β_2	-5 ps ² /km
Fibre loop length	3 km

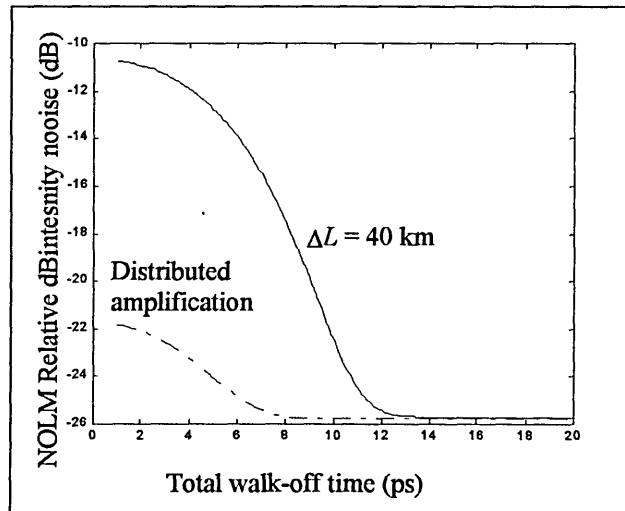


Fig. 8.3: RIN_{NOLM} versus total walk-off time.

8.3 Receiver Model

The receiver model for the BER analysis is adapted from [3], [65], [150]. Figure 8.4 shows a typical block diagram of a high-speed optical receiver employing an all-optical time division demultiplexer, an optical pre-amplifier, an optical band-pass filter (BPF) and a conventional optical receiver using PIN photodiode. The all-optical demultiplexer could be a NOLM or TOAD demultiplexer. Comparisons in terms of BER between the two types of demultiplexers will be presented in the next section based on the configuration illustrated in Fig. 8.4.

Since the intensity of high capacity OTDM signals needs to be kept sufficiently low in order to avoid the nonlinear effects described in Chapter 2, an optical pre-amplifier is required to boost the low-intensity demultiplexed signal for improving the BER performance. The optical pre-amplifier is especially important for TOAD demultiplexer as the additional limitation of signal intensity in order not to perturb the gain/phase dynamics of the SLA inside the fibre loop, as was discussed in Chapter 7. The optical filter in Fig. 8.4 reduces the noise generated from the optical amplifier, which will be described later in

this section. The conventional optical receiver consists of a PIN photodiode, and electrical amplifier and a decision circuit.

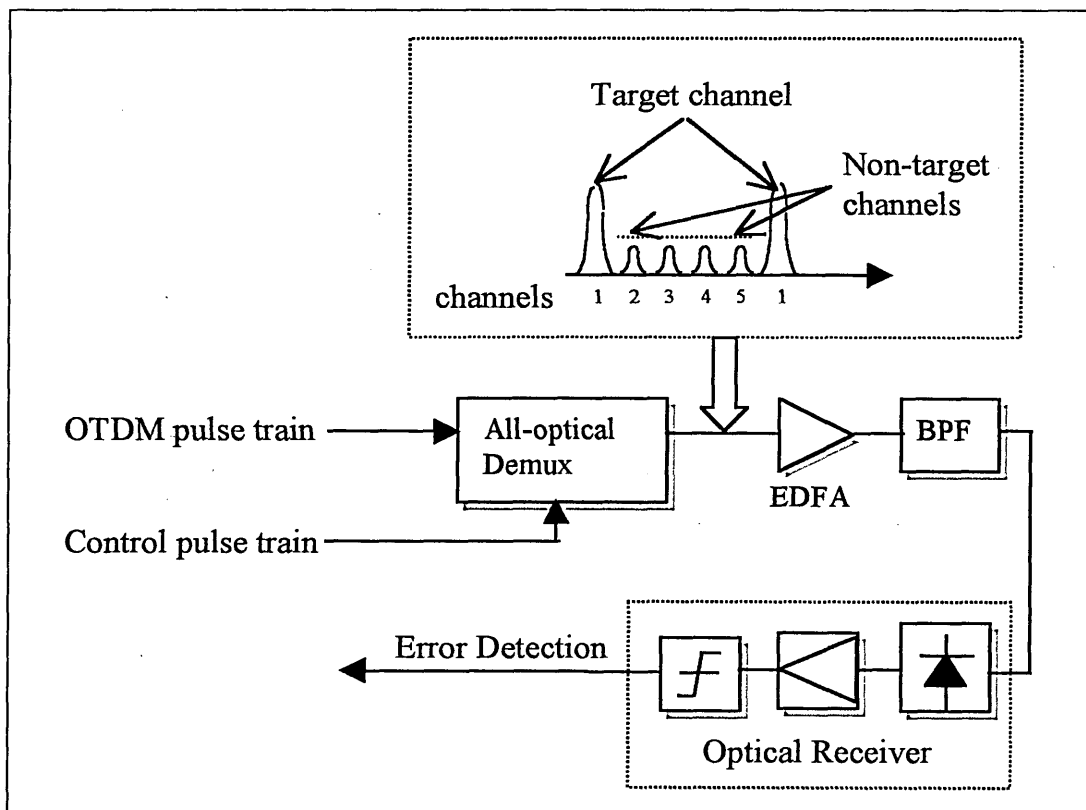


Fig. 8.4. Block diagram for the receiver model.

The incoming OTDM signal, with a bit rate $R_B = M_{TDM}R_b$, where M_{TDM} and R_b are the time division multiplication factor and the baseband data rate, respectively, is fed into the all-optical time division demultiplexer. A control pulse train is also coupled into the demultiplexer for extracting the target channel from the OTDM signal. Due to the crosstalk introduced in the demultiplexing process, the demultiplexed optical signal contains not only the target channel but also the non-target channels with reduced amplitude, as shown in the inset of Fig. 8.4. The intensity of the demultiplexed optical signal is boosted by the optical pre-amplifier. The amplified spontaneous emission from the optical preamplifier adds a wide spectrum of optical field onto the demultiplexed optical signal. After being detected by the PIN photodiode, the ASE optical field will eventually become one of the major noise sources. The function of the optical filter is to cut off the excess ASE optical

field beyond the signal spectrum. The PIN photodiode converts the received optical power into an equivalent electrical current, which is then converted to voltage signal by an electrical amplifier. The input to the electrical amplifier is assumed to be terminated with a standard 50Ω load resistor (a low impedance front-end design). This straightforward approach has the advantage of high bandwidth, but at the expense of high thermal noise [150]-[151]. Finally, the output voltage is sampled periodically by a decision circuit for estimating the correct state (mark/space) of each bit.

Assuming that the probabilities of mark and space are equal, the average photo current for mark \overline{I}_m ; and space \overline{I}_s are given as, respectively:

$$\overline{I}_m = R \cdot \eta_{in} \cdot \eta_{out} \cdot G \cdot L_f \cdot \eta_{DEMUX} \cdot P_{sig} \cdot [1 + RXT_{DEMUX} + NXT_{DEMUX}], \quad (8.8)$$

$$\overline{I}_s = R \cdot \eta_{in} \cdot \eta_{out} \cdot G \cdot L_f \cdot \eta_{DEMUX} \cdot P_{sig} \cdot [RXT_{DEMUX} + NXT_{DEMUX}], \quad (8.9)$$

where R is the responsivity of the photo-detector, G is the gain of the optical pre-amplifier, L_f is the loss due to the optical filter, η_{DEMUX} is the switching ratio of the target pulse energy, P_{sig} is the pre-amplified average signal power for a mark (excluding crosstalk), η_{in} and η_{out} are the input and output coupling efficiencies of the optical amplifier, respectively. The subscript $DEMUX$ is either $NOLM$ or $TOAD$, representing for NOLM and TOAD crosstalk, respectively. The calculation procedures for RXT_{NOLM} , RXT_{TOAD} , NXT_{NOLM} and NXT_{TOAD} were outlined in Chapters 6 and 7. \overline{I}_m and \overline{I}_s are the average values of photo-current for mark and space, respectively. The average photo-current (\overline{I}_m or \overline{I}_s) is calculated over the bit duration of the demultiplexed channel, not the high-capacity OTDM signal. The generated photo-current is then converted to voltage signal, which is sampled by the decision circuit to determine the binary level (i.e. mark or space)

of the for individual bits of the demultiplexed data signal. The output voltage of the optical receiver is related to the photo-current by:

$$V_{out}(\omega) = R_T \cdot H_T(\omega) \cdot I_{ph}(\omega), \quad (8.10)$$

where $V_{out}(\omega)$ is the output voltage's spectrum, $I_{ph}(\omega)$ is the photo-current's spectrum, $H_T(\omega)$ is the overall transfer function of the optical receiver, and R_T is the a frequency-independent constant with dimensions of resistance. For an on-off keying signal, the voltage signal in time domain can be represented by [150]:

$$V_{out}(t) = \sum_{k=-\infty}^{\infty} S_k \cdot h_{out}(t - k \cdot T), \quad (8.11)$$

where S_k takes on one of two discrete values $S(1)$ and $S(0)$, which represent mark and space, respectively, T is the bit duration of the demultiplexed signal, and h_{out} is the output pulse profile. If $h_{out}(t)$ peaks at $t = 0$, the sampling points of $V_s(t)$ for determining mark and space should be at $t = 0, T, 2T, 3T \dots$ etc. At the decision circuit, the sampled voltage for determining mark and space depends on the input photo-current and the system transfer function, according to (8.10). Nevertheless, using the normalisation method given in Ref. 150, the sampled output voltage can be directly related to the input photo-current regardless of the system transfer function, as given by:

$$S(1) = R_T \cdot \overline{I_m}. \quad (8.12a)$$

$$S(0) = R_T \cdot \overline{I_s}. \quad (8.12b)$$

According to (8.12), the sampled voltages for mark and space are proportional to $\overline{I_m}$ and $\overline{I_s}$, respectively. It is convenient to remove the constant R_T from (8.12) and define the mark and space in terms of current, i.e. to $\overline{I_m}$ and $\overline{I_s}$.

Because of the existence of various noise sources, the average photo-current will not always take on two discrete states, \overline{I}_m and \overline{I}_s . Instead, the average photo-current for mark and space would be two Gaussian probability functions with mean values equal to \overline{I}_m and \overline{I}_s , respectively [3], [150]. The variances of the two probability functions represent the noise variances of the average photo-current. Expressions for calculating variances of relative intensity noise [65], optical pre-amplifier noise [3] and receiver noise [65] for mark and space are given by:

$$\sigma_{RIN,m}^2 = \overline{I}_m^{-2} \cdot RIN_T \cdot B_e + \overline{I}_{sig}^{-2} \cdot RIN_{DEMUX}, \quad (8.13)$$

$$\sigma_{RIN,s}^2 = \overline{I}_s^{-2} \cdot RIN_T \cdot B_e, \quad (8.14)$$

$$\sigma_{amp,x}^2 = 4 \cdot \overline{I}_x \cdot I_{sp} \cdot B_e / B_o + I_{sp}^2 \cdot B_e \cdot (2 \cdot B_o - B_e) / B_o^2, \quad (8.15)$$

$$\sigma_{rece,x}^2 = 2 \cdot q \cdot (\overline{I}_x + I_{sp}) \cdot B_e + \left(\frac{4 \cdot K \cdot T_k}{R_L} + \overline{i_a}^2 \right) \cdot B_e, \quad (8.16)$$

where \overline{I}_x is the average photo-current, with x representing mark or space, RIN_T is the relative intensity noise associated with the transmitter, \overline{I}_{sig} is the average photo-current for a mark excluding crosstalk, the subscript $DEMUX$ in (8.13) represents RIN_{NOLM} or RIN_{TOAD} , B_e is the electrical bandwidth, B_o is the bandwidth of the optical filter, q is the electron charge, K is the Boltzman constant, T_k is the temperature in Kelvin, R_L is the load resistance of the photo-detector, and $\overline{i_a}^2$ is the power spectral density of the electrical input noise current.

In (8.15), the first and second terms represent the beat noise between the signal and amplified spontaneous emission, and the beat noise between ASE-ASE components, respectively. I_{sp} in (8.15) represents the average photo-current equivalent of ASE and is given by:

$$I_{sp} = N_{sp} \cdot (G-1) \cdot q \cdot B_o \cdot \eta_{out} \cdot L_f, \quad (8.17)$$

where N_{sp} is the population inversion factor of the optical pre-amplifier. For TOAD demultiplexing, the SLA inside the fibre loop will also generate some ASE noise. The ASE noise of the SLA can be accounted for by replacing the TOAD gain at the output port of the TOAD demultiplexer with G in (8.17).

As mentioned earlier, the decision circuit samples the output voltage for determining mark and space for individual bits. The variances given in (8.13)-(8.16) are the equivalent current noises prior to the decision circuit, excluding the effective resistance of the receiver system (i.e. R_T in (8.12)). In deriving (8.13)-(8.16), the system transfer function of the optical receiver is assumed to be a rectangular spectrum with bandwidth B_e , using the normalisation method given in Ref. 150. Higher BER performance could be achieved by using a matched filter to maximise the signal-to-noise ratio at the sample points or to minimise the inter-symbol interference between adjacent bits [152]. However, the matched filter design is not adopted in the BER analysis as this approach requires tailoring the system transfer function with the bandwidth and shape of the input photo-current. The receiver model described in this section only serves the function of providing a common ground for performance comparisons between the two types of all-optical demultiplexers.

The expression for calculating BER is adopted from Ref. 3, and is given as:

$$BER = \frac{1}{\sqrt{2 \cdot \pi}} \cdot \frac{\exp\left(-\frac{Q^2}{2}\right)}{Q}, \quad (8.18)$$

where Q is defined as

$$Q = \frac{\bar{I}_m - \bar{I}_s}{\sqrt{\sigma_{RIN,m}^2 + \sigma_{RIN,s}^2 + \sigma_{amp,m}^2 + \sigma_{amp,s}^2 + \sigma_{rece,m}^2 + \sigma_{rece,s}^2}}.$$

8.4 BER Analysis

In this section, the receiver model described in Section 8.3 is adopted for the BER analysis. The objective of this analysis is to compare the power penalty of NOLM and TOAD demultiplexers for various aggregate bit rates. The parameters used for the receiver model are similar to Ref. 65, as listed in Table 8.2. Table 8.2 is used as simulation parameters for 100 Gb/s and 300 Gb/s demultiplexing in this section. The root-mean-square timing jitter RMS_{jitter} used for the simulations is 1.25 ps. According to the simulation results of Figs. 8.1 and 8.2, RMS_{jitter} increases as the pulse width decreases. A fixed value of RMS_{jitter} for both 100 Gb/s and 300 Gb/s demultiplexing implies that the propagation distance of the 300 Gb/s signal is shorter than that of the 100 Gb/s signal.

Figure 8.5 shows a plot of BER versus average received optical power (P_{sig}) for baseline detection. The baseline bit rate is 10 Gb/s, which corresponds to $M_{TDM} = 10$ and 30 for total bit rates of 100 Gb/s and 300 Gb/s, respectively. As can be seen from Fig. 8.5, to achieve a BER 10^{-9} the average received power requirement is -32.75 dBm.

Parameters	Values
η_{in}	-2 dB
η_{out}	-2 dB
G (preamplifier gain)	30 dB
L_f	-2 dB
R	1.25 A/W
R_L	50 Ω
T_k	293 K
N_{sp}	2
$\overline{i_a^2}$	100 pA ²
B_e	0.7 R_b
B_o	374 GHz
RIN_T	-150 dB/Hz
RMS_{jitter}	1.25 ps
Duty Cycle of the OTDM signal	0.25

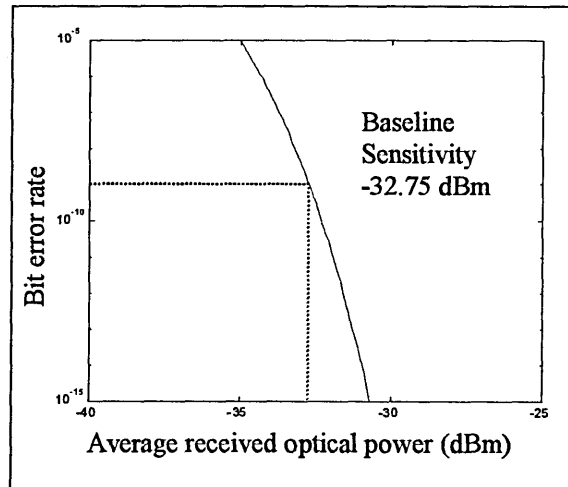


Fig. 8.5. BER versus the average received optical power for baseline bit rate 10 Gb/s.

Figure 8.6 shows a plot of BER versus average received optical power for baseline detection at bit rate of 1 Gb/s. This baseline bit rate corresponds to $M_{TDM} = 100$ and 300 for total bit rates of 100 Gb/s and 300 Gb/s, respectively. Comparing Fig. 8.6 with Fig. 8.5, the sensitivity is increased by about 7 dBm for a decrease of baseline bit rate from 10 Gb/s to 1 Gb/s. This is due to the lower electrical bandwidth required in the optical receiver for the detection of lower bit rates. The electrical bandwidth is 0.7 of the baseline bit rate, according to Table 8.2. A smaller electrical bandwidth results in decreased noise variances (see (8.13) – (8.16)), thus improving the receiver sensitivity.

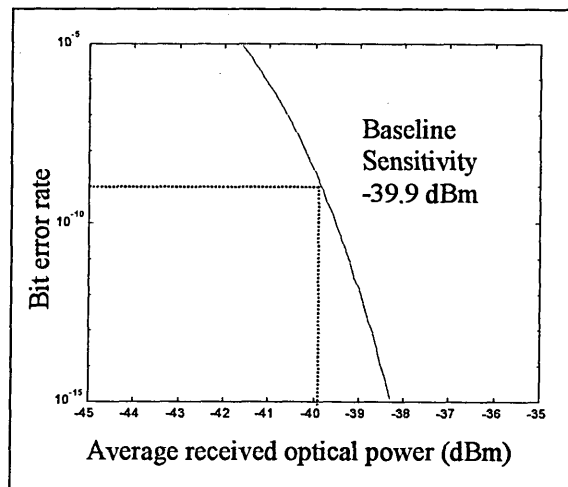


Fig. 8.6: BER versus the average received optical power for baseline bit rate 1 Gb/s.

Figures 8.5 and 8.6 show the benchmark performances of BER for baseline signals. For an incoming high-capacity OTDM signal, an all-optical time division demultiplexer (NOLM or TOAD) is required to demultiplex the target channel from the OTDM signal, as shown in Fig. 8.4. With the inclusion of noise and crosstalk due to the demultiplexer, the BER at the output of the optical receiver will degrade from its benchmark performances shown in Figs. 8.5 and 8.6. A signal power penalty P_{sig} is attributed to the demultiplexer for maintaining the BER of 10^{-9} . In the rest of this section, the minimum power penalties of NOLM and TOAD demultiplexing for various OTDM bit rates are calculated and compared.

8.4.1 Simulation results for 100 Gb/s demultiplexing

8.4.1.1 100 Gb/s demultiplexing (10 OTDM channels)

All-optical time division demultiplexers (NOLM or TOAD) degrade the sensitivity of the optical receiver in four ways as outlined below:

- (i) Relative intensity noise (RIN_{NOLM} or RIN_{TOAD}),
- (ii) Residual crosstalk (RXT_{NOLM} or RXT_{TOAD}),
- (iii) Neighbour channel crosstalk (NXT_{NOLM} and NXT_{TOAD}),
- (iv) Energy switching ratio (η_{DEMUX}).

The crosstalk and noise associated with the two types of demultiplexers have been discussed in Chapters 6 and 7. η_{DEMUX} is defined as the energy ratio between the demultiplexed target pulse and the input target pulse. In NOLM-based demultiplexer, the maximum η_{DEMUX} will approach 100% by employing a square switching window. η_{DEMUX} could be greater than one in TOAD-based demultiplexer, due to the gain of the asymmetric SLA. The TOAD gain amplifies the demultiplexed signal energy and leads to a larger Q factor in (8.8). As a result, the effective gain of the demultiplexed signals, before the photo-detector, is equal to TOAD gain + preamplifier gain. The effective gain of TOAD

demultiplexer is greater than that of NOLM demultiplexer. The difference of effective gain between TOAD and NOLM demultiplexers makes it difficult to compare the power penalty performance between the two. Furthermore, an excessive effective gain results in gain saturation of the preamplifier. In practice, higher gain will decrease the dynamic range of the OTDM signal. In order to have the same value of effective gain for both TOAD and NOLM receivers, the preamplifier gain in the receiver model is adjusted to compensate for the TOAD gain. For example, if the TOAD gain is 3 dB, the preamplifier gain is reduced from 30 dB to 27 dB, making the overall gain equal to a constant value of 30 dB.

The first and second half of this subsection are dedicated for minimisation of power penalties of NOLM and TOAD demultiplexers, respectively. Figure 8.7 shows RIN_{NOLM} versus the total walk-off time for different values of fibre loop length L and first order dispersion coefficient β_2 . Some RIN_{NOLM} characteristics shown in Fig. 8.7 have already been discussed in Chapter 6. For all simulations shown in Fig. 8.7, RIN_{NOLM} keep decreasing with the total walk-off time until it reaches its minimum value of -25.7dB, where the total walk-off time is greater than 9 ps. Simulations using other NOLM parameters (not shown here) lead to the same minimum RIN_{NOLM} , as illustrated in Fig. 8.7. The flat residual RIN_{NOLM} Vs. total walk-off time is a phenomenon that is contradictory of what is intuitively expected. If the total walk-off time is increased to infinity, RIN_{NOLM} will approach zero rather than remain at -25.7 dB. This phenomenon can be explained by the relatively ratio between NOLM window size and RMS_{jitter} . The RMS timing jitter used in the simulation is 1.25 ps. When the total walk-off time has been increased to the point where the NOLM window size is much larger than RMS_{jitter} , further widening of NOLM window will not affect the RMS_{jitter} -induced fluctuation of demultiplexed signal energy in a significant way. Of course, theoretically, if the total-walk-off time is increased to infinity, the RIN_{NOLM} will approach to absolute zero. However, the rate of decrease of RIN_{NOLM}

beyond -25.7 dB is so slow that RIN_{NOLM} can be considered to be independent of the total walk-off time. The minimum attainable RIN_{NOLM} (-25.7 dB) set a lower limit of the power penalty of NOLM demultiplexer. Using the minimum RIN_{NOLM} for calculating the BER 100 Gbps NOLM demultiplexing (10 channels), the associated power penalty is calculated to be 0.37 dB, with the assumption of zero NOLM crosstalk and maximum energy switching ratio.

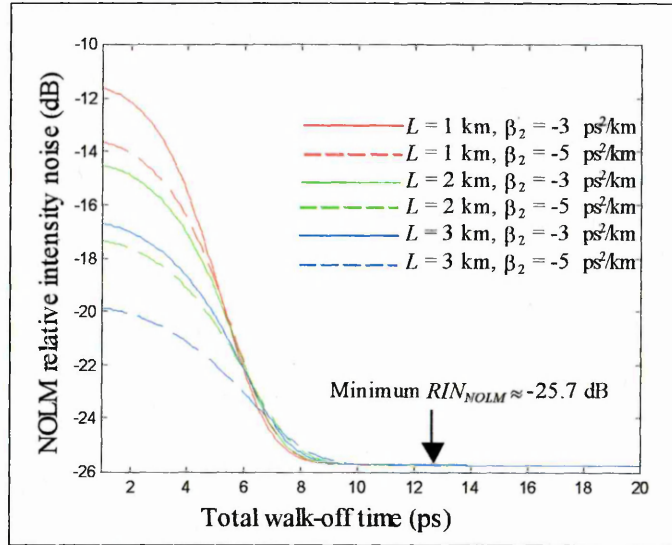


Fig. 8.7. NOLM relative intensity noise versus the total walk-off time for different values of L and β_2 .

Apart from RIN_{NOLM} , another important factor that increases the NOLM power penalty is the NOLM crosstalk (RXT_{NOLM} and NXT_{NOLM}). Figure 8.8 shows the total walk-off time versus RXT_{NOLM} and NXT_{NOLM} for various NOLM parameters at 100 Gbps demultiplexing (10 channels). Details of NOLM crosstalk characteristics can be referred to Chapter 6. A marked feature shown in Fig. 8.8 is the dominance of RXT_{NOLM} over RIN_{NOLM} for all simulation parameters, with the exception of the very large walk-off time (> 20 ps). Therefore, for demultiplexing the 10 Gb/s target signal from the 100 Gb/s OTDM signal, the effect of the neighbour channel crosstalk is negligible in the calculation of NOLM power penalty.

In this subsection, RIN_{NOLM} and RXT_{NOLM} of NOLM demultiplexing are optimised for minimisation of the power penalty. The effects of NXT_{NOLM} are excluded from the calculation due to the reason outlined in the previous paragraph. RIN_{NOLM} and RXT_{NOLM} vary with fibre loop length L , first order dispersion coefficient β_2 and the total walk-off time between the control and signal pulses (T_wL) (see Chapter 6). According to Table 6.1, RIN_{NOLM} (RXT_{NOLM}) decreases (increases) with L , β_2 , and T_wL . For example, increasing L will decrease RIN_{NOLM} at the expense of an increased RXT_{NOLM} . Minimisation of NOLM power penalty can be achieved by optimising L , β_2 , and T_wL .

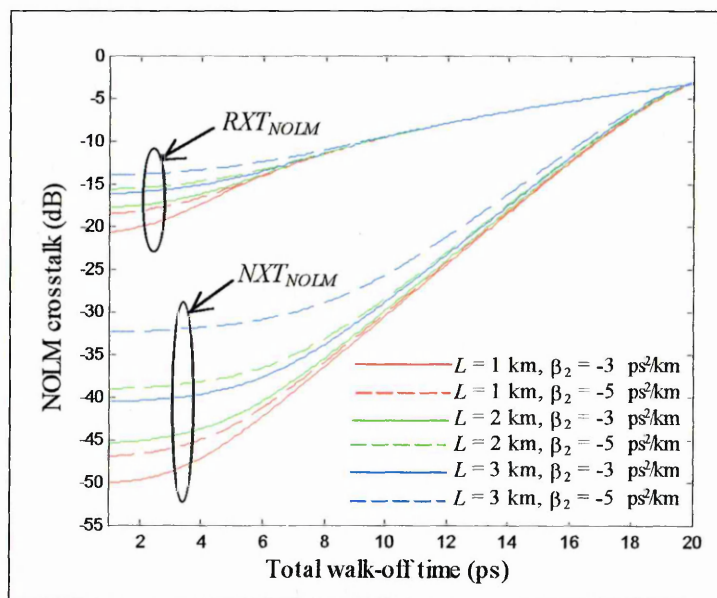


Fig. 8.8. NOLM crosstalk versus the total walk-off time for different values of L and β_2 .

Referring back to Fig. 8.7, RIN_{NOLM} decreases with the total walk-off time until it drops to -25.7 dB at a total walk-off time of 9 ps. No further increase in RIN_{NOLM} is observed by increasing the total walk-off time beyond 9 ps. Figure 8.9 shows RIN_{NOLM} and RXT_{NOLM} versus the total walk-off time for $\beta_2 = -5 \text{ ps}^2/\text{km}$ and $L = 1 \text{ km}$. Here, the minimum walk-off time required to maintain RIN_{NOLM} of -25.7 dB is 11.5 ps, at which the NOLM residual crosstalk is equal to -8.2 dB. Assuming that RIN_{NOLM} is fixed at -25.7 dB, the minimum NOLM power penalty can be calculated by substituting RIN_{NOLM} (-25.7 dB) and RXT_{NOLM}

(-8.2 dB) into the receiver model described in Section 8.3. The minimum power penalty for $\beta_2 = -5 \text{ ps}^2/\text{km}$ and $L = 1 \text{ km}$ is 1.15 dB. The above calculation procedures are applied to optimise other values of RIN_{NOLM} and NOLM parameters for minimising the power penalty. The results are shown in Table 8.3.

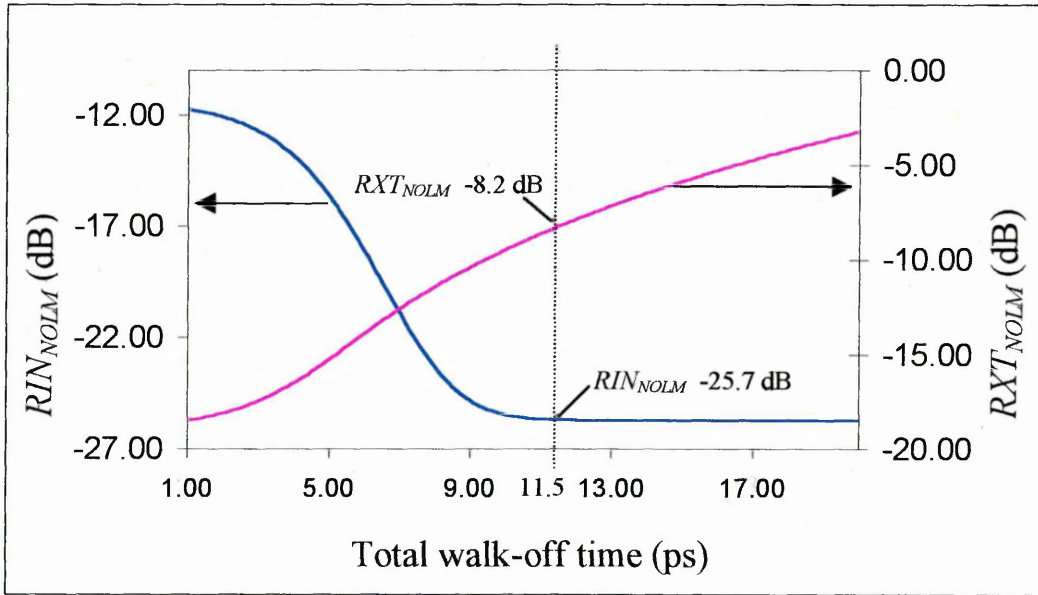


Fig. 8.9. RIN_{NOLM} and RXT_{NOLM} versus the total walk-off time for $\beta_2 = -5 \text{ ps}^2/\text{km}$ and $L = 1 \text{ km}$.

The simulation results listed in Table 8.3 are grouped into three values of RIN_{NOLM} : -25.7 dB, -25 dB and -24 dB. For each of simulation results, the first column shows the minimum walk-off time required to keep RIN_{NOLM} not larger than -25.7 dB, -25 dB and -24 dB, respectively. The second column shows the residual crosstalk for the minimum walk-off time. The third column is the power penalty calculated from RXT_{NOLM} and RIN_{NOLM} . As shown in Table 8.3, decreasing L and $|\beta_2|$ will decrease the NOLM power penalty. The minimum power penalty for the RIN_{NOLM} of -25.7 dB is 1.15 dB. Increasing RIN_{NOLM} to -25 dB leads to a decrease of power penalty to 0.94 dB (yellow box in Table 8.3). Further decrease of RIN_{NOLM} will increase the power penalty. The minimum power penalty of NOLM demultiplexing is 0.94 dB. The NOLM parameters for the minimum power penalty are $\beta_2 = -3 \text{ ps}^2/\text{km}$, $L = 1 \text{ km}$, and the total walk-off time = 9.1 ps. Further

decrease of L and $|\beta_2|$ (not shown here) can only maintain (not decrease) the minimum power penalty. The calculation described above assumes 100% energy switching ratio (η_{DEMUX}). The validity of this assumption is verified by Fig. 8.10, which shows the energy switching ratio of 99.95% for the optimised NOLM parameters.

Table 8.3: NOLM parameters for minimum power penalty for 100 Gb/s demultiplexing (10 channels)

β_2 ps ² / km	L (km)	$RIN_{NOLM} = -25.7$ dB			$RIN_{NOLM} = -25$ dB			$RIN_{NOLM} = -24$ dB		
		$T_{\omega L}$ (ps)	RXT_{NOLM} (dB)	Power Penalty (dB)	$T_{\omega L}$ (ps)	RXT_{NOLM} (dB)	Power Penalty (dB)	$T_{\omega L}$ (ps)	RXT_{NOLM} (dB)	Power Penalty (dB)
-3	1	11.4	-8.3	1.15	9.1	-10.3	0.94	8.3	-11.1	0.99
-3	2	11.6	-8.2	1.17	9.2	-10.2	0.96	8.4	-11	1.00
-3	3	11.8	-8	1.20	9.3	-10.1	0.97	8.5	-10.9	1.01
-3	4	12.3	-7.6	11.28	9.4	-10	0.98	8.6	-10.7	1.03
-5	1	11.5	-8.2	1.17	9.2	-10.2	0.96	8.4	-11	1.00
-5	2	11.7	-8.1	1.19	9.4	-10	0.98	8.6	-10.8	1.02
-5	3	12	-7.9	1.22	9.7	-9.7	1.02	8.7	-10.5	1.05
-5	4	12.3	-7.6	1.28	9.8	-9.4	1.06	8.6	-10.2	1.08
-7	1	11.6	-8.2	1.17	9.3	-10.1	0.97	8.5	-10.9	1.01
-7	2	12	-7.9	1.22	9.7	-9.7	1.02	8.8	-10.4	1.06
-7	3	12.5	-7.5	1.30	9.9	-9.3	1.07	8.8	-10	1.11
-7	4	12.8	-7.2	1.36	9.9	-8.8	1.14	8.2	-9.7	1.14

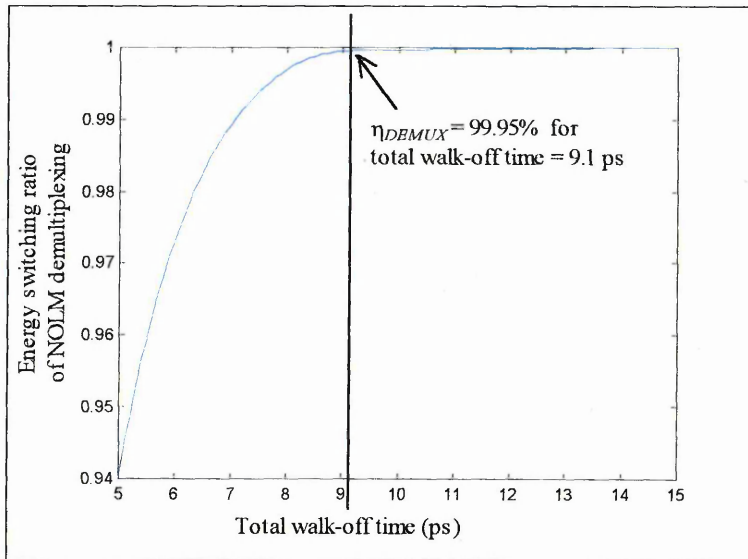


Fig. 8.10. η_{DEMUX} versus the total walk-off time for $\beta_2 = -3$ ps²/km, $L = 1$ km.

As discussed in Chapter 7, the TOAD parameters that affect the noise and crosstalk are T_{asy} and L_{SLA} . Simulation results of noise and crosstalk for the TOAD demultiplexer were presented and analysed in Chapter 7. Apart from noise and crosstalk, an essential factor that influences the power penalty is the switching ratio. Figure 8.11 shows η_{DEMUX} versus the SLA asymmetry for $L_{SLA} = 0.5$ mm, 0.3 mm and 0.1 mm. The unsaturated SLA gain is 5. The switching ratio is calculated from dividing the energy of the demultiplexed pulse by the energy of the input target pulse. The procedures of evaluating TOAD window for the demultiplexed pulse can be found in Chapter 7. In Fig. 8.11, η_{DEMUX} for all values of L_{SLA} increases from their minimum values to around 2.7 as the SLA asymmetry increases. The switching ratio is at its minimum for the SLA asymmetry close to zero, where double switching windows appear (see Chapter 7). For a shorter L_{SLA} , the switching ratio rises to its maximum level from a lower minimum value by a smaller increase of SLA asymmetry.

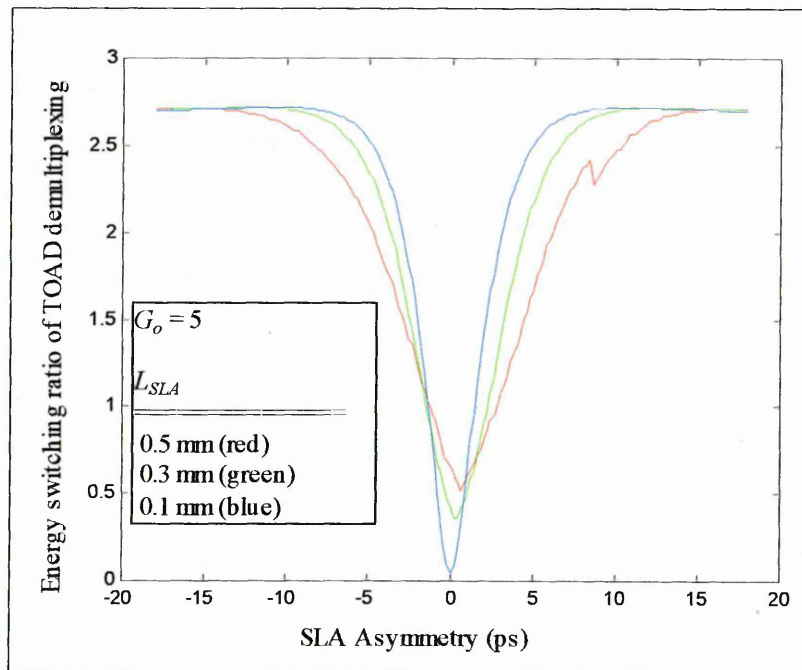


Fig. 8.11. TOAD energy switching ratio versus the SLA asymmetry for different values of SLA length.

The TOAD power penalty is calculated by substituting RIN_{TOAD} , RXT_{TOAD} , NXT_{TOAD} and η_{DEMUX} into the receiver model. Figure 8.12 shows TOAD power penalty versus the SLA

asymmetry for $L_{SLA} = 0.5$ mm, 0.3 mm and 0.1 mm. As shown in Fig. 8.12, the power penalty does not have physical solutions for -5 ps $< T_{asy} < 5$ ps. In this region, the BER at the receiver output will always be higher than 10^{-9} , even for very large input pulse energy. This is due to the large RIN_{TOAD} (see Chapter 7) and low switching ratio (shown in Fig. 8.11) in small SLA asymmetry. At $T_{asy} \approx 5$ ps / -5 ps, the highest calculable values of power penalty for $L_{SLA} = 0.5$ mm, 0.3 mm, 0.1 mm are 16 dB, 14 dB and 12 dB, respectively. Increasing the SLA asymmetry will decrease RIN_{TOAD} (see Chapter 7) and increase TOAD switching ratio (shown in Fig. 8.11). From $T_{asy} \approx -5$ ps to $T_{asy} \approx -10$, TOAD power penalty drops exponentially from more than 10 dB to less than 2 dB. The minimum power penalty is 0.55 dB. The TOAD parameters for minimisation of power penalty are $L_{SLA} = 0.1$ mm and $T_{asy} = -10.2$ ps. At $T_{asy} = -10.2$ ps, the power penalty drops no further when the SLA asymmetry is increased. As shown in Fig. 8.11 and the RIN_{TOAD} simulations in Chapter 7, RIN_{TOAD} (η_{DEMUX}) ceases decreasing (increasing) for large SLA asymmetry. On the other hand, since TOAD crosstalk increases with SLA asymmetry (see Chapter 7), the power penalty goes up for SLA asymmetry greater than 10.2 ps.

Also shown in Fig. 8.12, the red line in the positive T_{asy} region displays a spike characteristic for 8 ps $< T_{asy} < 11$ ps. This is due to the asymmetric shape of the TOAD window. In calculating the power penalty, the target pulse is positioned at the centre of the FWHM width of the TOAD window. Widening an asymmetric window moves the mid-point of the FWHM window width away from the asymmetric peak, causing an increase of RIN_{TOAD} and a decrease of switching ratio. In most cases, the decrease of power penalty due to the widened TOAD window will override the increase of power penalty due to the effect described above. Nevertheless, the spike (the sharp increase of the power penalty with the SLA asymmetry) in Fig. 8.12 occurs if the increase of power penalty due to the poor location of the target pulse cannot be compensated by the decrease of power penalty

due to the widened TOAD window. The spike shown in Fig. 8.12 is well beyond the minimised power penalty region. Therefore, no further investigation is done on this effect.

As concluded by the simulation results in Chapter 7, changing G_o does not have a significant effect on RIN_{TOAD} , RXT_{TOAD} and NXT_{TOAD} . Although increasing G_o will increase the output gain of the demultiplexed target pulse, the preamplifier gain is adjusted on the basis of the TOAD gain to make the overall gain equal to a constant value of 30 dB. Therefore, it can be predicted that G_o is not an important factor for the minimisation of power penalty. This is illustrated by Fig. 8.13, which shows the TOAD power penalty versus the SLA asymmetry for $G_o = 10$. Although G_o of Fig. 8.13 is doubled of that of Fig. 8.12, the minimum power penalty is still 0.55 dB.

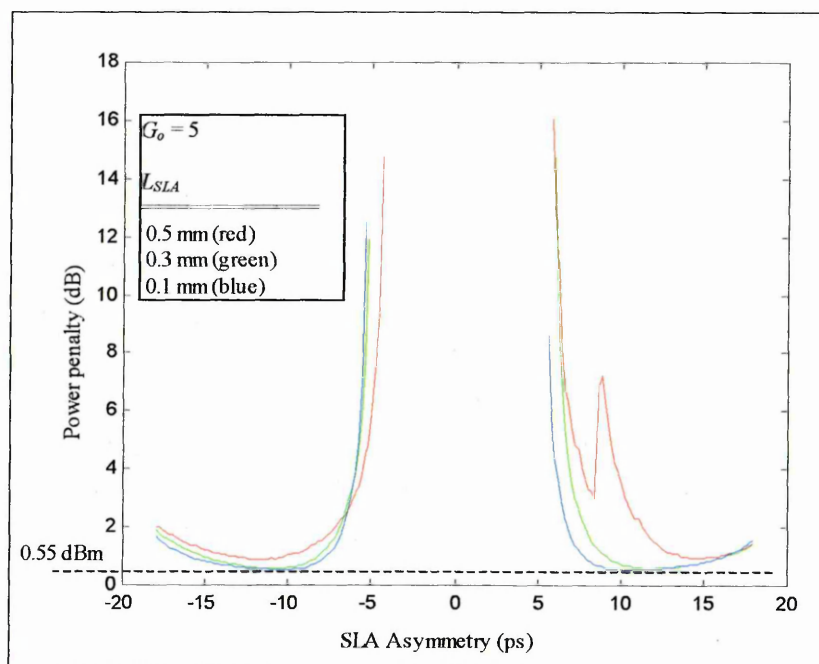


Fig. 8.12. TOAD power penalty versus the SLA asymmetry for 100 Gb/s demultiplexing (10 channels).

BER versus average received optical power for optimised NOLM and TOAD demultiplexers are plotted in Fig. 8.14. The demultiplexers' parameters used in the simulation are optimised for minimum power penalty. Also shown in Fig. 8.14 is the

baseline BER for comparison purpose. Figure 8.14 shows that TOAD has a slightly better BER performance than NOLM demultiplexer for 100 Gb/s OTDM signal of 10 channels.

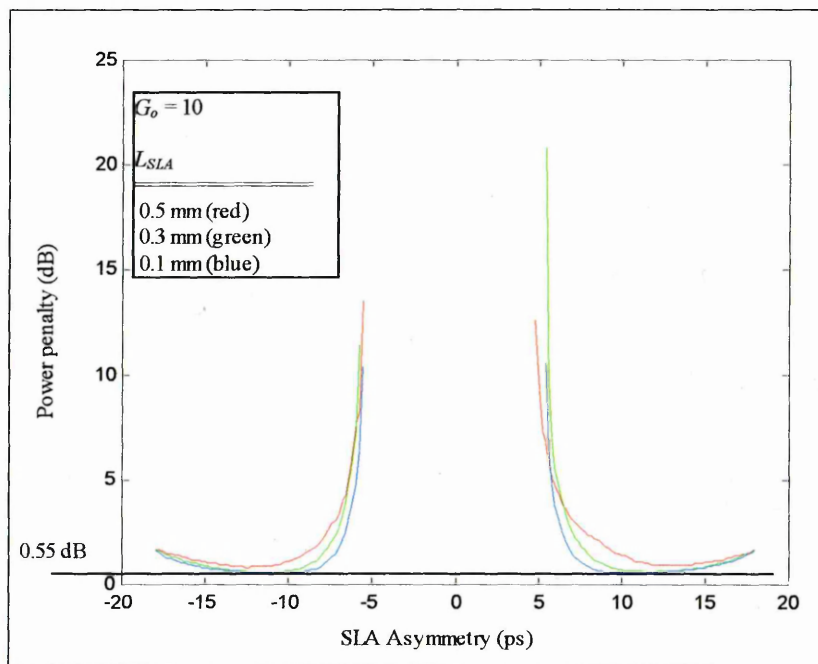


Fig. 8.13: TOAD power penalty versus the SLA asymmetry for 100 Gb/s demultiplexing (10 channels).

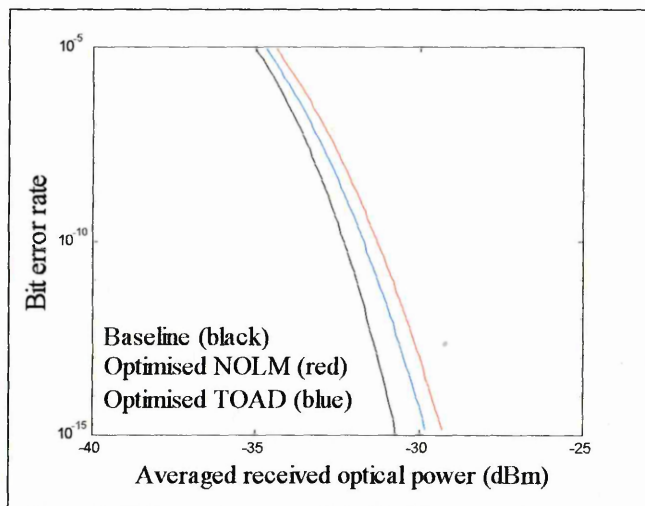


Fig. 8.14. BER versus the average received optical power for 100 Gb/s (10 channels) optimised NOLM and TOAD demultiplexing.

8.4.1.2 100 Gb/s demultiplexing (100 OTDM channels)

Following the same optimization procedures described in Section 8.4.1.1, the NOLM and TOAD parameters for minimising power penalty of 100 Gb/s (100 OTDM channels)

demultiplexing are calculated and presented in this subsection. The optimised parameters enable one to compare the BER performance of the two demultiplexers.

The calculated power penalties of NOLM demultiplexing for different values of β_2 and L are tabulated in Table 8.4, which is presented in a similar format to Table 8.3. Unlike Table 8.3, which only includes RXT_{NOLM} in the calculation of power penalty, both RXT_{NOLM} and NXT_{NOLM} are required here for evaluating power penalty. It has been shown in Chapter 6 that RXT_{NOLM} dominates over NXT_{NOLM} at high repetition rate of the control pulse (i.e. a smaller number of OTDM channels). However, since RXT_{NOLM} decreases as the number of channels increases (see Chapter 6), RXT_{NOLM} becomes comparable to NXT_{NOLM} for an increase of OTDM channels from 10 to 100.

Table 8.4: NOLM parameters for minimum power penalty for 100 Gb/s demultiplexing (100 channels)

β_2 ps ² /k m	L (km)	$RIN_{NOLM} = -25.7$ dB			$RIN_{NOLM} = -25$ dB			$RIN_{NOLM} = -24$ dB		
		$T_w L$ (ps)	$RXT_{NOLM} + NXT_{NOLM}$ (dB)	Power Penalty (dB)	$T_w L$ (ps)	$RXT_{NOLM} + NXT_{NOLM}$ (dB)	Power Penalty (dB)	$T_w L$ (ps)	$RXT_{NOLM} + NXT_{NOLM}$ (dB)	Power Penalty (dB)
-3	1	11.4	-17.4	0.37	9.1	-19.8	0.4	8.3	-20.7	0.49
-3	2	11.6	-17.1	0.37	9.2	-19.7	0.4	8.4	-20.4	0.49
-3	3	11.8	-16.8	0.38	9.3	-19.5	0.41	8.5	-20.2	0.5
-3	4	12.3	-15.9	0.39	9.4	-19.1	0.41	8.6	-20	0.5
-5	1	11.5	-17.2	0.37	9.2	-19.7	0.4	8.4	-20.5	0.49
-5	2	11.7	-16.8	0.38	9.4	-19.3	0.41	8.6	-20.1	0.5
-5	3	12	-15.9	0.39	9.7	-18.5	0.41	8.7	-19.4	0.5
-5	4	12.3	-14.8	0.4	9.8	-17.5	0.42	8.6	-18.5	0.51
-7	1	11.6	-17	0.37	9.3	-19.5	0.41	8.5	-20.3	0.5
-7	2	12	-16.1	0.38	9.7	-18.6	0.41	8.8	-19.5	0.5
-7	3	12.5	-14.3	0.41	9.9	-17.1	0.42	8.8	-18	0.51
-7	4	12.8	-12.5	0.45	9.9	-15.3	0.45	8.2	-16.5	0.52

According to Table 8.4, the minimum power penalty is 0.37 dB, which is attained by setting $\beta_2 = -3$ ps²/km, $L = 1$ km and $T_w L = 11.4$ ps. Comparing Tables 8.3 and 8.4, increasing the number of channels of 100 Gb/s NOLM demultiplexing from 10 to 100 will result in a decrease of power penalty by about 0.57 dB.

The power penalty versus the SLA asymmetry for different values of L_{SLA} and T_{asy} at 100 Gb/s TOAD demultiplexing (100 channels) are plotted in Fig. 8.15. The minimum power penalty is calculated to be 0.44 dB. According to Fig. 8.15, the optimum TOAD parameters for the minimum power penalty are $L_{SLA} = 0.1$ mm and $T_{asy} = -10.4$ ps.

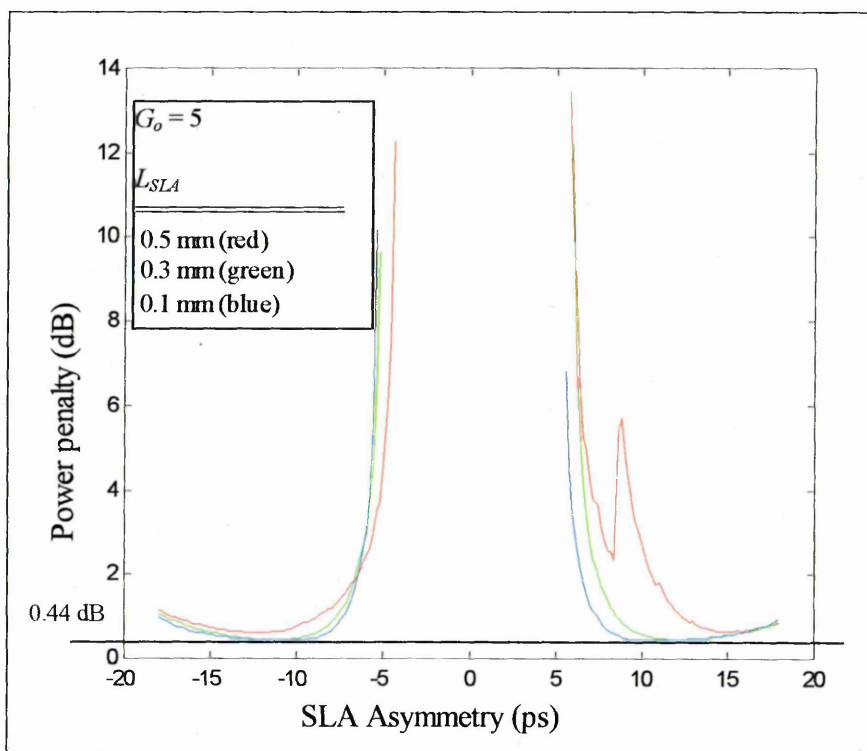


Fig. 8.15. TOAD power penalty versus the SLA asymmetry for 100 Gb/s demultiplexing (100 channels).

BER versus the average received optical power for 100 Gb/s (100 channels) optimised NOLM and TOAD demultiplexing are plotted in Fig. 8.16. As shown in Fig. 8.16, the optimised NOLM and TOAD schemes have nearly the same BER performance for 100 Gb/s (100 channels) demultiplexing.

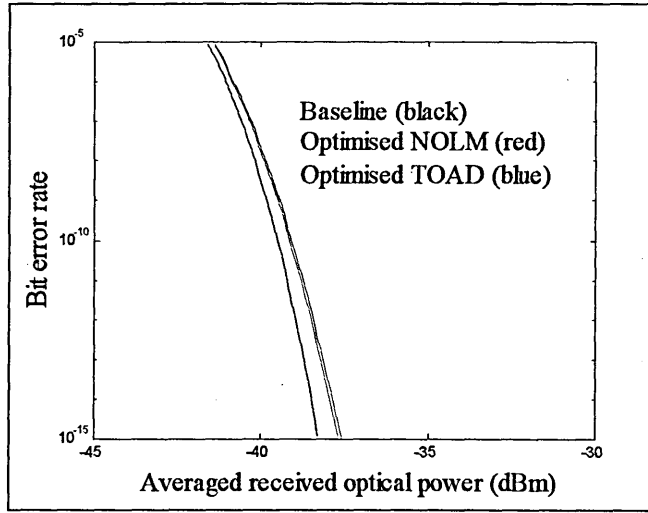


Fig. 8.16: BER versus the average received optical power for 100 Gb/s (100 channels) optimised NOLM and TOAD demultiplexing.

8.4.2 Simulation results for 300 Gb/s demultiplexing

8.4.2.1 300 Gb/s demultiplexing (30 OTDM channels)

Simulation results in Chapter 6 show that RIN_{NOLM} increases as crosstalk decreases. Minimisation of NOLM power penalty is a compromise between RIN_{NOLM} and NOLM crosstalk. According to Tables 8.3 and 8.4, the values of RIN_{NOLM} for optimised 100 Gb/s NOLM demultiplexing from 10 and 100 OTDM channels are -25 dB and -25.7 dB, respectively. The crosstalk for 100 Gb/s demultiplexing is inherently small, thus RIN_{NOLM} is the major factor affecting the power penalty. Nevertheless, the balance of RIN_{NOLM} and crosstalk is different for higher bit rate OTDM signals. The optimisation results for 300 Gb/s NOLM demultiplexing (30 OTDM channels) are shown in Table 8.5. The minimum power penalty is 3.82 dB. The value of RIN_{NOLM} for the minimum power penalty is -21 dB, which is considerably higher than the cases of 100 Gb/s demultiplexing. A larger RIN_{NOLM} is required to suppress the higher crosstalk in 300 Gb/s demultiplexing. Also shown in Table 8.5, the NOLM parameters for the minimum power penalty are $\beta_2 = -3$ ps²/km, $L = 1$ km and $T_w L = 6.4$ ps.

The power penalty of 300 Gb/s (30 channels) TOAD demultiplexing for various L_{SLA} are plotted in Fig. 8.17. In the positive region of T_{asy} , the change of power penalty for $L_{SLA} = 0.5$ mm against T_{asy} is so large that a discontinuity is observed at around $T_{asy} = 9$ ps. This is due to the spike effect of RIN_{TOAD} discussed in Section 8.4.1. As shown in Fig. 8.17, the minimum power penalty for 300 Gb/s (30 channels) TOAD demultiplexing is 3.5 dB. The optimised TOAD parameters for the minimum power penalty are $L_{SLA} = 0.1$ mm and $T_{asy} = -6.8$ ps.

Table 8.5: NOLM parameters for minimum power penalty for 300 Gb/s demultiplexing (30 channels).

β_2 ps ² /k m	L (km)	$RIN_{NOLM} = -22$ dB			$RIN_{NOLM} = -21$ dB			$RIN_{NOLM} = -20$ dB		
		$T_w L$ (ps)	$RXT_{NOL}^M +$ NXT_{NOL}^M (dB)	Power Penalty (dB)	$T_w L$ (ps)	$RXT_{NOL}^M +$ NXT_{NOL}^M (dB)	Power Penalty (dB)	$T_w L$ (ps)	$RXT_{NOL}^M +$ NXT_{NOL}^M (dB)	Power Penalty (dB)
-3	1	6.7	-1.6	3.99	6.4	-2.6	3.82	6.2	-3.3	3.95
-3	2	6.7	-1.6	3.99	6.5	-2	4.11	6.2	-2.7	4.22
-3	3	6.8	-1.3	4.15	6.5	-1.7	4.26	6.2	-2.13	4.5
-3	4	6.7	-1.1	4.26	6.3	-1.3	4.48	5.9	-1.9	4.62
-5	1	6.7	-1.7	3.94	6.5	-2.1	4.06	6.2	-2.9	4.13
-5	2	6.9	-1.1	4.26	6.5	-1.6	4.32	6.2	-2	4.56
-5	3	6.6	-0.9	4.37	6.1	-1.3	4.48	5.5	-1.7	4.72
-5	4	5.9	-0.7	4.49	5	-1.1	4.59	3.9	-1.5	4.83
-7	1	6.8	-1.4	4.1	6.5	-2	4.11	6.3	-2.4	4.36
-7	2	6.8	-0.9	4.37	6.3	-1.3	4.48	5.7	-1.7	4.72
-7	3	5.8	-0.7	3.78	4.8	-1.0	4.65	3.4	-1.4	4.88

BER versus average received optical power for optimised NOLM and TOAD demultiplexing are plotted in Fig. 8.18. Also shown for comparison is the plot for the base line. Figure 8.18 shows that, for 300 Gb/s OTDM signal of 30 channels, TOAD offers a slightly improved BER performance compared with NOLM demultiplexer. At BER of 10^{-9} , the average received power for the base line case is ~ 32.5 dB, whereas for TOAD and NOLM the required power are 29.5 dB and 29 dB, respectively.

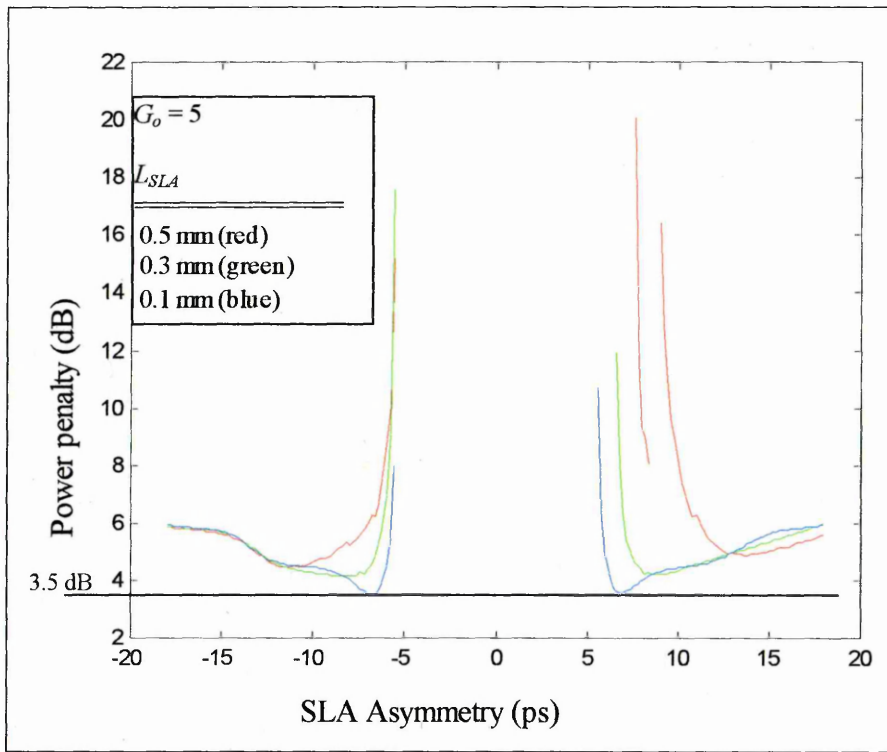


Fig. 8.17. TOAD power penalty versus the SLA asymmetry for 300 Gb/s demultiplexing (30 channels).

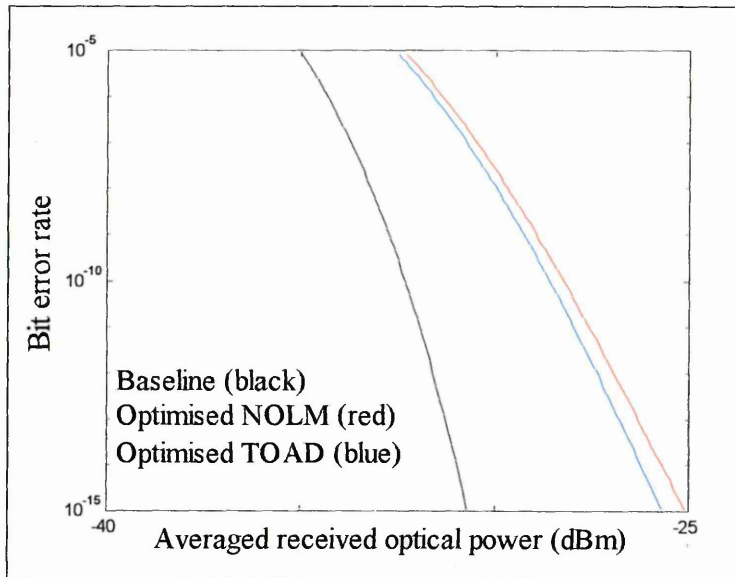


Fig. 8.18. BER versus the average received optical power for 300 Gb/s (30 channels) optimised NOLM and TOAD demultiplexing.

8.4.2.2 300 Gb/s demultiplexing (300 OTDM channels)

The optimisation results for 300 Gb/s NOLM demultiplexing (300 OTDM channels) are shown in Table 8.6. The minimum power penalty is 1.98 dB. The NOLM parameters for the minimum power penalty are $\beta_2 = -3 \text{ ps}^2/\text{km}$, $L = 1 \text{ km}$, and $T_w L = 6.4 \text{ ps}$. Comparing Table 8.5 with Table 8.6, the optimised 300 Gb/s NOLM demultiplexing shows a decrease in power penalty from 3.82 to 1.98 when the number of channels is increased from 30 to 300.

Table 8.6: NOLM parameters for minimum power penalty for 300 Gb/s demultiplexing (300 channels).

β_2 ps ² /k m	L (km)	$RIN_{NOLM} = -22 \text{ dB}$			$RIN_{NOLM} = -21 \text{ dB}$			$RIN_{NOLM} = -20 \text{ dB}$		
		$T_w L$ (ps)	$KAI_{NOLM} +$ M NXT_{NOLM} (dB)	Power Penalty (dB)	$T_w L$ (ps)	$KAI_{NOLM} +$ M NXT_{NOLM} (dB)	Power Penalty (dB)	$T_w L$ (ps)	$KAI_{NOLM} +$ M NXT_{NOLM} (dB)	Power Penalty (dB)
-3	1	6.7	-2.7	1.99	6.4	-3.8	1.98	6.2	-4.6	2.12
-3	2	6.7	-2.6	2.02	6.5	-3.1	2.15	6.2	-3.9	2.32
-3	3	6.8	-2.3	2.1	6.5	-2.7	2.25	6.2	-3.2	2.48
-3	4	6.7	-2.1	2.16	6.3	-2.6	2.28	5.9	-3	2.54
-5	1	6.7	-2.7	1.99	6.5	-3.2	2.12	6.2	-4.1	2.27
-5	2	6.9	-2.1	2.16	6.5	-2.7	2.26	6.2	-3.1	2.51
-5	3	6.6	-2	2.19	6.1	-2.4	2.34	5.5	-2.8	2.59
-5	4	5.9	-1.9	2.22	5	-2.3	2.37	3.9	-2.7	2.62
-7	1	6.8	-2.5	2.05	6.5	-3.1	2.15	6.3	-3.5	2.41
-7	2	6.8	-2	2.19	6.3	-2.4	2.34	5.7	-2.9	2.56
-7	3	5.8	-1.8	2.26	4.8	-2.2	2.4	3.4	-2.6	2.65

As concluded in Chapter 6, RXT_{NOLM} decreases as the number of channels increases. NXT_{NOLM} and RIN_{NOLM} are independent of the number of OTDM channels. Figure 8.19 shows RXT_{NOLM} versus the total walk-off time for 300 Gb/s demultiplexing. The same set of optimised NOLM parameters are applied to both cases of 30 and 300 channels for simulations. (See Tables 8.5 and 8.6). NXT_{NOLM} is also shown in the figure for comparison purpose. As shown in Fig. 8.19, RXT_{NOLM} is about 5 dB and 15 dB lower compared with NXT_{NOLM} for OTDM channels of 30 and 300, respectively. In both cases, NXT_{NOLM} is the

dominant crosstalk. The total crosstalk is decreased from -2.6 dB to -3.8 dB for an increase of OTDM channels from 30 to 300 (see Tables 8.5 and 8.6).

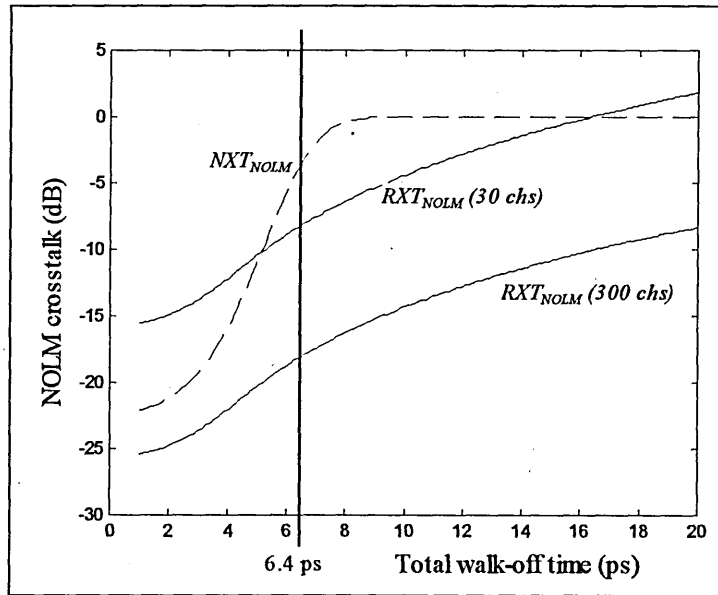


Fig. 8.19. NOLM crosstalk versus the total walk-off time for 300 Gb/s demultiplexing.

One may wonder why a small decrease of crosstalk (~ 1.2 dB) leads to a decrease of power penalty by 1.84 dB (from 3.82 dB to 1.98 dB). A scrutiny of the receiver model is required in order to answer this question. In the equation of calculating BER (8.18), the noise terms that are affected by the NOLM crosstalk are $\sigma_{RIN,s}^2$, $\sigma_{amp,s}^2$ and $\sigma_{rece,s}^2$, which represent the relative intensity noise, optical amplifier noise and receiver noise for space, respectively. Referring to (8.13) to (8.16), all these noise terms are directly proportional to the electrical bandwidth B_e , which is equal to $0.7 \cdot R_b$. For 300 channels demultiplexing, the electrical bandwidth is decreased from 7 GHz to 0.7 GHz as the number of channels is increased from 30 to 300. Thus, increasing the number of OTDM channels effectively reduce the amount of noise. The substantial decrease of power penalty by increasing the number of channels is mainly due to the decreased electrical bandwidth, rather than the decrease of RXT_{NOLM} . Given the same values of RIN_{NOLM} , RXT_{NOLM} and

NXT_{NOLM} , increasing the number of OTDM channels will decrease the power penalty of NOLM demultiplexer.

The power penalty of 300 Gb/s (300 channels) TOAD demultiplexing for various L_{SLA} are plotted in Fig. 8.20. As shown in Fig. 8.20, the minimum power penalty for 300 Gb/s (300 channels) TOAD demultiplexing is 2.06 dB, which is nearly the same as that of NOLM demultiplexing (1.98 dB). The optimised TOAD parameters for the minimum power penalty are $L_{SLA} = 0.1$ mm and $T_{asy} = -7$ ps.

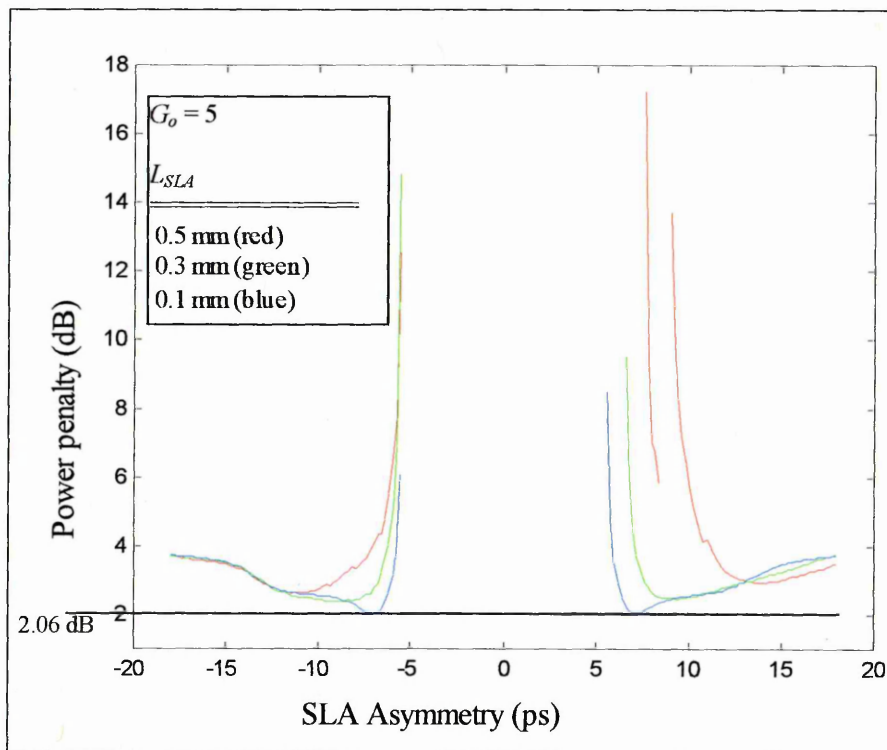


Fig. 8.20. TOAD power penalty versus the SLA asymmetry for 300 Gb/s demultiplexing (300 channels).

BER versus average received optical power for 300 Gb/s (300 channels) optimised NOLM and TOAD demultiplexing are plotted in Fig. 8.21. The optimised NOLM and TOAD schemes have nearly the same BER performance, and require about 0.5 dB more optical power compared with the base line case of no demultiplexer.

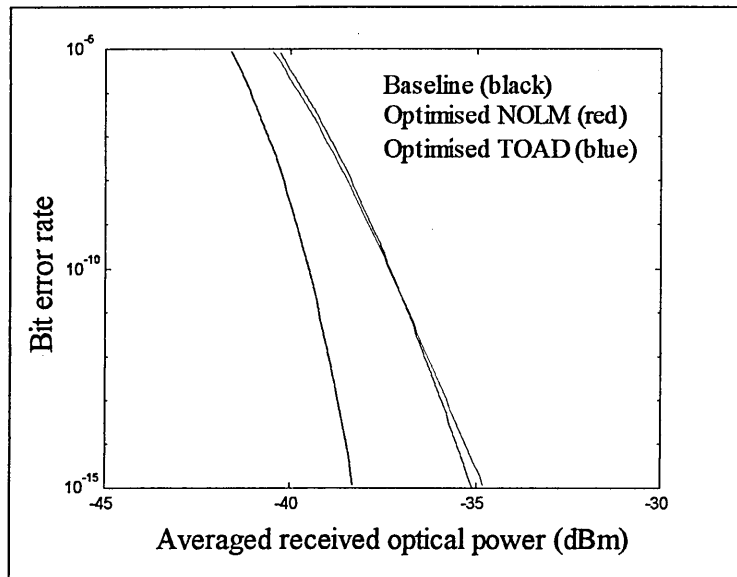


Fig. 8.21. BER versus the average received optical power for 300 Gb/s (30 channels) optimised NOLM and TOAD demultiplexing.

8.5 Summary

This chapter outlined the BER performance of NOLM and TOAD demultiplexers. First, the timing jitter of high capacity OTDM signal was investigated on the basis of the pioneer work by Gordon and Haus. Then a model for the simulation of BER performance of the receiver system was described in detail. The NOLM and TOAD demultiplexers were then optimised with the aim of minimising the power penalty of the OTDM system. The BER performances of the NOLM and TOAD demultiplexing were compared using the optimised parameters. It was found that optimised NOLM and TOAD demultiplexers have similar BER performances for 100 Gb/s and 300 Gb/s OTDM signals. The simulation results also showed that TOAD has a slightly better BER performance for a smaller number of OTDM channels.

CHAPTER NINE – CONCLUSIONS AND FURTHER WORKS

9.1 Conclusions

All optical time division demultiplexer is an essential element in high capacity OTDM transmission systems. The nonlinear optical loop mirror and terahertz optical asymmetric demultiplexer are two promising candidates for realising all optical time division demultiplexing. The demultiplexing operations of NOLM and TOAD have been demonstrated experimentally in laboratories. However, very little work has been reported on their noise and crosstalk characteristics. This PhD study has attempted to address them.

Chapter 2 is dedicated to a historical and technical review of OTDM and WDM technologies. The review concluded that all-optical time division demultiplexer is potentially a key device for realising the next generation long-haul communication systems. The operation principles of NOLM and TOAD demultiplexers are based on the nonlinear properties of optical fibres and semiconductor laser amplifier. The theoretical backgrounds of these two important branches of nonlinear optics are described in Chapters 3 and 4, respectively. In order to investigate the noise and crosstalk characteristics of NOLM and TOAD demultiplexing, new mathematical models are developed for evaluating the switching windows of the two demultiplexers. The mathematical models are also used for optimising the demultiplexing operations of NOLM and TOAD. The NOLM and TOAD models are presented in the first half of Chapter 5 and in Chapter 6, respectively. The NOLM model consists of four analytical equations. The first two equations are used to optimise NOLM parameters for maximising transmission window at the output port of the demultiplexer. The third and fourth equations are used for calculating window width and window profile, respectively. In the TOAD model, the switching energy of the control pulse is optimised for maximising the transmission gain of the TOAD window. All

computer simulations presented in this thesis were carried out using a software package called Matlab.

The simulation results obtained from the NOLM and TOAD models are used to investigate the noise and crosstalk characteristics of the two demultiplexers. The noise and crosstalk analysis of NOLM demultiplexer were discussed in the second half of Chapter 5. It was found that the demultiplexer noise and crosstalk are varied with the NOLM parameters, which include (i) first order dispersion coefficient, (ii) length of the fibre loop, and (iii) the total walk-off time between control and signal pulses. There is a compromise between noise and crosstalk for minimising the overall power penalty of NOLM demultiplexing.

The simulation results obtained from the optimised TOAD parameters are used to investigate the noise and crosstalk characteristics of TOAD demultiplexers in Chapter 7. The noise and crosstalk are largely independent of the gain of the asymmetrically located SLA. Apart from that, the dependence of the noise and crosstalk on other TOAD parameters displayed complex characteristics. The bit-error-rate performance can be maximised by plotting the power penalty against different values of TOAD parameters. The device parameters that affect the power penalty of TOAD demultiplexer are SLA length and SLA asymmetry.

The bit-error-rate performances of NOLM and TOAD demultiplexing are compared for 100 Gb/s and 300 Gb/s OTDM signals in Chapter 8. The OTDM channels used in the analysis are 10 and 100 for the 100 Gb/s signal, 30 and 300 for the 300 Gb/s signal. The simulation results show that, for a smaller number of OTDM channels and a fixed total bit rate, TOAD offers a slightly improved bit-error-rate performance compared with NOLM. This improvement is due to the presence of NOLM residual crosstalk, which increases with the repetition rate of the control pulses. Since the repetition rate of the control pulses is

inversely proportional to the number of OTDM channels, NOLM residual crosstalk is larger for a smaller number of OTDM channels. Nevertheless, for a large number of OTDM channels, NOLM and TOAD demultiplexers have almost the same bit-error-rate performance.

The mathematical models presented in this thesis can be employed as design reference models of the NOLM and TOAD demultiplexers for determining the desirable values of device parameters at minimum power penalty. The device parameters of the NOLM demultiplexer include the first order dispersion coefficient β_2 , the walk-off time per unit length T_w , the FWHM pulse width of the soliton control pulse T_{FWHM} and the fibre loop length L . Equation 5.17 is used to calculate the optimised values of T_{FWHM} from other NOLM parameters for maximising peak transmittance of the switching window. Then the optimised NOLM parameters are used to calculate NOLM switching profile using Eqn 5.34. The NOLM switching profiles are substituted into Eqns 6.1 and 6.11 for calculating RIN_{NOLM} and NXT_{NOLM} , respectively. The NOLM parameters, being optimised by Eqn 5.17, are substituted into Eqn 6.10 for calculating RXT_{NOLM} . The crosstalk and noise performances of the NOLM demultiplexers are characterised by RIN_{NOLM} , NXT_{NOLM} and RXT_{NOLM} , which are the input parameters to the receiver model presented in Chapter 8 for evaluating the power penalty of NOLM demultiplexing. The system parameters describing the characteristics of the OTDM signal are the aggregate bit rate of the OTDM signal R_B , the time division multiplication factor M_{TDM} and the RMS timing jitter between signal pulses RMS_{jitter} . Following the procedures illustrated in Chapter 8, a software package for the design reference model could be developed to evaluate the desirable values of NOLM device parameters at minimum power penalty. The three important user-defined parameters of this software package are R_B , M_{TDM} and RMS_{jitter} .

The design reference model for TOAD demultiplexing can be applied to optimise the device parameters of the TOAD demultiplexers in a way that is similar to the one described above for the NOLM demultiplexers. The device parameters of the TOAD demultiplexers include the unsaturated gain of the SLA G_o , the energy of the control pulse E_{CTRL} , the SLA asymmetry T_{asy} , and other SLA's parameters. The first step is to optimise E_{CTRL} for maximising the peak gain of the TOAD switching window using Eqns 7.15 and 7.19. Then the SLA model presented in Chapter 7 is used to calculate the switching profile of the optimised E_{CTRL} . The calculated switching profile is substituted into Eqns. 7.23, 7.24 and 7.25 for calculating RIN_{TOAD} , NXT_{TOAD} and RXT_{TOAD} , respectively. The crosstalk and noise performances of the TOAD demultiplexers are characterised by RIN_{TOAD} , NXT_{TOAD} and RXT_{TOAD} , which are the input parameters to the receiver model presented in Chapter 8 for evaluating the power penalty of NOLM demultiplexing. The values of the TOAD parameters that lead to the lowest power penalty are the output of the design reference model.

9.2 Further Works

The ideal transmission window of NOLM demultiplexer is in rectangular shape, with a width that is just wide enough to demultiplex the target pulses. A rectangular-shape transmission window is made possible only if ultra-short control pulses are used. The window width is adjusted by changing the walk-off time between control and signal pulses. According to (3.23), a narrow soliton pulse leads to high peak power. For high power soliton propagation, stimulated Raman scattering (SRS) will continuously downshift the mean frequency of subpicosecond soliton pulses [132]. In the NOLM demultiplexer, the effect of SRS on a high power control pulse is a downshift of its central frequency. The change of central frequency will be accompanied with a change of propagating velocity of the control pulse. More importantly, as the SRS-induced downshift of the central frequency

is proportional to the propagation distance, the velocity of the propagating control pulse will be varied with its instantaneous position along the fibre loop. Since the walk-off time between the control and signal pulses depends on their velocity difference, the walk-off time per unit length T_w will also be varied with the instantaneous position of the propagating control pulse. Because of the SRS effect, T_w in the NOLM demultiplexer will no longer be a constant value. As the NOLM model presented in Chapter 5 treats T_w as a constant value, the model will be no longer valid if the high optical power of the control pulse triggers the SRS effect. In that case, the whole NOLM model needs to be reworked to cater for the changing T_w .

In TOAD, the target channel is demultiplexed by control pulses, which periodically change the carrier dynamics of the SLA. The carrier density of the SLA is first depleted by a control pulse, then recovers back to the equilibrium level for the next cycle of carrier dynamics to begin. The highest bit rate of individual OTDM channels in the BER analysis (Chapter 8) is 10 Gb/s. This is restricted by the recovery time of the SLA. In the TOAD model, the recovery time of the SLA is assumed to be 100 ps, which is equivalent to the baseband bit rate of 10 Gb/s. For a further increase of baseband bit rate, the recovery time of the SLA needs to be decreased for stable operations. The shortest recovery time of the current state-of-the-art SLA is about 100 ps, which limits the highest baseband bit rate to 10 Gb/s. R.J.Manning and D.A.O Davies demonstrated that the recovery time of a SLA can be shortened to less than 10 ps, provided that a continuous light beam passes through the SLA [153]-[154]. If the bit rate of OTDM channels is increased to greater than 10 Gb/s, the TOAD model in Chapter 6 needs to be modified for incorporating the effect of the continuous light beam into the demultiplexing mechanism.

REFERENCES

- [1] K. J. Blow, J. K. Lucek, and K. Smith, 'Optical switching', *SPIE*, Vol. 1983 (Optics as a Key to High Technology), 1993, pp. 480-484.
- [2] C. M. Miller, R. King, M. J. Woodward, T. L. Bagwell, D. L. Faller, Jr. J. Straznicky, and N. L. Whang, 'Design of optical receiver modules for digital communications analysis', *Hewlett-Packard Journal*, December 1996, Article 3.
- [3] N. A. Olsson, 'Lightwave systems with optical amplifiers', *Journal of Lightwave Technology*, Vol. 7, No. 7, 1989, pp. 1071-1082.
- [4] J. G. Zhang, 'Very-high-speed fibre optic networks for broadband communications', *I.E.E. Electronics & Communication Engineering Journal*, Dec. 1996, pp. 257-267.
- [5] M. Nakazawa, E. Yoshida, T. Yamamoto, E. Yamada, and A. Sahara, 'TDM single channel 640Gbit/s transmission experiment over 60km using a 400fs pulse train and a walk-off free dispersion-flattened nonlinear optical loop mirror' *OFC'98*, San Jose, USA, 1998, PD 14.
- [6] K. Struyve, N. Wauters, P. Falcao, P. Arijs, D. Colle, P. Demeester, and P. Lagasse, 'Application, design, and evolution of WDM in GTS's pan-European transport network', *IEEE Communications Magazine*, March 2000, pp. 114-121.
- [7] J. P. Ryan, R. H. Kent, 'WDM: North American deployment trends', *IEEE Communications Magazine*, Feb. 1998, pp. 40-44.
- [8] E. Lowe, 'Current European WDM deployment trends', *IEEE Communications Magazine*, Feb. 1998, pp. 46-50.
- [9] M. Sexton, A. Reid, 'Broadband networking: ATM, SDH and SONET', Artech House Publishers, 1997.
- [10] J. C. Bellamy, 'Digital network synchronization', *IEEE Communications Magazine*, April 1995, pp. 70-83.
- [11] U. Black, 'Emerging communications technologies', Prentice Hall series in advanced communications technologies, 2nd Edition, 1997.
- [12] B. Jopson, A. Gnauck, 'Dispersion compensation for optical fiber systems', *IEEE Communications Magazine*, June 1995, pp. 96-102.
- [13] M. Nakazawa, K. Suzuki, E. Yoshida, E. Yamada, T. Kitoh, and M. Kawachi, '160Gbit/s soliton data transmission over 200km', *Electronics Letters*, Vol. 31, No. 7, 1995, pp. 565-566.
- [14] K. S. Lee, 'Optical loop mirror multiplexer', *IEEE Photonics Technology Letters*, Vol. 7, No. 12, 1995, pp. 1444-1446.

- [15] R. Langenhorst, M. Eiselt, W. Pieper, G. Großkopf, R. Ludwig, L. Küller, E. Dietrich, and H. G. Weber, 'Fiber loop optical buffer', *Journal of Lightwave Technology*, Vol. 14, No. 3, 1996, pp. 324-334.
- [16] K. J. Blow, N. J. Doran, B. K. Nayar, and B. P. Nelson, 'Two-wavelength operation of the nonlinear fiber loop mirror', *Optics Letters*, Vol. 15, No. 4, 1990, pp. 248-250.
- [17] J. P. Sokoloff, P. R. Prucnal, I. Glesk, M. Kane, 'A terahertz optical asymmetric demultiplexer (TOAD)', *IEEE Photonics Technology Letters*, Vol. 5, No. 7, 1993, pp. 787-790.
- [18] S. Fischer, M. Dülk, E. Gamper, W. Vogt, E. Gini, H. Melchior, W. Hunziker, D. Nessel, and A. D. Ellis, 'Optical 3R regenerator for 40Gbit/s networks', *Electronics Letters*, Vol. 35, No. 23, 1999, pp. 2047-2049.
- [19] K. Iwatsuki, S. Kawai, N. Shigendo, and M. Saruwatari, 'Timing jitter due to carrier linewidth of laser-diode pulse sources in ultra-high soliton transmission', *Journal of Lightwave Technology*, Vol. 13, No. 4, 1995, pp. 639-649.
- [20] J. M. H. Elmirghani, H. T. Mouftah, 'Technologies and architectures for scalable dynamic dense WDM networks', *IEEE Communications Magazine*, Feb. 2000, pp. 58-66.
- [21] D. M. Spirit, M. J. O'Mahony, 'High capacity optical transmission explained', The Wiley – BT Series, 2nd Edition, 1995.
- [22] H. Takahashi, K. Oda, H. Toba, and Y. Inoue, 'Transmission characteristics of arrayed waveguide $N \times N$ wavelength multiplexer', *Journal of Lightwave Technology*, Vol. 13, No. 3, 1995, pp. 447-455.
- [23] Y. Inoue, Y. Ohmori, M. Kawachi, S. Ando, T. Sawada, and H. Takashashi, 'Polarization-insensitive arrayed-waveguide grating multiplexer with polyimide waveplate as TE/TM mode converter', *Dig. Conf. Integrated Photonics*, Res., OSA, Feb. 1994, Paper ThE3.
- [24] P. Trishitta, M. Colas, M. Green, G. Wuzniak, and J. Arena, 'The TAT-12/13 cable network', *IEEE Communications Magazine*, Feb. 1996, pp. 24-28.
- [25] E. Desurvire, 'Erbium-doped fiber amplifier', Wiley Inter-science, 1994.
- [26] Y. Yamada, S. I. Nakagawa, K. Takashina, T. Kawazawa, H. Taga, and K. Goto, '25GHz spacing ultra-dense WDM transmission experiment of 1Tbit/s (100 WDM \times 10Gbit/s) over 7300km using non pre-chirped RZ format', *Electronics Letters*, Vol. 35, No. 25, 1999, pp. 2212-2213.

- [27] Y. Tachikawa, Y. Inoue, M. Kawachi, H. Takahashi, and K. Inoue, 'Arrayed-waveguide grating add-drop multiplexer with loop-back optical paths', *Electronics Letters*, Vol. 29, 1993, pp. 2133-2134.
- [28] S. J. B. Yoo, 'Wavelength conversion technologies for WDM network application', *Journal of Lightwave Technology*, Vol. 14, No. 6, 1996, pp. 955-966.
- [29] S. Yao, S. Dixit, 'Advances in photonic packet switching: an overview', *IEEE Communications Magazine*, Feb. 2000, pp. 84-94.
- [30] N. Ghani, S. Dixit, and T. S. Wang, 'On IP-over-WDM integration', *IEEE Communications Magazine*, March 2000, pp. 72-84.
- [31] T. Durhuus, B. Mikkelsen, C. Joergensen, S. L. Danielsen, and K. E. Stubkjaer, 'All-optical wavelength conversion by semiconductor optical amplifiers', *Journal of Lightwave Technology*, Vol. 14, No. 6, 1996, pp. 942-954.
- [32] M. Nakazawa, K. Suzuki, E. Yamada, H. Kubota, Y. Kimura, and M. Takaya, 'Experimental demonstration of soliton data transmission over unlimited distances with soliton control in time and frequency domains', *Electronics Letters*, Vol. 29, 1993, pp. 729-730.
- [33] K. Iwatsuki, K. Suzuki, S. Nishi, and M. Saruwatari, '80 Gb/s optical soliton transmission over 80 km with time/polarization division multiplexing', *IEEE Photonics Technology Letters*, Vol. 5, 1993, pp. 245-248.
- [34] A. Takada, M. Saruwatari, 'Pulse-width-tunable subpicosecond pulse generation from an actively mode-locked monolithic MQW laser electroabsorption modulator', *CLEO '94*, 1994, paper CWN5.
- [35] G. P. Agrawal, 'Nonlinear Fiber Optics', 2nd Edition, Academic Press, 1995
- [36] G. P. Agrawal, N. A. Olsson, 'Amplification and compression of weak picosecond optical pulses by using semiconductor-laser amplifiers', *Optics Letters*, Vol. 14, No. 10, 1989, pp. 500-502.
- [37] K. Uchiyama, H. Takara, S. Kawanishi, T. Morioka, M. Saruwatari, and T. Kitoh, '100 Gbit/s all-optical demultiplexing using nonlinear optical loop mirror with gating-width control', *Electronics Letters*, Vol. 29, No. 21, 1993, pp. 1870-1871.
- [38] W. A. Pender, T. Widdowson, and A. D. Ellis, 'Error free operation of a 40Gbit/s all-optical regenerator', *Electronics Letters*, Vol. 32, No. 6, 1999, pp. 230-231.
- [39] H. J. Thiele, A. D. Ellis, and I. D. Phillips, 'Recirculating loop demonstration of 40Gbit/s all-optical 3R data regeneration using a semiconductor nonlinear interferometer', *Electronics Letters*, Vol. 35, No. 3, 1999, pp. 230-231.

- [40] S. Kawanishi, K. Okamoto, M. Ishii, O. Kamatani, H. Takara, and K. Uchiyama, 'All-optical time-division-multiplexing of 100Gbit/s signal based on four-wave mixing in a travelling-wave semiconductor laser amplifier', *Electronics Letters*, Vol. 33, No. 11, 1997, pp. 976-977.
- [41] E. Jahn, N. Agrawal, H. J. Ehrke, R. Ludwig, W. Pieper, and H. G. Weber, 'Monolithically integrated asymmetric mach-Zehnder interferometer as a 20Gbit/s all-optical add/drop multiplexer for OTDM systems', *Electronics Letters*, Vol. 32, No. 3, 1996, pp. 216-217.
- [42] H. Yoshimura, K. Sato, N. Takachio, 'Future photonic transport networks based on WDM technologies', *IEEE Communications Magazine*, Feb. 1999, pp. 74-81.
- [43] C. G. Atkins, J. F. Massicott, J. R. Armitage, R. Wyatt, B. J. Ainslie, and S. P. Craig-Ryan, 'High-gain broad spectral bandwidth erbium-doped fibre amplifier pumped near 1.5 μm ', *Electronics Letters*, Vol. 25, No. 14, 1989, pp. 910.
- [44] H. S. Chung, D. Lee, S. J. Ahn, H. K. Cho, and Y. C. Chung, 'Demonstration of 37nm gain bandwidth from 40 cascaded EDFA system using an equaliser based on all-fibre acousto-optic tunable filters', *Electronics Letters*, Vol. 34, No. 21, 1998, pp. 2045-2047.
- [45] T. Sakamoto, J. Kani, M. Jinno, S. Aisawa, M. Fukui, M. Yamada, and K. Oguchi, 'Wide wavelength band (1535-1560nm and 1574-1600nm), 28 \times 10Gbit/s WDM transmission over 320km dispersion-shifted fibre', *Electronics Letters*, Vol. 34, No. 4, 1998, pp. 392-394.
- [46] Y. Emori, K. Tanaka, and S. Namiki, '100nm bandwidth flat-gain Raman amplifiers pumped and gain-equalised by 12-wavelength-channel WDM laser diode unit', *Electronics Letters*, Vol. 35, No. 16, 1999, pp. 1355-1356.
- [47] S. A. E. Lewis, S. V. Chernikov, and J. R. Taylor, 'Gain saturation in silica-fibre Raman amplifier', *Electronics Letters*, Vol. 35, No. 11, 1999, pp. 923-924.
- [48] M. J. O'Mahony, 'Optical multiplexing in fiber networks: progress in WDM and OTDM', *IEEE Communication Magazine*, Dec. 1995, pp. 82-88.
- [49] M. Eiset, 'Limits on WDM systems due to four-wave-mixing: a statistical approach', *Journal of Lightwave Technology*, Vol. 17, No. 11, 1999, pp. 2261-2267.
- [50] L. Rapp, 'Experimental investigation of signal distortions induced by cross-phase modulation combined with dispersion', *IEEE Photonics Technology Letters*, Vol. 9, No. 12, 1997, pp. 1592-1594.
- [51] M. Shtaif, M. Eisele, 'Analysis of intensity interference caused by cross-phase modulation in dispersive optical fibers', *IEEE Photonics Technology Letters*, Vol. 10, No. 7, 1998, pp. 979-981.

- [52] P. Forghieri, R. W. Tkach, and A. R. Chraplyvy, 'Performance of WDM systems with unequal channel spacing to suppress four wave mixing', *Proceedings of ECOC'94*, Florence, Sept. 1994, pp. 741-744.
- [53] J. P. Gordon, H. A. Haus, 'Random walk of coherently amplified solitons in optical fiber transmission', *Optics Letters*, Vol. 11, No. 10, 1986, pp. 665-667.
- [54] M. J. Potasek, G. P. Agrawal, and S. C. Pinault, 'Analytic and numerical study of pulse broadening in nonlinear dispersive optical fibers', *Journal of Optical Society of America B*, Vol. 3, No. 2, 1986, pp. 205-211.
- [55] L. F. Mollenauer, E. Lichtman, M. J. Neubelt, and J. T. Harvey, 'Demonstration, using sliding-frequency guiding filters of error-free soliton transmission over more than 20Mm at 10Gbit/s, single channel and over more than 13Mm at 20Gbit/s in a two channel WDM', *Electronics Letters*, Vol. 29, 1993, pp. 910-911.
- [56] Y. Kodama, M. Romagnoli, and S. Wabnitz, 'Soliton stability and interactions in fibre lasers', *Electronics Letters*, Vol. 28, 1992, pp. 1981-1983.
- [57] M. Matsumoto, H. Ikeda, T. Uda, and A. Hasegawa, 'Stable soliton transmission in the system with nonlinear gain', *Journal of Lightwave Technology*, Vol. 13, No. 4, 1995, pp. 658-665.
- [58] L. F. Mollenauer, J. P. Gordon, and S. G. Evangelides, 'The sliding-frequency guiding filter: An improved form of soliton jitter control', *Optics Letters*, Vol. 17, 1992, pp. 1575-1577.
- [59] W. Forysiak, N. J. Doran, 'Reduction of Gordon-Haus jitted in soliton transmission systems by optical phase conjugation', *Journal of Lightwave Technology*, Vol. 13, No. 5, 1995, pp. 850-855.
- [60] J. M. Arnold, 'Solitons in communications', *IEE Electronics & Communication Engineering Journal*, April 1996, pp. 88-96.
- [61] K. Bertilsson, P. A. Andrekson, 'Numerical study of moderate distance high bit-rate alternating-amplitude soliton systems', *Journal of Lightwave Technology*, Vol. 14, No. 3, 1996, pp. 237-241.
- [62] E. Yoshida, T. Yamamoto, A. Sahara, and M. Nakazawa '320Gbit/s TDM transmission over 120km using 400fs pulse train', *Electronics Letters*, Vol. 34, No. 10, 1998, pp. 1004-1005.
- [63] S. Kawanishi, H. Takara, K. Uchiyama, I. Shake, and K. Mori, '3Tbit/s (160Gbit/s \times 19 channel) optical TDM and WDM transmission experiment', *Electronics Letters*, Vol. 35, No. 10, 1999, pp. 826-827.
- [64] P. A. Andrekson, N. A. Olsson, J. R. Simpson, T. Tanbun-ek, R. A. Logan, and M. Haner, '16 Gbit/s all-optical demultiplexing using four-wave-mixing', *Electronics Letters*, Vol. 27, No. 11, 1991, pp. 922-924.

- [65] K. Uchiyama, T. Morioka, S. Kawanishi, H. Takara, and M. Saruwatari, 'Signal-to-noise ratio analysis of 100 Gb/s demultiplexing using nonlinear optical loop mirror', *Journal of Lightwave Technology*, Vol. 15, No. 2, 1997, pp. 194-201.
- [66] A. Majewski, A. Prądziecki, 'Propagation of ultra-short optical pulses in nonlinear optical fibers: an analysis by the beam propagation method', Lviv, Ukraine, *MMET'96 Proceedings*, pp. 409-411.
- [67] R. N. Bracewell, 'Fourier Transform And Its Application', 2nd Edition, McGraw-Hill, 1986.
- [68] V. E. Zakharov, A. B. Shabat, 'Exact theory of two-dimensional self-focusing and one-dimensional self-modulation of waves in nonlinear media', *Sov. Phys. JETP*, Vol. 34, No. 1, 1972, p. 62
- [69] J. M. Senior, 'Optical Fiber Communications, Principles and Practices', Prentice-Hall International Series in Optoelectronics, 1985.
- [70] M. J. O'Mahony, I. W. Marshall, H. J. Westlake, W. J. Devlin, and J. C. Regnault, 'A 200-km 1.5- μm optical transmission experiment using a semiconductor laser amplifier repeater', *OFC 1986*, Atlanta, GA, paper WE5.
- [71] J. C. Simon, 'Semiconductor laser amplifier for single mode optical fiber communications', *Journal of Optical Communications*, Vol. 4, 1983, pp. 51-62.
- [72] M. J. O'Mahony, 'Semiconductor laser optical amplifiers for use in future fiber systems', *Journal of Lightwave Technology*, Vol. 6, No. 4, 1986, pp. 531-544.
- [73] H. Taga, N. Edagawa, S. Yamamoto, and S. Akiba, 'Recent progress in amplified undersea systems', *Journal of Lightwave Technology*, Vol. 13, No. 5, 1995, pp. 829-840.
- [74] K. C. Lee, O. K. Li, S. M. Hwang, and A. E. Willner, 'Multi-wavelength all-optical networks with wavelengths outside the erbium-doped fiber amplifier bandwidth', *Journal of Lightwave Technology*, Vol. 13, No. 5, 1995, pp. 791-801.
- [75] J. Wilson, J. F. B. Hawkes: "Optoelectronics: An Introduction", Prentice-Hall International Series in Optoelectronics, 1983.
- [76] A. E. Siegman, 'Lasers', Oxford University Press, 1986.
- [77] L. Gillner, 'Modulation properties of a near travelling-wave semiconductor laser amplifier', *IEE Proceedings-J*, Vol. 139, No. 5, 1992, pp. 331-338.
- [78] M. J. Adams, J. V. Collins, I. D. Henning, 'analysis of semiconductor laser optical amplifiers', *IEE Proceedings*, Vol. 132, Pt. J, No. 1, 1985, pp. 58-63.

- [79] A. J. Lowery, 'New inline wideband dynamic semiconductor laser amplifier model', *IEE Proceedings*, Vol. 135, Pt. J, No. 3, 1988, pp. 242-250.
- [80] Dietrich Marcuse, 'Computer model of an injection laser amplifier', *IEEE Journal of Quantum Electronics*, Vol. QE-19, No. 1, 1983, pp. 63-73.
- [81] T. Muka, Y. Yamamoto, 'Gain, frequency bandwidth, and saturation output power of AlGaAs DH laser amplifier', *IEEE Journal of Quantum Electronics*, Vol. QE-17, Vol. 6, 1981, pp. 1028-1034.
- [82] M. L. Ligne, Y. Sorel, and J. F. Kerdiles, 'Theoretical and experimental study of a saturated near travelling wave amplifier working at 1 Gbit/s and 4.8 Gbit/s', *Journal of Optical Communications*, Vol. 11, No. 3, 1990, pp. 104-106.
- [83] I. D. Henning, M. J. Adams, J. V. Collins, 'Performance predictions from a new optical amplifier model', *IEEE Journal of Quantum Electronics*, Vol. QE-21, No. 6, 1985, pp. 609-613.
- [84] L. Gillner, 'Comparative study of some travelling-wave semiconductor laser amplifier models', *IEE Proceedings-J*, Vol. 139, No. 5, 1992, pp. 339-347.
- [85] M. Connelly, 'Wideband semiconductor optical amplifier steady-state model', CSNDSP 2000, 18-20 July 2000, p. 96-101.
- [86] G. P. Agrawal, N. A. Olsson, 'Self-phase modulation and spectral broadening of optical pulses in semiconductor laser amplifiers', *IEEE Journal of Quantum Electronics*, Vol. 25, No. 11, 1989, pp. 2297-2306.
- [87] G. P. Agrawal, 'Fiber-optic Communication System', 2nd Edition, Wiley 1997.
- [88] G. Swift, Z. Ghassemlooy, and A. K. Ray, J. R. Travis, 'Modelling of semiconductor laser amplifier for the terahertz optical asymmetric demultiplexer', *IEE Proc.-Circuits Devices Syst.*, Vol. 145, No. 2, 1998, pp. 61-65.
- [89] Y. Z. Huang, 'On the rate equation of semiconductor lasers for measuring spontaneous emission factor', *IEEE Photonics Technology Letters*, Vol. 7, No. 9, 1995, pp. 977-979
- [90] J. Manning, R. Olshansky, and C. B. Su, 'The carrier-induced index change in AlGaAs and 1.3 μm InGaAsp diode lasers', *IEEE Journal of Quantum Electronics*, Vol. QE-19, No. 10, 1983, pp. 1525-1530.
- [91] S. P. Dijaili, J. M. Wiesenfeld, G. Raybon, C. A. Burrus, A. Dines, J. S. Smith, and J. R. Whinnery, 'Cross-phase modulation in a semiconductor laser amplifier determined by a dispersive technique', *IEEE Journal of Quantum Electronics*, Vol. 28, No. 1, 1992, pp. 141-150.

- [92] M. S. Stix, M. P. Kesler, and E. P. Ippen, 'Observations of subpicosecond dynamics in GaAlAs laser diodes', *Applied Physics Letters*, Vol. 48, No. 25, 1986, pp. 1722-1724.
- [93] M. P. Kesler, E. P. Ippen, 'Subpicosecond gain dynamics in GaAlAs laser diodes', *Applied Physics Letters*, Vol. 51 No. 22, 1987, pp. 1765-1767.
- [94] Y. Lai, K. K. Hall, E. P. Ippen, and G. Eisenstein, 'Short pulse gain saturation in InGaAsP diode laser amplifiers', *IEEE Photonics Technology Letters*, Vol. 2, No. 10, 1990, pp. 711-713.
- [95] P. J. Delfyett, Y. Silberberg, 'Hot-carrier thermalization induced self-phase modulation in semiconductor traveling wave amplifiers', *Applied Physics Letters*, Vol. 59, No. 1, 1991, pp. 10-12.
- [96] C. T. Hultgren, E. P. Ippen, 'Ultrafast refractive index dynamics in AlGaAs diode laser amplifiers', *Applied Physics Letters*, Vol. 59, No. 6, 1991, pp. 635-637.
- [97] J. Mark, J. Mørk, 'Subpicosecond gain dynamics in InGaAsP optical amplifiers: experiment and theory', *Applied Physics Letters*, Vol. 61, No. 19, 1992, pp. 2281-2283.
- [98] K. L. Hall, A. M. Darwish, E. P. Ippen, U. Koren, and G. Raybon, 'Femtosecond index nonlinearities in InGaAsP optical amplifiers', *Applied Physics Letters*, Vol. 62, No. 12, 1993, pp. 1320-1322.
- [99] M. Y. Hong, Y. H. Chang, A. Dienes, J. P. Heritage, and P. J. Delfyett, 'Subpicosecond pulse amplification in semiconductor laser amplifiers: theory and experiment', *IEEE Journal of Quantum Electronics*, Vol. 30, No. 4, 1994, pp. 1122-1131.
- [100] P. J. Delfyett, A. Dienes, J. P. Heritage, M. Y. Hong, and Y. H. Chang, 'Femtosecond hybrid mode-locked semiconductor laser and amplifier dynamics', *Applied Physics B*, Vol. 58, 1994, pp. 183-195.
- [101] S. Schuster, H. Haug, 'Influence of carrier kinetics on subpicosecond gain dynamics in diode laser amplifiers', *Applied Physics Letters*, Vol. 66, No. 22, 1995, pp. 2987-2989.
- [102] J. M. Tang, P. S. Spencer, and K. A. Shore, 'Influence of fast gain depletion on the dynamic response of TOAD's', *Journal of Lightwave Technology*, Vol. 16, No. 1, 1998, pp. 86-90.
- [103] H. C. Casey, M. B. Panish, 'Heterostructure Lasers Part A: Fundamental Principles', Academic Press, 1978.
- [104] N. J. Doran, D. Wood, 'Nonlinear-optical loop mirror', *Optics Letters*, Vol. 13, No. 1, January 1988, pp. 56-58.

- [105] N. J. Doran, D. S. Forrester, and B. K. Nayar, 'Experimental investigation of all-optical switching in fibre loop mirror device', *Electronics Letters*, Vol. 25, No. 4, 1989, pp. 267-269.
- [106] M. N. Islam, E. R. Sunderman, R. H. Stolen, W. Pleibel, and J. R. Simpson, 'Soliton switching in a fiber nonlinear loop mirror', *Optics Letters*, Vol. 14, No. 15, 1989, pp. 811-813.
- [107] K. J. Blow, N. J. Doran, B. K. Nayar, and B. P. Nelson, 'Two-wavelength operation of the nonlinear fibre loop mirror', *Optics Letters*, No. 15, 1990, pp. 248-250.
- [108] K. J. Blow, N. J. Doran, and B. P. Nelson, 'Demonstration of the nonlinear fibre loop mirror as an ultrafast all-optical demultiplexer', *Electronics Letters*, Vol. 26, No. 14, 1990, pp. 962-964.
- [109] B. P. Nelson, K. J. Blow, P. D. Constantine, N. J. Doran, J. K. Lucek, I. W. Marshall, and K. Smith, 'All-optical Gbit/s switching using nonlinear optical loop mirror', *Electronics Letters*, Vol. 27, No. 9, 1991, pp. 704-705.
- [110] N. A. Whitaker, H. Avramopoulos, P. M. W. French, M. C. Gabriel, R. E. Lamarche, D. J. Digovanni, and H. M. Presby, 'All-optical arbitrary demultiplexing at 2.5 Gbit/s with tolerance to timing jitter', *Optics Letters*, Vol. 16, No. 23, 1991, pp. 1838-1840.
- [111] M. Jinno, T. Matsumoto, 'Nonlinear sagnac interferometer switch and its applications', *IEEE Journal of Quantum Electronics*, Vol. 28, No. 4, 1992, pp. 875-882.
- [112] K. Uchiyama, H. Takara, S. Kawanishi, T. Morioka, and M. Saruwatari, 'Ultrafast polarisation-independent all-optical switching using a polarisation diversity scheme in the nonlinear optical loop mirror', *Electronics Letters*, Vol. 28, No. 20, 1992, pp. 1864-1866.
- [113] N. A. Whitaker, P. M. W. French, M. C. Gabriel, and H. Avramopoulos, 'Polarization-independent all-optical switching', *IEEE Photonics Technology Letters*, Vol. 4, No. 3, 1992, pp. 260-262.
- [114] H. Bülow, G. Veith, 'Polarisation-independent switching in a nonlinear optical loop mirror by a dual-wavelength switching pulse', *Electronics Letters*, Vol. 29, No. 7, 1993, pp. 588-589.
- [115] D. M. Patrick, A. D. Ellis, and D. M. Spirit, 'Bit-rate flexible all-optical demultiplexing using a nonlinear optical loop mirror', *Electronics Letters*, Vol. 29, No. 8, 1993, pp. 702-703.
- [116] M. Takara, S. Kawanishi, K. Uchiyama, M. Saruwatari, and T. Kitoh, 'Nearly-penalty-free, fully TDM 100-Gbit/s optical transmission by using two tunable mode-locked Er-doped fiber lasers', *OFC '94 Technical Digest*, TuD5, pp. 15-16.

- [117] K. Uchiyama, S. Kawanishi, H. Takara, T. Morioka, and M. Saruwatari, '100 Gbit/s to 6.3 Gbit/s demultiplexing experiment using polarisation-independent nonlinear optical loop mirror', *Electronics Letters* Vol. 30, No. 11, 1994, pp. 873-875.
- [118] B. Desruelle, E. Desurvire, and S. Bigo, 'Analysis of the polarization group-velocity dispersion effect in polarization-independent nonlinear-optical loop mirror demultiplexers', *Optics Letters*, Vol. 20, No. 5, 1995, pp. 516-518.
- [119] K. Uchiyama, H. Takara, S. Kawanishi, T. Morioka, and M. Saruwatari, 'Ultrafast polarisation-independent all-optical switching using a polarisation diversity scheme in the nonlinear optical loop mirror', *Electronics Letters*, Vol. 28, No. 20, 1992, pp. 1864-1866.
- [120] L. P. Barry, P. Guignard, J. Debeau, R. Boittin, B. Kennedy, and J. D. Harvey, 'Effect of control pulse deformation on the switching characteristics of a NOLM', *ACFT'96*, pp. 197-200.
- [121] D. Wang, E. A. Golovchenko, A. N. Pilipetskii, C. R. Menyuk, and M. F. Arend, 'Nonlinear optical loop mirror based on standard communication fiber', *Journal of Lightwave Technology*, Vol. 15, No. 4, 1997, pp. 642-646.
- [122] W. S. Man, H. Y. Tam, and M. S. Demokan, 'Optimal loop length of a nonlinear optical loop mirror in switching solitons', *Journal of Lightwave Technology*, Vol. 16, No. 1, 1998, pp. 100-105.
- [123] D. B. Mortimore, 'Fiber loop reflectors', *Journal of Lightwave Technology*, Vol. 6, No. 7, 1988, pp. 1217-1224.
- [124] B. S. Kawasaki, K. O. Hill, and R. G. Lamont, 'Biconical-taper single-mode fiber coupler', *Optics Letters*, Vol. 6, No. 7, 1981, pp. 327-328.
- [125] D. B. Mortimore, 'Low-loss 8×8 single-mode star coupler', *Electronics Letters*, Vol. 21, No. 11, 1985, pp. 502-504.
- [126] F. P. Payne, C. D. Hussey, and M. S. Yataki, 'Modelling fused single-mode fibre couplers' *Electronics Letters*, Vol. 21, No. 11, 1985, pp. 461-462.
- [127] J. V. Wright, 'Wavelength dependence of fused couplers', *Electronics Letters*, Vol. 22, No. 6, 1986, pp. 320-321.
- [128] A. Takagi, K. Jinguji, M. Kawachi, 'Broadband silica-based optical waveguide coupler with asymmetric structure', *Electronics Letters*, Vol. 16, No. 2, 1990, pp. 132-133.
- [129] D. B. Mortimore, 'Wavelength-flattened fused couplers', *Electronics Letters*, Vol. 21, No. 17, 1985, pp. 742-743.
- [130] K. A. Stroud, 'Engineering Mathematics', 4th Edition, Macmillan.

- [131] P. R. Turner: "Numerical Analysis", Macmillan.
- [132] J. P. Gordon, 'Theory of the soliton self-frequency shift', *Optics Letters*, Vol. 11, No. 10, 1986, pp. 662-664.
- [133] B. D. Hahn, 'Essential Matlab for Scientists and Engineers', Arnold 1997.
- [134] A. N. Pinto, G. P. Agrawal, and J. F. Rocha, 'Effect of soliton interaction on timing jitter in communication systems', *Journal of Lightwave Technology*, Vol. 16, No. 4, 1998, pp. 515-519.
- [135] K. Suzuki, K. Iwatsuki, S. Nishi, and M. Saruwatari, '160 Gbit/s single polarisation subpicosecond transform limited pulse signal demultiplexing using ultrafast optical loop mirror including MQW travelling wave semiconductor laser amplifier', *Electronics Letters*, Vol. 30, No. 8, 1994, pp. 660-661.
- [136] D. Zhou, K. I. Kang, I. Glesk, and P. R. Prucnal, 'Saturation effects in a terahertz asymmetric optical demultiplexer', *Lasers and Electro-optics Society Annual Meeting – LEOS*, Orlando, TuA5, 1-4 Dec. 1998, pp. 16-17.
- [137] A. D. Ellis, D. A. O. Davies, A. Kelly, and W. A. Pender, 'Data driven operation of semiconductor amplifier loop mirror at 40 Gbit/s', *Electronics Letters*, Vol. 31, No. 15, 1995, pp. 1245-1247.
- [138] I. Glesk, P. R. Prucnal, '250-Gb/s self-clocked optical TDM with a polarization-multiplexed clock', *Fiber and Integrated Optics*, Vol. 14, 1994, pp. 71-82.
- [139] D. A. O. Davies, A. D. Ellis, and G. Sherlock, 'Regenerative 20Gbit/s wavelength conversion and demultiplexing using a semiconductor laser amplifier nonlinear loop mirror', *Electronics Letters*, Vol. 31, No. 12, 1995, pp. 1000-1001.
- [140] D. A. O. Davies, A. D. Ellis, T. Widdowson, and G. Sherlock, '10Gbit/s data switched semiconductor laser amplifier nonlinear loop mirror', *Electronics Letters*, Vol. 31, No. 2, 1995, pp. 111-112.
- [141] A. D. Ellis, D. M. Spirit, 'Compact 40Gbit/s optical demultiplexer using a GaInAsP optical amplifier', *Electronics Letters*, Vol. 29, No. 24, 1993, pp. 2115-2116.
- [142] J. P. Sokoloff, I. Glesk, P. R. Prucnal, 'Performance of 50 Gbit/s optical time domain multiplexed system using a terahertz optical asymmetric demultiplexer', *IEEE Photonics Technology Letters*, Vol. 6, No. 1, 1994, pp. 98-100.
- [143] R. J. Manning, A. E. Kelly, A. J. Poustie, K. J. Blow, 'An improved semiconductor optical amplifier for ultrafast all-optical signal processing', *IEEE Nonlinear Optics Topical Meeting, Proc. 1998*, Princeville USA, TuB7, pp. 159-161.

- [144] J. M. Tang, P. S. Spencer, and K. A. Shore, 'Analysis of operating characteristics of TOADs using gain saturation and nonlinear gain in SOAs', *IEE Proc-Optoelectronics*, Vol. 145, No. 1, 1998, pp. 83-87.
- [145] Z. Xiang, P. Ye, K. J. Guan, and J. T. Lin, 'A novel OTDM frame synchronization scheme based on a terahertz optical asymmetric demultiplexer with feedback', *IEEE Photonics Technology Letters*, Vol. 11, No. 1, 1999, pp. 125-127.
- [146] K. Suzuki, K. Iwatsuki, S. Nishi, and M. Saruwatari, 'Error-free demultiplexing of 160Gbit/s pulse signal using optical loop mirror including semiconductor laser amplifier', *Electronics Letters*, Vol. 30, No. 18, 1994, pp. 1501-1503.
- [147] M. Eiselt, W. Pieper, and H. G. Weber, 'SLALOM: Semiconductor laser amplifier in a loop mirror', *Journal of Lightwave Technology*, Vol. 13, No. 10, 1995, pp. 2099-2110.
- [148] D. Zhou, K. I. Kang, I. Glesk, and P. R. Prucnal, 'An analysis of signal-to-noise ratio and design parameters of a terahertz optical asymmetric demultiplexer', *Journal of Lightwave Technology*, Vol. 17, No. 2, 1999, pp. 298-307.
- [149] M. Pickering, 'An Introduction to Fast Fourier Transform methods for partial differential equations, with applications', Research Studies Press: Wiley, 1986.
- [150] H. Kressel, 'Topics in Applied Physics', Vol. 39, 2nd Edition, Springer-Verlag, 1987.
- [151] G. Einarsson, 'Principles of Lightwave Communications', John Wiley, 1996.
- [152] M. Schwartz, 'Information transmission, modulation, and noise', 4th Edition, McGraw-Hill, 1990
- [153] R. J. Manning, D. A. O. Davies, D. Cotter, and J. K. Lucek, 'Enhanced recovery rates in semiconductor laser amplifiers using optical pumping', *Electronics Letters*, Vol. 30, 1994, pp. 787-788.
- [154] R. J. Manning, D. A. O. Davies, and J. K. Lucek, 'Recovery rates in semiconductor laser amplifier: Optical and electrical bias dependencies', *Electronics Letters*, Vol. 30, No. 15, 1994, pp. 1233-1235.
- [155] M. Nakazawa, T. Yamamoto, K. R. Tamura, '1.28Tbit/s-70km OTDM transmission using third- and fourth-order simultaneous dispersion compensation with a phase modulator', *Electronics Letters*, Vol. 36, No. 24, 2000, pp. 2027-2029.

- [156] B. Zhu, L. Leng, L.E. Nelson, Y. Qian, S. Stulz, C. Doerr, L. Stulz, S. Chandrasekar, S. Radic, D. Vengsarkar, Z. Chen, J. Park, K. Feder, H. Thiele, J. Bromage, et al, '3.08 Tb/s (77×42.7 Gb/s) transmission over 1200 km of non-zero dispersion-shifted fiber with 100-km spans using C- and L-band distributed Raman amplification', Conference on Optical Fiber Communication, Technical Digest Series, Vol. 54, No. 4, 2001, pp. PD23/1-PD23/3.
- [157] R. Scarmozzino, B. K. Whitlock, E. K. Heller, R. M. Jr. Osgood, 'Numerical methods for modeling photonic devices and systems', Proceedings of SPIE - The International Society for Optical Engineering, v 3944 (II), (2000), pp. 548-560.

APPENDIX MATLAB PROGRAM FOR BPM

```

%%%%%%%%%%%%%%%%%%%%%%%%%%%%%%%%%%%%%%%%%%%%%%%%%%%%%%%%%%%%%%%%%%%%%%%%
% program: pul_prop.m
% author : Nelson Cheung
% Desc.  : this program solves the nonlinear schrodinger equation by using beam propagation
%         method.
%%%%%%%%%%%%%%%%%%%%%%%%%%%%%%%%%%%%%%%%%%%%%%%%%%%%%%%%%%%%%%%%%%%%%%%%
% variables
%=====
% p_p = peak power of the optical pulse
% fwhm_w = Full Width at Half Maximum pulse width
% n_of_intv = number of time interval for numerical analysis
%           (it should be an interger of 2^r for fast fourier transform)
% t_intv = time interval for numerical analysis of the gaussian pulse
% t = time axis
% f_o_d is the first order dispersion coefficient
% loss_db is the power loss in dB
% loss is the amplitude loss ratio per kilometre
% r is the nonlinear coefficient
% tot_walkoff is the total walkoff time
% k is factor of increased resolution for the calculation of phase change
% f_factor is a factor for calculating the frame period of the control pulse for fft
% p_p = 1.73;

fwhm_w = 7.4516e-12;
n_of_intv = 128;
t_frame = 50e-12;
t_intv = t_frame/n_of_intv;
t = -t_frame/2:t_intv:t_frame/2-t_intv;
f_o_d = -10*1e-24*1e-3;

loss_db = 0.2;
loss = 1 - 10^(-1*loss_db/1000/10);
r = 2e-3;
tot_walkoff = 3e-12;
k = round(t_intv/(tot_walkoff/1500));
p_p = abs(f_o_d)*3.11/r/(fwhm_w^2);

%%%%%%%%% initialisation of phase change
phase_change = zeros(1,(length(t)-1)*k+1);

% pulse intensity profile
power = p_p .* soliton(t,fwhm_w/1.763);

% convert light power to amplitude
a = power.^0.5;

% initialise variables for the main loop
% -----
% f is the frequency axis
% d_t is the dispersion and loss term
% tdomain_a is an array of signal amplitude in time domain for fast fourier transform
% fdomain_a is an array of signal amplitude in frequency domain for the operation of
%         inverse fourier transform
% rearrange_f = rearrange fdomain_a to a form that is suitable for calculation of
%         chromatic dispersion (central frequency has a value 0)

f = four_f(t_intv,n_of_intv);

d_t = exp(-loss/2 + ((f.*(2*pi)).^2)./2.*f_o_d.*sqrt(-1));

spm_const = 2 * r * sqrt(-1);

figure(1)

for length_ctr = 1:1500

    fdomain_a = fftshift(fft(fftshift(a))); % fast fourier transform

    fdomain_a = fdomain_a.*d_t; % multiply the amplitude in frequency domain by the
dispersion
% terms

    a = fftshift(ifft(fftshift(fdomain_a)));

```

```

new_p = real(a).^2 + imag(a).^2;

spm = exp(new_p.*spm_const);

a = a.*spm;

fdomain_a = fftshift(fft(fftshift(a)));
fdomain_a = fdomain_a.*d_t;

a = fftshift(ifft(fftshift(fdomain_a)));

if rem(length_ctr,100) == 0
    new_p = real(a).^2 + imag(a).^2;
    subplot(3,1,1)
    plot3(2.*length_ctr.*ones(size(t))./1000,t.*1e12,new_p)
    xlabel('Propagation Distance (km)')
    ylabel('Time (ps)')
    zlabel('Optical Power (W)')
    hold on
    length_ctr
end

%%%%%%%%%%%%%%%%%%%%%%%%%%%%%%%%%%%%%%%%%%%%%%%%%%%%%%%%%%%%%%%%%%%%%%%%
%% calculation of phase change
%%%%%%%%%%%%%%%%%%%%%%%%%%%%%%%%%%%%%%%%%%%%%%%%%%%%%%%%%%%%%%%%%%%%%%%%
%% high_r_p is the high resolution p
%% high_r_inc is the small increment between two low resolution P
%%%%%%%%%%%%%%%%%%%%%%%%%%%%%%%%%%%%%%%%%%%%%%%%%%%%%%%%%%%%%%%%%%%%%%%%

new_p = real(a).^2 + imag(a).^2;

high_r_p = zeros(size(phase_change));

high_r_p(1:k:length(high_r_p)) = new_p;

high_r_inc = (new_p(2:length(new_p)) - new_p(1:length(new_p)-1))./k;

for ctrl = 1:k-1
    high_r_p(1+ctrl:k:length(high_r_p)) = new_p(1:length(new_p)-1) +...
        high_r_inc .* (ctrl);
end

phase_change(1+length_ctr:length(phase_change)) =
    phase_change(1+length_ctr:length(phase_change)) ...
    +(4*r).*high_r_p(1:length(high_r_p)-length_ctr);

end

Tx = 1 - cos(phase_change./2).^2;

subplot(3,2,2)

%plot((min(t):t_intv/k:max(t)).*1e12,phase_change)
%xlabel('Time (ps)')
%ylabel('Phase Change')

plot((min(t):t_intv/k:max(t)).*1e12,1-cos(phase_change./2).^2,'--')
xlabel('Time (ps)')
ylabel('Transmittance')

axis([-6 25 0 1])

hold on

%slope=zeros(1,length(Tx)-1);
%for ctr = 1:1:length(Tx)-1
% temp = Tx(ctr+1) - Tx(ctr);
% if temp > 0
%     slope(ctr) = 1;
% elseif temp < 0
%     slope(ctr) = -1;
% end
% end
%end
%pos = (1:length(slope)).*1e-7;
%Tx = round(Tx./max(Tx).*1e4);
%slope_Tx = Tx(1:length(Tx)-1) .* slope;

```

```
%end_pt = min(abs(slope_Tx+0.9.*1e4)+pos);
%st_pt = min(abs(slope_Tx-0.9.*1e4)+pos);
%end_pt = (end_pt - floor(end_pt)) * 1e7;
%st_pt = (st_pt - floor(st_pt)) * 1e7;
%width1 = (end_pt - st_pt) .* (t_intv/k);
%end_pt = min(abs(slope_Tx+0.5.*1e4)+pos);
%st_pt = min(abs(slope_Tx-0.5.*1e4)+pos);
%end_pt = (end_pt - floor(end_pt)) * 1e7;
%st_pt = (st_pt - floor(st_pt)) * 1e7;
%width2 = (end_pt - st_pt) .* (t_intv/k)
```